

Microstrip Antennas: Future Trends and New Applications

Guest Editors: Hala A. Elsadek, Esmat A. Abdallah,
Dalia M. Elsheakh, and Heba Badr El-Din El-Shaarawy





Microstrip Antennas: Future Trends and New Applications

Microstrip Antennas: Future Trends and New Applications

Guest Editors: Hala A. Elsadek, Esmat A. Abdallah,
Dalia M. Elsheakh, and Heba Badr El-Din El-Shaarawy



Copyright © 2013 Hindawi Publishing Corporation. All rights reserved.

This is a special issue published in “International Journal of Antennas and Propagation.” All articles are open access articles distributed under the Creative Commons Attribution License, which permits unrestricted use, distribution, and reproduction in any medium, provided the original work is properly cited.

Editorial Board

M. Ali, USA
Charles Bunting, USA
Felipe Cátedra, Spain
Dau-Chyrh Chang, Taiwan
Deb Chatterjee, USA
Z. N. Chen, Singapore
Michael Yan Wah Chia, Singapore
Christos Christodoulou, USA
Shyh-Jong Chung, Taiwan
Lorenzo Crocco, Italy
Tayeb A. Denidni, Canada
Antonije R. Djordjevic, Serbia
Karu P. Esselle, Australia
Francisco Falcone, Spain
Miguel Ferrando, Spain
Vincenzo Galdi, Italy
Wei Hong, China
Hon Tat Hui, Singapore
Tamer S. Ibrahim, USA
Nemai Karmakar, Australia

Se-Yun Kim, Republic of Korea
Ahmed A. Kishk, Canada
Tribikram Kundu, USA
Byungje Lee, Republic of Korea
Ju-Hong Lee, Taiwan
L. Li, Singapore
Yilong Lu, Singapore
Atsushi Mase, Japan
Andrea Massa, Italy
Giuseppe Mazzearella, Italy
Derek McNamara, Canada
C. F. Mecklenbräuker, Austria
Michele Midrio, Italy
Mark Mirotznik, USA
Ananda S. Mohan, Australia
P. Mohanan, India
Pavel Nikitin, USA
A. D. Panagopoulos, Greece
Matteo Pastorino, Italy
Massimiliano Pieraccini, Italy

Sadasiva M. Rao, USA
Sembiam R. Rengarajan, USA
Ahmad Safaai-Jazi, USA
Safieddin Safavi-Naeini, Canada
Magdalena Salazar-Palma, Spain
Stefano Selleri, Italy
Krishnasamy T. Selvan, India
Zhongxiang Q. Shen, Singapore
John J. Shynk, USA
Mandeep S. Jit Singh, Malaysia
Seong-Youp Suh, USA
Parveen Wahid, USA
Yuanxun Ethan Wang, USA
Daniel S. Weile, USA
Quan Xue, Hong Kong
Tat Soon Yeo, Singapore
Young Joong Yoon, Korea
Wenhua Yu, USA
Jong Won Yu, Republic of Korea
Anping Zhao, China

Contents

Microstrip Antennas: Future Trends and New Applications, Hala A. Elsadek, Esmat A. Abdallah, Dalia M. Elsheakh, and Heba Badr El-Din El-Shaarawy
Volume 2013, Article ID 890764, 1 page

Comparative Study of Antenna Designs for RF Energy Harvesting, Sika Shrestha, Sun-Kuk Noh, and Dong-You Choi
Volume 2013, Article ID 385260, 10 pages

Reconfigured and Notched Tapered Slot UWB Antenna for Cognitive Radio Applications, Tamer Aboufoul, Akram Alomainy, and Clive Parini
Volume 2012, Article ID 160219, 8 pages

An Efficient Analysis Method for Cylindrical Conformal Microstrip Antenna Fed by Microstripline, Chengyou Yin and Mengzhong Hu
Volume 2012, Article ID 629748, 8 pages

Adaptive Forming of the Beam Pattern of Microstrip Antenna with the Use of an Artificial Neural Network, Janusz Dudczyk and Adam Kawalec
Volume 2012, Article ID 935073, 13 pages

Rapid Beam Forming in Smart Antennas Using Smart-Fractal Concepts Employing Combinational Approach Algorithms, Mounissamy Levy, Sumanta Bose, D. Sriram Kumar, and Anh Van Dinh
Volume 2012, Article ID 467492, 10 pages

Design of RFID Reader Antenna for Exclusively Reading Single One in Tag Assembling Production, Chi-Fang Huang and Yi-Feng Huang
Volume 2012, Article ID 162684, 5 pages

Compact MIMO Microstrip Antennas for USB Dongle Operating in 2.52.7 GHz Frequency Band, Vladimir Ssorin, Alexey Artemenko, Alexander Maltsev, Alexey Sevastyanov, and Roman Maslennikov
Volume 2012, Article ID 793098, 12 pages

Harmonic Suppressed Slot Antennas Using Rectangular/Circular Defected Ground Structures, Mohammad Saeid Ghaffarian, Gholamreza Moradi, and Reza Zaker
Volume 2012, Article ID 721565, 7 pages

Hybrid Dielectric Resonator Antenna Composed of High-Permittivity Dielectric Resonator for Wireless Communications in WLAN and WiMAX, Yih-Chien Chen
Volume 2012, Article ID 531436, 6 pages

Design and Analysis of a Novel Compact Wideband Antenna with Two Excited Modes, Li Li, Zhi-Li Zhou, and Jing-Song Hong
Volume 2012, Article ID 351038, 5 pages

A Novel Low RCS Design Method for X-Band Vivaldi Antenna, XiaoXiang He, Teng Chen, and Xin Wang
Volume 2012, Article ID 218681, 6 pages

Novel Compact CPW-Fed Antennas with Harmonic Suppression and Bandwidth Enhancement, Zhi-Li Zhou, Li Li, and Jing-Song Hong
Volume 2012, Article ID 589467, 8 pages

Study on Glass-Epoxy-Based Low-Cost and Compact Tip-Truncated Triangular Printed Antenna,
Rajeev Kumar Kanth, Pasi Liljeberg, Hannu Tenhunen, Qiang Chen, Lirong Zheng, and Harish Kumar
Volume 2012, Article ID 184537, 8 pages

Design of Multilevel Sequential Rotation Feeding Networks Used for Circularly Polarized Microstrip Antenna Arrays, Aixin Chen, Chuo Yang, Zhizhang Chen, Yanjun Zhang, and Yingyi He
Volume 2012, Article ID 304816, 10 pages

A Small UWB Antenna with Dual Band-Notched Characteristics, J. Xu, D.-Y. Shen, G.-T. Wang, X.-H. Zhang, X.-P. Zhang, and K. Wu
Volume 2012, Article ID 656858, 7 pages

Compact Multiband Planar Fractal Cantor Antenna for Wireless Applications: An Approach,
Gopalakrishnan Srivatsun and Sundaresan Subha Rani
Volume 2012, Article ID 839520, 6 pages

Design of Two Novel Dual Band-Notched UWB Antennas, Bing Li and Jing-song Hong
Volume 2012, Article ID 303264, 7 pages

A Reconfigurable Coplanar Waveguide Bowtie Antenna Using an Integrated Ferroelectric Thin-Film Varactor, K. C. Pan, D. Brown, G. Subramanyam, R. Penno, H. Jiang, C. H. Zhang, M. Patterson, D. Kuhl, K. Leedy, and C. Cerny
Volume 2012, Article ID 249019, 6 pages

Flexible Microstrip Antenna for Skin Contact Application, Sudhir Shrestha, Mangilal Agarwal, Parvin Ghane, and Kody Varahramyan
Volume 2012, Article ID 745426, 5 pages

High Gain and High Directive of Antenna Arrays Utilizing Dielectric Layer on Bismuth Titanate Ceramics, F. H. Wee, F. Malek, Farid Ghani, S. Sreekantan, and A. U. Al-Amani
Volume 2012, Article ID 375751, 8 pages

Editorial

Microstrip Antennas: Future Trends and New Applications

**Hala A. Elsadek,¹ Esmat A. Abdallah,¹ Dalia M. Elsheakh,¹
and Heba Badr El-Din El-Shaarawy²**

¹ *Microstrip Department, Electronics Research Institute, National Research Center Buildings, Elthrir Street, Dokki, Giza 12622, Egypt*

² *Micro and Nano Systems for Wireless Communications (MINC), Laboratoire d'Analyse et d'Architectures des Systems, Centre National de la Recherche Scientifique (LAAS-CNRS), 75794 Paris, France*

Correspondence should be addressed to Hala A. Elsadek; helsadek@mcit.gov.eg

Received 14 February 2013; Accepted 14 February 2013

Copyright © 2013 Hala A. Elsadek et al. This is an open access article distributed under the Creative Commons Attribution License, which permits unrestricted use, distribution, and reproduction in any medium, provided the original work is properly cited.

The explosive growth in the demand for wireless communication and information transfer using handsets and personal communications (PCS) devices has created the need for major advancements of antenna designs as a fundamental part of any wireless system. One type of antennas that fulfills most of the wireless systems requirements is the microstrip antennas. These antennas are widely used on base stations as well as handheld devices. Microstrip antennas have a variety of configurations and are currently the most active field in antenna research and development. The microstrip antennas, due to their great advantages, have increasingly wide range of applications in wireless communication systems as handheld mobile devices, satellite communication systems, and biomedical applications. In most PCS, the handheld antenna is placed on a small plastic/shielding box that is in close proximity to biological tissue of user body hence its radiation may cause health hazardous effects. Added to the operational requirements, the users and service providers usually demand wireless units with antennas that are small and compact, cost effective for manufacturability, low profile, and easy to integrate with other wireless communication system components. The antenna designer must consider all these issues besides the electrical characteristics of the antenna performance which include antenna tuning (operating frequency), VSWR and return loss (input impedance), bandwidth, gain and directivity, radiation pattern, diversity, and size of the chassis (expressed as a function of wavelengths) and specific absorption rate (SAR) of the antenna. These design considerations have led antenna designers to

consider a wide variety of structures to meet the often conflicting needs for different applications.

This special issue contains different topics about microstrip antennas. New designs are investigated for several wireless communication applications. Papers are classified from survey about most literature publications in several topics as RF energy harvesting to new designs in UWB antennas, reconfigurable antennas, smart MIMO systems, and so forth.

We hope the readers and researches of microstrip antenna systems will find in this special issue not only new designs about different microstrip antenna characteristics but also valuable information about numerical analysis and fabrications.

*Hala A. Elsadek
Esmat A. Abdallah
Dalia M. Elsheakh
Heba Badr El-Din El-Shaarawy*

Review Article

Comparative Study of Antenna Designs for RF Energy Harvesting

Sika Shrestha,¹ Sun-Kuk Noh,² and Dong-You Choi¹

¹ Department of Information and Communication Engineering, Chosun University, 309 Pilmun-daero Dong-gu, Gwangju 501-759, Republic of Korea

² Department of Photoelectronics Information, Chosun College of Science and Technology, Republic of Korea

Correspondence should be addressed to Dong-You Choi; dychoi@chosun.ac.kr

Received 2 February 2012; Accepted 17 January 2013

Academic Editor: Hala A. Elsadek

Copyright © 2013 Sika Shrestha et al. This is an open access article distributed under the Creative Commons Attribution License, which permits unrestricted use, distribution, and reproduction in any medium, provided the original work is properly cited.

In the last few years, several antenna designs of rectenna that meet various objectives have been proposed for use in RF energy harvesting. Among various antennas, microstrip patch antennas are widely used because of their low profile, light weight, and planar structure. Conventional patch antennas are rectangular or circular in shape, but variations in their basic design are made for different purposes. This paper begins with an explanation and discussion of different designs, put forward with an aim of miniaturization, harmonic rejection, and reconfigurability. Finally, microstrip patch structured rectennas are evaluated and compared with an emphasis on the various methods adopted to obtain a compact rectenna, harmonic rejection functionality, and frequency and polarization selectivity.

1. Introduction

As the demand for power increases, the need for alternate energy sources has become essential. Energy from external sources such as solar power, thermal energy, wind energy, and RF energy has been harvested for various purposes in the last few recent decades. Energy harvesting uses inexhaustible sources with little or no adverse environmental effect and can provide unlimited energy for the lifespan of electronic devices. The work presented here focuses on RF energy harvesting, in which the abundant RF energy from surrounding sources, such as nearby mobile phones, wireless LANs (WLANs), FM/AM radio signals, and broadcast television signals, is captured by a receiving antenna and rectified into a usable DC voltage.

Ambient RF energy is pervasive, especially that from mobile and Wi-Fi networks. ABI Research and IHS iSuppli estimated that the number of mobile phone subscriptions recently surpassed five billions, and the ITU estimated that there is more than one billion subscriptions for mobile broadband. Mobile phones represent a large source of transmitters from which to harvest RF energy and will potentially enable

users to provide power-on-demand for a variety of close-range sensing applications. The number of Wi-Fi routers and wireless end-point devices such as laptops is also significant [1].

At short range (e.g., within the same room), a tiny amount of energy (microwatts) can be harvested from a typical Wi-Fi router transmitting at a power level of 50–100 mW. For longer-range operation, antennas with higher gain are needed for practical harvesting of RF energy from mobile base stations and broadcast radio towers. In 2005, Powercast demonstrated ambient RF energy harvesting at 1.5 miles (~2.4 km) from a small, 5-kW AM radio station. Subsequent demonstrations have included the harvesting of RF energy from an iPhone in the GSM band and from a nearby mobile base station [1].

We can categorize RF energy source into three general groups: intentional sources, anticipated ambient sources, and unknown ambient sources [2]. RF energy harvesting can be implemented as direct power for battery-free systems or battery activation, an auxiliary power source for battery recharging, or remote power with battery backup. A power source combined with energy harvesting can provide wireless

devices with low maintenance cost or extended battery life by implementing the ability to receive power or charge the stored energy when needed, or to wake up remote sensors in sleep mode. The possibility of recycling the ambient electromagnetic energy especially in densely populated urban zones is actively being explored [3]. The major component used to convert this RF energy into utilizable DC power is a rectifying antenna, also termed as rectenna.

Among various entities of rectenna, antenna is one of the major elements which is responsible for collecting the incoming RF signals of various frequencies. The source of incoming RF energy can be WLAN (2.4 GHz, 5.8 GHz), WiMax, RFID (microwave band: 2.45, 5.8, 24.125 GHz) and so forth with various frequency ranges. Antennas with resonance at single or multiple applicable frequencies are designed with various ambitions. The variation made in antenna design that was designed with an aim of miniaturizing patch antenna, rejecting unwanted harmonics, and having reconfigurability in frequency and polarization is evaluated in this paper.

The paper is organized as follows. Rectennas are introduced briefly in Section 2. Several antenna designs of rectenna are discussed and compared with an emphasis on antenna size reduction, harmonic rejection, and reconfigurability in terms of frequency and polarization, in Sections 3, 4, and 5, respectively.

2. Rectennas

A rectenna is a particular type of antenna that rectifies incoming electromagnetic waves into DC current. Over the last century, the development of rectennas for wireless power transmission and space solar power transmission has achieved great success in implementing specific functions and applications, such as RFID tagging systems, sensor batteries or capacitors, WLANs, WiMax, and cognitive radio systems, and also in medical applications.

A typical rectenna consists of four main components: antenna, prerectification filter, rectifying circuit, and DC pass filter. Figure 1 shows a block diagram of a typical rectenna. A microwave antenna collects incoming RF power. An input low-pass filter (LPF; prerectification filter) suppresses the unwanted higher harmonics rejected by the rectifying circuit and also provides matching between the antenna and the rectifier. A rectifying circuit rectifies the AC current induced in the antenna by the microwaves, and an output DC pass filter (postrectification filter) provides a DC path to the load by separating the high-frequency components from the DC signal.

A conventional rectenna consists of a dipole element or a mesh of dipoles that capture microwave energy and a Schottky diode for the rectification process. Several types of rectenna element have been proposed in the last few recent years. The antenna can be of any type, for example, dipole, Yagi-Uda, microstrip, monopole, loop, coplanar patch, spiral, or even parabolic. The rectenna can also take any type of rectifying circuit, such as a single shunt full-wave rectifier, a full-wave bridge rectifier, or another type of hybrid rectifier. A single diode in a serial configuration that also acts as a

half-wave rectifier is the most common rectifying circuit. We can also use a half-wave parallel rectifier, a voltage doubler structure to theoretically double the output DC voltage, or a dual-diode full-wave rectifier to increase the conversion efficiency.

As the primary function of a rectenna is to convert RF energy to DC power, the main design challenge is to obtain high conversion efficiency, and there are basically two approaches to achieve this goal. The first option is to collect the maximum power and deliver it to the rectifying diode, and the second one is to suppress the harmonics generated by the diode that reradiate from the antenna as the power lost. In order to increase the conversion efficiency by the first method, several broadband antennas, large antenna arrays, and circularly polarized antennas have been designed. The broadband antenna receives relatively high RF power from various sources, and antenna array increases incident power delivered to the diode for rectification. Antenna array is an effective means of increasing the receiving power but a tradeoff arises between the antenna size and the radiation gain. The circularly polarized antenna offers power reception with less polarization mismatch. To increase the efficiency by second method, LPF is placed between antenna and rectifying circuit or antenna with the property of harmonic rejection is designed.

Among various types of antenna used in rectennas, microstrip patch antennas are gaining popularity for use in wireless applications owing to their low profile, light weight, low production cost, and being conformable to planar and nonplanar surface, simple, and inexpensive to manufacture using modern printed-circuit technology. The other reason for wide use of patch antenna is the versatility of patch antenna in terms of resonant frequency, polarization, pattern, and impedance when particular patch shape and mode are chosen. Therefore, they are extremely suitable for use as embedded antennas in handheld wireless devices and portable devices.

The rapid development of microstrip antenna technology began in the late 1970s. By the early 1980s, basic microstrip antenna elements and arrays were fairly well established in terms of design and modeling. The early work of Munson on microstrip antennas for use as a low profile flush mounted antennas on rockets and missiles showed that this was a practical concept for use in many antenna system problems. Various mathematical models were developed for this antenna, and its applications were extended to many other fields. A major contributing factor for advances of microstrip antennas is the revolution in electronic circuit miniaturization brought about by developments in large-scale integration. As conventional antennas are often bulky and costly part of an electronic system, microstrip antennas based on photolithographic technology are seen as an engineering breakthrough.

In its most basic forms, a microstrip patch antenna consists of a radiating patch on one side of a dielectric substrate with a ground plane on the other side. Figure 2 shows a diagram of a simple rectangular patch antenna. The patch is generally made of a conducting material such as copper or gold and can take any possible shape, such as

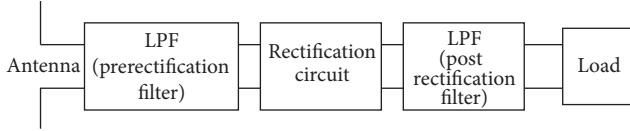


FIGURE 1: Block diagram of rectenna.

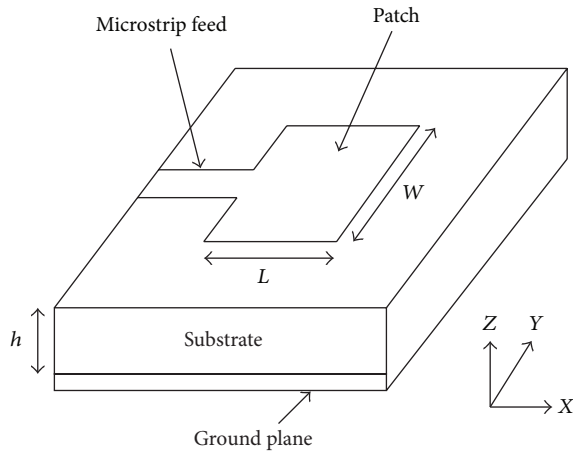


FIGURE 2: 3D view of rectangular patch antenna.

square, rectangular, thin strip (dipole), circular, elliptical, or triangular ones. Square, rectangular, dipole, and circular shapes are the most common because of ease of analysis and fabrication, and their attractive radiation characteristics, especially low cross-polarization radiation. The radiating patch and feed lines are usually photoetched on the dielectric substrate.

Several configurations can be used to feed microstrip antennas. The four most popular ones are the microstrip line, coaxial probe, aperture coupling, and proximity coupling. The microstrip feed line is a conducting strip usually of smaller width connected to the patch. It is easy to fabricate and simple to match by controlling the inset position but spurious radiation increases with the increase in substrate thickness that limits the bandwidth. In coaxial-line feeds, the inner conductor of the coax is attached to the radiation patch, and the outer conductor is attached to the ground plane. It is also easy to fabricate and match, and it has low spurious radiation, but it has narrow bandwidth and is difficult to model especially for thick substrate [4].

Aperture coupled feed consists of two substrates separated by the ground plane. The energy of the microstrip feed line present on the bottom side of the lower substrate is coupled to the patch through a slot on the ground plane separating the two substrates. The ground plane isolates the feed from radiation element and minimizes interference of spurious radiation. Proximity coupling has the largest bandwidth and low spurious radiation. The patch is present on top of the first substrate while the second substrate

contains microstrip feed line on the upper side and the ground plane on the lower side in this technique [4].

3. Antenna Miniaturization

The design of compact antenna for rectennas has been inevitable to cope with the rapid growth of wireless applications. Several methods of reducing the size of microstrip antennas have been suggested. They include the use of high dielectric constant substrates, modification of the basic patch shapes, short circuiting the patch to the ground plane, and other techniques that combine these three methods. When high dielectric constant substrates are used, the guided wavelength underneath the patch is reduced; hence, the resonating patch size is also reduced. The reduction ratio is approximately related to the square root of the relative permittivity " ϵ_r ". Employing high dielectric constant substrates is the simplest method of miniaturization, but the resulting antenna exhibits narrow bandwidth, high loss, and poor efficiency due to surface wave excitation. The modification of the basic patch shapes allows for substantial size reduction; however, some of these shapes will cause inefficient use of the available area. Shorting posts have been used in different arrangements to reduce the overall dimensions of the microstrip patch antenna. These shorting posts were modeled and analyzed as short pieces of transmission line with a series inductance and shunt capacitance [5].

This section is focused on the techniques adopted to reduce the size of the antenna through geometry optimization, slots with different shapes, or both of these techniques. Five miniaturized designs are shown in Figure 3. Figure 3(a) depicts a circular patch antenna with unbalance slots placed on the diameter line, having 45° counter clockwise rotation of the vertical diameter with different size and position relative to the center of the circular disk. By introducing slots in the circular microstrip disk antenna at 2.45 GHz, the antenna radius is reduced from the calculated result of 16.5 mm to 15.5 mm of the proposed one, yielding 12% size reduction [6]. Figure 3(b) consists of a square aperture coupled patch antenna with a cross-shaped slot etched on its surface that permits a patch size reduction of 32.5%. The rectenna has a compact size due to the use of a cross-shaped slot at the patch surface [7].

A two-port, meandered, square patch antenna with forty slits on the perimeter, ten on each side, is investigated at Figure 3(c) obtaining 48% reduction in size. Each group of slits is symmetrically placed with respect to the center of the side where it belongs. The slits disturb the currents flowing on the surface, forcing them to meander and thus increasing the electrical length of the patch antenna in both dimensions. Accordingly, the operating frequency decreases, whereas the physical size of the patch is unaffected. In the similar manner, operation at a fixed frequency with reduced size is possible by increasing the slit length [8]. A square patch with two orthogonal pairs of irregular and unsymmetrical slits is proposed in Figure 3(d). The presence of slits in this antenna is a way to increase the surface current path length compared with that of the conventional square patch

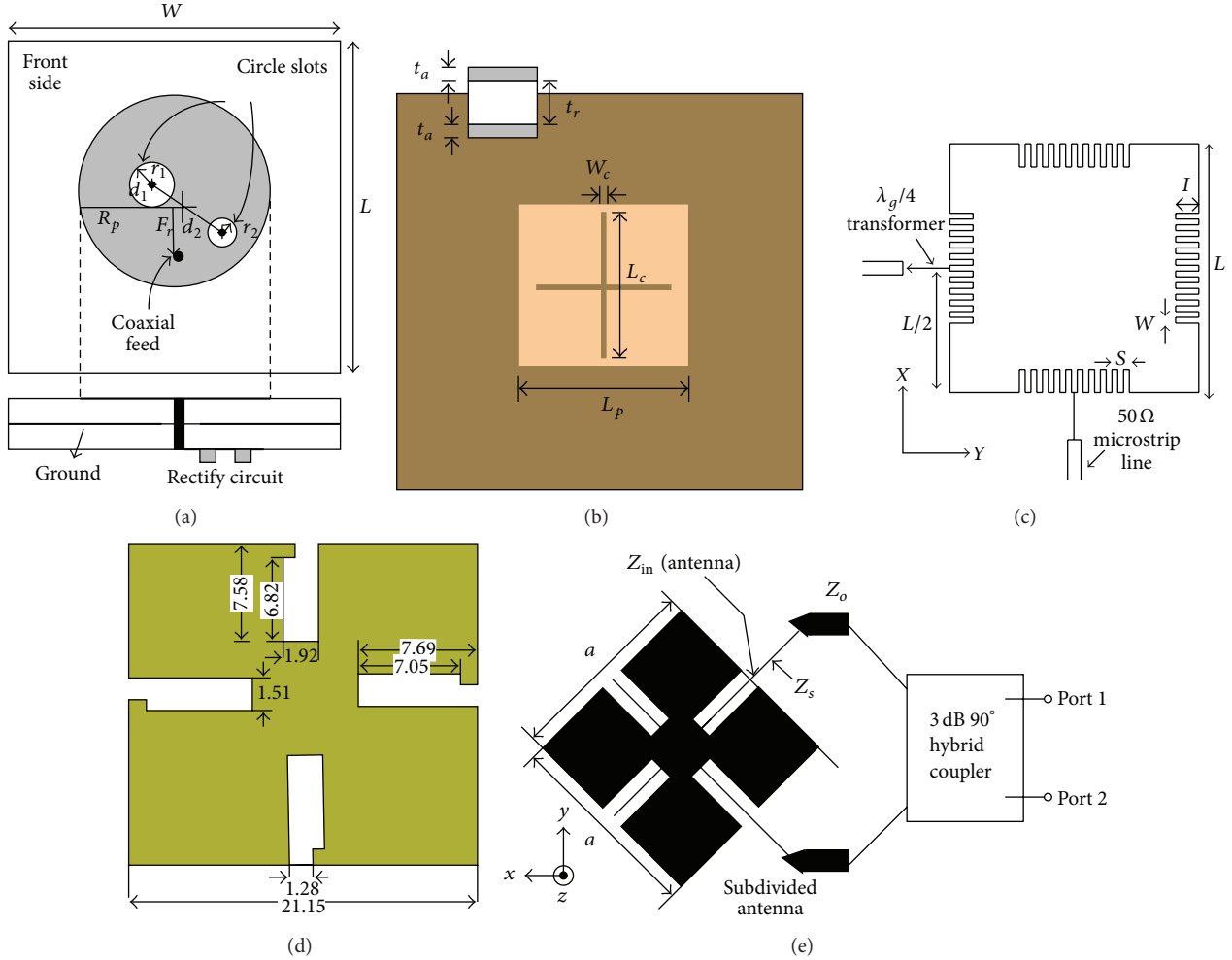


FIGURE 3: Various miniaturized antenna designs.

antenna and to reduce the size to 40% [9]. The antenna shown in Figure 3(e) is composed of the interconnection of four corner patches alternating with four strips and a fifth central patch representing a surface reduction of 60%. The resonance frequency in the proposed antenna is significantly lowered by the subdivided nature of the metal geometry, which introduces longer current paths along its contours, and simultaneously by the strong inductive/capacitive loadings associated with the branch/gap elements [10].

The aforementioned designs were miniaturized by modifying the basic patch shapes and embedding suitable slots in the radiating patch. The application of modifying the conventional antenna and placing slots is to increase their electrical length that lengthens the surface current paths and causes a shift in the resonance frequency. Thus, by reducing the dimensions of the patch, we can get much more compact antenna than their conventional counterpart with the same resonance frequency. We compared the various ways of modifying the conventional patch antenna to obtain small sized antenna. Table 1 briefly does the comparison of Figures 3(a), 3(b), 3(c), 3(d), and 3(e) on the basis of changes done on their basic shape and their corresponding percentage

of size reduction, whose detailed description is present in [6–10], respectively.

4. Harmonic Rejection

Rectifying circuits are used in rectennas to rectify the AC current induced in the antenna by microwaves. The nonlinear components of rectifying circuits, such as diodes, generate harmonics of the fundamental frequency. These unwanted harmonics cause harmonic reradiation and electromagnetic interference with nearby circuits and antennas and reduce efficiency. Therefore, microwave components such as an LPF must be added between the antenna and the diode to suppress these harmonics that improves system performance and prevent harmonic interference. Several rectenna designs having harmonic-rejecting antennas have been proposed to reduce the size and cost by eliminating the prerectification filter. With the removal of prerectification filter, the additional insertion loss at the fundamental frequency associated with it can be eliminated, increasing the efficiency. Hence, the antenna with the harmonic rejection functionality will bring

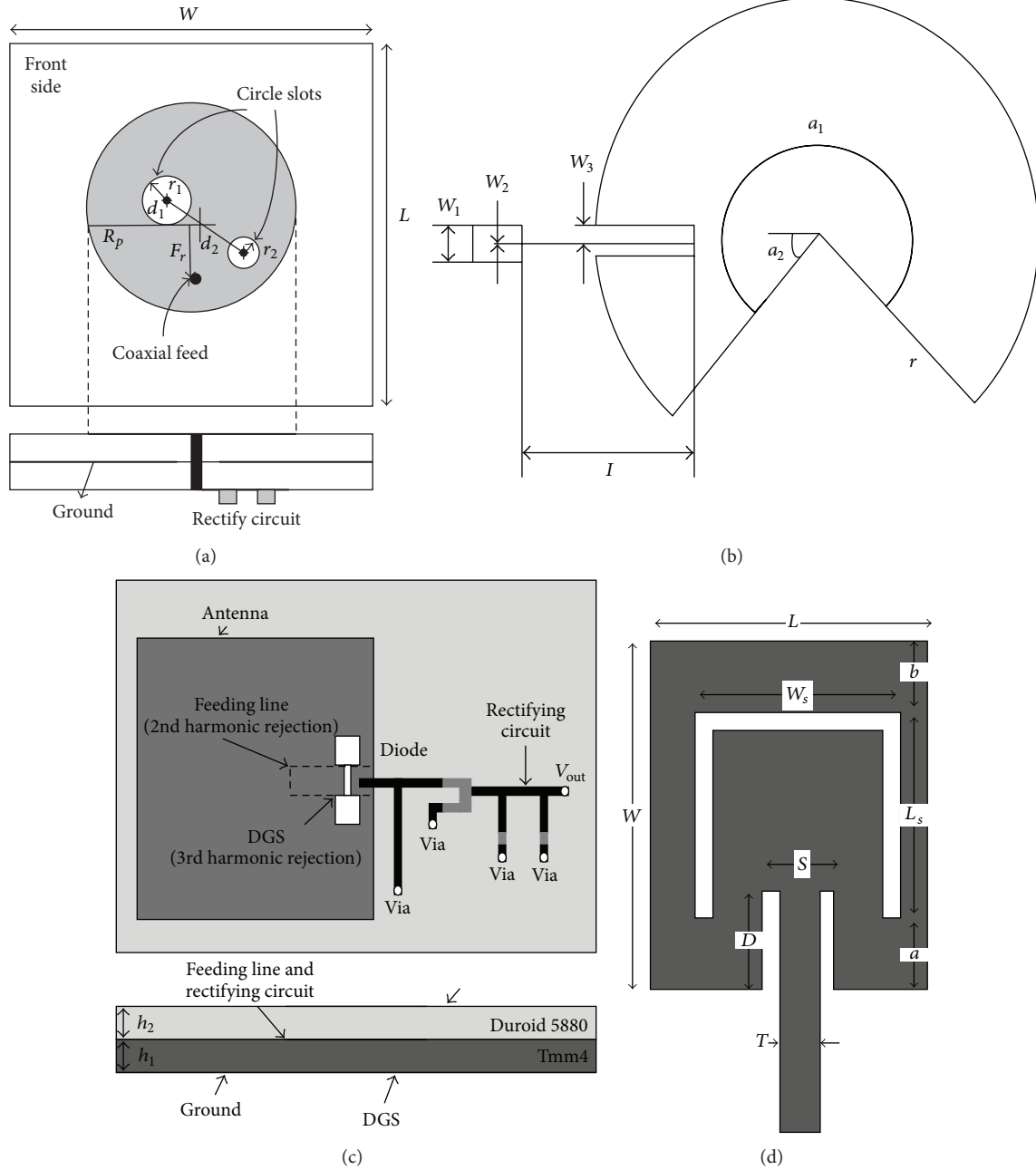


FIGURE 4: Various antenna designs for harmonic rejection.

the advantages of low cost, simpler design, and conversion efficiency enhancement.

Some of the designs having the behavior of harmonic rejection are shown in Figure 4. Figure 4(a) is similar to Figure 3(a), where the unbalanced slot can achieve second harmonic rejection too omitting the requirement of LPF [6]. The diode of rectenna with microstrip square patch antenna operating at 2.4 GHz creates harmonics such as 4.8 and 7.2 GHz, but a microstrip circular-sector antenna with a circular sector angle of 240° and a feeding angle of 30° from

the edge of the circular sector as shown in Figure 4(b) blocks these second and third harmonics from reradiation [11]. Rectangular patch antenna with dumbbell-shaped slot on the ground plane also called as defected ground structure (DGS) resonating at 2.45 GHz as depicted in Figure 4(c) has return loss of -1.95 dB and -1.75 dB at the harmonics frequencies 4.9 GHz and 7.35 GHz, respectively [12]. Figure 4(d) is an inset fed u-slot antenna at 2.4 GHz which exhibits high reflection coefficient at the second and third harmonics. The length of the inset in the particular point not only causes deep

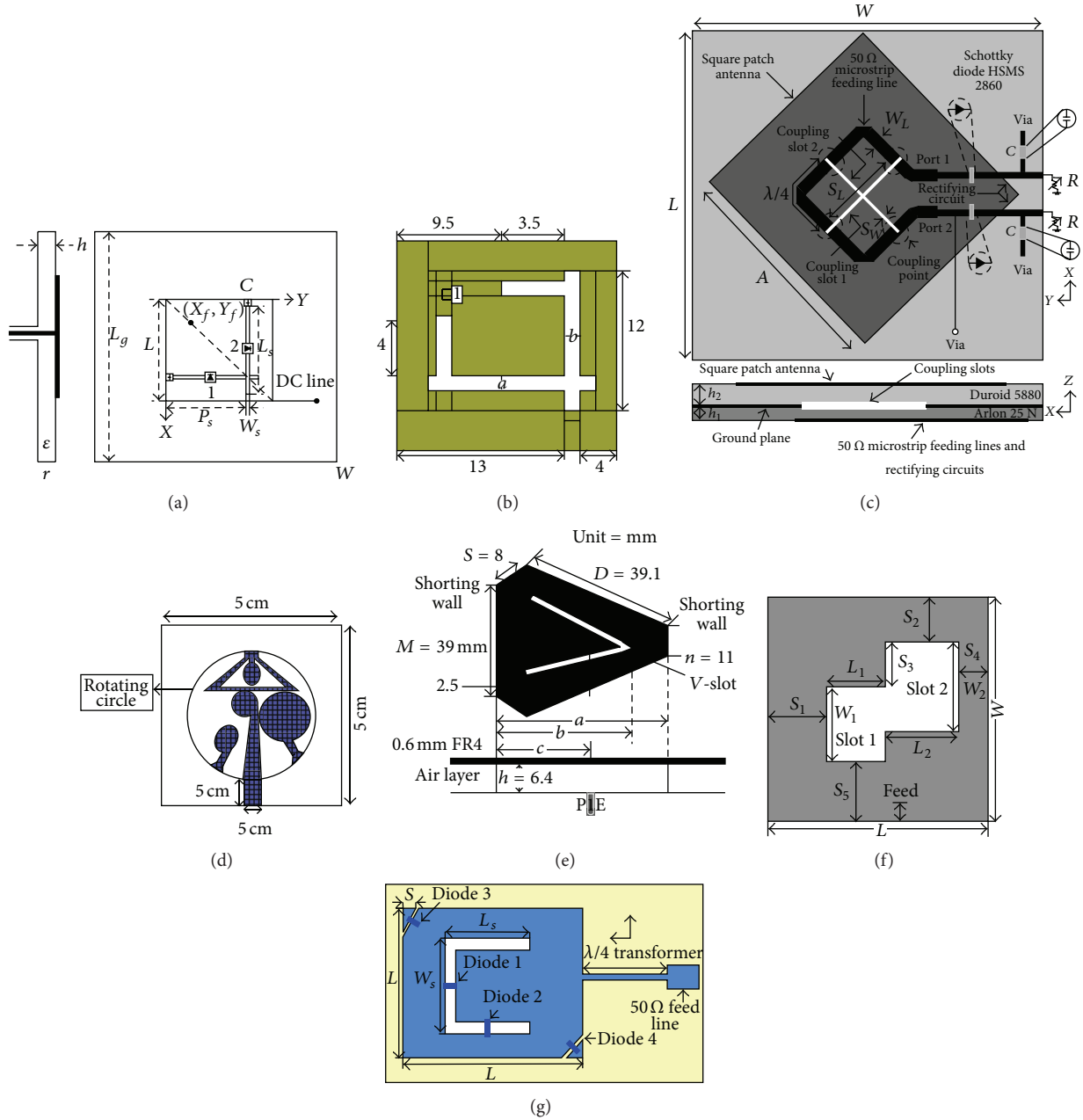


FIGURE 5: Various antennas designed for reconfigurability.

resonance of the antenna in the desired frequency but also suppresses harmonics increasing the efficiency of the system [13].

It is also seen that along with rejecting harmonics the antennas presented in Figure 4 also have higher gain than the conventional antennas. Comparison made between Figures 4(a), 4(b), 4(c), and 4(d) on the basis of modified shape with the cause behind the harmonic rejection, their corresponding gain, and conversion efficiency is shown in Table 2. These antennas are described in detail in [6, 11–13], respectively.

5. Reconfigurable Antennas

Reconfigurable antennas have received much attention in RF energy harvesting models owing to their selectivity for operating frequency and polarization. The characteristic of having frequency selectivity and polarization selectivity can be termed as frequency diversity and polarization diversity, respectively. Frequency diversity accommodates multiband or wideband frequency ranges and automatic frequency tuning. A reconfigurable microstrip antenna can achieve

TABLE 1: Various antenna shapes and size reduction.

Figure	Antenna shape	Freq.	Substrate	Size reduction (%)
3(a)	Circular patch with slots placed on the diameter	2.45 GHz	FR-4 substrate ($\epsilon_r = 4.4$)	12
3(b)	Square patch with cross-shaped slot etched on its surface	2.45 GHz	Two Arlon A25N substrates separated by ROHACELL 51 foam layer	32.5
3(c)	Forty slits on the perimeter of a square patch, ten on each side	2.36 GHz	Taconic, TLY-5 laminate ($\epsilon_r = 2.21$)	48
3(d)	Square patch with two orthogonal pairs of irregular, unsymmetrical slits	GPS design frequency (L_1)	RT/Duroid 6010 LM substrate ($\epsilon_r = 10.2$)	40
3(e)	Square patch with interconnection of four corner patches alternating with four strips and a fifth central patch	5.85 GHz	RT/Duroid 5870 substrate ($\epsilon_r = 2.33$)	60

TABLE 2: Various antenna shapes and the associated harmonic rejection

Figure	Shape	Freq.	Harmonic rejection	Gain	Conversion efficiency
4(a)	Circular patch with slots on the diameter	2.45 GHz	Unbalanced slots achieve second harmonic rejection	3.36 dBic CP gain	Efficiency would reach 53% and 75% with 1 K resistor load under ANSI/IEEE uncontrolled and controlled RF human exposure limit, respectively.
4(b)	Microstrip circular sector antenna	2.4 GHz	Circular sector antenna with sector angle of 240° and inset feeding point at 30° from the edge avoids harmonic radiation	4.677 dBi	Maximum efficiency of 77.8% is achieved with a load resistor of 150Ω and input power of 10 dBm
4(c)	Rectangular patch with DGS	2.45 GHz	An optimized length of the feeding line and DGS are used to reject the second and third harmonics	6.4 dB	Conversion efficiency is 74% using a 1300Ω load resistor at a power density of 0.3 mW/cm^2
4(d)	U-shaped slot in middle surface of inset-fed rectangular patch antenna	2.4 GHz	U-slot antenna with inset feeding suppresses the harmonics	6.96 dBi	Not specified

polarization diversity among linear polarization (LP), right-hand circular polarization (RHCP), and left-hand circular polarization (LHCP). RF reconfigurability is basically achieved by dynamically altering the physical structure of the antenna by connecting and/or disconnecting different parts of the antenna structure that interact with its radiation properties and thereby alter its RF response.

A multiband antenna is needed in order to avoid using two antennas and to allow simultaneous transmission of video, voice, and data information. It can be realized by frequency diversity, which increases the power output, potentially expands the mobility options, and simplifies installation. Two approaches are typically used to obtain wideband frequency ranges: the use of stacked patches and the activation of different modes of the patch. The first approach incorporates a multilayered patch substrate that will resonate at different frequencies. However, this method increases the height of the antenna. The second approach achieves dual-frequency operation by activating two modes under the patch, such as the TM_{10} and TM_{30} modes or the TM_{10} and TM_{01} modes.

The patch elements radiate primarily linear polarized waves; however, by using various feed arrangements with slight modifications of the elements, circular and elliptical polarization can be obtained. Circular polarization can be obtained if two orthogonal modes are excited with a 90° time-phase difference between them. Circular polarization can be LHCP or RHCP. A circularly polarized system is more suitable in several cases because of its insensitivity to transmitter and receiver orientation; for instance, in rotating platforms, circularly polarized rectennas help in achieving the same DC voltage irrespective of rectenna rotation, thus avoiding polarization mismatch and loss. The polarization diversity of reception is important for countering the effects of detrimental fading loss caused by multipath effects and for achieving a high degree of polarization control in order to optimize the system performance.

The design of reconfigurable antennas requires the inclusion of certain switching elements. These elements perform the job of connecting different parts of the antenna. This allows the antenna's shape to be modified, which causes a corresponding change in its RF response (return loss/radiation

TABLE 3: Various antenna shapes and their reconfigurability.

Figure	Antenna shape	Freq.	Reconfigurable feature	Cause of reconfigurability	Application
5(a)	Square patch with orthogonal slots and two pin diodes on the slots	4.64 GHz	Polarization diversity (LHCP or RHCP)	By turning the diodes on or off, either RHCP or LHCP can be obtained with the same feeding probe, which is located on the diagonal line of the patch	WLANs, satellite links, and space robots
5(b)	Square patch consisting of two orthogonal L-shaped slots with two pin diodes on the slots	4.44 GHz and 4.49 GHz	Polarization diversity (LHCP or RHCP)	Reconfigurability is achieved by switching two pin diodes. In RHCP antenna, diode a is turned ON, and diode b is turned OFF; in LHCP antenna, diode b is turned ON, and diode a is turned OFF.	Unlicensed and licensed WiMax (IEEE 802.16a), future planetary missions, and satellite links
5(c)	Square patch coupled to a microstrip line by an aperture in the ground plane	2.45 GHz	Polarization diversity (LHCP or RHCP)	Reconfigurability is obtained by selecting one of two excitation points and terminating the other with a 50-resistive load. RHCP is obtained if the excitation point is located on Port 1, and LHCP is obtained if the antenna is fed at Port 2	Not available
5(d)	A circular patch rotates to feed different shapes. The rotating circular part includes three circular patches and one slotted triangle	Covers five different bands (from 2 GHz up to 7 GHz)	Frequency diversity	Reconfigurability is achieved by rotational motion of part of the antenna patch. With every rotation, a different antenna structure is fed in order to produce a different set of resonant frequencies	Cognitive radio systems
5(e)	Short-circuited triangular patch antenna with truncated corner having two shorting walls and a V-shaped slot patch	2.5–2.55 GHz and 3.4–3.7 GHz WiMax bands	Frequency diversity	By placing two shorting walls with a V-shaped slot patch, two resonant modes can be excited simultaneously, yielding frequency diversity	Covers 2.5–2.55 GHz and 3.4 to 3.7 GHz WiMax bands
5(f)	Two rectangular slots properly positioned along the diagonal of a square patch antenna	5.15–5.35 GHz and 5.5 GHz	Frequency diversity and polarization diversity (LHCP or RHCP)	Positioning the slots along the left diagonal and right diagonal generates RHCP and LHCP, respectively	Can function as a rectenna for wireless battery charging at 5.5 GHz and data telemetry in the 5.15–5.35 GHz WLAN band
5(g)	Square patch with two pin diodes on a U-slot along with two diodes on the truncated corners	2.415 GHz and 2.650 GHz	Frequency diversity and polarization diversity (LP, LHCP, or RHCP)	The switching of the PIN diode on the U-slot realizes frequency diversity and polarization diversity among LP, RHCP, and LHCP is obtained by switching three PIN diodes on the slot and the truncating corners of a square patch on and off	WLAN/digital multimedia broadcasting applications

pattern). The switching job can be performed by lumped elements (capacitors/inductors), RF microelectromechanical systems, PIN diodes, or photoconductive switches. The use of these switching elements (except the photoconductive switches) requires the design of an appropriate biasing network for activation and deactivation [14]. Photoconductive switches usually require a high laser pumped power level to excite sufficient electrons from the valence band to the conduction band to make the switch conductive [15].

Several techniques have been explored, and various approaches have been proposed for the methods of obtaining reconfigurable antennas. This section highlights various methods adopted for the diversity in terms of frequency and polarization, in microstrip patch antennas that have been used as reconfigurable rectennas. Seven different designs proposed for either frequency diversity or polarization diversity or both are shown in Figure 5. Among these figures, the first three designs exhibit polarization diversity, the fourth and

fifth designs demonstrate frequency diversity, and the last two designs reveals both frequency and polarization diversity.

Square patch antenna having two orthogonal slots and two pin diodes at the center of the slot is shown in Figure 5(a). When diode on the horizontal slot is on and diode on vertical slot is off, the radiation fields of the TM_{10} and TM_{01} mode have the same magnitude and 90° out of phase at a midpoint frequency, generating RHCP pattern. Similarly for the opposite scenario, the roles of the modes are reversed and LHCP pattern can be obtained [16]. Figure 5(b) consists of square patch antenna incorporated by two L-shaped slots having pin diodes inserted in these slots. This design also adopts the similar way of obtaining polarization diversity, by making diodes “a” and “b” ON and OFF, respectively, for LHCP and vice versa for RHCP [17].

The third design evaluated in this paper for polarization diversity is shown in Figure 5(c). In this design, the microstrip feeding line is coupled to the square patch antenna through a cross-slot etched on the ground plane. For polarization diversity, two feeding accesses are chosen arbitrarily. When the excitation point is located on port 2, the opposed coupling points on slot 2 have a peak of excitation current in phase while the opposed coupling points on slot 1 have a null of magnetic current. After a quarter period, the excitation current is totally inverted and opposed coupling points have a null of magnetic current on slot 2 and are maximum on slot 1. This provides two linear polarizations with a phase difference of 90° . LHCP polarization is then emitted, and RHCP is emitted when excitation is located at port 1 [18].

Figures 5(d) and 5(e) are designed with the purpose of frequency reconfigurability. In Figure 5(d), the frequency tuning is achieved through rotational motion of the circular patch that contains four different shapes corresponding to a different set of resonant frequencies. The different RF shapes are three circular patches and one slotted triangle. The four sets of frequencies, “2.4–2.6 GHz,” “2.6–3.4 GHz,” “4–5 GHz,” and “3–4 GHz/5.26–7 GHz,” are covered by the four different shapes [19]. A triangular-shaped corner truncated short-circuited antenna with V-shaped slot for dual band operation (2.5–2.55 GHz and 3.4 to 3.7 GHz WiMax bands) is proposed in Figure 5(e). The two resonant modes are excited simultaneously by placing two shorting walls with a V-shaped slot in the patch [20].

The patch antenna can have both the feature of polarization diversity and frequency diversity. Figure 5(f) displays a circularly polarized microstrip patch antenna which can function as wireless battery charging at 5.5 GHz and data telemetry in the 5.15–5.35 GHz WLAN band. This dual-band and dual-polarized antenna is a square patch antenna containing two rectangular slots properly positioned along its diagonal. The two slots positioned along the left diagonal of the microstrip patch antenna generate RHCP and along the right diagonal generate LHCP [21].

The last design of Figure 5 is also a patch antenna with frequency and polarization diversities. It consists of a corner truncated square patch incorporating U-slot and pin diodes, as shown in Figure 5(g). Frequency diversity is achieved by controlling the electrical length through the switching of the pin diode on the U-slot. When all diodes are off it operates

at resonant frequency of 2415 MHz. It operates at 2650 MHz in three situations: when all diodes are on, when diodes 1, 3, and 4 are on and diode 2 is off, and when diode 1 is on and diodes 2, 3, and 4 are off. Polarization diversity is achieved by switching pin diodes on the slot and truncated corners. If diodes 1, 3, and 4 are turned on and diode 2 is turned off it exhibits LP characteristic. RHCP characteristic is exhibited when diode 1 is turned on and diodes 2, 3, and 4 are turned off. If all diodes are on, then LHCP is emitted [22].

A comparison between the abovementioned seven figures of Figure 5 was performed. These antennas having the option of either polarization selectivity or frequency selectivity or both have found application in several areas. Table 3 depicts the comparison of these figures in terms of antenna shape, operating frequency, brief summary of the reason behind the cause of reconfigurability, and their application. The details of these antennas shown in Figures 5(a), 5(b), 5(c), 5(d), 5(e), 5(f), and 5(g) are present in [16–22], respectively.

6. Conclusions

Antenna being a vital component of rectenna, the modification on its design can yield a compact size, suppress unwanted harmonics, and provide frequency and polarization diversity. Among various antennas used in rectenna, microstrip patch antenna is chosen for the evaluation and comparison because of its simplicity and easy fabrication. Various forms of microstrip patch antenna different from the conventional shape are analyzed with the explanation of the modification made in the design to obtain reduced size, harmonic rejection functionality, and reconfigurability in polarization and frequency. This attempt can be helpful to understand the behavior of patch antenna in different circumstances. We hope that this work will be helpful for researchers who are interested in improving rectenna design to obtain better RF energy harvesting performance.

Acknowledgment

This study was supported by a research fund from the Chosun University, 2012.

References

- [1] http://www2.electronicproducts.com/RF_energy_harvesting_and_wireless_power_article-FAJH_Energy_Aug2011-html.aspx.
- [2] S. Kim, “RF Energy Harvesting techniques for wirelessly powered devices,” in *Proceedings of the IEEE MTT-S International Microwave Workshop Series on Intelligent Radio for Future Personal Terminals (IMWS-IREPT '11)*, Daejeon, Republic of Korea, 2011.
- [3] Y. Kawahara, K. Tsukada, and T. Asami, “Feasibility and potential application of power scavenging from environmental RF signals,” in *Proceedings of the IEEE International Symposium on Antennas and Propagation and USNC/URSI National Radio Science Meeting (APSURSI '09)*, Charleston, SC, USA, June 2009.
- [4] C. A. Balanis, *Antenna Theory Analysis & Design*, John Wiley & Sons, New York, NY, USA, 2nd edition, 1997.

- [5] E. Krantz, S. Riley, and P. Large, "The design and performance of the zephyr geodetic antenna," in *Proceedings of the 14th International Technical Meeting of the Satellite Division of The Institute of Navigation (ION GPS '01)*, pp. 1942–1951, Salt Lake City, Utah, 2001.
- [6] T. C. Yo, C. M. Lee, C. M. Hsu, and C. H. Luo, "Compact circularly polarized rectenna with unbalanced circular slots," *IEEE Transactions on Antennas and Propagation*, vol. 56, no. 3, pp. 882–886, 2008.
- [7] G. A. Vera, A. Georgiadis, A. Collado, and S. Via, "Design of a 2.45 GHz rectenna for electromagnetic (EM) energy scavenging," in *Proceedings of the IEEE Radio and Wireless Symposium, (RWW '10)*, pp. 61–64, January 2010.
- [8] D. T. Notis, P. C. Liakou, and D. P. Chrissoulidis, "Dual polarized microstrip patch antenna, reduced in size by use of peripheral slits," in *Proceedings of the 7th European Conference on Wireless Technology, (ECWT '04)*, pp. 273–276, October 2004.
- [9] J. K. Ali, "A new compact size microstrip patch antenna with irregular slots for handheld gps application," *Engineering & Technology*, vol. 26, no. 10, 2008.
- [10] J. Y. Park, C. Caloz, Y. Qian, and T. Itoh, "A compact circularly polarized subdivided microstrip patch antenna," *IEEE Microwave and Wireless Components Letters*, vol. 12, no. 1, pp. 18–19, 2002.
- [11] J. Y. Park, S. M. Han, and T. Itoh, "A rectenna design with harmonic-rejecting circular-sector antenna," *IEEE Antennas and Wireless Propagation Letters*, vol. 3, no. 1, pp. 52–54, 2004.
- [12] Z. Harouni, L. Osman, and A. Gharsallah, "Efficient 2.45 GHz rectenna design with high harmonic rejection for wireless power transmission," *International Journal of Computer Science*, vol. 7, no. 5, 2010.
- [13] R. Dehbashi, Z. Atlasbaf, and K. Forooghi, "New compact size microstrip antennas with harmonic rejection," *IEEE Antennas and Wireless Propagation Letters*, vol. 5, no. 1, pp. 395–398, 2006.
- [14] D. E. Anagnostou, G. Zheng, M. T. Chrysomallis et al., "Design, fabrication, and measurements of an RF-MEMS-based self-similar reconfigurable antenna," *IEEE Transactions on Antennas and Propagation*, vol. 54, no. 2, pp. 422–432, 2006.
- [15] C. J. Panagamuwa, A. Chauraya, and J. C. Vardaxoglou, "Frequency and beam reconfigurable antenna using photoconducting switches," *IEEE Transactions on Antennas and Propagation*, vol. 54, no. 2, pp. 449–454, 2006.
- [16] F. Yang and Y. Rahmat-Samii, "A reconfigurable patch antenna using switchable slots for circular polarization diversity," *IEEE Microwave and Wireless Components Letters*, vol. 12, no. 3, pp. 96–98, 2002.
- [17] S. Raghavan, D. S. Kumar, and M. S. K. Kumar, "Reconfigurable patch slot antenna for circular polarization diversity," *International Journal of Microwave and Optical Technology*, vol. 3, no. 4, pp. 419–425, 2008.
- [18] Z. Harouni, L. Cirio, L. Osman, A. Gharsallah, and O. Picon, "A dual circularly polarized 2.45-GHz rectenna for wireless power transmission," *IEEE Antennas and Wireless Propagation Letters*, vol. 10, pp. 306–309, 2011.
- [19] Y. Tawk, J. Costantine, and C. G. Christodoulou, "A frequency reconfigurable rotatable microstrip antenna design," in *Proceedings of the IEEE Antennas and Propagation Society International Symposium (APSURSI '10)*, Toronto, Canada, July 2010.
- [20] N. Singh, D. P. Yadav, S. Singh, and R. K. Sarin, "Compact corner truncated triangular patch antenna for WiMax application," in *Proceedings of the 10th Mediterranean Microwave Symposium, (MMS '10)*, pp. 163–165, Guzelyurt, Cyprus, August 2010.
- [21] M. Ali, G. Yang, and R. Dougal, "A new circularly polarized rectenna for wireless power transmission and data communication," *IEEE Antennas and Wireless Propagation Letters*, vol. 4, no. 1, pp. 205–208, 2005.
- [22] K. Chung, Y. Nam, T. Yun, and J. Choi, "Reconfigurable microstrip patch antenna with switchable polarization," *ETRI Journal*, vol. 28, no. 3, pp. 379–382, 2006.

Research Article

Reconfigured and Notched Tapered Slot UWB Antenna for Cognitive Radio Applications

Tamer Aboufoul, Akram Alomainy, and Clive Parini

School of Electronic Engineering and Computer Science, Queen Mary University of London, Mile End Road, London E1 4NS, UK

Correspondence should be addressed to Tamer Aboufoul, ta302@eeecs.qmul.ac.uk

Received 22 February 2012; Accepted 22 October 2012

Academic Editor: Hala A. Elsadek

Copyright © 2012 Tamer Aboufoul et al. This is an open access article distributed under the Creative Commons Attribution License, which permits unrestricted use, distribution, and reproduction in any medium, provided the original work is properly cited.

A compact reconfigurable and notched ultra-wideband (UWB) tapered slot antenna (TSA) is presented. The antenna reconfiguration operation principle relies on 2 mechanisms: in the first mechanism a resonator parasitic microstrip line electrically coupled to the TSA is used to notch the TSA at a specific frequency and the second mechanism relies on changing the input impedance matching of the antenna by means of changing the length of a stub line extended from an additional tiny partial ground on the back side of the antenna. The reflection coefficient, radiation patterns, and gain simulations and measurements for the proposed antenna are presented to verify the design concepts featuring a very satisfactory performance. Total efficiency simulations and measurements are also presented to highlight the filtering performance of the reconfigured antenna. When the antenna was reconfigured from the UWB to work into multiple frequency bands, the radiation patterns were still the same and the total peak gain has slightly improved compared to the UWB case. In addition, when the antenna operated in the notched mode, the gain has significantly dropped at the notch frequency. The simplicity and flexibility of the proposed multimode antenna make it a good candidate for future cognitive radio front ends.

1. Introduction

Reconfigurable UWB antennas can be deployed in cognitive radio (CR) front ends by reconfiguring UWB antenna to work into multiple predefined frequency bands. When the antenna is in the UWB mode, it can be used for sensing the spectrum and when it is operating in the reconfigured modes, the antenna can be used for communication purpose [1–4]. Several designs of UWB antenna with band rejection characteristics have also targeted the cognitive radio applications [5, 6]. The proposed reconfigurable antenna here is mixing both approaches (e.g., reconfiguration and band rejection in the same antenna design). The reference antenna which will be reconfigured is presented in [7]. This antenna features wide operating bandwidth, very simple and compact structure, ease of fabrication, good radiation patterns over the entire bandwidth, and good time domain performance. In the proposed antenna design, reconfigurability is introduced by employing stubs and changing the electrical length of the stubs by using multiple switches. These stubs are connected to an additional tiny partial ground printed on the

back side of the tapered slot antenna (TSA). When the stub is disconnected from the ground it can be used as a parasitic resonator to notch the UWB antenna at specific unwanted frequency. In Section 2, the antenna design is presented and the operation of the antenna is briefly discussed. In Section 3 we show the simulated and measured results for the performance of the antenna. In Section 4 we briefly discuss the applicability of this new design in cognitive radio applications. Finally, conclusions are drawn and presented in Section 5.

2. Antenna Design and Operation

Figure 1 shows the geometry of the proposed reconfigured UWB TSA antenna. The proposed antenna substrate is a Taconic board with thickness of 1.52 mm, relative dielectric constant of 3, and loss tangent of 0.003. The width of the antenna is 16 mm ($0.28 \lambda_g$) and the length of the antenna is 27 mm ($0.47 \lambda_g$) where λ_g is the guided wavelength at 3 GHz. On the back side of the substrate, a small partial ground (12 mm \times 1 mm) is printed and there is a stub

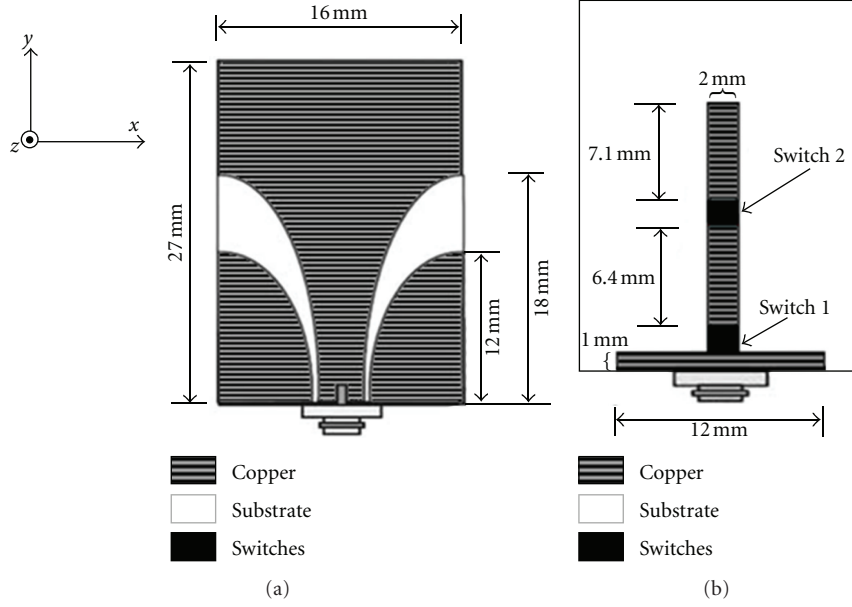


FIGURE 1: Geometry of the reconfigured tapered slot antenna: (a) top view, (b) bottom view.



FIGURE 2: Antenna prototype: (a) top view, (b) bottom view.

connected to this ground by switch 1. By changing the length of the stub, we can change the input impedance matching of the antenna to work in predefined frequency bands. The length of the ground stub is determined from circuit analysis using ADS [8]. When the stub length is 8.4 mm, the antenna should be working between 3 and 4 GHz. When the stub length increases to 17.5 mm when both switches 1 and 2 are ON, the frequency band of operation will change to 4.5–5.5 GHz. When the ground stub is not connected to the partial ground (e.g., switch 1 is OFF and switch 2 is ON), the stub will act as a parasitic element electrically coupled to the TSA. The length of the parasitic resonator determines the notch frequency and if we want to notch the upper band of WLAN at 5.8 GHz, the length of the resonator should be around 15 mm which is equal to $\lambda_g/2$ where λ_g is the guided wavelength at 5.8 GHz. Full UWB operation without any notches can be achieved if we can kill the resonance coupling of the parasitic element (e.g., the total length of the parasitic

TABLE 1: Operation modes of the antenna.

Switch 1	Switch 2	
	ON	OFF
ON	Band II	Band I
OFF	Notched-UWB	UWB

resonator is changed when switch 2 is OFF); consequently, it cannot support the resonating currents and no notch occurs at 5.8 GHz. The operation modes of the antenna for different switch states are summarized in Table 1.

A prototype antenna was fabricated to verify the performance. Figure 2 shows the proposed prototype antenna. RF switches used in this prototype are realized as metal pads with dimensions 2 mm × 2 mm. Although this model is ideal, it gives a good approximation for the commercial PIN diode switches.

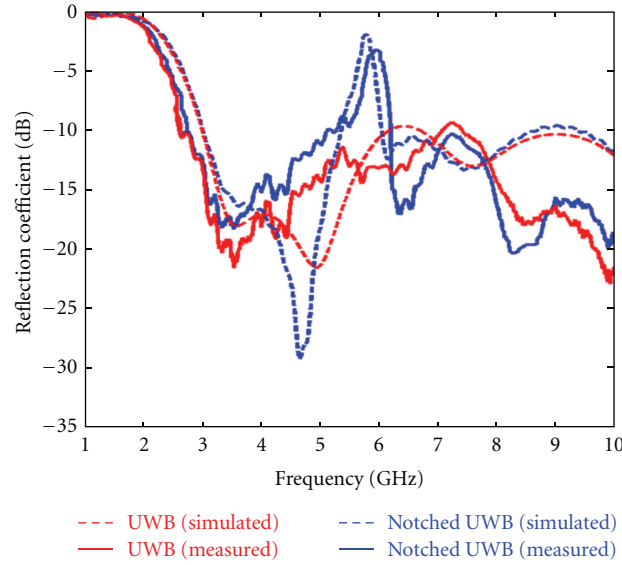


FIGURE 3: Simulated (dashed lines) and measured (solid lines) reflection coefficient curves when antenna is in UWB mode and in the notched UWB mode.

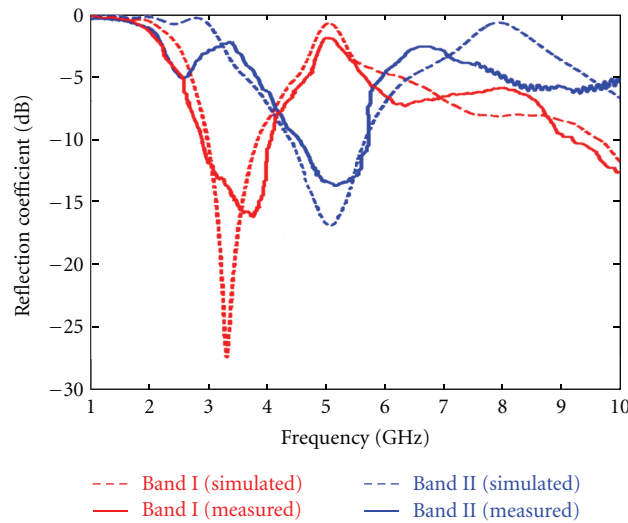


FIGURE 4: Simulated (dashed lines) and measured (solid lines) reflection coefficient curves when antenna is reconfigured in Band I: 3–4 GHz and Band II: 4.5–5.5 GHz.

3. Simulation and Measurements Results

3.1. Reflection Coefficient. All the simulations in this paper are performed using the CST microwave studio package which utilizes the finite integration technique for electromagnetic computation [9]. Figure 3 shows the simulated results for the reflection coefficient of the antenna when it is in the UWB mode and when it is notched around 5.8 GHz. Figure 4 depicts the simulated reflection coefficient when the antenna is configured to work into Band I and Band II. In general, a good agreement between simulated and measured results has been achieved. Small frequency shift (<200 MHz) between the simulated and measured results has occurred; this can be accounted for by fabrication and material tolerances.

3.2. Surface Current. Figures 5(a) and 5(b) show the surface current distributions for the notched UWB antenna at (3.4 GHz) in the passband and at the stopband (5.8 GHz) respectively. At the stop band, the surface currents are condensed around the parasitic resonator and a strong coupling occurs (the direction of current flow on the resonator is opposite to the flow of the current on the nearby slots edges). Eventually, the surface current is largely reduced along the edges of the 2 slots and no radiation occurs, while in the pass band frequency (3.4 GHz) the current flows smoothly on the edges of the slots without any perturbation by the resonator and hence radiation is as normal. Figure 6(a) shows the surface current distributions for the UWB antenna when it is operating in Band I at (3.4 GHz) in the passband, and Figure 6(b) shows the surface current distributions for the

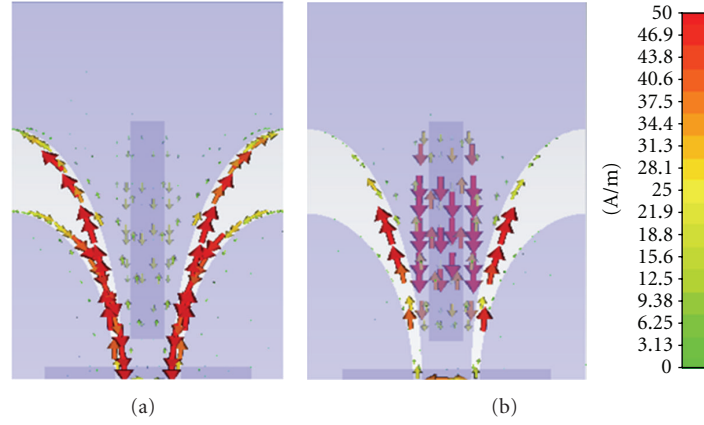


FIGURE 5: Simulated current distribution of the notched UWB antenna at (a) 3.4 GHz (normal operation frequency) and (b) 5.8 GHz (notched frequency).

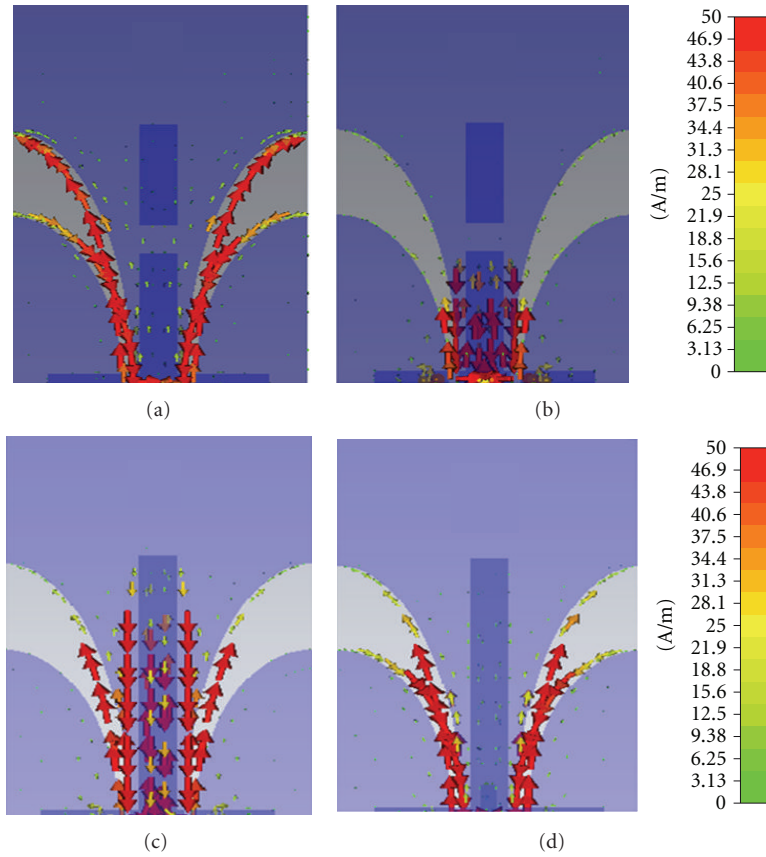


FIGURE 6: Simulated current distribution of the reconfigured UWB antenna in Band I: (a) 3.4 GHz, (b) 5 GHz, Band II: (c) 3.4 GHz, (d) 5 GHz.

UWB antenna when it is operating in the same band but at 5 GHz which is out of band frequency, respectively. Figures 6(c) and 6(d) show the surface current distributions for the UWB antenna when it is operating in Band II at (3.4 GHz) out of band frequency and Band II at (5 GHz) which is in the passband, respectively. At the out of band frequency, the stub which is connected to the partial ground will change the input impedance of the antenna and the surface current will be more dominant around the stub while the surface current

along the slots of the antenna is reduced. The effect of the stubs on matching the input impedance of the antenna can also be highlighted from Figure 7 which depicts the input impedance of the UWB antenna when it is reconfigured to work in Band I. For the UWB operation, the antenna input resistance (R_i) should be around 50Ω and the input reactance (X_i) should be close to 0Ω for the whole operating bandwidth. After reconfiguring the antenna to work into Band I, R_i is close to 50Ω and X_i is around 0Ω only at

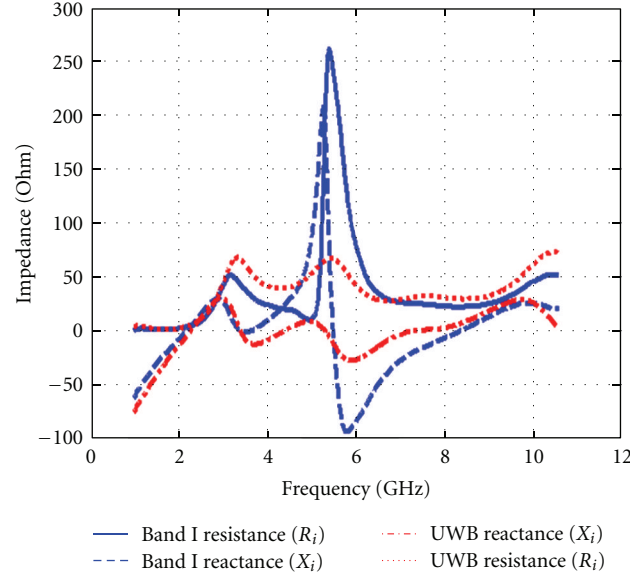


FIGURE 7: Simulated input impedance curves for the UWB antenna when the antenna is configured to operate in Band I.

TABLE 2: Simulated (S) and measured (M) realized gain.

Frequency (GHz)	Gain (dBi)							
	UWB		Notched UWB		Band I		Band II	
	S	M	S	M	S	M	S	M
3.4	1.9	2.4	1.9	2.5	2.1	3	0.8	0.7
5	2.9	3	3.0	3	-6.4	-4	3.7	3.5
5.8	3.6	3	-7	-4	1.9	2	3.8	3.7

TABLE 3: Measured total efficiency.

Frequency (GHz)	Total efficiency (%)			
	UWB	Notched UWB	Band I	Band II
3.4	87	88	90	40
5	90	87	30	91
5.8	85	45	55	88

frequencies within the operating bandwidth (e.g., 3.4 GHz) and their values largely deviate from the nominal values outside the passband.

3.3. Radiation Patterns and Gain. The simulated and measured normalized radiation patterns at 3.4 and 5 GHz for the UWB mode operation are plotted in Figures 8(a) and 8(b), respectively. The simulated and measured normalized radiation patterns when the antenna is configured in Band I at 3.4 and in Band II at 5 GHz are plotted in Figures 9(a) and 9(b), respectively. The *H*-plane patterns are omnidirectional and the *E*-plane patterns look like number “8” like a traditional monopole.

For radiation patterns measurements, the quality of the far field anechoic chamber is critically important. Slight misalignment uncertainties in the antenna under test (AUT) positioning can lead to discrepancies between simulated and measured radiation patterns. Moreover, the effects of the connectors and cables connected to the AUT were not simulated in the computational domain in spite of their capability to add some reflection in the chamber and deteriorate the perfect line-of-sight (LOS) assumption and add some ripples on the radiation patterns.

It is worth mentioning here that the radiation patterns did not change when we reconfigure from the UWB operation to the reconfigured cases. Table 2 summarizes a comparison of the simulated and measured realized peak

gain between the UWB case, the notched UWB, and the 2 reconfigured cases. At 5.8 GHz (notch frequency), the UWB notched antenna showed hugely reduced broadside gain compared to the UWB case and the reconfigured cases show slight increase in peak gain for passband frequencies compared to the UWB case.

3.4. Efficiency. Radiation efficiency is the ratio of input power that ends up as radiated power to the net power accepted by the antenna and the total efficiency is the ratio of the total power radiated from the antenna to the total net power applied at the antenna input terminal. Total efficiency results usually give better indication than return loss results to highlight the filtering performance of the antenna; this is because the antenna total efficiency not only accounts for the input mismatch of the antenna but also accounts for the ohmic losses in the antenna. Figure 10 depicts the simulated values of the total efficiency, when the antenna is operating in the UWB mode and the notched UWB mode and when the antenna is configured to work in Band I and Band II. The total efficiency was measured using the modified wheeler cap methods as in [10–12]. Table 3 shows the measured total efficiency when the antenna is operating in the UWB mode and the notched UWB mode and when the antenna is configured to work in Band I and Band II. The measured values agree well with the simulated ones. From Figure 10 and Table 3 we can see how poor the total efficiency gets at

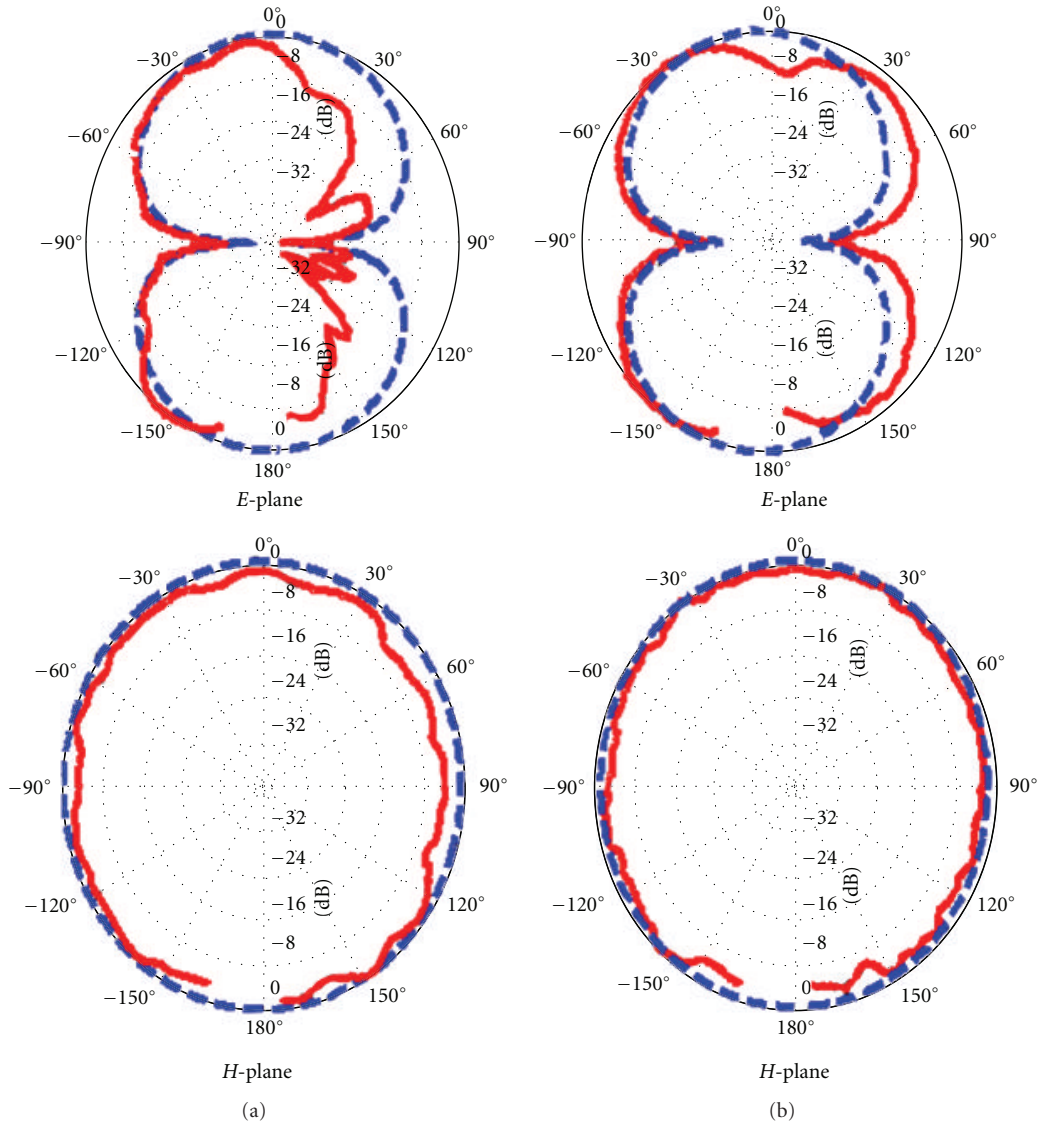


FIGURE 8: Simulated (dashed blue line) and measured (solid red line) normalised E -plane (X - Y) and H -plane (X - Z) radiation patterns, when antenna is in the UWB mode: (a) 3.4 GHz and (b) 5 GHz.

the notch frequency in UWB notched case or at out-of-band frequencies in the reconfigured bands I and II.

4. Applicability to Cognitive Radio

The previously discussed antenna can be easily integrated into cognitive radio; when the antenna is operating in the UWB mode, it can sense the whole spectrum to find the spectrum holes and then from sensing information it will decide to switch to work in one of the available predefined bands (e.g., Band I or II). Usually sensing places severe requirements on sensitivity, linearity, and dynamic range of the cognitive radio RF front end. This is because the RF signal presented at the antenna of a cognitive radio includes signals from close or separated transmitters and from transmitters operating at different power levels [13]. Detection of weak signals might frequently be performed in

the presence of very strong signals. Thus, to relax the strict requirements placed on the RF analogue circuits, it would be beneficial from a system point of view if we can mitigate an interferer before it saturate our RF front end. This can be done by using the UWB notched mode during sensing. It is worth mentioning here that not only this notched UWB mode can be good for sensing, but also it can be helpful in communication between cognitive secondary users who can still communicate more efficiently using the notched UWB channel (e.g., more allowed transmitted power and longer transmission range with higher data rate) without affecting or being affected by a specific legacy primary user who is currently operating at the notched frequency band.

5. Conclusion

A reconfigurable UWB tapered slot antenna (TSA) has been demonstrated and reconfigurability is introduced by

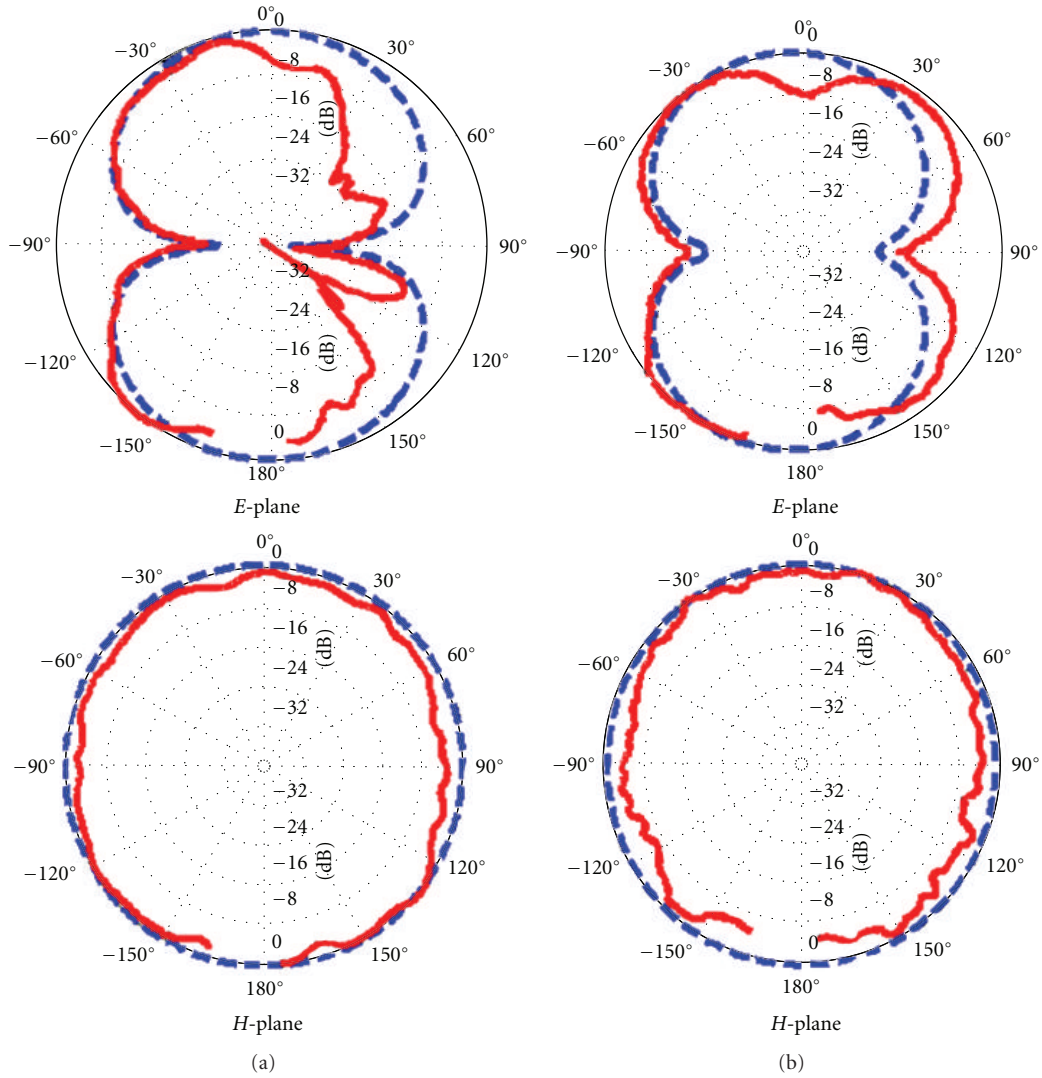


FIGURE 9: Simulated (dashed blue line) and measured (solid red line) normalised *E*-plane (*X*-*Y*) and *H*-plane (*X*-*Z*) radiation patterns, when the antenna is configured at: (a) 3.4 GHz in Band I and (b) 5 GHz in Band II.

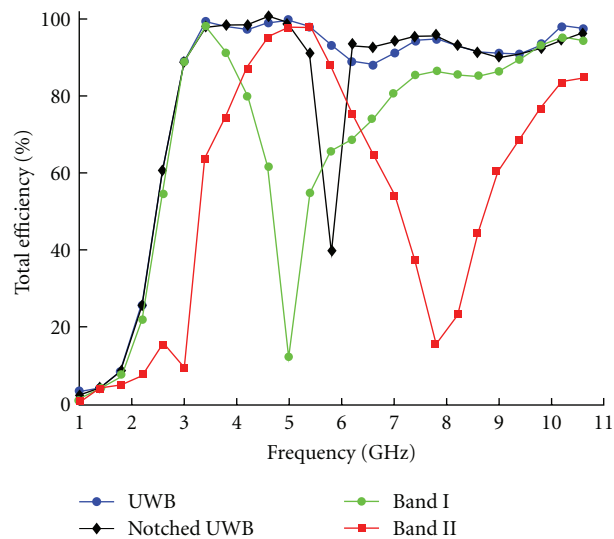


FIGURE 10: Simulated total efficiency when the antenna is operating in different modes.

varying the length of a stub connected to an additional tiny partial ground on the back of the antenna. The proposed topology is versatile in terms of the availability of different reconfiguration bands and the antenna is very compact and simple. Another interesting feature of the antenna is that this ground stub can be used as a parasitic element electrically coupled to the TSA antenna to notch the UWB operation at a specific frequency. The simulated and measured reflection coefficient, radiation patterns, and gain for the UWB mode, the notched UWB mode, and the reconfigured Bands I and II were presented and they all showed a very good performance. Applications requiring frequency band switching such as cognitive radio could benefit from the proposed reconfigurable TSA antenna as we can use the UWB mode or the notched UWB mode in sensing and the reconfigured bands for communication purpose.

References

- [1] J. R. Kelly, P. S. Hall, and P. Gardner, "Integrated wide-narrow band antenna for switched operation," in *Proceedings of the 3rd European Conference on Antennas and Propagation (EuCAP '09)*, pp. 3757–3760, March 2009.
- [2] T. Aboufoul and A. Alomainy, "Reconfigurable printed UWB circular disc monopole antenna," in *Proceedings of the Antennas & Propagation Conference (LAPC '11)*, pp. 1–4, Loughborough, UK, November 2011.
- [3] T. Aboufoul and A. Alomainy, "Single-element reconfigurable planar ultra wideband antenna for cognitive radio front end," in *Proceedings of the 4th International Conference on Cognitive Radio and Advanced Spectrum Management (CogART '11)*, Barcelona, Spain, October 2011.
- [4] T. Aboufoul, A. Alomainy, and C. Parini, "Reconfiguring UWB monopole antenna for cognitive radio applications using GaAs FET switches," *IEEE Antennas and Wireless Propagation Letters*, vol. 11, pp. 392–394, 2012.
- [5] X. Artiga, J. Perruisseau-Carrier, P. Pardo-Carrera, I. Llamas-Garro, and Z. Brito-Brito, "Halved Vivaldi antenna with reconfigurable band rejection," *IEEE Antennas and Wireless Propagation Letters*, vol. 10, pp. 56–58, 2011.
- [6] J. Perruisseau-Carrier, P. Pardo-Carrera, and P. Miskovsky, "Modeling, design and characterization of a very wideband slot antenna with reconfigurable band rejection," *IEEE Transactions on Antennas and Propagation*, vol. 58, no. 7, pp. 2218–2226, 2010.
- [7] A. Rahman and Y. Hao, "A novel tapered slot CPW-fed antenna for ultra-wideband applications and its on/off-body performance," in *Proceedings of the IEEE International Workshop on Antenna Technology (iWAT '07)*, pp. 503–506, Cambridge, UK, March 2007.
- [8] Advanced Design System (ADS), "Agilent Technologies," Santa Clara, Calif, USA, 2005, <http://www.agilent.com>.
- [9] CST-Microwave Studio, "User's Manual," 2011.
- [10] H. A. Wheeler, "The radian sphere around a small antenna," in *Proceedings American Institute of Electrical Engineers (IRE '59)*, vol. 47, pp. 1325–1331, August 1959.
- [11] H. G. Schantz, "Measurement of UWB antenna efficiency," in *Proceedings of the IEEE VTS 53rd Vehicular Technology Conference (VTS SPRING '01)*, vol. 2, pp. 1189–1191, May 2001.
- [12] M.-C. Huynh, *Wideband compact antennas for wireless communication [Ph.D. dissertation]*, Department of Electrical and Computer Engineering, Virginia Polytechnic Institute, 2004.
- [13] D. Cabric, S. M. Mishra, and R. W. Brodersen, "Implementation issues in spectrum sensing for cognitive radios," in *Proceedings of the Conference Record of the 38th Asilomar Conference on Signals, Systems and Computers*, vol. 1, pp. 772–776, November 2004.

Research Article

An Efficient Analysis Method for Cylindrical Conformal Microstrip Antenna Fed by Microstripline

Chengyou Yin¹ and Mengzhong Hu²

¹Department of Information Engineering, Hefei Electronic Engineering Institute, 460 Huangshan Road, Anhui, Hefei 230037, China

²Branch Team 91, Troops 92941, PLA, Liaoning, Huludao 125000, China

Correspondence should be addressed to Chengyou Yin, cyouyin@sina.com

Received 25 December 2011; Accepted 27 October 2012

Academic Editor: Hala A. Elsadek

Copyright © 2012 C. Yin and M. Hu. This is an open access article distributed under the Creative Commons Attribution License, which permits unrestricted use, distribution, and reproduction in any medium, provided the original work is properly cited.

Firstly, a domain-division solution is provided in this paper, which can solve Hankel function's singular problem of Sommerfeld integral in calculating the spatial domain Green function for cylindrically stratified media and realize the computation for all elements of Z-matrix in the method of moment. Then, the arbitrary shape cylindrical conformal microstrip antenna (CCMA) fed by microstripline is theoretically analysed using the RWG basis function. Numerical results are presented in the form of mutual coupling between two current modes and electromagnetic characteristics of a CCMA fed by microstripline. The results show that, comparing with the planar counterpart microstrip antenna, the reflection coefficient of the CCMA increases, the current on the microstripline varies sharply, and the backward radiation field appears. However, the frontward radiation field of the CCMA is similar to the planar case.

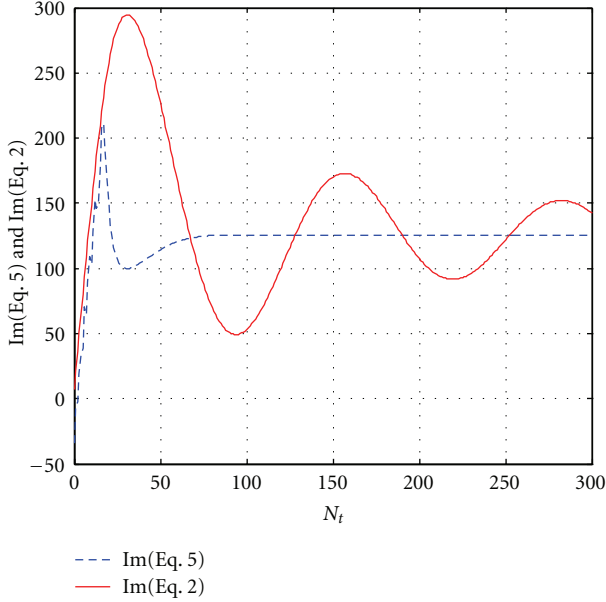
1. Introduction

Microstrip antennas find many applications in satellite and mobile communication because of their many advantages, such as low profile, light weight, easy fabrication, and conformability to mounting hosts. With the development of technology, people find it is not enough to do researches only on planar microstrip antennas, so they begin to study and analyse conformal microstrip antennas, such as cylindrical, spherical, conical, or paraboloidal conformal microstrip antennas. This paper just focuses on cylindrical conformal microstrip antenna (CCMA). It is found that the development of analysis method for CCMA is not as mature as the planar case. At present, researchers usually use the transmission line model, cavity model [1–3], or their improved models to analyse CCMA in engineering projects. However, these models are only accurate for regular shape (such as rectangle, triangle, or circle) CCMA with thin substrate and cannot be applied to analyse arbitrary shape CCMA. As full-wave solutions are more accurate and applicable to many structures, some researchers begin to study the MoM-based solution for CCMA, such as [4–13] in recent years. Reading these references, one can find

that the spatial domain Green function of cylindrically stratified media is the focused problem. A quasistatic images extraction technique has been proposed to solve the spatial domain Green function of electric field and mixed potential, respectively, in [4, 5], but when the source and observation points are located at the same radial distance from the axis of conductive cylinder, it is not valid along axial line (defined as $\rho = \rho'$ and $\varphi = \varphi'$). An eigenfunction solution of the Green function for arbitrary source and observation locations has been provided in [6–8]; however it needs a lot of computer resources, time consuming, and does not adapt to analyse big size or complex shape CCMA. The spatial and spectral MoM for CCMA is studied in [8–11], but all of them used the rooftop basis function which is not the general basis function compared with RWG for complex shape CCMA. In addition, recent relative MoM-based electromagnetic simulation software (such as IE3D, FEKO, or ADS) does not realize the calculation of Green's function of cylindrically stratified media too. Therefore, based on the former research works, this paper will provide a method which can analyse arbitrary shape CCMA because of the RWG basis function used in MoM. The paper is documented in the following structure. In Section 2, theory

TABLE 1: The values of e_1 , e_2 , and e_3 for different uv .

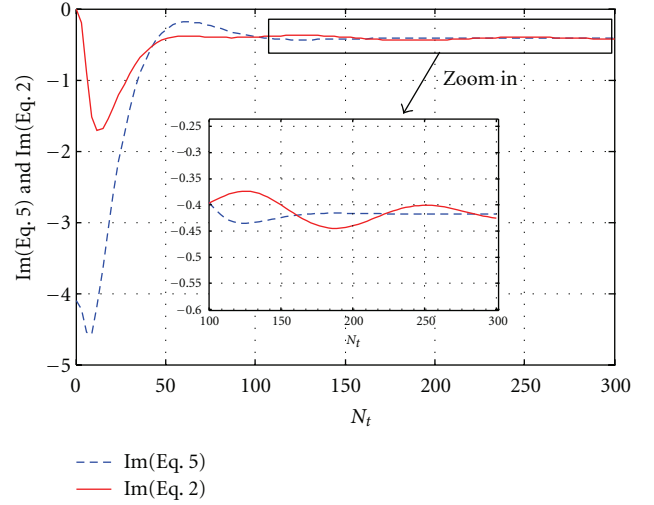
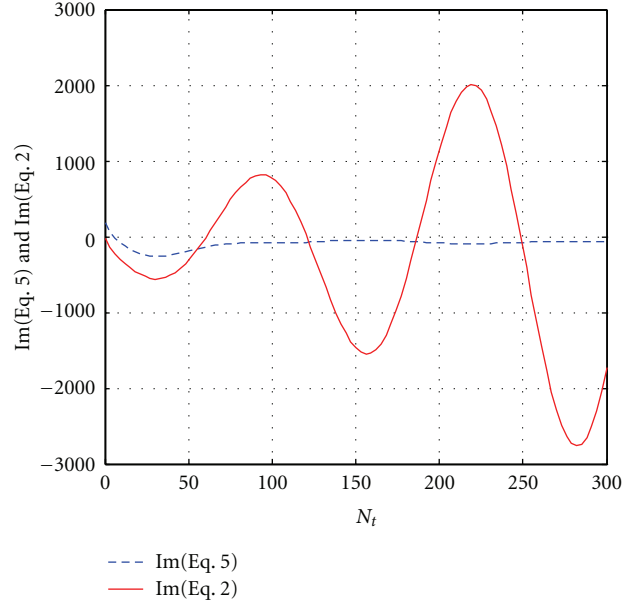
uv	e_1	e_2	e_3
zz	1	0	0
φz	0	1	1
$z\varphi$	0	1	1
$\varphi\varphi$	0	2	0

FIGURE 1: Comparison of \tilde{G}_{zz}^E imaginary part versus N_t using (2) and (5).

and formulation of the domain-division solution for the Green's function for CCMA will be introduced in detail firstly. Then, based on RWG-MoM, theoretical analysis of arbitrary shape CCMA fed by microstripline will be done. In Section 3, a simulation example for investigating the effectiveness of the domain-division solution is presented and the electromagnetic characteristics of a CCMA fed by microstripline are gotten in another simulation example, in which results are compared with those of the planar case. A time convention of $e^{j\omega t}$ has been adopted in this paper.

2. Theory and Formulation

As we know, analysis of CCMA using MoM needs calculating the spatial Green function when source and observation points are located at the same radial distance from the axis of cylinder ($\rho = \rho'$), but, in this case, integral kernel function converges very slowly for electrically large conductive cylinders, because the Green's function involves Bessel and Hankel functions along with their derivatives. So the expressions of Green function gotten from [12, 13] cannot be directly used in the analysis of CCMA and some special work should be done. Combining the methods of [4–11], a domain-division solution can be provided to solve this problem which divides the computation of Green's function into two domain's problems. The first one is the unaxial line

FIGURE 2: Comparison of $\tilde{G}_{\varphi z}^E$ imaginary part versus N_t using (2) and (5).FIGURE 3: Comparison of $\tilde{G}_{\varphi\varphi}^E$ imaginary part versus N_t using (2) and (5).

problem (defined as $|\rho - \rho'| = 0$ and $|\varphi - \varphi'| > 0.05$), and the other one is the axial line problem (defined as $|\rho - \rho'| = 0$ and $|\varphi - \varphi'| < 0.05$).

2.1. Solution of the Unaxial Line Problem. Based on the formulation of spectral domain Green's function in [12, 13], the expressions of the spectral domain Green function components for the n th Harmonic wave can be rewritten as

$$\frac{\tilde{G}_{uv}^E}{k_z^{e_3}} = (k_{\rho i}^2)^{e_1} n^{e_2} H_n^{(2)}(k_{\rho i} \rho) J_n(k_{\rho i} \rho') f^{uv}(n, k_z). \quad (1)$$

For different uv , the values of e_1 , e_2 , and e_3 in the above formula are show in Table 1.

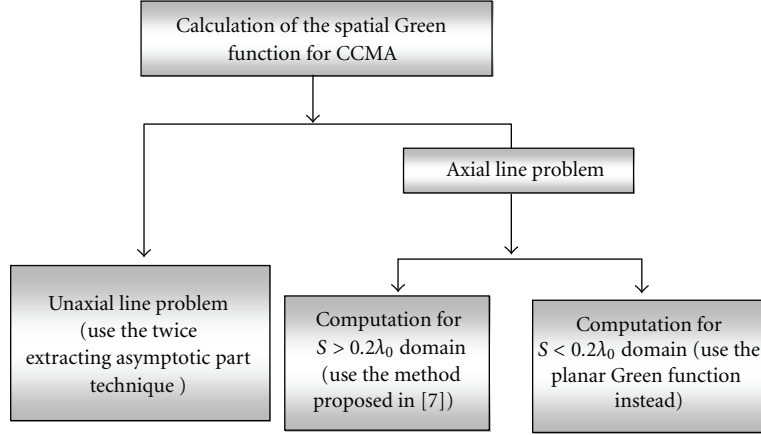


FIGURE 4: Calculation of the spatial Green function for MMCA.

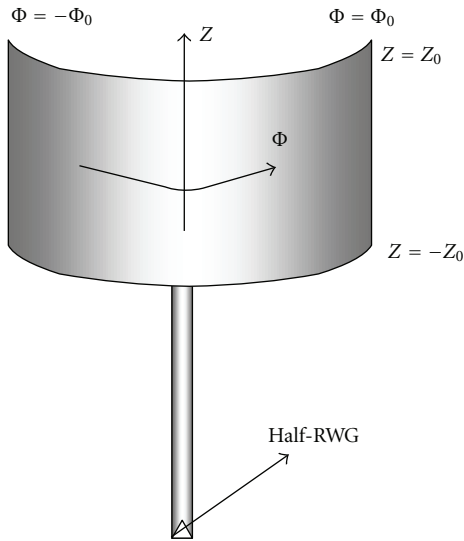


FIGURE 5: CCMA fed by microstripline.

Hence, the expressions of the spectral domain Green function for all tangential electric field components in cylindrical coordinates can be written as

$$\frac{\tilde{G}_{uv}^E}{k_z^3} = \frac{-1}{4\omega} \sum_{n=-\infty}^{\infty} (k_{\rho i}^2)^{e_1} n^{e_2} H_n^{(2)}(k_{\rho i} \rho) J_n(k_{\rho i} \rho') \times f^{uv}(n, k_z) e^{jn(\varphi - \varphi')}. \quad (2)$$

Using the expressions of the spectral domain Green function in [12, 13], f^{uv} (u and v can be z or φ) in the above formula is easy to get.

In (2), when $n \rightarrow \infty$, it is found that $f^{uv}(n, k_z)$ will converge to a function which is constant with respect to n ,

$$\lim_{n \rightarrow \infty} f^{uv}(n, k_z) \approx C_{uv}(k_z). \quad (3)$$

With the aid of the series expression of $H_0^{(2)}(k_{\rho i} |\boldsymbol{\rho} - \boldsymbol{\rho}'|)$, given by

$$\sum_{n=-\infty}^{\infty} H_n^{(2)}(k_{\rho i} \rho) J_n(k_{\rho i} \rho') e^{jn(\varphi - \varphi')} = H_0^{(2)}(k_{\rho i} |\boldsymbol{\rho} - \boldsymbol{\rho}'|), \quad (4)$$

then (2) can be expressed as

$$\begin{aligned} \frac{\tilde{G}_{uv}^E}{k_z^3} &= \frac{-1}{4\omega} \sum_{n=-\infty}^{\infty} (k_{\rho i}^2)^{e_1} n^{e_2} H_n^{(2)}(k_{\rho i} \rho) J_n(k_{\rho i} \rho') \\ &\times (f^{uv}(n, k_z) - C_{uv}(k_z)) e^{jn(\varphi - \varphi')} \\ &+ \frac{-1}{4\omega} C_{uv}(k_z) (k_{\rho i}^2)^{e_1} F_1^{uv} [H_0^{(2)}(k_{\rho i} |\boldsymbol{\rho} - \boldsymbol{\rho}'|)]. \end{aligned} \quad (5)$$

Expressions of $F_1^{uv}[H_0^{(2)}(k_{\rho i} |\boldsymbol{\rho} - \boldsymbol{\rho}'|)]$ in (5) can be gotten using (4) and its derivatives, which can be found in [5]. Computation of $F_1^{uv}[H_0^{(2)}(k_{\rho i} |\boldsymbol{\rho} - \boldsymbol{\rho}'|)]$ involves Bessel and Hankel functions' derivatives. With the aid of formula (1.2.34) in [14], their derivatives can be calculated easily.

From (5), one can find that the spectral domain Green function now includes two parts after extracting the asymptotic part with respect to n . The first part is still a summation of infinite series with respect to n , but it is now more rapidly convergent and the limits of the infinite summation can be truncated at relatively small values N_t . The second part is the asymptotic part of the spectral domain Green function which now is not an infinite summation but a function with respect to $H_0^{(2)}(k_{\rho i} |\boldsymbol{\rho} - \boldsymbol{\rho}'|)$.

To study the convergence of formulae (2) and (5), the spectral domain Green function is computed by (2) and (5), respectively. The results are shown in Figures 1, 2, and 3.

Parameters used in the above computation are set as follow: $\Delta\varphi = 0.05$, $a_0 = 3\lambda_0$, $a_1 = 3.06\lambda_0$, $\epsilon_r = 3.25$, $k_z = 0$ for computation of \tilde{G}_{zz}^E and $k_z = k_s(1 + jT_1)$ for computation of $\tilde{G}_{\varphi z}^E$, $\tilde{G}_{\varphi\varphi}^E$. As seen in Figures 1–3, it can be found that results of the spectral domain Green function using (2) converge difficultly even for $N_t = 300$. Especially for $\tilde{G}_{\varphi\varphi}^E$ shown in Figure 3, the numerical results seem to

be divergent. But the results of the spectral domain Green function using (5) converge very quickly and one can make $N_t = 200$ to get accurate results for the spectral domain Green function.

When $k_z \rightarrow \infty$, it is found that $C_{uv}(k_z)$ is convergent to C_{uv}^∞ , so, extracting the asymptotic part of the spatial domain Green function components with respect to k_z , the expressions for calculating the spatial domain Green function of electric field can be written as

$$G_{uv}^E = \left(\frac{j\partial}{\partial z} \right)^{e_3} \left\{ \frac{-1}{8\omega\pi} \int_{-\infty}^{\infty} (\hat{g}_{uv1}^E + \hat{g}_{uv2}^E) \times \cos[k_z(z-z')] dk_z \right\} + \frac{-1}{8\omega\pi} C_{uv}^\infty F_2^{uv},$$

$$\hat{g}_{uv1}^E = \sum_{n=-\infty}^{\infty} (k_{\rho i}^2)^{e_1} n^{e_2} H_n^{(2)}(k_{\rho i} \rho) J_n(k_{\rho i} \rho')$$

$$\times (f^{uv}(n, k_z) - C_{uv}(k_z)) e^{jn(\varphi - \varphi')},$$

$$\hat{g}_{uv2}^E = (C_{uv}(k_z) - C_{uv}^\infty) F_1^{uv} [H_0^{(2)}(k_{\rho i} |\boldsymbol{\rho} - \boldsymbol{\rho}'|)].$$

Using the following equations:

$$I_1 = \int_{-\infty}^{\infty} H_0^{(2)}(k_{\rho i} |\boldsymbol{\rho} - \boldsymbol{\rho}'|) e^{-jk_z(z-z')} = \frac{2je^{-jk_i|\mathbf{r}-\mathbf{r}'|}}{|\mathbf{r}-\mathbf{r}'|},$$

$$I_2 = \int_{-\infty}^{\infty} k_{\rho i} \frac{\partial [H_0^{(2)}(k_{\rho i} |\boldsymbol{\rho} - \boldsymbol{\rho}'|)]}{\partial (k_{\rho i} |\boldsymbol{\rho} - \boldsymbol{\rho}'|)} e^{-jk_z(z-z')} = 2j(-jk_s |\mathbf{r}-\mathbf{r}'| - 1) |\boldsymbol{\rho} - \boldsymbol{\rho}'| \frac{e^{-jk_s|\mathbf{r}-\mathbf{r}'|}}{|\mathbf{r}-\mathbf{r}'|^3},$$

$$I_3 = \int_{-\infty}^{\infty} k_{\rho i}^2 \frac{\partial^2 [H_0^{(2)}(k_{\rho i} |\boldsymbol{\rho} - \boldsymbol{\rho}'|)]}{\partial (k_{\rho i} |\boldsymbol{\rho} - \boldsymbol{\rho}'|)^2} e^{-jk_z(z-z')} = 2j[-k_s^2 |\boldsymbol{\rho} - \boldsymbol{\rho}'|^2 |\mathbf{r}-\mathbf{r}'|^2 - (z-z')^2 - j(z-z')^2$$

$$\times k_s |\mathbf{r}-\mathbf{r}'| + 2|\boldsymbol{\rho} - \boldsymbol{\rho}'|^2 + 2j|\boldsymbol{\rho} - \boldsymbol{\rho}'|^2 k_s |\mathbf{r}-\mathbf{r}'|] \times \frac{e^{-jk_s|\mathbf{r}-\mathbf{r}'|}}{|\mathbf{r}-\mathbf{r}'|^5}.$$

Expressions for calculating F_2^{uv} in (6) can be deduced. Analysing G_{uv}^E in (6), one can find that G_{uv}^E also includes two parts. The first part is an infinite integral with respect to k_z which is now fast decaying with respect to even for very small $|\varphi - \varphi'|$ values and can be solved by the method of deformed integration path proposed in [13]. The second part is the asymptotic part of the spatial domain Green function which has closed form expressions.

2.2. Solution for Axial Line Problem ($|\rho - \rho'| = 0$ and $|\varphi - \varphi'| < 0.05$). Although a twice-extracting technique is proposed to solve the unaxial line problem in the above section, as to axial line problem, $H_0^{(2)}(k_{\rho i} |\boldsymbol{\rho} - \boldsymbol{\rho}'|)$ in (6) shows more

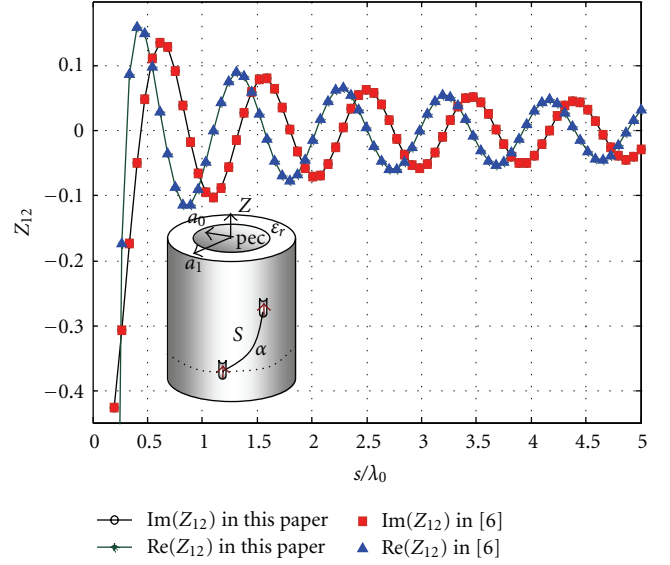


FIGURE 6: Real and imaginary parts of the mutual impedance (Z_{12}) between two identical z -directed current sources versus separation S when $\alpha = 700^\circ$ (unaxial line problem).

singular and is also difficult to calculate. Fortunately, [7] does much research on this problem and obtains an approximated representation of spatial Green's function for this case by performing Watson's transformation.

When $S \rightarrow 0$ (S is shown in Figure 6), the method of [7] is not valid because of high-order singular problem in this condition. Even using the asymptotic extraction approach in [15] convergence is still difficult in this case. However, the Green function of planar stratified media can be used instead, because cylindrical stratified media can be treated as planar stratified media approximately when $S < 0.2\lambda_0$ (λ_0 is the free space wave length). Therefore, to sum up, computation of the spatial Green function for CCMA can be divided into two parts which are shown in Figure 4. The first part is about the unaxial line problem (defined as $|\rho - \rho'| = 0$ and $|\varphi - \varphi'| > 0.05$), and the other is about the axial line problem (defined as $|\rho - \rho'| = 0$ and $|\varphi - \varphi'| < 0.05$). The axial line problem involves two subdomains. One is $S > 0.2\lambda_0$, and the other is $S < 0.2\lambda_0$. The method proposed in [7] is used to attack the problem in $S > 0.2\lambda_0$ domain, and the Green function of planar stratified media is used to solve the problem in $S < 0.2\lambda_0$ domain. Computation for the Green function of planar stratified media can be found in [14–17].

2.3. Theoretical Analysis of Arbitrary Shape CCMA Fed by Microstripline. Considering CCMA fed by microstripline, E_p^s does not need to be considered, so one can get

$$\begin{bmatrix} \mathbf{E}_\varphi^s \\ \mathbf{E}_z^s \end{bmatrix} = \left\langle \begin{bmatrix} \overline{\mathbf{G}}_{\varphi\varphi}^E & \overline{\mathbf{G}}_{\varphi z}^E \\ \overline{\mathbf{G}}_{z\varphi}^E & \overline{\mathbf{G}}_{zz}^E \end{bmatrix} \begin{bmatrix} \mathbf{J}_\varphi \\ \mathbf{J}_z \end{bmatrix} \right\rangle. \quad (8)$$

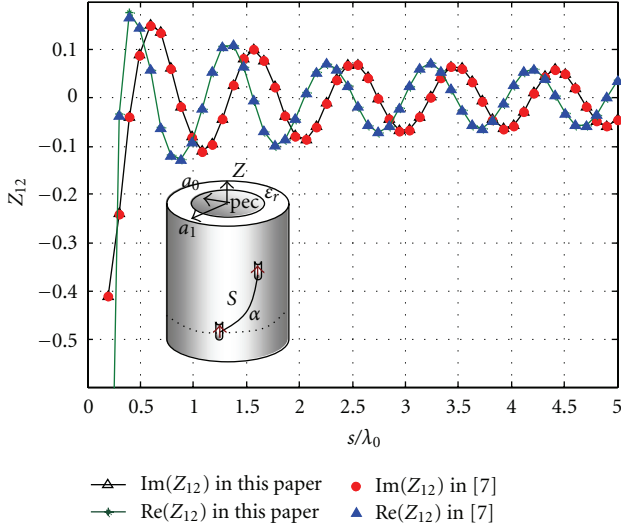


FIGURE 7: Real and imaginary parts of the mutual impedance (Z_{12}) between two identical z -directed current sources versus separation S when $\alpha = 90^\circ$ (axial line problem).

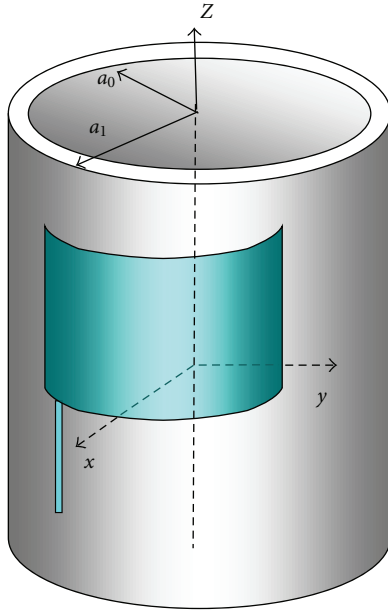


FIGURE 8: CCMA fed by microstripline.

If the source current $\mathbf{J}^i = [\mathbf{J}_\phi^i \ \mathbf{J}_z^i]^T$ is excited at the end of microstripline as shown in Figure 5, then excited electric field is written as

$$\begin{bmatrix} \mathbf{E}_\phi^i \\ \mathbf{E}_z^i \end{bmatrix} = \left\langle \begin{bmatrix} \overline{\mathbf{G}}_{\phi\phi}^E & \overline{\mathbf{G}}_{\phi z}^E \\ \overline{\mathbf{G}}_{z\phi}^E & \overline{\mathbf{G}}_{zz}^E \end{bmatrix} \begin{bmatrix} \mathbf{J}_\phi^i \\ \mathbf{J}_z^i \end{bmatrix} \right\rangle. \quad (9)$$

Using the Galerkin testing technique, on the patch of CCMA, we arrive at

$$\langle \mathbf{f}^w, \mathbf{E}^s|_t \rangle = -\langle \mathbf{f}^w, \mathbf{E}^i|_t \rangle, \quad (10)$$

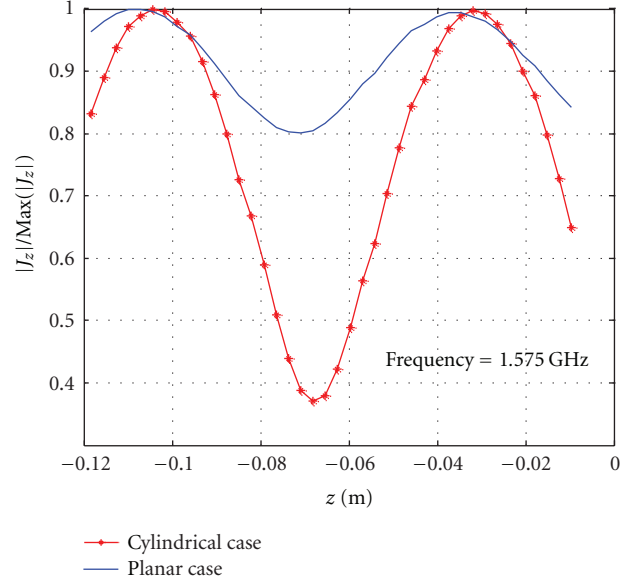


FIGURE 9: Comparison of the current distribution on microstripline.

where \mathbf{f}^w is the test basis function in MoM. Upon substituting (8) and (9) into (10), one obtains

$$\begin{aligned} & \int_S \int_{S'} [\mathbf{f}_\phi^w \cdot (\overline{\mathbf{G}}_{\phi\phi}^E \cdot \mathbf{J}_\phi + \overline{\mathbf{G}}_{\phi z}^E \cdot \mathbf{J}_z)] dS' dS \\ &= - \int_S \int_{S'} [\mathbf{f}_\phi^w \cdot (\overline{\mathbf{G}}_{\phi\phi}^E \cdot \mathbf{J}_\phi^i + \overline{\mathbf{G}}_{\phi z}^E \cdot \mathbf{J}_z^i)] dS^i dS, \\ & \int_S \int_{S'} [\mathbf{f}_z^w \cdot (\overline{\mathbf{G}}_{z\phi}^E \cdot \mathbf{J}_\phi + \overline{\mathbf{G}}_{zz}^E \cdot \mathbf{J}_z)] dS' dS \\ &= - \int_S \int_{S'} [\mathbf{f}_z^w \cdot (\overline{\mathbf{G}}_{z\phi}^E \cdot \mathbf{J}_\phi^i + \overline{\mathbf{G}}_{zz}^E \cdot \mathbf{J}_z^i)] dS^i dS. \end{aligned} \quad (11)$$

The current distribution on the patch of the antenna can be approximated in terms of \mathbf{f}_n as

$$\mathbf{J}_s = \sum_n I_n \mathbf{f}_n, \quad (12)$$

where \mathbf{f}_n is the RWG basis function in this paper, which is different from the traditional method in [8–10], and one can find the define about RWG in [18]. From (11) and (12), if \mathbf{f}^w is equal to \mathbf{f}_m , current coefficient I_n can be gotten from the following identity:

$$\begin{aligned} & I_n \int_S \int_{S'} [\mathbf{f}_m|_\phi \ \mathbf{f}_m|_z] \cdot \begin{bmatrix} \overline{\mathbf{G}}_{\phi\phi}^E & \overline{\mathbf{G}}_{\phi z}^E \\ \overline{\mathbf{G}}_{z\phi}^E & \overline{\mathbf{G}}_{zz}^E \end{bmatrix} \begin{bmatrix} \mathbf{f}_n|_\phi \\ \mathbf{f}_n|_z \end{bmatrix} dS' dS \\ &= - \int_S \int_{S'} [\mathbf{f}_m|_\phi \ \mathbf{f}_m|_z] \cdot \begin{bmatrix} \overline{\mathbf{G}}_{\phi\phi}^E & \overline{\mathbf{G}}_{\phi z}^E \\ \overline{\mathbf{G}}_{z\phi}^E & \overline{\mathbf{G}}_{zz}^E \end{bmatrix} \begin{bmatrix} \mathbf{J}_\phi^i \\ \mathbf{J}_z^i \end{bmatrix} dS^i dS. \end{aligned} \quad (13)$$

Considering $m, n = 1, 2, \dots, N$, formula (13) can be written in matrix form as

$$\begin{bmatrix} \mathbf{Z}_{11} & \mathbf{Z}_{12} & \cdots & \mathbf{Z}_{1N} \\ \mathbf{Z}_{21} & \mathbf{Z}_{22} & \cdots & \mathbf{Z}_{2N} \\ \vdots & \vdots & \ddots & \vdots \\ \mathbf{Z}_{N1} & \mathbf{Z}_{N2} & \cdots & \mathbf{Z}_{NN} \end{bmatrix} \begin{bmatrix} \mathbf{I}_1 \\ \mathbf{I}_2 \\ \vdots \\ \mathbf{I}_N \end{bmatrix} = \begin{bmatrix} \mathbf{V}_1 \\ \mathbf{V}_2 \\ \vdots \\ \mathbf{V}_N \end{bmatrix}, \quad (14)$$

where

$$\begin{aligned} \mathbf{Z}_{mn} &= \int_S \int_{S'} \begin{bmatrix} \mathbf{f}_m |_\varphi & \mathbf{f}_m |_z \end{bmatrix} \\ &\quad \cdot \begin{bmatrix} \bar{\mathbf{G}}_{\varphi\varphi}^E & \bar{\mathbf{G}}_{\varphi z}^E \\ \bar{\mathbf{G}}_{z\varphi}^E & \bar{\mathbf{G}}_{zz}^E \end{bmatrix} \begin{bmatrix} \mathbf{f}_n |_\varphi \\ \mathbf{f}_n |_z \end{bmatrix} dS' dS, \\ \mathbf{V}_m &= - \int_S \int_{S'} \begin{bmatrix} \mathbf{f}_m |_\varphi & \mathbf{f}_m |_z \end{bmatrix} \\ &\quad \cdot \begin{bmatrix} \bar{\mathbf{G}}_{\varphi\varphi}^E & \bar{\mathbf{G}}_{\varphi z}^E \\ \bar{\mathbf{G}}_{z\varphi}^E & \bar{\mathbf{G}}_{zz}^E \end{bmatrix} \begin{bmatrix} \mathbf{J}_\varphi^i \\ \mathbf{J}_z^i \end{bmatrix} dS' dS. \end{aligned} \quad (15)$$

In order to calculate \mathbf{V}_m in (15), \mathbf{J}^i can be treated as a half-RWG basis function added at the end of the microstripline which is shown in Figure 5.

After getting all the current coefficients in (14), one can obtain the current distributions on the patch and microstripline. Using GPOF method [19], current distributions on the microstripline can be expressed as

$$I(z) \approx \sum_{i=1}^K I_i e^{(\alpha_i + j\beta_i)z}, \quad (16)$$

where I_i , α_i , and β_i are parameters approximated by GPOF method. It is found that $\alpha_i \ll \beta_i$, so (16) can be approximated as follows:

$$I(z) = I_1 e^{-j\beta_1 z} + I_2 e^{j\beta_1 z} \dots I_K e^{j\beta_K z}. \quad (17)$$

In (17), I_1 and I_2 represent the two opposite travelling waves I^+ and I^- . The others (I_3, I_4, \dots, I_K) are the high-order travelling waves which can be ignored generally. So the reflection coefficient can be found as

$$\begin{aligned} S_{11} &= \frac{I_2}{I_1}, \\ \text{dB}(S_{11}) &= 20 \log_{10} \left| \frac{I_2}{I_1} \right|, \end{aligned} \quad (18)$$

and the impedance of the antenna is given by

$$Z_{\text{in}} = \frac{1 + S_{11}}{1 - S_{11}} Z_c, \quad (19)$$

where Z_c is the characteristic impedance of microstripline. In addition, to calculate the far field of the CCMA fed by microstripline, the method in [19] can be used. However, it should be noticed that this paper chooses the RWG basis function to approximate the current, so formulas for calculating current in [19] should be changed properly.

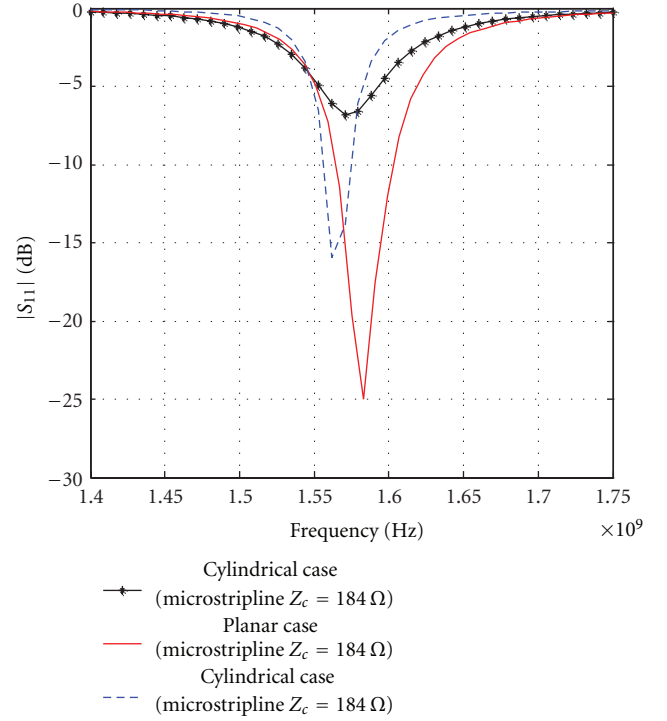


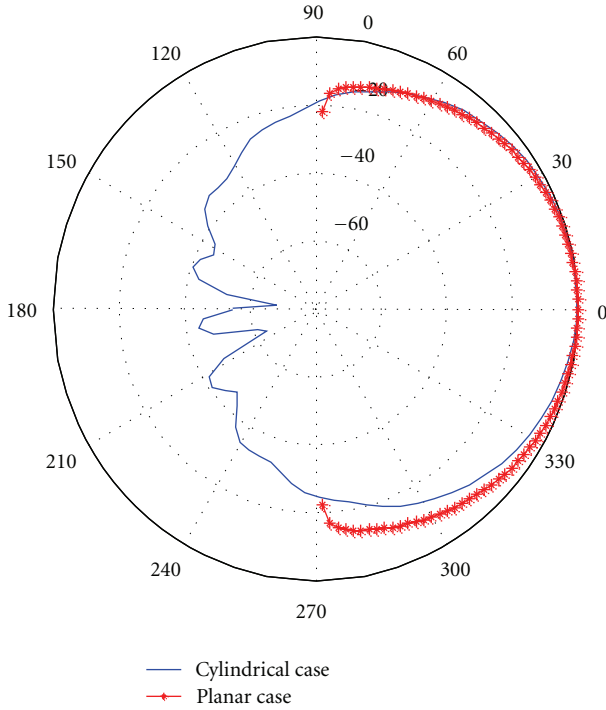
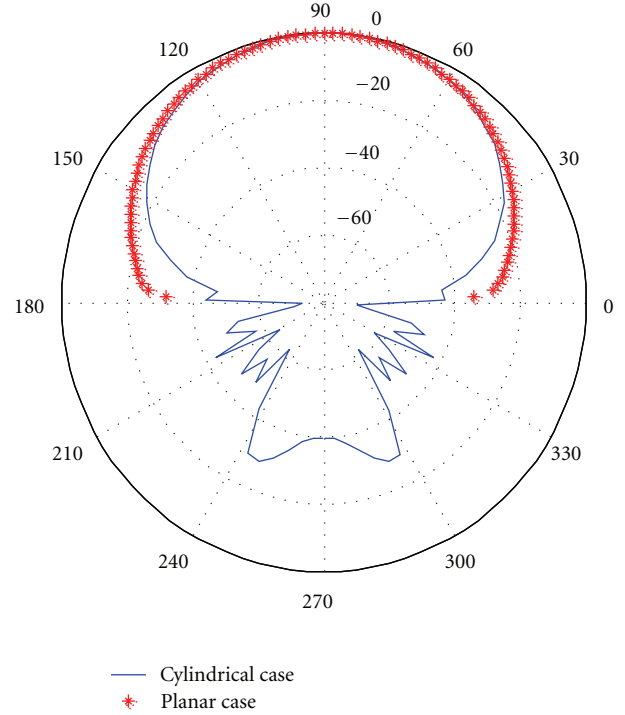
FIGURE 10: Comparison of the reflection coefficient.

3. Numerical Results

3.1. Mutual Impedance between the Current Modes. In order to assess the validity and accuracy of the method proposed in this paper, numerical results for the mutual impedance between two tangential electric current modes are obtained using the domain-division solution and compared with the results of [6, 7]. The numerical results are shown in Figures 6 and 7, and the parameters of the cylinder and substrate in these figures are set as $a_0 = 3\lambda_0$, $a_1 = 3.06\lambda_0$, $\epsilon_r = 3.25$. Figure 6 shows that results obtained by the twice-extracting technique in this paper are in good agreement with the results in [6], so the technique is effective for the unaxial line problem. As seen in Figure 7, the method of [7] is used successfully to solve axial line problem in this paper.

3.2. Analysis of a CCMA Fed by Microstripline. Using the method in this paper, a CCMA fed by microstripline illustrated in Figure 8 is analysed. Sizes of the antenna are set as φ - and z -direction lengths of patch are 0.0615 m and 0.0604, respectively, microstripline length is 0.1278 m, the feed point is 0.02696 m away from the bottom edge's centre of the patch in φ -direction, thickness of the substrate is 0.00234 m, the microstripline wide is 0.1 mm ($Z_c = 184$), $\epsilon_r = 2.32$, and $a_0 = 0.187451$ m. Results of the normalised current distribution on microstripline, reflection coefficient, and normalised radiation patterns are presented in Figures 9–12.

Figures 9 and 10 show that resonance frequency of the antenna in planar case is 1.575 GHz, but in cylindrical case, the reflection coefficient does not satisfy the request

FIGURE 11: Normalised radiation field in xoy -plane (dB).FIGURE 12: Normalised radiation field in xoz -plane (dB).

$\text{dB}(S_{11}) < -10$ dB at 1.575 GHz. The reason for it may be that characteristic impedance of the microstripline in cylindrical case does not match the impedance of the antenna. So the sizes of microstripline should be designed again to match the impedance of the CCMA. If the microstripline wide is designed to be 2.1 mm ($Z_c = 71\Omega$), then the reflection coefficient of the CCMA will decrease, which is shown in Figure 10.

Figures 11 and 12 show that backward radiation field appears in cylindrical case, but the frontward radiation field is similar to the planar case.

4. Conclusion

The development of the researches on CCMA is unmatured, and the Green functions of cylindrically stratified media are very difficult to calculate accurately and efficiently. Based on the former researches [1–14], this paper proposes a domain-division solution to solve Hankel function's singular problem of Sommerfeld integral in calculating the spatial domain Green function of cylindrically stratified media and realize the computation for all elements of Z -matrix in MoM. Then, theoretical analysis of arbitrary shape CCMA fed by microstripline is done by MoM with the RWG basis function which is more general than the rooftop basis function used in the traditional method. At last, numerical results in the form of mutual impedance between two current modes reveal that the proposed method is valid and efficient. In addition, comparison of the results of a CCMA and a planar microstrip antenna fed by microstripline depicts that the current distribution on microstripline, reflection coefficient, and

normalised radiation patterns are affected by antenna patch's curvature. It also shows that, comparing with the planar counterpart microstrip antenna, the reflection coefficient of the CCMA increases, the current on the microstripline varies sharply, and the backward radiation field appears. However, the frontward radiation field is similar to the planar case. In order to improve the performance of the CCMA, the sizes of microstripline should be designed properly to match the impedance of CCMA.

References

- [1] C. Y. Huang, Y. H. Liu, and K. L. Wong, "Input impedance calculation of cylindrical rectangular microstrip antennas using GTLM theory," in *Proceedings of the IEEE Antennas and Propagation Society International Symposium*, pp. 1792–1795, June 1995.
- [2] M. V. T. Heckler, M. Bonadiman, R. Schildberg, L. Cividanes, and J. C. D. S. Lacava, "CAD Package to Design Rectangular Probe-Fed Microstrip Antennas Conformed on Cylindrical Structures," in *Proceedings of the SMBO/IEEE MTT-S International Microwave and Optoelectronics Conference (IMOC '03)*, pp. 747–752, September 2003.
- [3] M. V. T. Heckler, M. Bonadiman, J. C. D. S. Lacava, and L. Cividanes, "Analysis of cylindrical circumferential array with circular polarization for space applications," in *Proceedings of the IEEE Antennas and Propagation Society Symposium*, pp. 117–120, June 2004.
- [4] J. Sun, C. F. Wang, L. W. Li, and M. S. Leong, "Further improvement for fast computation of mixed potential Green's functions for cylindrically stratified media," *IEEE Transactions on Antennas and Propagation*, vol. 52, no. 11, pp. 3026–3036, 2004.

- [5] S. Karan, V. B. Ertürk, and A. Altintas, "Closed-form Green's function representations in cylindrically stratified media for method of moments applications," *IEEE Transactions on Antennas and Propagation*, vol. 57, no. 4, pp. 1158–1168, 2009.
- [6] V. B. Ertürk and R. G. Rojas, "Efficient computation of surface fields excited on a dielectric-coated circular cylinder," *IEEE Transactions on Antennas and Propagation*, vol. 48, no. 10, pp. 1507–1516, 2000.
- [7] V. B. Ertürk and R. G. Rojas, "Paraxial space-domain formulation for surface fields on a large dielectric coated circular cylinder," *IEEE Transactions on Antennas and Propagation*, vol. 50, no. 11, pp. 1577–1587, 2002.
- [8] V. B. Ertürk and R. G. Rojas, "Efficient analysis of input impedance and mutual coupling of microstrip antennas mounted on large coated cylinders," *IEEE Transactions on Antennas and Propagation*, vol. 51, no. 4, pp. 739–749, 2003.
- [9] T. N. Kaifas and J. N. Sahalos, "Analysis of printed antennas mounted on a coated circular cylinder of arbitrary size," *IEEE Transactions on Antennas and Propagation*, vol. 54, no. 10, pp. 2797–2807, 2006.
- [10] M. He and X. Xu, "Closed-form solutions for analysis of cylindrically conformal microstrip antennas with arbitrary radii," *IEEE Transactions on Antennas and Propagation*, vol. 53, no. 1, pp. 518–525, 2005.
- [11] A. Svezhentsev and G. A. E. Vandenbosch, "Efficient spatial domain moment method solution of cylindrical rectangular microstrip antennas," *IEE Proceedings*, vol. 153, no. 4, pp. 376–384, 2006.
- [12] R. C. Acar and G. Dural, "Mutual coupling of printed elements on a cylindrically layered structure using closed-form green's functions," *Progress in Electromagnetics Research*, vol. 78, pp. 103–127, 2008.
- [13] C. Tokgöz and G. Dural, "Closed-form green's functions for cylindrically stratified media," *IEEE Transactions on Microwave Theory and Techniques*, vol. 48, no. 1, pp. 40–49, 2000.
- [14] W. C. Chew, *Waves and Fields in Inhomogeneous Media*, Van Nostrand, New York, NY, USA, 1995.
- [15] J. Wu, S. K. Khamas, and G. G. Cook, "An efficient asymptotic extraction approach for the green's functions of conformal antennas in multilayered cylindrical media," *IEEE Transactions on Antennas and Propagation*, vol. 58, no. 11, pp. 3737–3742, 2010.
- [16] K. A. Michalski and D. Zheng, "Electromagnetic scattering and radiation by surfaces of arbitrary shape in layered media—I: theory," *IEEE Transactions on Antennas and Propagation*, vol. 38, no. 3, pp. 335–344, 1990.
- [17] K. A. Michalski and D. Zheng, "Electromagnetic scattering and radiation by surfaces of arbitrary shape in layered media—II: implementation and results for contiguous half-spaces," *IEEE Transactions on Antennas and Propagation*, vol. 38, no. 3, pp. 345–352, 1990.
- [18] S. Makarov, "MoM antenna simulations with Matlab: RWG basis functions," *IEEE Antennas and Propagation Magazine*, vol. 43, no. 5, pp. 100–107, 2001.
- [19] K. Tapan and O. Pereira, "Using the matrix pencil method to estimate the parameters of a sum of complex exponentials," *IEEE Antennas and Propagation Magazine*, vol. 37, no. 1, pp. 48–55, 1995.

Research Article

Adaptive Forming of the Beam Pattern of Microstrip Antenna with the Use of an Artificial Neural Network

Janusz Dudczyk and Adam Kawalec

Institute of Radioelectronics, Faculty of Electronics, Military University of Technology, 00-908 Warsaw, Poland

Correspondence should be addressed to Janusz Dudczyk, jdudczyk@wp.pl

Received 16 January 2012; Accepted 2 September 2012

Academic Editor: Dalia N. Elshiekh

Copyright © 2012 J. Dudczyk and A. Kawalec. This is an open access article distributed under the Creative Commons Attribution License, which permits unrestricted use, distribution, and reproduction in any medium, provided the original work is properly cited.

Microstrip antenna has been recently one of the most innovative fields of antenna techniques. The main advantage of such an antenna is the simplicity of its production, little weight, a narrow profile, and easiness of integration of the radiating elements with the net of generators power systems. As a result of using arrays consisting of microstrip antennas; it is possible to decrease the size and weight and also to reduce the costs of components production as well as whole application systems. This paper presents possibilities of using artificial neural networks (ANNs) in the process of forming a beam from radiating complex microstrip antenna. Algorithms which base on artificial neural networks use high parallelism of actions which results in considerable acceleration of the process of forming the antenna pattern. The appropriate selection of learning constants makes it possible to get theoretically a solution which will be close to the real time. This paper presents the training neural network algorithm with the selection of optimal network structure. The analysis above was made in case of following the emission source, setting to zero the pattern of direction of expecting interference, and following emission source compared with two constant interferences. Computer simulation was made in MATLAB environment on the basis of Flex Tool, a programme which creates artificial neural networks.

1. Introduction

The problem of forming the beam pattern of radiating antenna arrays may be come down to the problem of precise updating the amplitude and phases of signals coming from every element of an antenna array before adding them up [1, 2]. There are some well-known ways of calculating weights which are based on maximization of the quotient of the desired signal to the interfering signal (Applebaum array, Shor array) or the conception of minimal mean (LMS array) [3, 4]. LMS and Applebaum arrays are able to follow in time several desired signals. Those can maximize the initial signal/interference quotient and control the shape of the beam pattern in order to set to zero the pattern on the direction of interfering signals [5]. The values of optimal weights are defined in such a way to provide minimal energy function, the definition of which is characteristic for particular algorithms. Artificial neural network both one-way, and recurrent ones in their work do the minimization of the energy function accompanied by a particular network.

The energy function which is defined on the stage of designing the structure of a network has a support role, but it is not the subject in this paper. The main aim of this paper is defining the vector of optimal weights. It can be also said that algorithms basing on ANN use high parallelism of actions which accelerate the realization of the process described above. With the use of appropriate learning constants theoretically it is possible to gain in time a solution close to the real time.

2. Microstrip Phased Arrays

Antenna phased arrays are constructed as conventional antenna arrays, the only difference between them is their architecture in which phase shifting modules are used. After entering, induced signals on particular radiators are added up in order to form the initial signal. The direction on which maximal pattern is expected is controlled by phase shift regulation between particular elements of an array [6, 7]. The beam pattern of an antenna linear array according to

the characteristic multiply factor is defined as relation (1), where $F_e(\theta, \phi)$ is the beam pattern of the radiation of a singular element of the array, and $F(\theta)$ is the pattern of the isotropic elements radiation system:

$$F(\theta, \phi) = F_e(\theta, \phi) \cdot F(\theta). \quad (1)$$

From the relation above, it can be said that mainly the beam pattern $F(\theta)$, called the system multiplier, determines the shape of a radiation system. The phasal shift of input signals on particular antennas is set in a way that maximum pattern covers with the planned direction of the desired emission source. A simplified block schema of the adaptation antenna was presented on Figure 1. The process of adding up the signals from particular elements is called the process of forming an antenna beam. The direction, on which the pattern of radiation array reaches its maximum, is adjusted to the desired signal. Steering the antenna beam can be made by appropriate delay of signals before connecting into an output signal as a result of the use of phase shifters. Elasticity, with which weights can be adjusted, implicates a crucial feature which can be used to eliminate the direction of the signal with a frequency identical to this of the expected signal. Removing one redundant signal by controlling the zero of the antenna beam pattern causes the consumption of one freedom degree. To limit setting to zero, only to redundant signals, the desired signal has to be paired with a steering vector, and then the weights calculation has to be done by using particular algorithms. The information about the steering vector is necessary as it protects the signal from being removed. Setting to zeros the antenna system beam pattern on the directions, on which there are emission sources, is done through weights calculation. These weights are represented by complex numbers which are assigned to particular elements of antenna arrays. The processes described above can be realized with the use of an ANN. A prototype of an artificial neural network is the biological nerve system with the structure consisting of nerve cells (neurons) with particular connections. Originally, artificial neural networks were an attempt of modelling mechanisms due to which nerve cells function in further perspective; they are quite useful while constructing artificial intelligence as it is similar in its structure to the human brain [8, 9]. Works on ANN can be divided into a few periods [10]. Early works concerning the first theoretical model of McCulloch and Pitts neuron [11] and later Hebb's work [12]. Further special interest in this subject is connected generally with Rosenblatt works [13] and Widrow's and Hoff's works [14]. Later low interest in this subject was caused by some limits of the single-layer perceptron which were presented in Minsky and Papert's work [15]. Only Hopfield's work [16] from 1982 and later works of different researchers concerning the backpropagation algorithm caused some increase in interest in artificial neural networks, which is still seen today.

Backpropagation is a famous training method used in the multilayer networks, but it often suffers from a local minima problem. To avoid this problem, a new backpropagation training based on chaos was proposed in [17]. The algorithm shown in [17] is comparable with the Levenberg-Marquardt

algorithm, but simpler and easier to implement comparing to Levenberg-Marquardt algorithm. Also neural networks and support vector machines (SVMs), idea of learning, fuzzy logic (FL), and data mining (DM) with computational intelligence are shown in [18, 19].

A single neuron consists of a kernel, dendrites which are entries, and an axon which is a single entry to the nerve cell. At the end of dendrites and an axon there are synapses which conduct information. The axon of a particular neuron is connected by synapses with dendrites of other neurons. Input signals x_i , $i = 1, 2, \dots, N$ have binary values depending on the appearance of an input impulse in the moment k . Defining the output signal by y , the rule of a single neuron activation can be written with respect to the following relation (2), where $k = 0, 1, 2, \dots$ are later moments of time, while w_i is multiplicative weight assigned to the connection of the entry i with the membrane of a neuron [11] as follows:

$$y^{k+1} = \begin{cases} 1, & \text{when } \sum_{i=1}^N w_i x_i^k \geq T \\ 0, & \text{when } \sum_{i=1}^N w_i x_i^k < T. \end{cases} \quad (2)$$

Generally it is assumed that between moments k and $k + 1$, the individual time of delay is passing for excitatory synapses $w_i = +1$ and for inhibitory synapses $w_i = -1$, where T is the threshold value determining the neuron's reaction. As McCulloch-Pitts model has several crucial simplifications (only binary operations, discrete work time, synchronization of all neurons work in one network, and unchanging thresholds and weights), a general description of an artificial neuron is introduced. Thus, now more complex models of a neuron are used to realize a neural network. Each neuron consists of a transforming element connected with synaptic entries and one entry according to the model Figure 2.

The transfer of signals in all connections is one way, and the output signal y of a neuron is defined with respect to following relation (3), where \mathbf{w} is a weights vector, while \mathbf{x} is the input vector defined by relations (4):

$$y = f(\mathbf{w}^T \mathbf{x}) = f\left(\sum_{i=0}^N w_i x_i\right), \quad (3)$$

$$\begin{aligned} \mathbf{w} &\stackrel{\text{def}}{=} [w_0, w_1, \dots, w_N]^T, \\ \mathbf{x} &\stackrel{\text{def}}{=} [x_0, x_1, x_2, \dots, x_N]^T. \end{aligned} \quad (4)$$

The function $f(\mathbf{w}^T \mathbf{x})$, whose domain is the set of all activation link connections of a neuron, is called the "activation function." Defining activation with the symbol net , the function can be defined as $f(\text{net})$, where the variable net is defined by the dot product of weights and input signals vector $\text{net} = \mathbf{w}^T \mathbf{x}$. Whole activation net is an equivalent of the activation potential in the biological neuron. Individual classes of neurons differ in the function of definition $f(\text{net})$. Due to (3), defining the output signal y appears the fact that firstly weighted input signals are added up in order to define the whole activation net . Then, the operation $f(\text{net})$ is done according to its own activation function. The most popular

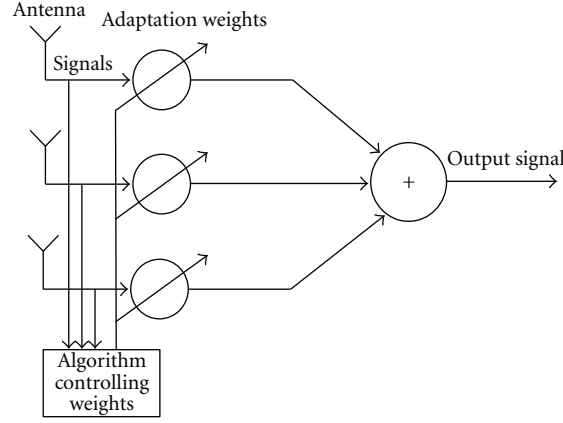


FIGURE 1: A simplified block schema of adaptation antenna system.

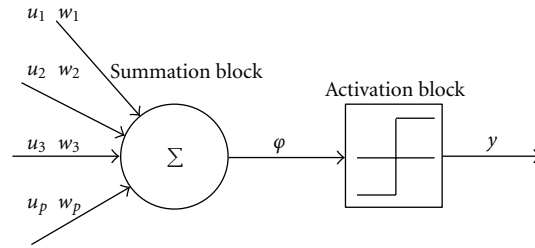


FIGURE 2: General model of an artificial neuron.

type of a neural network is one-way network example of which is a simple perceptron. As there are no connections between elements of the output layer, each element can be treated as a separate network with $N + 1$ inputs and one output. The perceptron network can be divided precisely into ordered classes and separated classes of elements called layers within which there is an input layer, an output layer, and hidden layers. Among layers of neurons which make up together a multilayered perceptron, the input layer with a linear activation function can be distinguished. The number of elements of this layer is precisely determined by the number of input data taken into account while doing the task of forming the microstrip antenna pattern.

3. Implementation of Artificial Neural Network Process

In the presented research the tool used to model the work of artificial neural networks was the modular programme Flex Tool. The implementation of the ANN process had several stages. Firstly, initial working conditions of the artificial neural network were defined and self-learning pairs were prepared. Secondly, the architecture optimization of this network was done. Later on, the process of learning and testing were conducted. What was next was defining initial conditions that concern aspects in which the ANN work will work. It was assumed that the network should form the beam pattern of a linear array consisting of six elements simultaneously following the emission source (ES) while

interference. The second condition was setting to zero the beam pattern on the direction of interference which changes its location. The second stage was preparing self-learning set. data that was used in the process of teaching the ANN was calculated for the array above ($n = 6$) with the use of the LMS algorithm. The algorithm used estimates the correlation vector \mathbf{S} of the coming signal \mathbf{x}_d with the desired reference signal \mathbf{r} . For the LMS algorithm which was used the general form of a signal and interference is presented in, the form of (5), where A_d and A_z define amplitudes of coming signal and interfering signal, θ_d and θ_z define the angle of coming signal and the angle of coming interference, and ϕ_d and ϕ_z define phasal shifts between elements of the antenna array as the following:

$$d_n = A_d \cdot e^{-in\phi_d}, \quad dz_n = A_z \cdot e^{-in\phi_z}. \quad (5)$$

Later on, signals are written in the form of $\mathbf{X}_d = [d_1, d_2, d_3, d_4, d_5, d_6]^T$ and $\mathbf{X}_z = [dz_1, dz_2, dz_3, dz_4, dz_5, dz_6]^T$, and then what is defined is the covariance matrix of a signal Φ_{sig} and the covariance matrix of interference Φ_{dis} according to the following relations:

$$\begin{aligned} \Phi_{\text{sig}} &= \bar{\mathbf{x}}_d \mathbf{x}_d^T, \\ \Phi_{\text{dis}} &= \bar{\mathbf{x}}_z \mathbf{x}_z^T. \end{aligned} \quad (6)$$

Next, the covariance matrix of both is calculated; the correlation vector \mathbf{S} and the weight vector \mathbf{W} are also estimated as follows:

$$\begin{aligned}\Phi &= \Phi_{\text{sig}} + \Phi_{\text{dis}}, \\ \mathbf{S} &= \bar{\mathbf{x}}_d \mathbf{r}, \\ \mathbf{W} &= \Phi^{-1} \mathbf{S}.\end{aligned}\quad (7)$$

Weights which are calculated with the use of the algorithm above are treated as model ones in the process of organizing. Then the architecture optimization of a network was prepared. It was done as a result of selecting the right number of hidden layers and neurons in these layers. Next, the defined network underwent the process of organizing and testing. Testing means drawing the power beam pattern, which weights were calculated with the use of LMS algorithm. When the results did not add up with the assumptions, other neurons were added to the network architecture. The process was carried on until the beam patterns of the microstrip antenna tallied with the model.

3.1. Self-Learning ANN Algorithm. To teach an artificial neural network, the Delta method was used which changes the learning error in the function of a number of self-learning epochs. The Delta rule is used with neurons which have constant activation function and is used as an equivalent of the perceptron rule which is also called the constant perceptron rule. This method can be easily introduced as a minimization of the square criterion error. Its general version can be used in multilayered networks. In the Delta rule each neuron after receiving particular signals on its inputs (from network inputs or other neurons which are earlier layers of the networks) defines its output signal using information in the form of weight values and (if necessary) thresholds, which were set earlier. The value of the output signal defined by the neuron in the particular learning stage of process is compared with the model reply given by the teacher in the learning sequence. If there is a disagreement that is when a neuron defines the difference between its output signal and the value of this signal, although which could be correct according to the teacher. Such difference is usually defined as δ (delta, a Greek letter) like the name of this method. The error signal (delta) is used by the neuron to correct its weight coefficients (and if necessary the threshold) applying following rules:

- (i) the more serious error was detected, the bigger change in weights is made,
- (ii) weights connected with the inputs on which there are high values of input signals are changed more than weights which input signal was not high.

With the use of Delta method in this work, the error function was defined with respect to the following relation (8), where d_{jp} is the model output signal j th element of the output layer while forcing with the learning signal p , and y_{jp} is the current

output signal j th element of the output layer while forcing with the learning signal p :

$$E_p = \frac{1}{2} \sum_{i=1}^n (d_{jp} - y_{jp})^2. \quad (8)$$

This method of calculating the function error is based on backpropagation algorithm where, first of all, errors in the last layer are calculated on the basis of comparison current and model output signals, and on such a ground connection weights are changed then in the layer before and previous ones until the first one. There are three stages in the backpropagation algorithm:

- (i) introduce the organizing signal \mathbf{x} on the input, and calculate current outputs \mathbf{y} ;
- (ii) compare the output signal \mathbf{y} with the model signal \mathbf{d} , and then calculate local errors for all network layers;
- (iii) do the weight adaptation.

For the energy function defined by (8) as a mean squared error, the updating weight method for the output layer can be defined with (9), where the index $(\cdot)^{[2]}$ is the output layer:

$$\Delta w_{ji}^{[2]} = -\eta \frac{\partial E_p}{\partial w_{ji}^{[2]}} = -\eta \frac{\partial E_p}{\partial u_j^{[2]}} \frac{\partial u_j^{[2]}}{\partial w_{ji}^{[2]}}. \quad (9)$$

Taking into account (10),

$$u_j^{[2]} = \sum_{i=1}^{n2} w_{ji}^{[2]} o_i^{[1]}, \quad (10)$$

and defining the local error with respect to the following equation (11):

$$\begin{aligned}\delta_j^{[2]} &= -\frac{\partial E_p}{\partial u_j^{[2]}} = -\frac{\partial E_p}{\partial e_{jp}} \frac{\partial e_{jp}}{\partial u_j^{[2]}} = -e_{jp} \frac{\partial (d_{jp} - y_{jp})}{\partial u_j^{[2]}} \\ &= e_{jp} \frac{\partial y_{jp}}{\partial u_j^{[2]}} = e_{jp} \frac{\partial \Psi}{\partial u_j^{[2]}},\end{aligned}\quad (11)$$

results in the relation defining updating weights in the output layer with respect to the following equation (12):

$$\begin{aligned}w_{ji}^{[2]}(t) &= w_{ji}^{[2]}(t-1) + \Delta w_{ji}^{[2]}, \\ \Delta w_{ji}^{[2]} &= \eta \delta_j^{[2]} o_i^{[1]}.\end{aligned}\quad (12)$$

More complicated problem is finding the local error for elements in hidden layers as the correct output signal from the elements of this layer is not known. Thus, available or

easily calculated data is used with respect to the formula (13) as follows:

$$\begin{aligned}\delta_j^{[1]} &= -\frac{\partial E_p}{\partial u_j^{[1]}} = -\frac{\partial E_p}{\partial o_{jp}^{[1]}} \frac{\partial o_{jp}^{[1]}}{\partial u_j^{[1]}} = -\frac{\partial E_p}{\partial o_{jp}^{[1]}} \frac{\partial \Psi}{\partial u_j^{[1]}}, \\ \frac{\partial E_p}{\partial o_j^{[1]}} &= \sum_{i=1}^{n_2} \frac{\partial E_p}{\partial u_i^{[2]}} \frac{\partial u_i^{[2]}}{\partial o_j^{[1]}} = \sum_{i=1}^{n_2} \left(\frac{\partial E_p}{\partial u_i^{[2]}} \right) \frac{\partial}{\partial o_j^{[1]}} \left(\sum_{k=1}^{n_2} w_{ik}^{[2]} o_k^{[1]} \right) \\ &= -\sum_{i=1}^{n_2} \delta_i^{[2]} w_{ij}^{[2]}.\end{aligned}\quad (13)$$

As a result; the formula for the local error was written according to (14), and allowance for weights was defined with the use of (15):

$$\delta_j^{[1]} = \frac{\partial \Psi}{\partial u_j^{[1]}} \sum_{i=1}^{n_2} \delta_i^{[2]} w_{ij}^{[2]}, \quad (14)$$

$$\Delta w_{ji}^{[1]} = \eta \delta_j^{[1]} x_i. \quad (15)$$

Firstly, the criterion finishing the process was the assumed number of learning epochs. However, analysing the graphs with the error change depending on the number of the epoch, this criterion does not react to the so-called effect of network overlearning which is decreasing the ability to generalize a net. More effective criterion finishing the process of learning artificial neural network is defining the learning error threshold after which the process is stopped.

3.2. Optimal Structure of ANN Selection. In the first stage of searching for an optimal structure of ANN was one hidden layer. The selection of number of neurons in the hidden layer starts with the least number and more of them are added gradually. The important role in this part of the process is testing the organized net and comparing the result with requirements defined in the assumption. The model beam pattern, marked with green colour, is compared with the results from artificial neural net simulation should be compared. The received ANN beam patterns are marked with black colour. These beam patterns were received with the use of an artificial neural net. The direction of the desired signal is marked with blue colour, and the direction of interfering signal is marked with red colour. The graphs which are presented are the patterns of power radiated from the array in the function of the radiating angle to the maximal values of radiated power.

4. Results of the Analysis

4.1. Optimal Architecture an ANN Selection for the Process of Following the Emission Source. The process of ANN learning in order to follow the emission source was started with ten neurons in the hidden layer. As a result of calculating weights; the ANN beam pattern was depicted on Figure 3. Influenced

by the level of side lobes, the decision about increasing the number of neurons was made. Next steps, which were finished with testing, show some shape improvement of the ANN beam pattern in comparison with the model pattern (marked with green colour). Figure 4 shows the beam pattern received with 14 neurons in the hidden layer and Figure 5 shows the beam pattern with 18 neurons in the hidden layer. With twenty neurons in the hidden layer, the shape of the ANN beam pattern and the level of side lobes were close enough to the model beam pattern (Figure 6).

4.2. Optimal Architecture an ANN Selection for the Process of Setting to Zero the Beam Pattern on the Expected Interference Direction. In case of optimal architecture, an artificial neural network selection with the setting to zero variant on the direction of expected interference the test of an ANN with twelve neurons in the hidden layer was started. On the basis of Figure 7, it can be said that the received results of an ANN beam pattern are far from expectations as on the direction of interference there is side lobe, which cannot be accepted. Gradual increasing of the number of neurons (Figures 8 and 9) improved the beam pattern making it closer to the shape of the assumed model beam pattern—marked with black colour. In this case as well as in the previous one, the minimal number of neurons in the hidden layer which meets the requirements provided in assumptions was defined as twenty neurons in the hidden layer presented on Figure 10.

4.3. Following the Emission Source with the Use of an ANN. The effect of further tests was receiving beam patterns with the use of an artificial neural network. Some models of ANN beam patterns were received with the use of an artificial neural network on Figures 11, 12, 13, and 14. The graphs presented here are patterns of radiation power from the antenna array in the function of radiation angle which were standardized to the maximal radiation power. In the process of following emission source, the beam patterns presented on Figures 11–14 are scanning a space beam and following the desired signal.

4.4. The Beam Pattern Setting to Zero on the Interference Direction with the Use of an ANN. The ANN beam patterns on Figures 15, 16, 17, and 18 present the process of elimination of interference (marked with red colour on the graphs) on particular directions taking into account the assumption that the desired signal comes from the direction perpendicular to the antenna array. The desired signal is marked with blue colour.

4.5. Following the Emission Source with Two Constant Interferences with the Use of an ANN. The ANN beam patterns presented on Figures 19, 20, 21, and 22 are showing the process of following the desired signal which was marked with blue colour on the interference background. The interference was marked with red colour on the models of interferences with 45 degrees and 135 degrees.

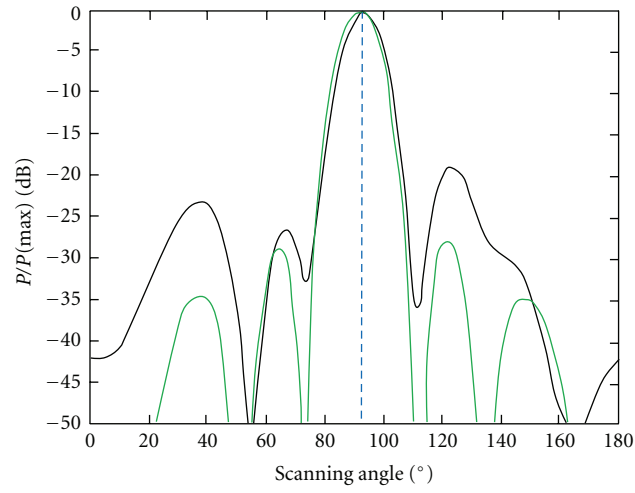


FIGURE 3: The beam pattern received with 10 neurons in the hidden layer—following ES.

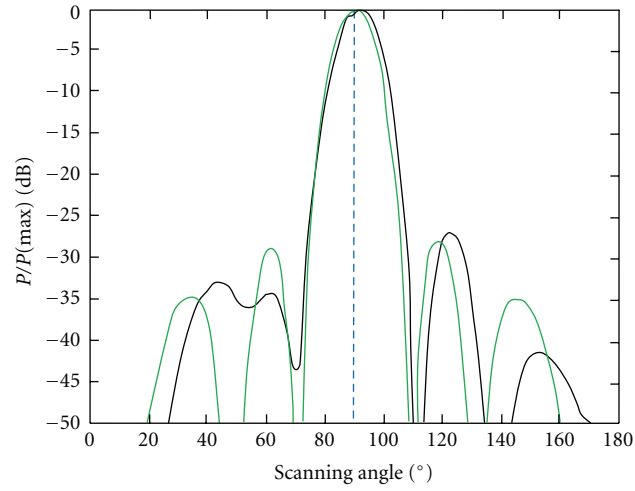


FIGURE 4: The beam pattern received with 14 neurons in the hidden layer—following ES.

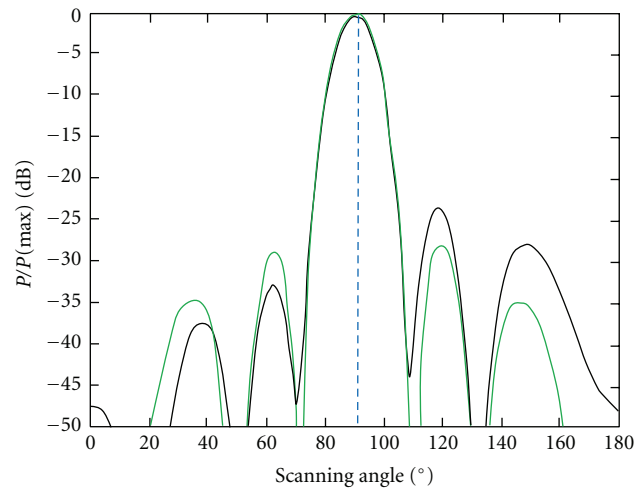


FIGURE 5: The beam pattern received with 18 neurons in the hidden layer—following ES.

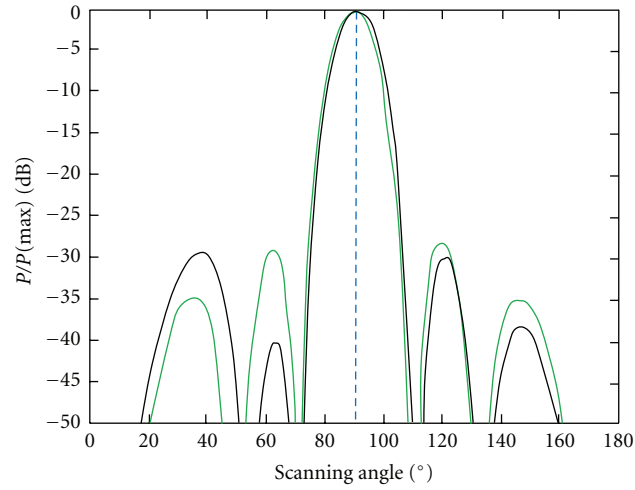


FIGURE 6: The beam pattern received with 20 neurons in the hidden layer—following ES.

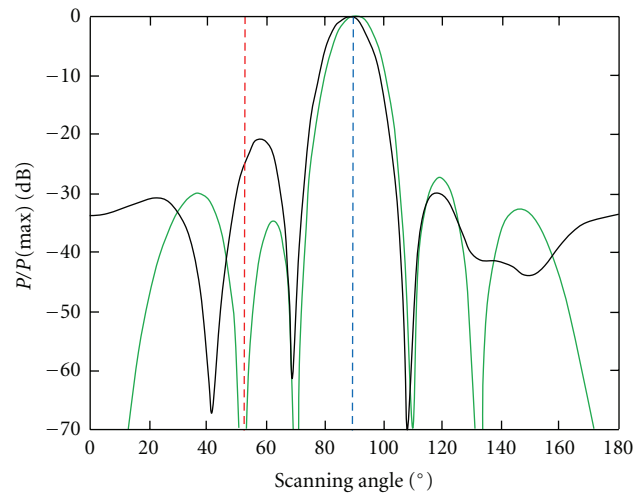


FIGURE 7: The ANN beam pattern received with 12 neurons in the hidden layer—the beam pattern setting to zero on the interference direction.

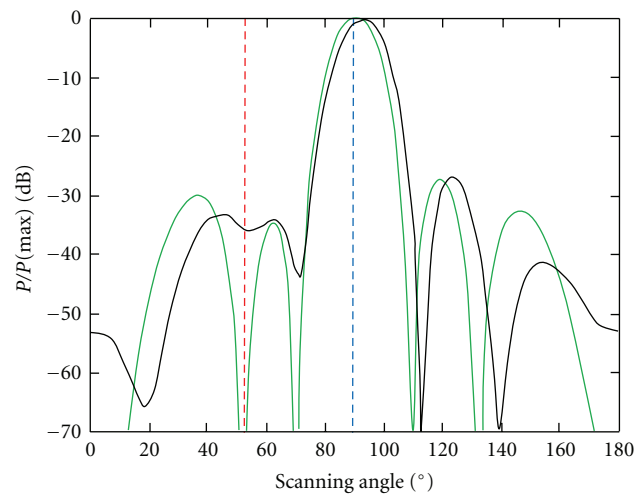


FIGURE 8: The ANN beam pattern received with 14 neurons in the hidden layer—the beam pattern setting to zero on the interference direction.

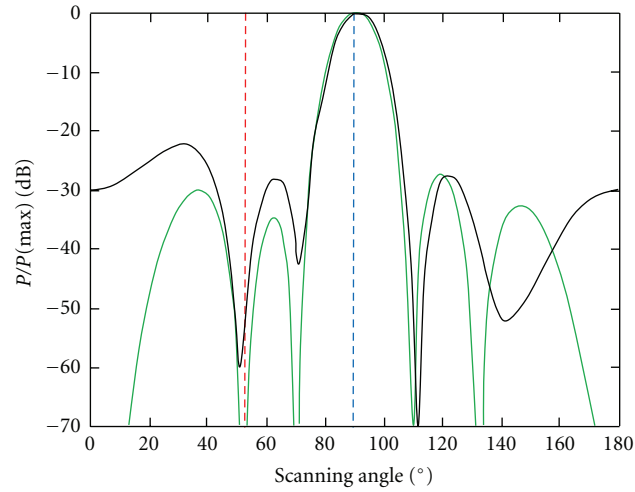


FIGURE 9: The ANN beam pattern received with 16 neurons in the hidden layer—the beam pattern setting to zero on the interference direction.

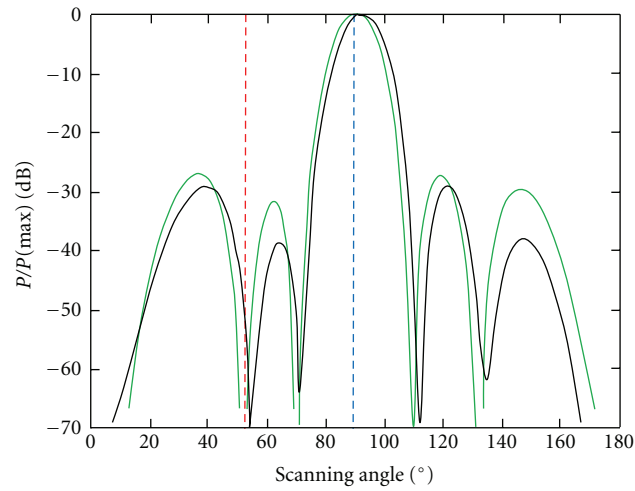


FIGURE 10: The ANN beam pattern received with 20 neurons in the hidden layer—the beam pattern setting to zero on the interference direction.

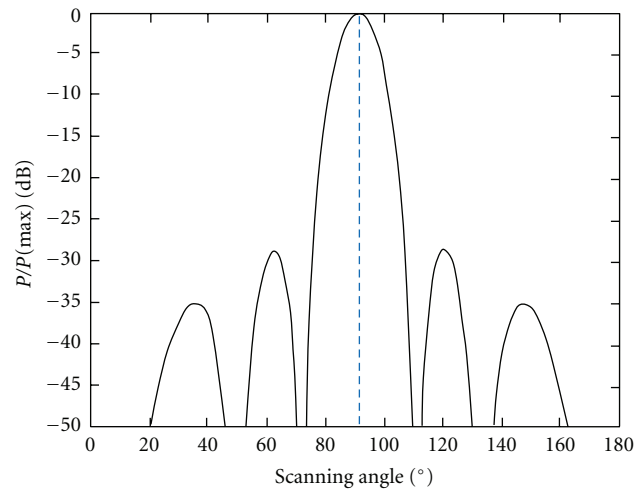


FIGURE 11: The beam pattern pointed towards the signal-glancing right.

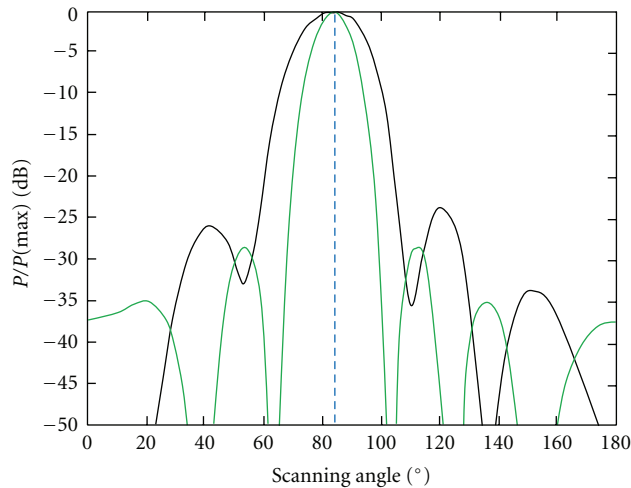


FIGURE 12: The beam pattern pointed towards the useful signal with the angle of 83 degrees.

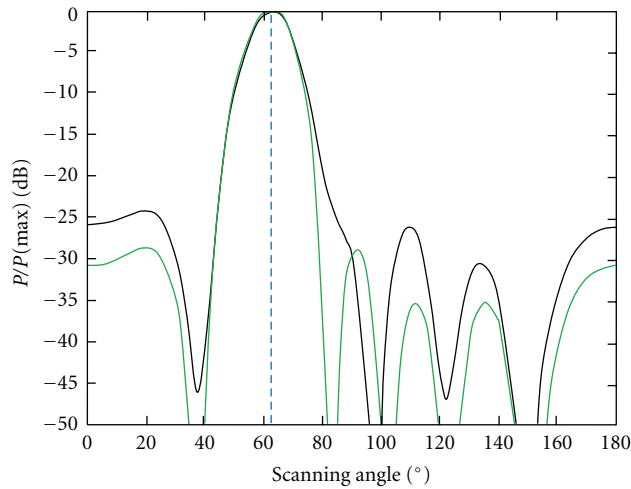


FIGURE 13: The beam pattern pointed towards the useful signal with the angle of 62 degrees.

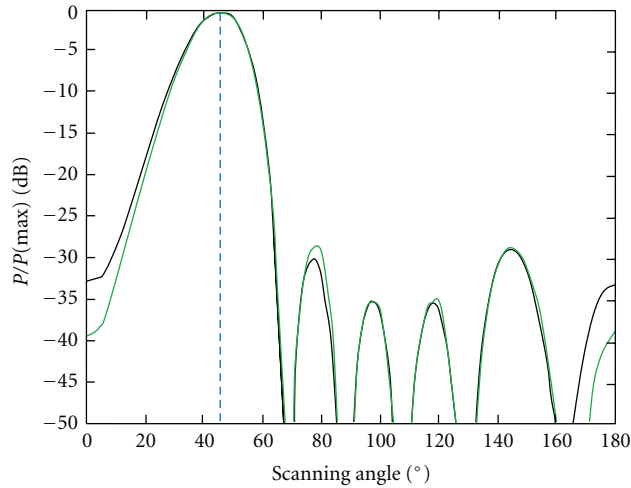


FIGURE 14: The beam pattern pointed towards the useful signal with the angle 45 degrees.

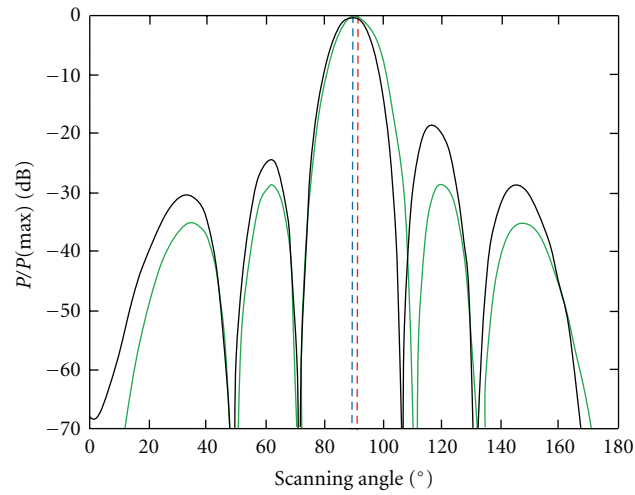


FIGURE 15: The beam pattern of the antenna array with 0 degree of interference.

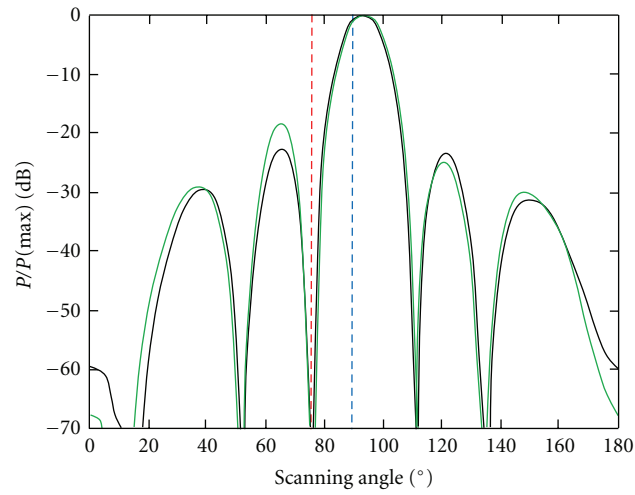


FIGURE 16: The beam pattern of the antenna array with 75 degrees of interference.

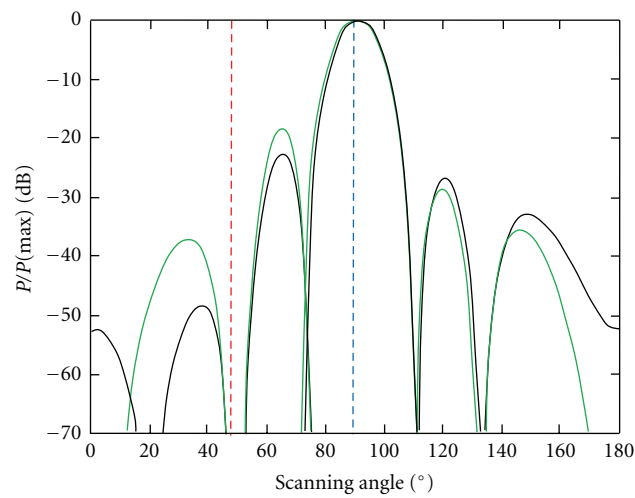


FIGURE 17: The beam pattern of the antenna array with the 47 degrees of interference.

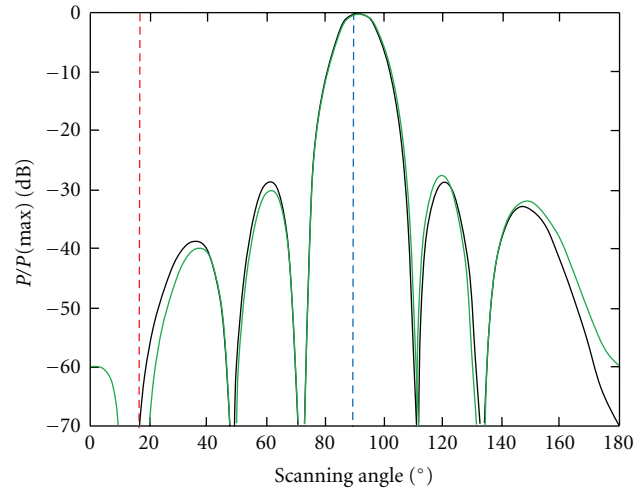


FIGURE 18: The beam pattern of the antenna array with the 15 degrees of interference.

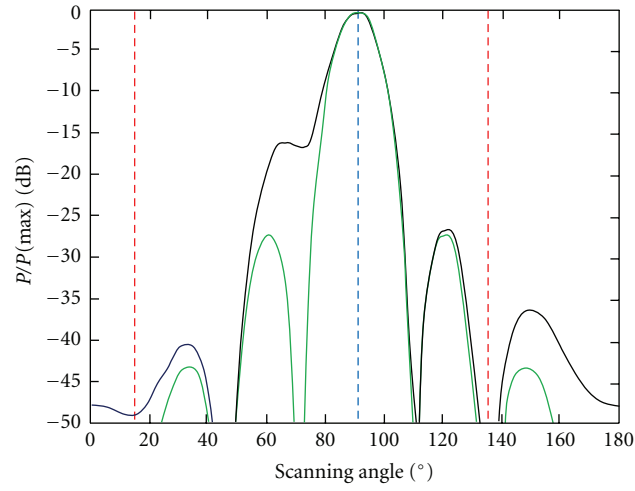


FIGURE 19: An ANN beam pattern pointed towards the signal with the right angle.

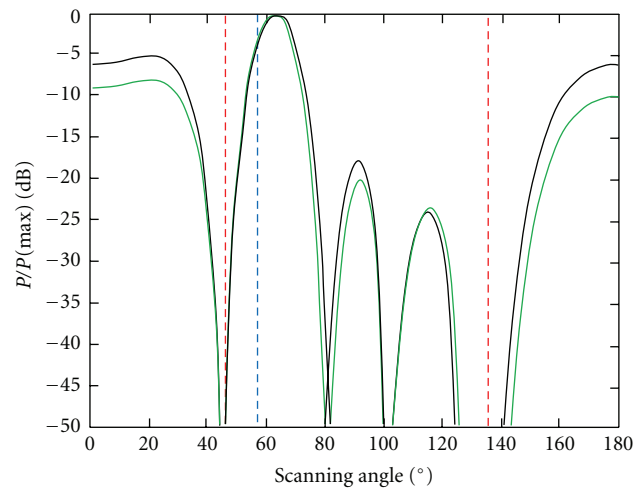


FIGURE 20: An ANN beam pattern pointed towards the signal with the angle of 55 degrees.

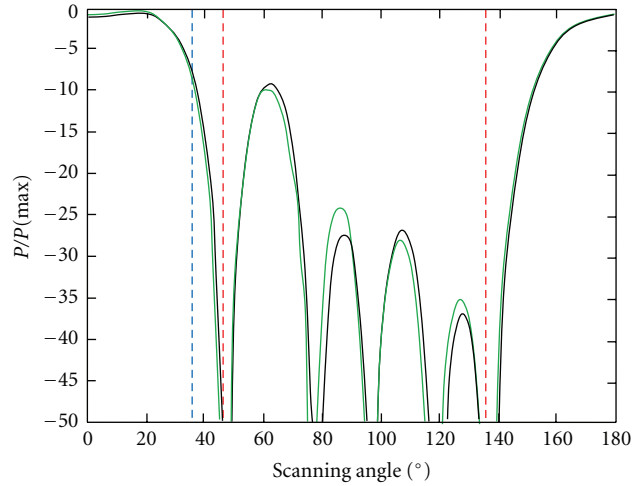


FIGURE 21: An ANN beam pattern pointed towards the useful signal with the angle of 35 degrees.

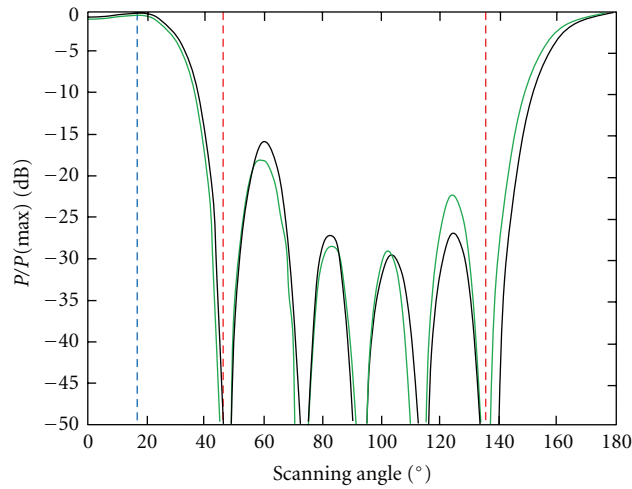


FIGURE 22: An ANN beam pattern pointed towards the useful signal with the angle of 15 degrees.

5. Conclusions

This paper presented the use of an artificial neural network to form a microstrip complex antenna array beam pattern. On the basis of the graph analysis of the ANN beam pattern received in the use of neural networks and comparing them with graphs received as a result of using traditional algorithms, it can be said that due to the adjustment of the neural network structure to the task (the appropriate number of hidden layers and the number of neurons in these layers), the results which were received agreed with the model beam pattern.

In case of an emission source following the main lobe of beam pattern goes after the signal. The only possible quibble about it may be the size of side lobes. Nevertheless, the main goal was achieved, and the case of side lobes minimization will probably be the topic of further tests in this aspect.

It was assumed that there will be an emission source of the desired signal on the direction perpendicular to the antenna array while setting to zero the beam pattern on

the direction of the expected interference. In comparison with the previous case, such an option increases the number of complications while controlling the pattern. However, even such an option provides satisfying results which are presented on Figures 15–18.

The most complicated issue was following the emission source while having simultaneously two interferences. This task required increasing the learning set which resulted in increasing the time of an ANN learning. Improvement of the shape of the beam pattern was made as a result of the extension of an artificial neural network in the layer. Some limitations are also introduced by the platform used in neural networks simulation which need to be considered while precisising the assumptions concerning the expected quality of the mapping pattern.

The artificial neural network tested here turned out to be a tool fair enough to make decisions about the signal which after learning is able to distinguish interference from the desired signal. In this case the criterion of making the

decision was connected only with the signal amplitude; however, further tests will be concentrated on increasing the parameters considered as the criterion. However, it must be emphasized that the model neural network requires another process of learning in every change of conditions resulting from the assumptions. This process of learning adjusts its weights to the ensuing situation, which complicates the use of an artificial neural network in cases where there are many changes. What should be also noticed is that work of an ANN is adding, multiplying, and comparing with the output signals' threshold which in comparison with mathematical operations used in typical algorithms (matrix inversion, correlation vectors calculation, and covariance matrix calculation) facilitates using the DSP technique.

Using complex microstrip antenna arrays decreases weights and production costs. The characteristic feature of microstrip antenna arrays is their simple change of the phase area decomposition in the aperture of the system, which makes them easy to use in electronic controlling the beam pattern.

Acknowledgment

This work was supported by the National Centre for Research and Development (NCBiR) from sources for science in the years 2010–2012 under Project O R00 0161 12.

References

- [1] R. A. Monzingo and T. W. Miller, *Introduction to Adaptive Array*, John Wiley & Sons, 1980.
- [2] B. Widrow, P. E. Mantey, L. J. Griths, and B. B. Goode, "Adaptive antenna systems," *Proceedings of the IEEE*, vol. 55, pp. 2143–2159, 1967.
- [3] S. P. Applebaum, "Adaptive Arrays," *IEEE Transactions on Antennas and Propagation*, vol. 24, no. 5, pp. 585–598, 1976.
- [4] S. W. W. Shor, "Adaptive technique to discriminate against coherent noise in a narrow-band systems," *Journal of the Acoustical Society of America*, vol. 34, no. 1, pp. 74–78, 1966.
- [5] R. L. Riegler and R. T. Compton, "Adaptive array for interference rejection," *Proceedings of the IEEE*, vol. 61, no. 6, pp. 748–758, 1973.
- [6] R. Garg, P. Bhartia, I. Bahl, and A. Ittipiboon, *Microstrip Antenna Design Handbook*, Artech House INC, London, UK, 2001.
- [7] J. F. Zurcher and F. E. Gardiol, *Broadband Patch Antennas*, Artech House INC, London, UK, 1995.
- [8] S. Osowski, *Neural Networks in Algorithms*, Scientifically Technical Press, Warsaw, Poland, 1996.
- [9] D. Rutkowska, M. Pilinski, and L. Rutkowski, *Neural Networks, Genetic Algorithms and Fuzzy Systems*, Scientifically Technical Press, Warsaw, Poland, 1997.
- [10] J. Hertz, A. Krogh, and R. G. Palmer, *Introduction to Neural Networks*, Scientifically Technical Press, Warsaw, Poland, 1993.
- [11] W. S. McCulloch and W. H. Pitts, "A logical calculus of the ideas immanent in nervous activity," *The Bulletin of Mathematical Biophysics*, vol. 5, no. 4, pp. 115–133, 1943.
- [12] D. O. Hebb, *The Organization of Behaviour*, John Wiley & Sons, New York, NY, USA, 1949.
- [13] F. Rosenblatt, *Principles of Neurodynamics*, Spartan, Greece, 1962.
- [14] B. Widrow and M. E. Hoff, "Adaptive switching circuits," in *1960 IRE WESCON Convention Record*, pp. 96–104, New York, NY, USA, 1960.
- [15] M. L. Minsky and S. A. Papert, *Perceptrons*, MIT Press, 1969.
- [16] J. J. Hopfield, "Neural networks and physical systems with emergent collective computational abilities," *Proceedings of the National Academy of Sciences of the United States of America*, vol. 79, no. 8, pp. 2554–2558, 1982.
- [17] F. Fazayeli, L. Wang, and W. Liu, "Back-propagation with chaos," in *Proceedings of the IEEE International Conference Neural Networks and Signal Processing (ICNNSP' 08)*, pp. 5–8, Zhenjiang, China, June 2008.
- [18] V. Kecman, *Learning and Soft Computing, Support Vector machines, Neural Networks and Fuzzy Logic Models*, The MIT Press, Cambridge, Mass, USA, 2001.
- [19] L. P. Wang and X. J. Fu, *Data Mining with Computational Intelligence*, Springer, Berlin, Germany, 2005.

Research Article

Rapid Beam Forming in Smart Antennas Using Smart-Fractal Concepts Employing Combinational Approach Algorithms

Mounissamy Levy,¹ Sumanta Bose,¹ D. Sriram Kumar,¹ and Anh Van Dinh²

¹ Department of Electronics and Communication Engineering, National Institute of Technology Trichy, Tamil Nadu 620015, India

² Department of Electrical and Computer Engineering, University of Saskatchewan, Saskatoon, SK, Canada S7N 5A9

Correspondence should be addressed to Mounissamy Levy, 408110003@nitt.edu

Received 6 February 2012; Revised 9 September 2012; Accepted 9 September 2012

Academic Editor: Dalia N. Elshiekh

Copyright © 2012 Mounissamy Levy et al. This is an open access article distributed under the Creative Commons Attribution License, which permits unrestricted use, distribution, and reproduction in any medium, provided the original work is properly cited.

Smart antennas offer a broad range of ways to improve wireless system performance. They provide enhanced coverage through range extension, hole filling, and better building penetration. Smart antennas use an array of low gain antenna elements which are connected by a network. Fractal concepts have been used in antenna arrays recently. The important properties of fractal arrays are frequency independent multiband characteristics, schemes for realizing low side lobe designs, systematic approaches to thinning, and the ability to develop rapid beam forming algorithms. In this paper, an attempt has been made to apply assignment of usage time and location tag algorithm for smart antennas combined with the fractal concepts to reduce the computational complexity and enhance resource allocation for rapid beam forming algorithms. Furthermore, two combinational approach algorithms are proposed for peer users within single base station and peer users between different base stations.

1. Introduction

Smart antennas are MIMO arrays that emphasize the signal of interest and minimizes the interfering signals by adjusting or adapting its own beam pattern. This is done by varying the relative phases of the respective signals feeding the antennas in such a way that the effective radiation pattern of the array is reinforced in the desired direction and suppressed in undesired directions to model any desired radiation pattern. Smart antenna techniques are used notably in signal processing, RADAR, radio astronomy, and cellular systems like W-CDMA and UMTS. The smart antenna concept can be used in optical antenna technology also to produce rapid beam scanning. Spatial time multiplexing techniques and space time block code techniques also widely use smart antennas. UWB communication also makes use of smart antennas with proper bandwidth allocated to it.

2. Fractal Concepts

A fractal is a recursively generated object having a fractional dimension. Many objects, including antennas, can be

designed using the recursive nature of a fractal. The important properties of fractal arrays are frequency independent multiband characteristic schemes for realizing low-side lobe designs, systematic approaches to thinning, and the ability to develop rapid beam-forming algorithms by exploiting the recursive nature of fractals. These arrays have fractional dimensions that are found from generating subarray used to recursively create the fractal array.

The term fractal, meaning *broken* or *irregular fragments*, was originally coined by Mandelbrot [1] to describe a family of complex shapes that possess an inherent self-similarity in their geometrical structure. Since the pioneering work of Mandelbrot and others, a wide variety of applications for fractals have been found in many branches of science and engineering. One such area is fractal electrodynamics, in which fractal geometry is combined with electromagnetic theory for the purpose of investigation of new class of radiation, propagation, and scattering problems. One of the most promising areas of fractal electrodynamics research is in its applications to antenna theory and design. We refer to this new and rapidly growing field of research as fractal antenna engineering. There are primarily two active areas

of research in fractal antenna engineering: study of fractal-shaped antenna elements and the use of fractals in antenna arrays [2–4].

The first application of fractals to the field of antenna theory was reported by Kim and Jaggard [5]. They introduced a methodology for designing low-side lobe arrays which is based on the theory of random fractals. Lakhtakia et al. [6] demonstrated that the diffracted field of a self-similar fractal screen also exhibits self-similarity. The fact that self-scaling arrays can produce fractal radiation patterns was first established and the work was later extended to the case of concentric ring arrays by Liang et al. [7]. Applications of fractal concepts to the design of multiband Koch arrays, as well as to low-side lobe Cantor arrays, are discussed by Puente-Baliarda and Pous [8]. Other types of fractal array configurations are discussed by Werner et al. [9].

A rich class of fractal arrays exists which can be formed recursively through the repetitive application of a generating subarray. A generating subarray is a small array at scale one ($P = 1$) where P is the scale factor and is used to construct larger arrays at higher scales (i.e., $P > 1$). In many cases, the generating subarray has elements that are turned on and off in a certain pattern. A set formula for copying, scaling, and translation of the generating subarray is then followed in order to produce the fractal array. Hence, fractal arrays that are created in this manner will be composed of a sequence of self-similar subarrays. In other words, they may be conveniently thought of as arrays of arrays [9].

The array factor for a fractal array of this type may be expressed in the general form:

$$AF_P(\psi) = \prod_{i=1}^P \hat{GA}(\delta^{i-1}\psi), \quad (1)$$

where $GA(\psi)$ represents the array factor associated with the generating subarray. The parameter δ is a scale or expansion factor that governs how large the array grows with each recursive application of the generating subarray. The expression for the fractal array factor given in (1) is simply the product of scaled versions of a generating subarray factor. Therefore, we may regard equation (1) as representing a formal statement of the pattern multiplication theorem for fractal arrays. Applications of this specialized pattern-multiplication theorem to the analysis and development of rapid beam forming algorithms will be considered in the following sections.

3. Smart Antennas: Beam Forming

There is an ever-increasing demand on mobile wireless operators to provide voice and high-speed data services. At the same time, these operators want to support more users per base station to reduce overall network costs and make the services affordable to subscribers. As a result, wireless systems that enable higher data rates and higher capacities are a pressing need. Unfortunately, because the availability of broadcast spectrum is limited, attempts to increase traffic within a fixed bandwidth create more interference in the system and degrade the signal quality [10–12].

In particular, when Omni-directional antennas, as shown in Figure 1(a) [13] are used at the base station, the transmission/reception of each user's signal becomes a source of interference to other users located in the same cell, making the overall system interference limited. An effective way to reduce this type of interference is to split up the cell into multiple sectors and use sectorized antennas, as shown in Figure 1(b) [13].

Smart antenna technology offers a significantly improved solution to reduce interference levels and improve the system capacity. With this technology, each user's signal is transmitted and received by the base station only in the direction of that particular user. This drastically reduces the overall interference in the system. A smart antenna system, as shown in Figures 2 and 3 [13], consists of an array of antennas that together direct different transmission/reception beams towards each user in the system. This method of transmission and reception is called beam forming and is made possible through smart (advanced) signal processing at the baseband.

In beam forming, each user's signal is multiplied with complex weights that adjust the magnitude and phase of the signal to and from each antenna. This causes the output from the array of antennas to form a transmit/receive beam in the desired direction and minimizes the intensities in other directions.

If the complex weights are selected from a library of weights that form beams in specific, predetermined directions, the process is called switched beam forming. Here, the base station basically switches between the different beams based on the received signal strength measurements. On the other hand, if the weights are computed and adaptively updated in real time, the process is called adaptive beam forming. Through adaptive beam forming, the base station can form narrower beams towards the desired user and nulls towards interfering users, considerably improving the signal-to-interference-plus-noise ratio.

4. Fractal Algorithm

One of the more intriguing attributes of fractal arrays is the possibility for developing algorithms, based on the compact product representation of (1), which are capable of performing extremely rapid pattern computations. For example consider a linear array of isotropic elements, uniformly spaced and a distance d apart along the z axis. The array factor corresponding to this linear array may be expressed in the form:

$$AF(\psi) = I_0 + 2 \sum_{n=1}^N I_n \cos\{n\psi\} \quad (2)$$

for odd number of elements and

$$AF(\psi) = 2 \sum_{n=1}^N I_n \cos\left\{\left(n - \frac{1}{2}\right)\psi\right\} \quad (3)$$

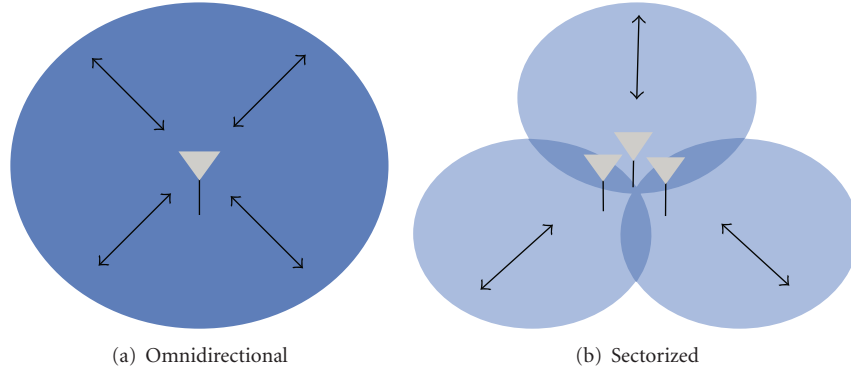


FIGURE 1: Non-smart (conventional) antenna system.

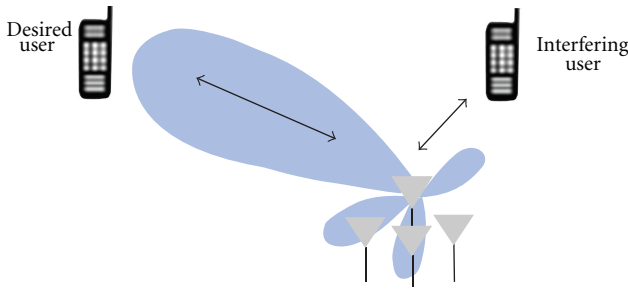


FIGURE 2: Smart antenna system-beam forming.

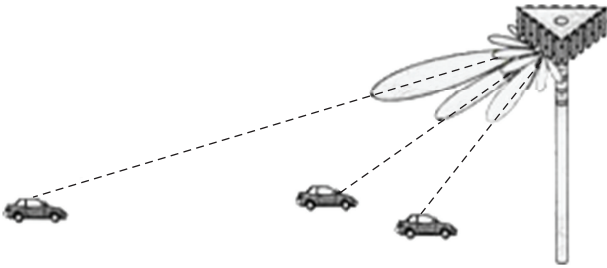


FIGURE 3: Separate beam for each user.

for even number of elements, where n is the total number of elements:

$$N = \left(\frac{n-1}{2} \right),$$

$$\psi = kd\{\cos \theta - \cos \theta_0\},$$

$$k = \frac{2\pi}{\lambda}.$$
(4)

The directivity for fractal array antenna is given by

$$D_P(u) = \frac{\hat{A}F_P^2((\pi/2)u)}{(1/2) \int_{-1}^1 \hat{A}F_P^2((\pi/2)u) du},$$
(5)

where

$$\psi = \frac{\pi}{2}u,$$

$$u = \cos \theta.$$
(6)

These arrays become fractal-like when appropriate elements are turned off or removed, such that

$$I_n = 1, \text{ if element } n \text{ is turned ON, \&}$$

$$I_n = 0, \text{ if element } n \text{ is turned OFF.}$$

Hence, fractal arrays produced by following this procedure belong to a special category of thinned arrays. If the above equations are used to calculate the array factor for an odd number of elements, then N cosine functions must be evaluated and N additions performed, for each angle. One of the simplest schemes for constructing a fractal linear array follows the recipe for the Cantor set. Cantor linear arrays were first proposed and studied in [8] for their great potential use in the design of low-side lobe arrays.

The basic triadic Cantor array may be created by starting with a three-element generating subarray, and then applying it repeatedly over P scales of growth. The generating subarray in this case has three uniformly spaced elements, with the center element turned off or removed, that is, 101. The triadic Cantor array is generated recursively by replacing 1 by 101 and 0 by 000 at each stage of the construction. For example, at the second stage of construction ($P = 2$), the array pattern would look like

$$1 \ 0 \ 1 \ 0 \ 0 \ 0 \ 1 \ 0 \ 1. \quad (7)$$

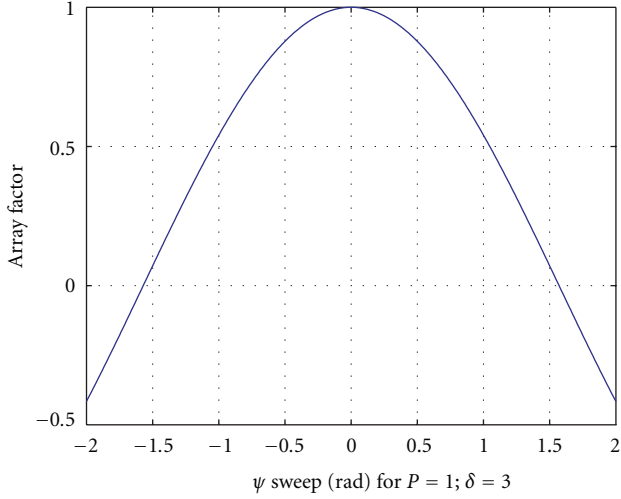
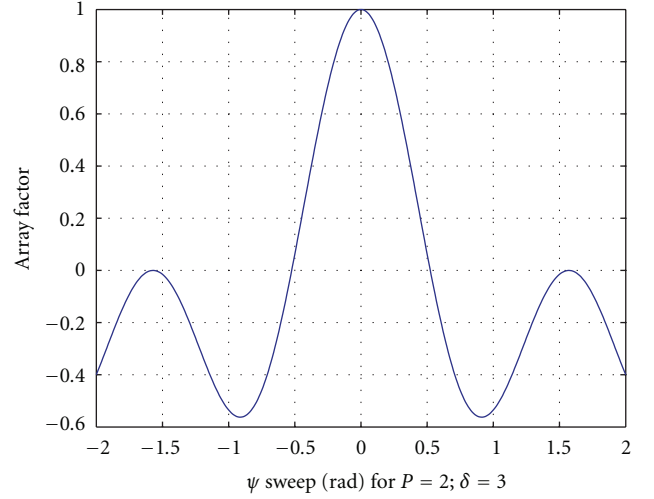
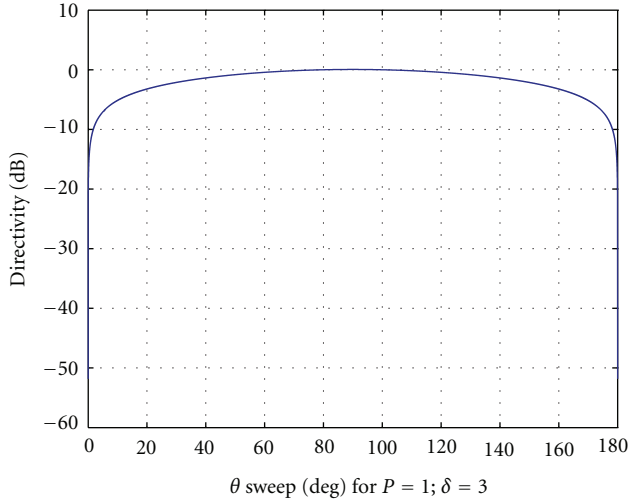
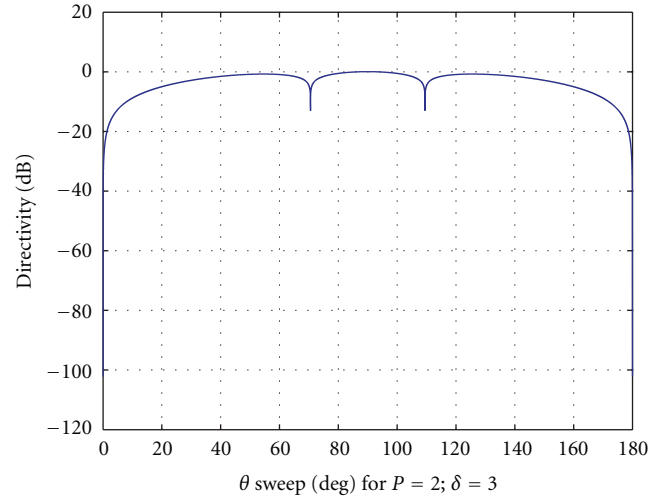
In this fashion the different stages of fractal pattern are grown. Starting with the basic stage whatever value we assume for the basic stage the value will be substituted for each stage and the antenna array grows in size rapidly. The same case can be applied for planar construction also. Current research and investigations on three-dimensional fractal arrays are in progress to refine and tailor the pattern of the required beam. Research is also in progress on nonlinear arrays with nonuniform amplitude and unequal spacing arrays to get the radiation pattern of desired extent.

At the third stage ($P = 3$), we would have

$$1 \ 0 \ 1 \ 0 \ 0 \ 0 \ 1 \ 0 \ 1 \ 0 \ 0 \ 0 \ 0 \ 0 \ 0 \ 0 \ 0 \ 1 \ 0 \ 1 \ 0 \ 0 \ 0 \ 1 \ 0 \ 1. \quad (8)$$

The array factor of the three-element generating subarray with the representation 101 is:

$$GA(\psi) = 2 \cos\{\psi\} \quad (9)$$

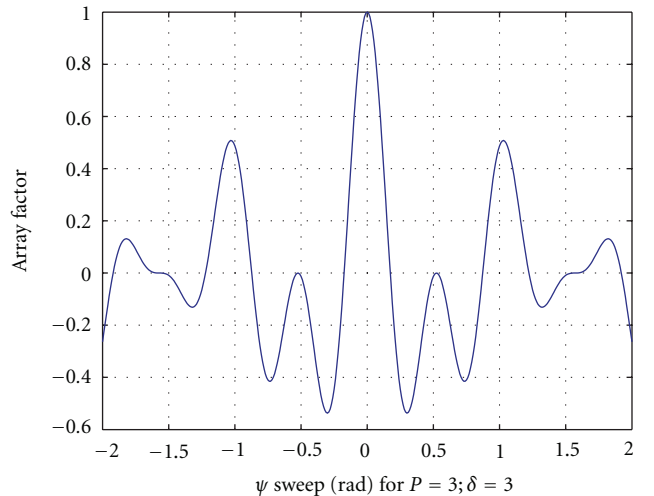
FIGURE 4: Fractal array factor pattern for $P = 1$; $\delta = 3$.FIGURE 6: Fractal array factor pattern for $P = 2$; $\delta = 3$.FIGURE 5: Directivity pattern for $P = 1$; $\delta = 3$.FIGURE 7: Directivity pattern for $P = 2$; $\delta = 3$.

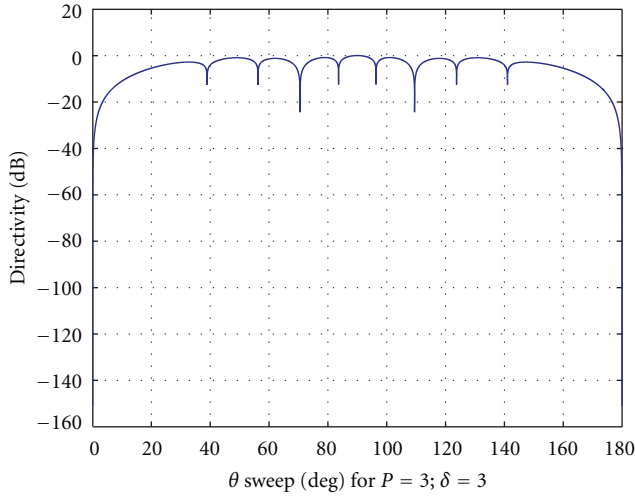
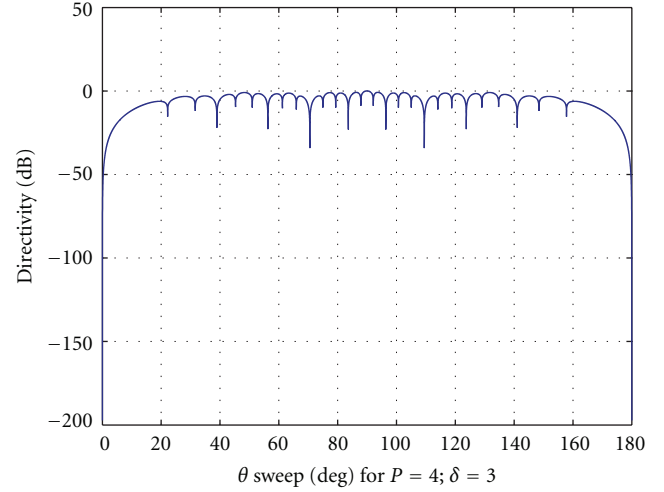
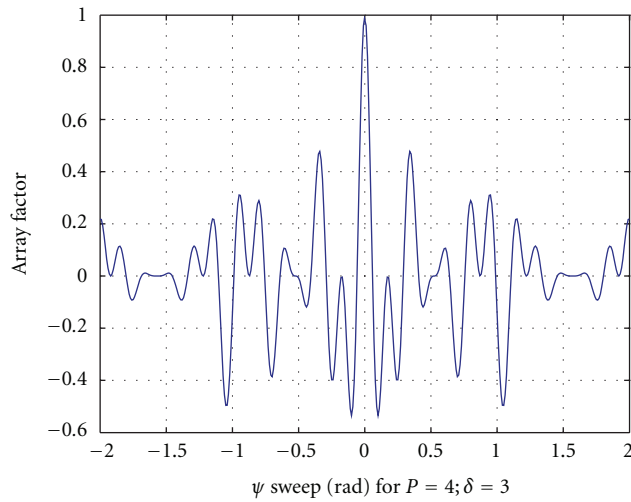
which may be derived from the array factor equation by setting $N = 1$, $I_o = 0$, and $I_1 = 1$. Substituting this equation into equation (1) and choosing an expansion factor of 3, result in an expression for the Cantor array factor given by

$$\hat{A}F_P(\psi) = \prod_{i=1}^P \hat{G}A(3^{i-1}\psi) = \prod_{i=1}^P \cos\{3^{i-1}\psi\}. \quad (10)$$

Here the hat notation indicates that the quantities have been normalized. The array factor pattern and the directivity pattern for $P \in \{1, 2, 3, 4\}$ and $\delta = 3$ are shown in Figures 4, 5, 6, 7, 8, 9, 10, and 11.

As both values increase the plot shows improvement in characteristics, the directivity increases, and the pattern becomes narrower. Another fantastic advantage is that equation (10) only requires P cosine-function evaluations and $P - 1$ multiplication. In the case of an 81 element triadic cantor array, the fractal array factor is at

FIGURE 8: Fractal array factor pattern for $P = 3$; $\delta = 3$.

FIGURE 9: Directivity pattern for $P = 3$; $\delta = 3$.FIGURE 11: Directivity pattern for $P = 4$; $\delta = 3$.FIGURE 10: Fractal array pattern for $P = 4$; $\delta = 3$.

least $N/P = 40/4 = 10$ times faster to calculate than the conventional discrete Fourier transform. The multiband characteristics of linear fractal array are discussed in [6, 7]. The same procedure can be applied for the Sierpinski carpet arrays for developing efficient algorithms which can be used in planar smart antennas. The multiband characteristics of Sierpinski carpet array are discussed in [8]. More about fractal arrays are discussed in [9].

Table 1 shows the increase in speed factor as the values of P and δ vary. As the value of P and δ increases the speed factor increases enormously. For example, with for $P = 4$ and $\delta = 7$ the fractal array factor is 300 times faster to calculate than the conventional case. This property can be utilized in smart antennas to produce rapid beam forming algorithms.

5. Assignment of Priorities Algorithm

After studying the advantages of fractal concepts over the development of rapid beam forming algorithms in smart

TABLE 1: Tabulation of the variation of P and δ .

	$P = 1$	$P = 2$	$P = 3$	$P = 4$	$P = 5$
$\delta = 3$	1	2	4	10	24
$\delta = 5$	2	6	20	78	312
$\delta = 7$	3	12	57	300	1680
$\delta = 9$	4	20	121	820	5904

TABLE 2: Initial look-up table.

Sl no.	User beam	Priority assigned	Computational complexity	Needed resource allocation
1	A	1	High	High
2	B	2	Medium	Medium
3	C	3	Low	Low
4	D	4	Very low	Very low

antennas, now we can propose a new algorithm technique of assigning priorities for each beam. Let us consider four users. Initially, each user is assigned an individual beam from smart antenna with uniform distribution. Consider the situation that user A is moving very fast, user B is medium speed, user C is low speed, and user D is pedestrian, as illustrated in Table 2. With these different speed users we can assign a new priority for each user with the beam.

Since user A is rapidly moving his beam needs more computation complexity than user B. Similarly user C needs less computation complexity than user B. Likewise, since user D is a pedestrian he needs even less computational complexity than user C. Now let us introduce a token passing technique between the users beam. The token named "X" mainly indicates the computational complexity effect. Initially let us consider the token is captured by the user D. The token X looks at the priority of user D. His priority is 4. The token checking algorithm will check for the next least number having the highest priority. Subsequently it will find that user C has a priority 3. Similarly after the second

TABLE 3: Token X caught by user D on random.

Sl no.	User beam	Priority assigned	Computational complexity	Resource allocation	Token
1	A	1	Uniform	Uniform	X
2	B	2	Uniform	Uniform	
3	C	3	Uniform	Uniform	
4	D	4	Uniform	Uniform	

TABLE 4: Token X caught by user C after first iteration.

Sl no.	User beam	Priority assigned	Computational complexity	Resource allocation	Token
1	A	1	Uniform	Uniform	X
2	B	2	Uniform	Uniform	
3	C	3	Uniform	Uniform	
4	D	4	Low	Low	

TABLE 5: Token X caught by user B after second iteration.

Sl no.	User beam	Priority assigned	Computational complexity	Resource allocation	Token
1	A	1	Uniform	Uniform	X
2	B	2	Uniform	Uniform	
3	C	3	Low	Low	
4	D	4	Very low	Very low	

iteration it will see the user B who is having still higher priority. Then the token will be passed to B. After the next iteration the user A is found to be having the highest priority among others and finally the token will be passed to A. The result after each iteration process is shown in the Tables 3, 4, 5, and 6 clearly. Since A is moving very fast, he needs highest computational complexity so that more computational resources can be allotted to the particular user compared to others and the rapid beam forming technique can be still enhanced. The tables illustrate this process in a step-by-step manner. Coverage performance analysis is discussed in [14] by Badjian et al. and uses genetic algorithm technique. But the proposed one in this paper is a novelistic approach to reduce the computational complexity and properly allocate the resource so that rapid beam forming can be enhanced.

6. Assignment of Scanning Beams Algorithm

Smart antenna technology uses the concept of locating the user beam and adaptive algorithms are used to adaptively trace the user along with the beam. For accomplishing this task efficiently so many adaptive algorithms are available. An alternative approach to this technology is scan antenna technology in which beams are allowed to scan randomly and depending upon the speed of the user, each user is allocated a scanning beam. This concept is new and greatly reduces the time needed for computation and thereby increasing the rapidness of rapid beam and saving the time needed for

TABLE 6: Token X caught by user A after third iteration matches exactly with the look-up table.

Sl no.	User beam	Priority assigned	Computational complexity	Resource allocation	Token
1	A	1	High	High	X
2	B	2	Medium	Medium	
3	C	3	Low	Low	
4	D	4	Very low	Very low	

TABLE 7: Initial lookup table with different user speed.

Sl no.	User	Moving speed	Computational complexity	Resource allocation
1	A	Very fast	High	High
2	B	Medium	Medium	Medium
3	C	Low	Low	Low
4	D	Pedestrian	Very low	Very low

TABLE 8: Initial scanning beam table from scan antenna.

Sl no.	Scanning beam	Moving speed	Computational complexity	Needed resource allocation
1	1	Very fast	High	High
2	2	Medium	Medium	Medium
3	3	Low	Low	Low
4	4	Pedestrian	Very low	Very low

TABLE 9: Matching algorithm matches the speed of beam and speed of user.

Sl no.	Scanning beam	User	Moving speed
1	1	A	Very fast
2	2	B	Medium
3	3	C	Low
4	4	D	Pedestrian

resource allocation. Let us consider the same case of four users. User A is moving very fast, user B is of medium speed, user C is of low speed, and user D is pedestrian. Initially the scan antenna technology produces four different beams independently at random speed. Let the four beams be named beam 1, beam 2, beam 3, and beam 4, respectively. Consider the situations such that beam 1 is moving very fast, beam 2 is of medium speed, beam 3 is of low speed, and beam 4 is of very low speed. Now a matching technique has to be used to carefully match the speed of the user with the speed of the beam. Once the matching has been done, then each user can lock with his beam as long as he uses it and release the beam free after the use so that other users can use the beam. Tables 7, 8, and 9 illustrate this process in a step-by-step manner.

7. Assignment of Usage Time and Location Tag Algorithm

While the advantages of fractal concepts over the development of rapid beamforming algorithms in smart antennas

TABLE 10: Look-up table for assignment of usage time and location tag.

Sl no.	User	Usage time (τ)	Location tag (σ)	Computation and resource allocation
1	A	Long duration	Slow moving	Very low
2	B	Long duration	Fast moving	Low
3	C	Short duration	Slow moving	Medium
4	D	Short duration	Fast moving	High

using new algorithms have been studied by the authors in [15, 16], the concept can now be extended to another new algorithm technique called “*Assignment of Usage Time and Location Tag Algorithm*.” Let us consider the same case of four users. Assume that the initial two proposed algorithms are applied and the system is working in efficient mode. We will simply call this as efficient mode as far as our case is considered. This can be considered as algorithm over algorithms to increase the effectiveness of the system. Now let us introduce the parameters called τ which refers to the effective usage time of each user and σ which refers to the location tag of each user. Assume that we have some mechanisms to know the probability of usage duration of each user and we got the location tag by global positioning systems. Note that we have already optimized the system with respect to user speed and having introduced a new technique called scan antenna technology; now these additional parameters can still enhance the system speed effectively. From the smart antenna side there is a considerable amount of time that is needed for the development of each new beam. With these two parameters, τ and σ , now there are four possible cases for each user if we take only two variables into account, that is, long and short duration user and fast and slow moving user. A user can be in long duration and slow moving, long duration and fast moving, short duration and slow moving, and finally short duration and fast moving as shown in Table 10.

From Table 10 it can be easily concluded that user A can be considered as stationary user since he is in long duration and slow moving. The term smart can be removed from user A antennas and can be allotted a single wide coverage beam antenna. The computational complexity time and resource allocation will be nullified. User B can be given less priority for he is taking long duration though moving fast. The type of beam pattern can be recognized and stored in memory. User C is taking short duration and moving slow, a type of medium complexity can that be allotted. And finally as User D is concerned, he is taking short duration and moving fast; therefore, more complexity is required for him. All this data can be observed for a long-time basis and stored in memory so that the observation database can help in allocating the resources which speeds up the process of producing rapid beams. Coverage performance analysis is discussed in [14] by Badjian et al. and uses genetic algorithm technique. But the proposed one in this paper is a novelistic approach to reduce the computational complexity and properly allocate the resource so that rapid beam forming can be enhanced.

8. Combinational Beam-Forming Algorithm among Peer Members within a Single Base Station

This is a new algorithm for the rapid beam forming in smart antennas which aims to bring different beams acquired at different times into geometric coincidence, possibly by different beam forming stations at different places, as shown in Figure 12. This aims at achieving time and space coincidence of various beams. Consider for example 12 users are using mobile phone at a time belonging to single cell served by a smart antenna. If each user is allocated a separate beam, then 12 different beams are required. The complexity of the system is increased and the time required for each beam will increase. The rapid beam forming will be still worsened if the number of user still increases. In this proposed new algorithm, the pattern of each user is observed for a specific amount of time and the users will be grouped in clusters say for example four clusters of three in each group, then the complexity can be reduced by a factor of four. In the first case, the cluster can be preknown numbers and in the extreme case the cluster can be assigned in random depending upon the number of users having the similar pattern. This pattern can be from a single base station or it can be from all the base stations forming a single hop among peer members.

The dramatic growth of the wireless communication industry has resulted in searches for new technologies to provide broader bandwidth per user channel, better quality, and new value added services. Employing smart antennas presents an elegant and relatively economical way to improve the performance of wireless transmission. Conditioned on the array factor of the form given in (1)–(3), fractal array is a sum of bounded independent and identically distributed complex random variables. Therefore by the strong law of large numbers for fixed, the resulting beam pattern should approach the ensemble average with the probability one as the number of antenna element increases.

However, in practice we are interested in finite relatively small values of N and in this case the average beam pattern does not necessarily represent the beam pattern of any particular realization. We are interested in the average beam pattern of these two particular realizations of randomly generated antenna arrays. The main lobes of the realization beam patterns closely match the average, but the side lobes may fluctuate with a large dynamic range and their peaks often well exceed the average level. Therefore, in practice, the statistical distributions of beam patterns and sidelobes, in particular, are of importance. The block diagram illustrates the algorithm. In the first stage all the clustered beam groups are tabulated and a mapping is done between the similar beams. In the next stage the sampling of all the beams in space and time domain is done. The next stage detects the similar beams and passes it to the space and time detection block. Again it is passed to the correlation detector.

The residual fitting for the similar beams is done using any residual preferences. The cluster is grouped among peer members and from this block the feedback is given for the next iteration. As per the output from this block the resource is allocated efficiently and the rapid beam forming

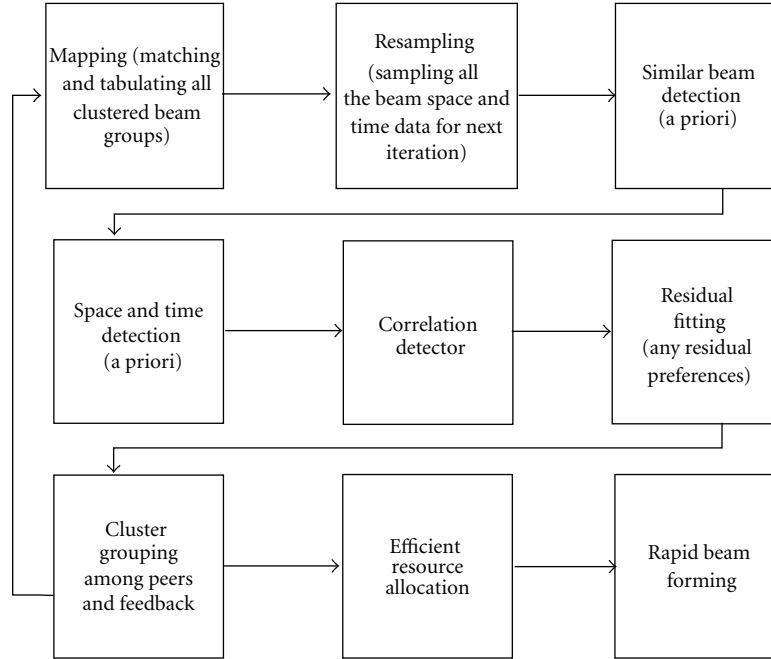


FIGURE 12: Block diagram for combinational beam-forming algorithm among peer members within a single base station.

is done. Different technical methods used can include Eigen combining algorithm, realistic beam forming algorithm, and maximal ratio combining. This signal processing methods can be employed for either receiving side or transmitting side smart antenna technology. The statistical beam forming techniques and maximal-ratio combining (MRC) techniques can be used along with conventional techniques. Due to array and diversity gain great performance benefits can be achieved in favorable propagating conditions. For unfavorable propagating conditions the performance can be little bit affected.

Furthermore although their numerical complexity remains fixed, the performance fluctuates when propagating conditions vary as in actual scenarios. Adaptive eigencombining can also considered for the beamforming. Maximal ratio eigencombining unifies the signal processing principles and analyses. The array signal processing has been applied for some decades as an attractive method for signal detection and estimation in hash environment. An array of sensors can be flexibly configured to exploit spatial and temporal characteristics of signal and noise and has many advantages over single sensor. This has many applications in radar, radio astronomy, sonar, wireless communication, seismology, speech acquisition, medical diagnosis and treatment, and so forth there are two kinds of array beamformers: fixed beamformer and adaptive beamformer. The weight of fixed beamformer is predesigned and it does not change in applications. The adaptive beamformer automatically adjusts its weight according to some criteria. It significantly outperforms the fixed beamformer in noise and interference suppression.

A typical representative is the linearly constrained minimum variance beamformer. A famous representative for linearly constrained minimum variance beamformer is the capon beamformer. In ideal cases the capon beamformer

has high performance in interference and noise suppression provided that the array steering vector is known. The performance of the adaptive beamformers highly degrades when there are array imperfections such as steering direction error, time delay error, and phase errors of the array sensors, multipath propagation effects, and wave front distortions. This is known as the target signal cancellation problem. Tremendous work has been done to improve the robustness of adaptive beamformer. To overcome the problem of target signal cancellation caused by the steering direction error, multiple point constraints were introduced in adaptive array. The idea of this approach is intuitive. With multiple gain constraints at different directions in the vicinity of the assumed one, the array processor becomes robust in the region where constraints are imposed.

However the available number of constraints is limited because the constraints consume the degrees of freedoms (DOFs) of array processor for interference suppression. If compact antennas are used for fast beam forming then the parasitic array antennas are suitable for power consumption limited mobile terminal applications. Two categories of parasitic antennas are there, namely, switched parasitic array antennas and reactively controlled directive array. In comparison with switched parasitic array antennas, reactively controlled directive array can realize a smoother beam pattern steering, thus achieving a better interference suppression performance. The reactively controlled directive array antenna is an analog adaptive antenna. Adaptive beam forming is achieved by adaptively adjusting the load reactance of parasitic elements. When the DOA of the impinging interference signal is close to that of the desired signal, the null forming ability degrades. This is due to the high spatial correlation between the desired signal and the interference signal.

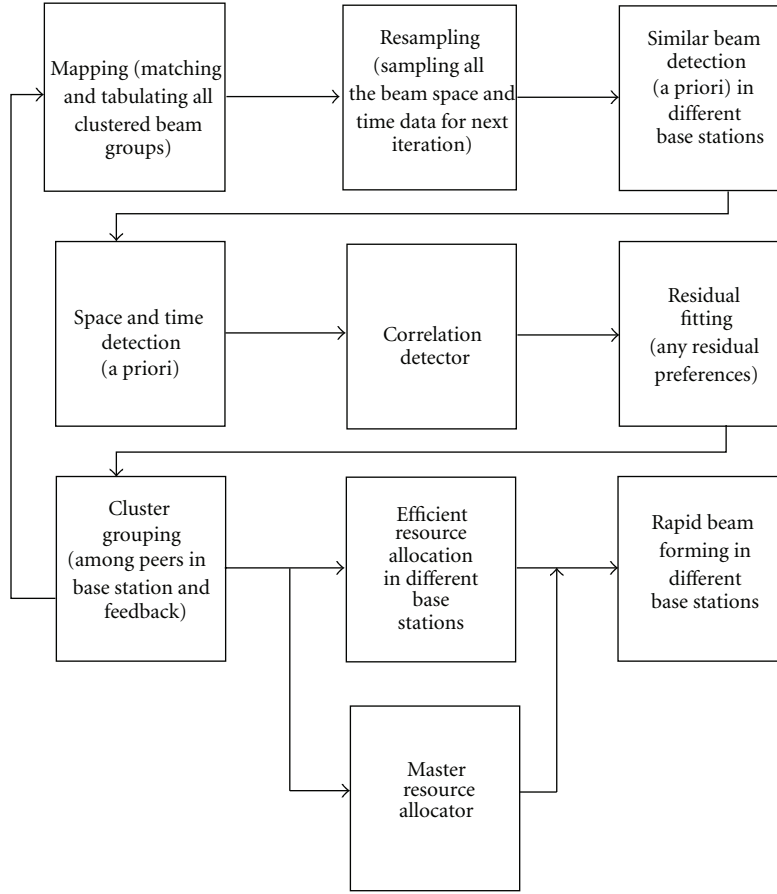


FIGURE 13: Block diagram for combinational beam-forming algorithm among peer members between different base stations.

9. Combinational Beam-Forming Algorithm among Peer Members among Different Base Stations

The evolution of wireless communication system requires new technologies to support better quality communications, new services, and applications. Smart antennas have become a hot topic of research employed in base stations. With a smart antenna directive beam patterns can be steered toward the desired signal and deep nulls can be formed toward the interference, thus spatial filtering is realized. This brings the benefits such as lower power transmission, higher spectrum efficiency, better link quality, and higher system capacity. Various beam-forming and direction of arrival estimation algorithms have been designed for single base station. Most of these algorithms are designed based on the digital beam forming antenna arrays. Signals received by individual antenna elements are down-converted into base band signals. These signals are digitized and fed into digital signal processing chip where the algorithms reside in. The master resource allocated decides the corresponding group as shown in Figure 13. However, radio frequency circuit branches connected to the array elements, analog-to-digital converters, and the baseband DSP chip consume a considerable amount of DC power. Furthermore, each channel connected

to the array sensor has the same structure, so the cost of fabrication increases with the number of array elements.

Thanks to the recent development of GaAs monolithic microwave integrated circuit (MMIC) technologies, the beamformer could be integrated to a single chip at the RF front end instead of the baseband. The advantages are the reduced quantization errors and the increased dynamic range. However, their costs of fabrication still limit the range of limitation. All these factors make DBF and MBF antennas suitable for low power consumption and low cost systems and thus hinder the mass application of the smart antenna technologies. For example, it could be too costly to equip DBF antenna arrays at battery powered laptops or mobile computing terminals within a wireless network. Same procedure used for single base station is used except here the base stations can be more than one.

10. Conclusion

In this paper a rapid beam forming algorithm for smart antennas was proposed using the concepts of fractal array and novel algorithms. It was further enhanced by using successive algorithms called “Assignment of Usage Time and Location Tag Algorithm.” It was found that the proposed method

greatly reduces the time needed for calculating the array factor and the proposed new techniques still enhance the allocation of computational resources for the development of rapid beam. It also reduces the memory requirements to a greater extent. Furthermore, new combinational beamforming algorithm among peer members within a single base station and combinational beamforming algorithm among peer members in different base stations have been proposed for performance enhancement and optimization.

References

- [1] B. B. Mandelbrot, *The Fractal Geometry of Nature*, W. H. Freeman and Company, New York, NY, USA, 1983.
- [2] J. P. Gianvittorio and Y. Rahmat-Samii, "Fractal antennas: a novel antenna miniaturization technique, and applications," *IEEE Antennas and Propagation Magazine*, vol. 44, no. 1, pp. 20–36, 2002.
- [3] S. R. Best, "The fractal loop antenna: a comparison of fractal and non-fractal geometries," in *Proceedings of the IEEE Antennas and Propagation Society International Symposium*, pp. 146–149, Boston, Mass, USA, July 2001.
- [4] D. H. Werner and S. Ganguly, "An overview of fractal antenna engineering research," *IEEE Antennas and Propagation Magazine*, vol. 45, no. 1, pp. 38–57, 2003.
- [5] Y. Kim and D. L. Jaggard, "The fractal random array," *Proceedings of the IEEE*, vol. 74, no. 9, pp. 1278–1280, 1986.
- [6] A. Lakhtakia, N. S. Holter, V. K. Varadan, and V. V. Varadan, "Self-similarity in diffraction by a self-similar fractal screen," *IEEE Transactions on Antennas and Propagation*, vol. AP-35, no. 2, pp. 236–239, 1987.
- [7] X. Liang, W. Zhenson, and W. Wenbing, "Synthesis of fractal patterns from concentric-ring arrays," *IEE Electronics Letters*, vol. 32, no. 21, pp. 1940–1941, 1996.
- [8] C. Puente-Baliarda and R. Pous, "Fractal design of multiband and low side-lobe arrays," *IEEE Transactions on Antennas and Propagation*, vol. 44, no. 5, pp. 730–739, 1996.
- [9] D. H. Werner, R. L. Haupt, and P. L. Werner, "Fractal antenna engineering: the theory and design of fractal antenna arrays," *IEEE Antennas and Propagation Magazine*, vol. 41, no. 5, pp. 37–59, 1999.
- [10] M. Chryssomallis, "Smart antennas," *IEEE Antennas and Propagation Magazine*, vol. 42, no. 3, pp. 129–136, 2000.
- [11] W. C. Lee and S. Choi, "Adaptive beamforming algorithm based on eigen-space method for smart antennas," *IEEE Communications Letters*, vol. 9, no. 10, pp. 888–890, 2005.
- [12] M. Z. Shakir and T. S. Durrani, "Narrowband beamforming algorithm for smart antennas," in *Proceedings of the 5th International Bhurban Conference on Applied Sciences and Technology (IBCAST '07)*, pp. 49–54, Islamabad, Pakistan, January 2007.
- [13] J. Liberti and T. S. Rappaport, *Smart Antennas for Wireless Communications: IS-95 and Third Generation CDMA Applications*, Prentice Hall, New York, NY, USA, 1999.
- [14] M. M. Badjian, K. Thirappa, T. S. Kiong, J. K. S. Paw, and P. S. Krishnan, "Coverage performance analysis of genetic algorithm controlled smart antenna system," in *Proceedings of the 8th IEEE Student Conference on Research and Development—Engineering: Innovation and Beyond (SCoReD '10)*, pp. 81–85, Putrajaya, Malaysia, December 2010.
- [15] M. Levy and D. S. Kumar, "Novel algorithms for rapid beam forming in optical antennas for microwave photonics applications using smart-fractal concepts," in *Proceedings of the IETE ICon Conference*, October 2011.
- [16] M. Levy, D. S. Kumar, A. Dinh et al., "A novelistic approach for rapid beam forming in smart antennas for wireless applications using smart-fractal concepts and new algorithm," in *Proceedings of the International Conference on Advances in Mobile Network, Communication and its Applications (MNCAPPS '12)*, pp. 5–10, Bangalore, India, August 2012.

Application Article

Design of RFID Reader Antenna for Exclusively Reading Single One in Tag Assembling Production

Chi-Fang Huang and Yi-Feng Huang

*Graduate Institute of Communication Engineering, Tatung University, 40 Zhongshan, North Road,
Section 3, Taipei 104, Taiwan*

Correspondence should be addressed to Chi-Fang Huang, ras@ttu.edu.tw

Received 5 December 2011; Revised 1 July 2012; Accepted 19 July 2012

Academic Editor: Dalia N. Elshiekh

Copyright © 2012 C.-F. Huang and Y.-F. Huang. This is an open access article distributed under the Creative Commons Attribution License, which permits unrestricted use, distribution, and reproduction in any medium, provided the original work is properly cited.

A design of RFID reader antenna including a fixture, which is equipped with a chip-attaching machine producing the RFID tags, is presented. Such an antenna is constrained to read exclusively one tag only for the purpose of functional check of the whole tag when it passes the reader antenna. Namely, the other neighbor tags on the same rolling band are ignored that time. A wideband microstrip antenna is designed and a fixture with shielding material is set up for such a reading constraint. Low efficiency with high return loss is allowed for this constraint, yet wideband is still a must to treat all possible produced tags used in different countries and areas in the world.

1. Introduction

Based on the diverse applications, different spectrum bands are allocated for RFID (radio frequency Identification) [1], for example, LF (125–134.2 kHz and 140–148.5 kHz) for animal control, HF (13.56 MHz) for electronic ticket and portal control, and UHF (868 MHz–928 MHz) for logistics and fast portal control, and so forth. Most of the frequencies are located in the ISM (industrial, scientific, and medical) bands [1]. However, recently, the applications of RFID have been profoundly emphasized mainly because of the need of supply chains [2]. By proposing an international standard for the format of electronic data used for various items of goods, of which EPC (electronic product code) [3] is an example, and by establishing an infrastructure network of RFID worldwide, the products can be registered at once when they are shipped out from the factories (say, in China) and be released when they are checked out at the counter of a supermarket somewhere else (say, in USA). This is called “product tracking” and is being implemented in an “Internet of Thing (IOT)” [4].

The RFID tags [1] of supply chains are assumed to be very low cost, and also the RFID chips on them, since they are not reused after being attached on products. Therefore,

taking the cost into account, usually the chips for tags do not afford to have a 100% quality assurance after foundry and package. Consequently, the risk of producing RFID tags with chips which probably do not work well does exist. Such a sort of tags with flaw is termed as dead or silent tags.

This kind of potential risk is not acceptable after the tag is made by attaching the chip on the tag antenna, especially for supply-chain purpose. Hence, the cost should be paid by carrying a functional check for tags one by one by an RFID reader after the chip is attached on the antenna as a tag, just as shown in Figure 1. That means, the production machine should be able to exclusively read the target tag under test only, and the other neighbor tags are not allowed to response when being read.

In this paper, a design of antenna plus a fixture is proposed. Considering the antenna's characteristics, the low efficiency of antenna with high return loss is allowed, since the antenna is so close to the tags under test, and tags are almost set in the near field range of reader antenna. In the present project, the return-loss criterion is set to be -5 dB. Anyway, the designed antenna for the assembling machine is still to work with a wideband to deal with all possible tags used in the world. For example, RFID and UHF bands are 866–869 MHz in Europe, 902–928 MHz in North

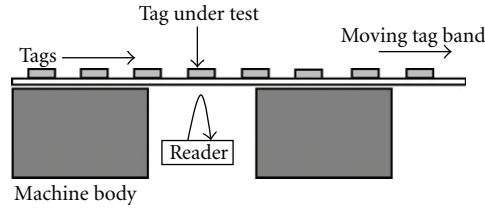


FIGURE 1: Setup for exclusively reading one single tag on a production machine.

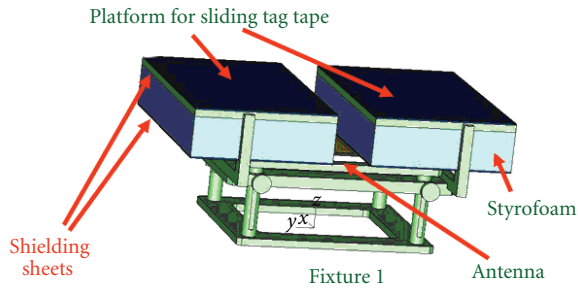


FIGURE 2: The proposed fixture.



FIGURE 3: An RFID tag printed on a paper substrate [4].

and South America, and 950–956 MHz in Japan and some Asian countries. The assigned RFID band is 902–928 MHz in Taiwan. The wideband characteristics both of simulation and measurement of this antenna do cover these different bands.

Furthermore, this paper addresses a design of a fixture, see Figure 2, containing that reader antenna to meet the purpose mentioned above. This fixture is installed on a production machine of RFID tags. Measurement of the proximate-field strength on this fixture is done to verify the field distribution which is necessary for the present reading constraint. For reference, Figure 3 shows a typical RFID tag printed on a paper substrate, where the chip is attached at the center of tag antenna [4].

2. Design of Reader Antenna

Firstly, the reader antenna is designed. The concept of microstrip antenna [5] is adopted for this task. The reasons for choosing microstrip antenna are (a) low profile, so

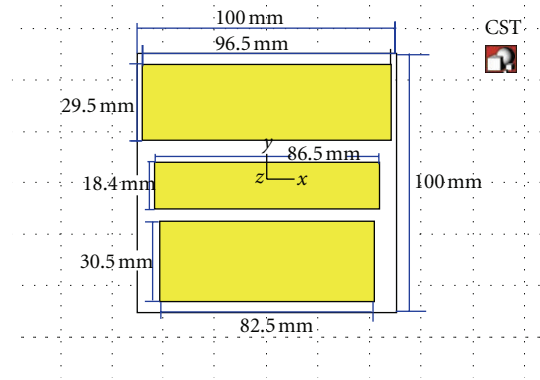


FIGURE 4: Simulation model of the wideband reader antenna.

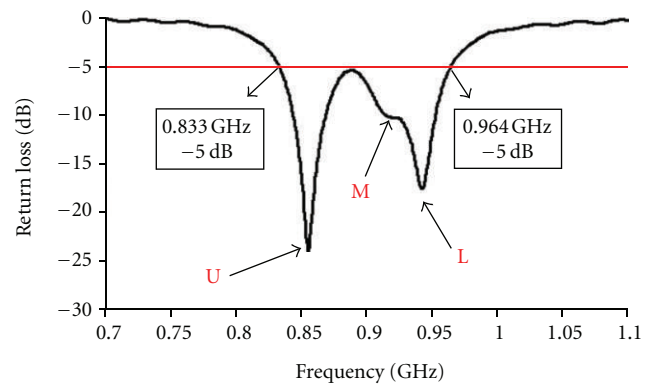


FIGURE 5: The simulated frequency response of return loss.



FIGURE 6: The realized broadband microstrip antenna.

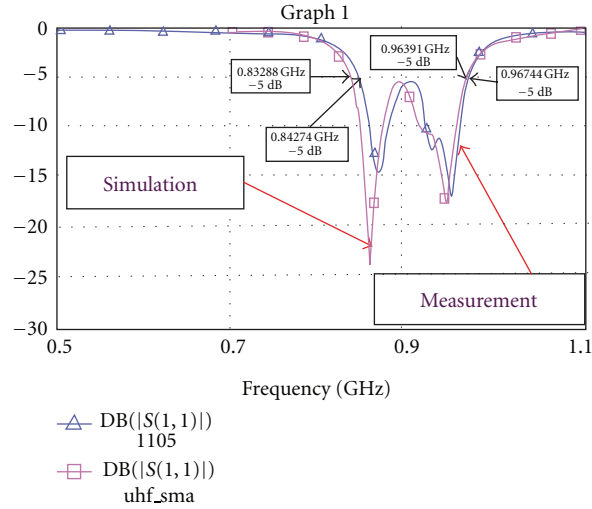


FIGURE 7: Measured return loss.

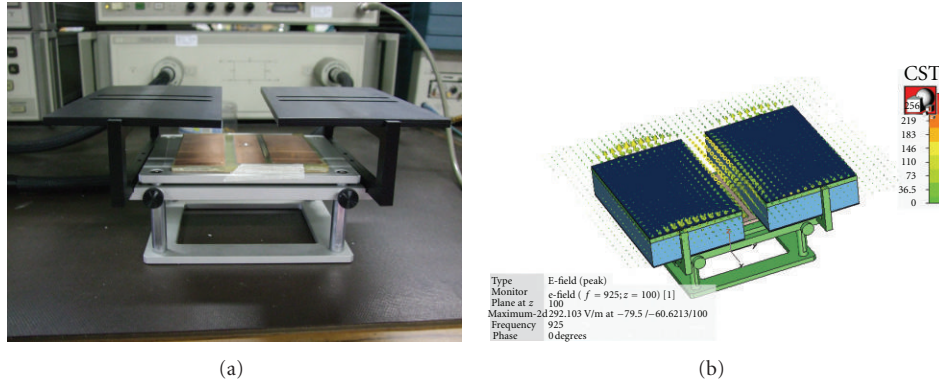


FIGURE 8: The laboratory fixture for testing.

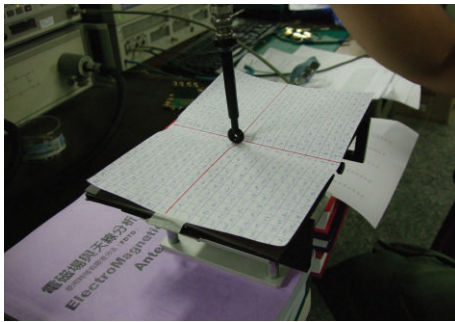


FIGURE 9: Measurement of the proximity field on the platform surface.

occupying not much room in machine, (b) easy to fabricate, because it can be etched on a printed circuit board (PCB), and (c) its fundamental mode [5] is naturally to have a broadside radiation pattern, which is suitable for the present application as shown in Figure 1. A microstrip antenna can be seen as a loose resonator due to radiation [6].

However, the obvious disadvantage of microstrip antenna is its narrow band. The target bandwidth of this work is about 860 MHz~960 MHz which is for covering all RFID standards worldwide. Consequently, a special design technique is necessary to have such a broadband design of microstrip antenna.

The electromagnetic package CST [7] is employed for the simulation before fabricating the antenna, which is a full 3D tool for antenna simulation. Figure 4 is the simulation model, and it is also the final determination of the geometrical and material parameters. Fr4 is used as the substrate. The central rectangle is the main microstrip antenna, whose horizontal side of 86.5 mm approximately follows the theoretical resonant length of half wavelength in substrate. The other upper and lower rectangles play the parasitic parts which have also strong coupling effect with the central radiator. This technique has been widely used [8] for broadening the bandwidth of microstrip antenna. However, usually, parasitic parts are set at the ends of the resonant side. Putting them along the resonant sides is a unique feature in the present work. Figure 5 shows the simulated result based

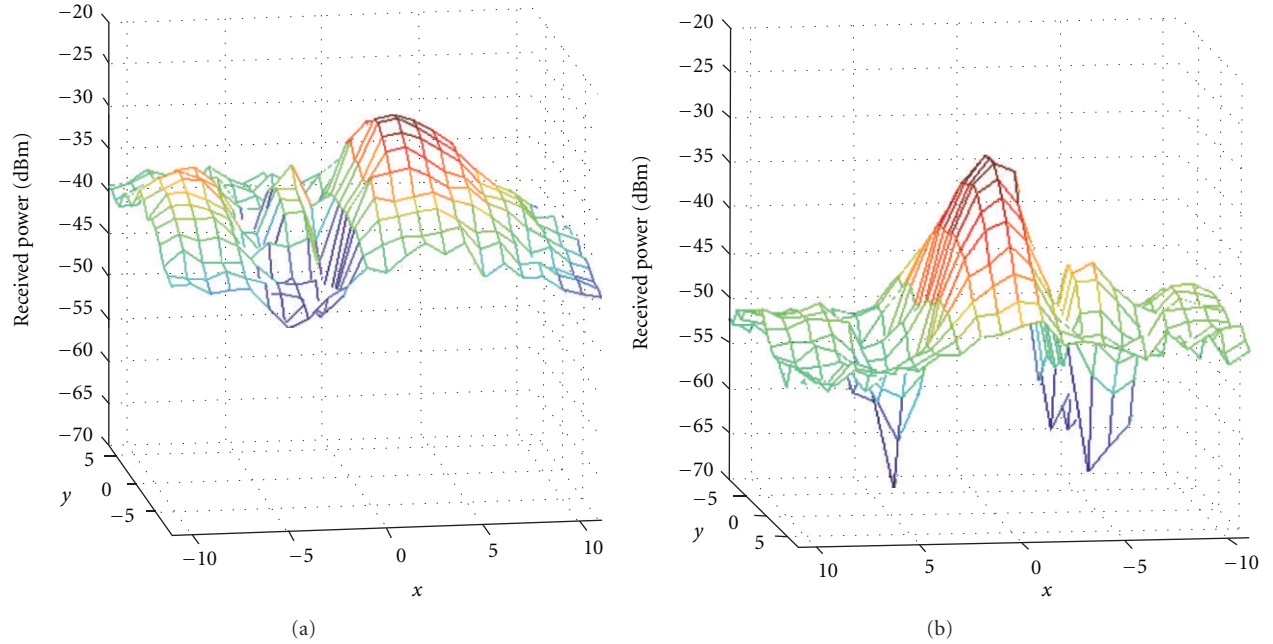


FIGURE 10: Distribution of proximity field (a) no shielding sheets, (b) sheets on and beneath the platforms.

on such an idea of broadband design. It is obvious to see the three generated modes, namely, U mode, M mode, and L mode are caused by the upper, middle, and lower patches displayed in Figure 4, respectively.

It should be remembered that the present design of RFID communication is a short-range one, therefore, we trade off in obtaining the broadband while sacrificing the performance of return-loss response. We set the -5 dB of return loss as the index for the matching condition in this design, and it predicts in simulation an $833\text{ MHz}\sim 964\text{ MHz}$ bandwidth as shown in Figure 5. After simulation in design, the antenna is realized by being etched on a PCB with a substrate thickness 4 mm as shown in Figure 6. Its measured return loss is shown in Figure 7. Referring to the bandwidth requirement again, the results both of simulated and measured ones are quite close to each other.

3. Fixture Design for Reading

As shown in Figure 1, in the fast process of attaching chips on the RFID tags, the moving band on which the preproduced tag antennas are being carried, is supported by a mechanical fixture. For simulating the fixture of a real machine in the laboratory, a nonmetal fixture is assembled as shown in Figure 8(a). Its top platforms are made of plastics and serve to support the tag band. Furthermore, the reader antenna designed above sits under the platforms and sits at the central position as well.

From the first idea, for depressing the response of the neighbor tags, we adopt the shielding sheets of Nanonix [9] and put them on and beneath the top platforms. The left and right sliding platforms are adjustable to find an optimal window width for antenna below to read as the

purpose. Figure 8(b) is a computational model of platform for CST simulation. The whole structure of Figure 8(a) is built into this CST model, including the patch antenna itself. When the reader antenna is excited, the electromagnetic field around the open window of platform can be displayed in time domain as that shown in Figure 8(b). It can be seen clearly that there is a strong field distribution inside the open window, on the other hand, the field on the platform is depressed obviously. Such a field distribution is to make the other tags which are not above the window to be not easily readable. Consequently, the aim of reading exclusively one tag only for the purpose of functional check of the whole tag when it passes the reader antenna is achieved. As expected, in one experiment in the laboratory simulating the real chip-attachment process in factory, there are three tags side by side on the platform, yet only the middle one is readable because of the present design for reader antenna plus the fixture.

4. Analysis of Proximity Field and Discussion

For analyzing the field distribution on the surface of the platforms, a setup for the proximity field measurement is also designed. By drawing grids in advance on a paper which is fixed on the platforms, a field probe suitable for the frequency range of reader antenna is used in a way of point-by-point to measure on the surface the proximity field radiated from the reader antenna, see Figure 9.

Two configurations are under evaluation, namely, (a) no shielding sheets and (b) with shielding sheets on and beneath the platforms, simultaneously. As an example, the measurement results of 910 MHz are shown in Figure 10. The vertical dimension is to present the received power in dBm on the tested surface. It should be noted that the y -direction in

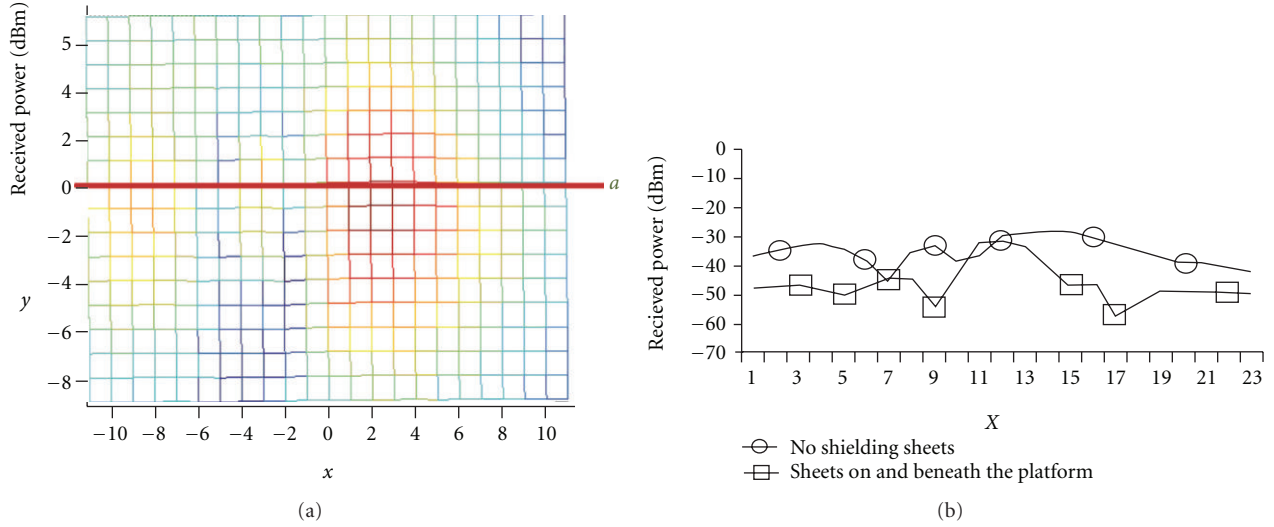


FIGURE 11: One-dimensional distribution of proximity field (a) line for measurement, (b) comparison with and without sheets on and beneath the platforms.

Figure 10 (same as the x -direction in Figure 8) on the spatial measuring coordinates is along with the long side of the open window. As expected, at the middle point of x -axis, the field peak does happen, namely, it occurs at the center of the open window. This is to ensure easily reading one tag only which stops at the center of the open window of the platform.

Figure 11(a) shows a two-dimensional proximity field distribution by color on the platform of fixture. For a quantity comparison of field in one dimension, along the x -axis and at the middle point of y -axis, a line is set to cross the open window on the platform, see Figure 11(a) also. The measured fields along this line of cases in Figures 10(a) and 10(b) are extracted and represented in Figure 11(b). Those two lines show that the effect of shielding sheets is indeed produced to have a higher contrast of fields for central and side parts of the window. More than 10 dB at least is achieved for the aim of this present work. Consequently, the field on the region of side tags is lower than that above the center of the window when the shielding sheets are applied.

5. Conclusions

In this paper, we have proposed a design of fixture for the machines of RFID tag production. After attaching the chips on antennas of a band of tags, this machine needs to check each tag if its chip does work or not at the end of production procedure. A broadband microstrip antenna is also designed for this fixture. By using the shielding sheets on the fixture, the requirement of reading exclusively only one tag is achieved. The proximity electromagnetic fields, which are radiated from the designed reader antenna, are measured as well on the surface of fixture platforms to evaluate the proper configuration of shielding sheets. This present work has demonstrated itself as a reference design for production machines of RFID tags, which need to have a functional check for each tag described in this work.

Acknowledgment

The Highlight Tech Corp. [10], Tainan, Taiwan, who is a company providing machines of RFID tag production, is deeply appreciated for their grant support in this project.

References

- [1] K. Finkenzeller, *RFID Handbook: Fundamentals and Applications in Contactless Smart Cards and Identification*, Wiley & Sons, New York, NY, USA, 2nd edition, 2003.
- [2] R. Bansal, "Coming Soon to a Wal-Mart Near You," *IEEE Antennas and Propagation Magazine*, vol. 45, no. 6, pp. 105–106, 2003.
- [3] S. Sarma, D. Brock, and D. Engels, "Radio frequency identification and the electronic product code," *IEEE Micro*, vol. 21, no. 6, pp. 50–54, 2001.
- [4] C.-F. Huang, "Low-cost solution for RFID tags in terms of design and manufacture," in *Current Trends and Challenges in RFID*, C. Turcu, Ed., InTech.
- [5] K. R. Carver and J. W. Mink, "Microstrip antenna technology," *IEEE Transactions on Antennas and Propagation*, vol. AP-29, no. 1, pp. 2–24, 1981.
- [6] Y. T. Lo, D. Solomon, and W. Richards, "Theory and experiment on microstrip antennas," *IEEE Transactions on Antennas and Propagation*, vol. AP-27, pp. 137–146, 1979.
- [7] <http://www.cst.com/>.
- [8] J. R. James, P. S. Hall, and C. Wood, *Microstrip Antenna: Theory and Design*, vol. 12 of *IEE Electromagnetic Waves Series*, 1981.
- [9] http://www.nanonix.com/nanonix_china/company/index.htm.
- [10] <http://www.high-light.com.tw/>.

Research Article

Compact MIMO Microstrip Antennas for USB Dongle Operating in 2.5–2.7 GHz Frequency Band

**Vladimir Ssorin, Alexey Artemenko, Alexander Maltsev,
Alexey Sevastyanov, and Roman Maslennikov**

*Wireless Competence Center, Lobachevsky State University of Nizhny Novgorod, Gagarina Avenue 23,
Nizhny Novgorod 603950, Russia*

Correspondence should be addressed to Vladimir Ssorin, vladimir.ssorin@wcc.unn.ru

Received 11 February 2012; Accepted 11 August 2012

Academic Editor: Hala A. Elsadek

Copyright © 2012 Vladimir Ssorin et al. This is an open access article distributed under the Creative Commons Attribution License, which permits unrestricted use, distribution, and reproduction in any medium, provided the original work is properly cited.

This paper considers design of microstrip MIMO antennas for an LTE/WiMAX USB dongle operating in the 2.5–2.7 GHz frequency band. The MIMO system includes two antenna elements with an additional requirement of high isolation between them that is especially difficult to realize due to size limitations of a USB dongle. Three approaches to achieve the needed system characteristics using microstrip PCB antennas are proposed. For the first design, high port-to-port isolation is achieved by using a decoupling techniques based on a direct connection of the antenna elements. For the second approach, high port-to-port isolation of the MIMO antenna system is realized by a lumped decorrelation capacitance between antenna elements feeding points. The third proposed antenna system does not use any special techniques, and high port-to-port isolation is achieved by using only the properties of a developed printed inverted-F antenna element. The designed MIMO antenna systems have the return loss S_{11} and the insertion loss S_{21} bandwidths of more than 200 MHz at the -8 dB level with the correlation coefficient lower than 0.1 and exhibit pattern diversity when different antenna elements are excited. Experimental measurements of the fabricated antenna systems proved the characteristics obtained from electromagnetic simulation.

1. Introduction

Modern wireless communication systems should simultaneously provide high reliability and channel capacity. One of the most effective ways to achieve these goals is utilization of the multiple-input-multiple-output (MIMO) technology [1]. Antennas of a MIMO communication system consist of multiple elements and should ensure high isolation between them for efficient operation of different space-time transmission techniques. The MIMO technology is currently used by different modern communication devices such as laptops, mobile phones, USB dongles, and others. An essential marketing trend is miniaturization of these devices that makes achieving high isolation between the antenna elements to be a challenging task due to a small (often $< 0.25\lambda_0$, where λ_0 is the operating wavelength) strictly limited area available for the antenna system. Especially, this is complicated for modern USB dongles where the total size of the

device does not exceed $0.5\lambda_0$. Thus, conventional diversity techniques based on different orthogonal polarizations of the antenna elements or spatial diversity with a distance between the antenna elements greater than a half of the wavelength are not always applicable for MIMO antenna systems design.

For a long time, many works were focused on developing special techniques that allow increasing the isolation between the antenna elements in a MIMO antenna system. These diversity techniques are based on different approaches: defected ground structures [2], split ring resonators [3], the electromagnetic bandgaps [4], or utilize a coupling antenna element between the antennas [5]. But application of these techniques for MIMO antenna systems requires sufficient antenna area (more than $0.25\lambda_0$) or a very complex structure and therefore is not always suitable for the antenna systems in a modern USB dongle. Also, the isolation between the antenna elements can be increased with the help of an appropriate antenna element as, for example, a printed

inverted-F antenna (PIFA) [6, 7]. However, in most cases the PIFAs has a 3D structure for satisfying the compact antenna area requirement that leads to increasing a production cost.

One of the most effective approaches for development of a compact MIMO antenna system is a diversity technique based on a direct connection of the antenna elements [8–10]. A direct connection of the antenna elements allows the current induced from one antenna element to flow to the other antenna element through the connection and not to the load. The MIMO antenna system for the 2.5–2.7 GHz frequency band with the diversity technique based on direct connection of antenna elements proposed in [8] has a 3D structure, and implies that the antenna should be separately soldered to the PCB board. A 3D structure of the antenna is not cost effective and can lead to the performance degradation due to soldering misalignments in the manufacturing process. The work [9] describes a planar dual-band antenna system for the long-term evolution (LTE) communication systems in the 700 MHz/2.5–2.7 GHz bands. The designed antenna system in [9] uses the diversity technique based on direct connection of the antenna elements for providing high port-to-port isolation in the frequency band around 700 MHz while the diversity in the 2.5–2.7 GHz band is achieved by conventional spatial diversity with large antenna elements separation. For the first band around 700 MHz, a relative bandwidth is only 2.5% at the -7.4 dB return loss and insertion loss levels, simultaneously. The 2.5% relative bandwidth is very narrow and it is not enough for the 2.5–2.7 GHz frequency band (more than 8% of relative bandwidth) for the considered USB dongle device.

This work aims to design a planar microstrip two-element MIMO antenna system operating in the 2.5–2.7 GHz frequency band for the application in modern USB dongles for LTE or WiMAX communication systems. The common size of a modern USB dongle does not exceed $60 \text{ mm} \times 20 \text{ mm}$, that is, about 2 and 6 times lower in a corresponding dimension than the operating wave length λ_0 (11.5 cm at 2.6 GHz). Besides, the antenna area should be as compact as possible (no more than $20 \times 20 \text{ mm}$).

The current paper proposes and describes three different designs of a compact planar microstrip antenna system. All the three antennas meet the specified requirements and offer different tradeoffs between various parameters as considered below.

This paper is organized as follows. Section 2 describes the requirements that are set for a modern compact MIMO antenna system. Section 3 introduces compact two-element MIMO antenna system #1 that uses a diversity technique based on a direct connection with a transmission line between the antenna elements [10]. Section 4 describes compact two-element MIMO antenna system #2 that uses a diversity technique based on a lumped capacitance introduced between the antenna elements [11]. Proposed MIMO antenna system #3 that achieves the required diversity properties without any connection of the antenna elements is described in Section 5. Finally, the conclusions are drawn in Section 6.

2. MIMO Antenna System Requirements and Their Experimental Verification

This section describes the requirements applying to antenna systems for correct MIMO mode operation.

The standard characteristics for MIMO antenna system analysis are scattering matrix (return loss S_{11} and S_{22} , and insertion loss S_{21} and S_{12}), diversity characteristics (envelope correlation coefficient), and radiation characteristics (radiation pattern and radiation efficiency).

A scattering matrix describes the values of the return loss (S_{11} and S_{22}) and the insertion loss (S_{21} and S_{12}) of an antenna system. In this work, the reference level both for the return loss and for the insertion loss of the MIMO antenna is defined in the required frequency bandwidth as -8 dB.

Diversity characteristics of a MIMO antenna system are usually described using an envelope correlation coefficient. An envelope correlation coefficient can be calculated from a 3D radiation pattern or a scattering matrix. The scattering matrix-based approach allows simplifying the procedure of envelope correlation coefficient calculation, that is, found from the scattering parameters as [12]:

$$\rho_e = \frac{|S_{11}^* S_{12} + S_{21}^* S_{22}|^2}{(1 - (|S_{11}|^2 + |S_{21}|^2))(1 - (|S_{22}|^2 + |S_{12}|^2))}. \quad (1)$$

According to the literature sources (see, e.g., [12]), the envelope correlation coefficient of less than 0.25 is recommended for efficient MIMO operation. In order to achieve the envelope correlation coefficient below 0.25, the level of the scattering matrix coefficients with appropriate phase distribution of their complex values should be lower than -8 dB as defined in the above requirements. The radiation characteristics of an antenna system are also very important. A 3D radiation pattern provides a full description about radiation characteristics including an antenna gain, a main radiation direction, and antenna efficiency. Because of the measurement complexity for the full 3D radiation pattern, three different orthogonal planes are often considered instead in practice.

The MIMO antenna systems designed and optimized in this work were fabricated and experimentally tested. The experimental test procedures that were used are as follows. Coaxial cables with SMA connectors were soldered directly to each antenna port to provide proper feeding of the antenna elements. It should be noted that for small antenna testing the coaxial feed cable used to connect to the measurement equipment influences on the measurement results [13]. To avoid this influence, the cables were soldered to the microstrip feed lines where the antenna elements have an E -field minimum [14].

The antenna return loss (S_{11} and S_{22}) and insertion loss (S_{21} and S_{12}) characteristics were measured using Agilent ENA 5071B network analyzer with a two-port calibration procedure. In addition, the soldered coaxial cables with SMA connectors were accurately deembedded in order to extract characteristics of the MIMO antenna system only. After that the envelope correlation coefficient was calculated from scattering matrix (S_{11} , S_{12} , S_{21} , S_{22}).

The radiation pattern measurements of the designed antenna systems were performed in an anechoic chamber using Agilent network analyzer N5230A. The radiation pattern was measured in three different orthogonal cut planes that are introduced relative to the spherical coordinate system shown in Figure 1. Two elevation cut planes at $\phi = 0^\circ$ and $\phi = 90^\circ$ and one azimuth plane at $\theta = 90^\circ$ are considered. For each cut plane, horizontally and vertically polarized components of the radiated fields were measured and then combined with the help of vector summation to find the absolute E -field value.

Another requirement formulated for the antennas designed in this work was to use a planar structure so that a PCB implementation was feasible for a low cost of production. An inexpensive FR4 ($\epsilon_r = 4.6$) PCB material was used for the design of the MIMO antennas. The total thickness of the PCB board was 1.56 mm, that is, a typical value for PCBs used in modern USB dongles. The PCB structure consists of four metal layers, where the thickness of the dielectric layer between the first two metal layers (used for the implementation of the microstrip line with the $50\ \Omega$ characteristic impedance) is 0.2 mm (the width of the microstrip line is equal to 0.3 mm).

3. MIMO Antenna System Based on Direct Connection Line (#1)

This section describes the designed compact two-element MIMO antenna system #1 that utilizes the diversity technique based on a direct connection line between the antenna elements [8–10].

3.1. MIMO Antenna System Description. The structure and the simulation model from CST Microwave Studio of the proposed compact two-element MIMO antenna system #1 are shown in Figures 2(a) and 2(b), respectively.

For constructing this MIMO antenna system, a single antenna element was designed first. A monopole antenna was chosen, since a USB dongle PCB includes a large ground plane (where IC components are placed) that can be used as a monopole reference ground plane. Because of the antenna area being strictly compact, a meander line configuration of the monopole is chosen that reduces the occupied space of the antenna element to less than $0.1\lambda_0$ in each dimension. Simulation results of the designed single antenna element show that it is well matched across the required 2.5–2.7 GHz frequency band with the return loss level below -11 dB. After that two identical monopole antenna elements are placed near each other to form a MIMO antenna system. The total occupied antenna system area is less than $10\text{ mm} \times 20\text{ mm}$ that is $0.085\lambda_0 \times 0.17\lambda_0$, where λ_0 is the wavelength in free space at the central frequency of 2.6 GHz. The distance between the two meander line monopoles was set to 6 mm that is about $0.05\lambda_0$. In this case, the isolation between the antenna elements without applying special diversity techniques is only 2.5 dB that is unacceptable for the effective MIMO performance.

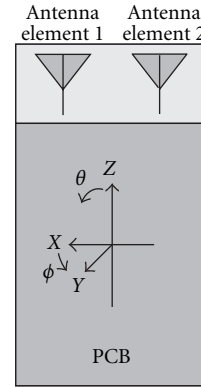


FIGURE 1: Spherical coordinate system.

In order to improve the MIMO characteristics, the monopole antennas were connected to each other by a connection line in low impedance connection points of the monopoles. The main concept of this technology is described in Figure 3 which shows two parallel dipole antennas (for simplicity). In Figure 3(a), two separate antennas are shown without any connection between each other. Some part of the signal being transmitted by one of the dipoles will be coupled directly into the neighboring dipole that leads to poor isolation between them. Figure 3(b) illustrates antenna system comprised of two closely separated dipoles with connection elements between them. In this case, the current induced from one antenna element flows through the connection to the other antenna element and does not pass through the load. Thus, both antennas form a radiation pattern with some dedicated direction of main radiation. When another antenna element is excited, the radiation pattern of the MIMO antenna system has an opposite direction of main radiation. It provides the pattern diversity when different antenna elements are excited or, equivalently, high port-to-port isolation is achieved.

The direct connection line provides high port-to-port isolation at some resonant frequency that was found to be slightly lower than the central radiation bandwidth frequency. This effect is due to an additional electrical length of the connection line that increases the electrical length of the antenna elements. Moreover, at this case, it was observed that the resonance of the antenna elements return loss (S_{11} and S_{22}) is shifted from the required 2.5–2.7 GHz frequency band to higher frequency (2.6–2.8 GHz), that leads to the -2.5 dB return loss level in the needed band. In order to adjust the resonant bandwidth of the return loss and the insertion loss to the required 2.5–2.7 GHz frequency band, the matching circuit consisting of lumped inductors (L_1) connected in series to each of the antenna elements is introduced into the antenna structure (see Figure 2(a)).

It was observed that the usage of the direct connection line and the matching circuit lead to return loss bandwidth shrinkage comparing to the case without the diversity technique implementation (without direct connection line). However, the bandwidth shrinkage depends on the connection line parameters. Hence, the optimization of the

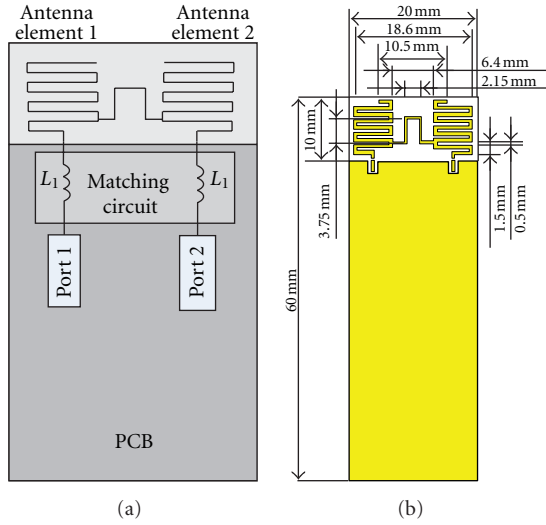


FIGURE 2: Structure (a) and CST Microwave Studio model (b) of the designed compact two-element MIMO antenna system #1.

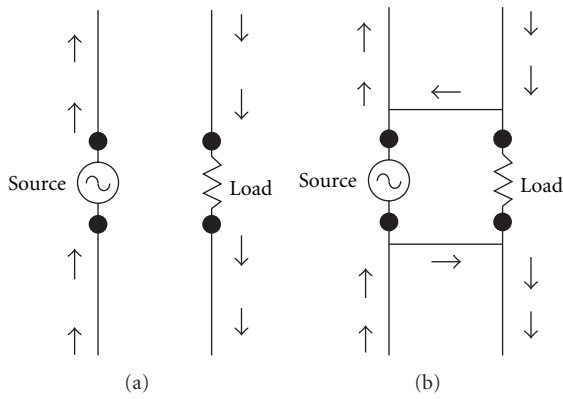


FIGURE 3: Antenna elements without (a) and with (b) direct connection lines.

two-element MIMO antenna system structure should be performed in order to provide the maximum achievable bandwidth of the return loss (S_{11} and S_{22}) and the insertion loss (S_{21} and S_{12}) simultaneously.

The bandwidth optimization was performed by variation of the connection line parameters: length, width, and connection point position. Preliminary optimization revealed that the maximum impact on the antenna bandwidth has the connection line length (viz. L parameter) that is shown in Figure 4.

Thus, in the final optimization process, the length of the connection line was varied while the width and the connection points positions were fixed after the preliminary optimization. The variation range of the connection line length L for the optimization was chosen from 1 to 6 mm. During the optimization of the connection line length, the resonant frequency of S_{21} and S_{11} was kept equal to 2.6 GHz. This was done by adjusting of the meander line length and the matching circuit inductance values.

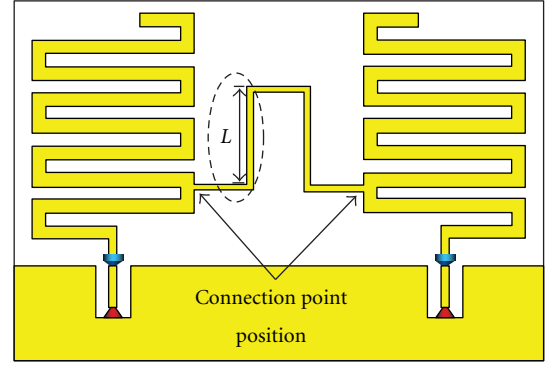


FIGURE 4: Simulation model with varied connection line length L of the MIMO antenna system #1.

Table 1 shows the return loss (S_{11} and S_{22}) and the insertion loss (S_{12} and S_{21}) bandwidths around the central frequency of 2.6 GHz for different connection line lengths. The bandwidths were estimated at the -8 dB level of S_{11} and S_{22} and at the -8 dB level of S_{12} and S_{21} .

The results presented in Table 1 show that the return loss bandwidth decreases and the insertion loss bandwidth increases while increasing the connection line length. Also, it is observed that the optimum value of the connection line length L , which corresponds to the equal values of the S_{21} and S_{11} bandwidths of about 210 MHz, is equal to 4 mm. For all other values of the connection line length, either the return or the insertion loss bandwidths are smaller than 210 MHz. Note, that the optimal MIMO antenna system parameters were achieved with the matching circuit consisting of a lumped inductance $L_1 = 4.5$ nH.

3.2. Simulation and Measurement Results. The MIMO antenna system with the optimal connection line parameters was fabricated and tested. A photo of the fabricated MIMO antenna system with assembled coaxial cables is shown in Figure 5.

The measured and simulated S -parameters for the optimized MIMO antenna system are shown in Figure 6. Good correspondence between the measurement and simulation results is observed. The measurement results indicate that the return loss S_{11} and the insertion loss S_{21} of the fabricated MIMO antenna system are below -8.5 dB levels in the required 2.5–2.7 GHz frequency band.

The measured and simulated results for the envelope correlation coefficient are shown in Figure 7. It may be seen that the measured and simulated envelope correlation coefficients are lower than 0.16 across the required bandwidth of 2.5–2.7 GHz that provides effective MIMO operation.

Figure 8 presents measured and simulated absolute values of the radiation pattern cuts for each antenna port in all the three planes at 2.6 GHz. During the measurements, one of the two-ports was excited, while the other was terminated with a 50Ω matching load. Thus, two different radiation patterns were obtained—one for each of the ports.

The measurement and simulation results show that the designed MIMO antenna system has pattern diversity at both

TABLE 1: S_{11} and S_{21} bandwidths for different L .

L value, mm	S_{11} and S_{22} bandwidth, MHz	S_{12} and S_{21} bandwidth, MHz
1	226	130
2	221	146
3	216	173
4	209	207
5	196	425
6	184	435

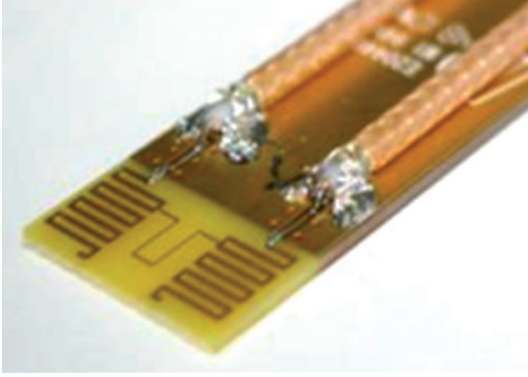


FIGURE 5: Photo of the fabricated MIMO antenna system #1 with assembled cables.

azimuth cut $\theta = 90^\circ$ (Figure 8(c)) and elevation cut $\phi = 0^\circ$ (Figure 8(a)) that proves the effectiveness of the diversity technique based on a direct connection of the antenna elements. At the elevation cut $\phi = 90^\circ$ (Figure 8(b)) almost an omnidirectional radiation pattern is observed as expected since the antenna elements are placed symmetrically to this cut plane. The maximum measured gain of the MIMO antenna system at the 2.6 GHz frequency is 1.5 dBi.

The measured characteristics satisfy all the requirements that were set to the MIMO antenna system of a modern USB dongle.

4. MIMO Antenna System Based on a Lumped Decorrelation Capacitance (#2)

This section describes the second designed compact two-element MIMO antenna system that uses the diversity technique utilizing a lumped capacitance introduced between the antenna elements [11].

4.1. MIMO Antenna System Description. The structure and the simulation model from CST microwave studio of the MIMO antenna system #2 are shown in Figures 9(a) and 9(b), respectively.

Similar to the first MIMO antenna system, a monopole antenna with a modified configuration was used as an antenna element of the second antenna system. A triangular antenna element configuration allows reducing its occupied space to less than $0.1 \lambda_0$ in each dimension. Simulation results

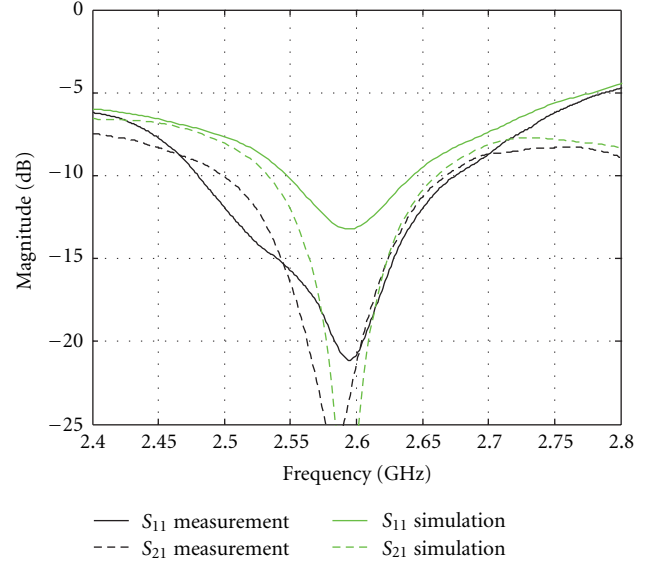


FIGURE 6: S-parameters for the optimized structure of the MIMO antenna system #1 (measurements versus simulations).

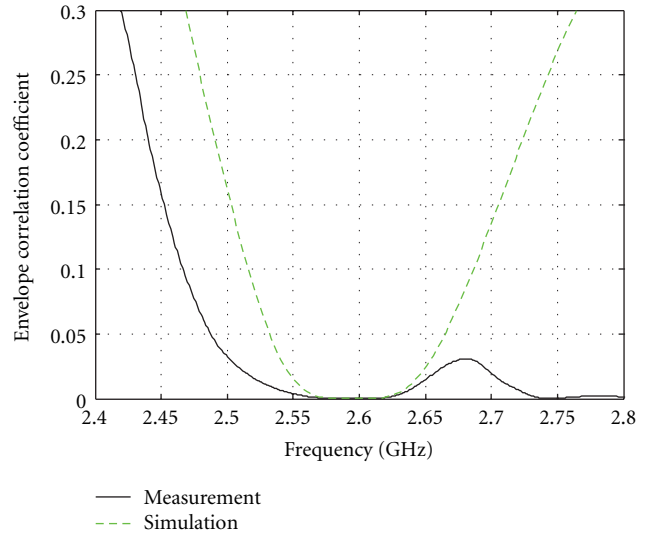


FIGURE 7: Envelope correlation coefficient of the MIMO antenna system #1 (measurements versus simulations).

of the designed single antenna element show that it is well matched with the return loss level below -15 dB across the required 2.5–2.7 GHz frequency band. Two identical monopole antennas occupy area less than $10 \text{ mm} \times 20 \text{ mm}$ with 5.5 mm ($0.048 \lambda_0$) distance between them. However, such antenna system configuration without additional diversity techniques provides only 3 dB isolation between the antenna elements.

In order to improve isolation between the antenna elements a lumped decorrelation capacitance is mounted between the antenna elements feeding points. The concept of this technology is the same as for the diversity technique

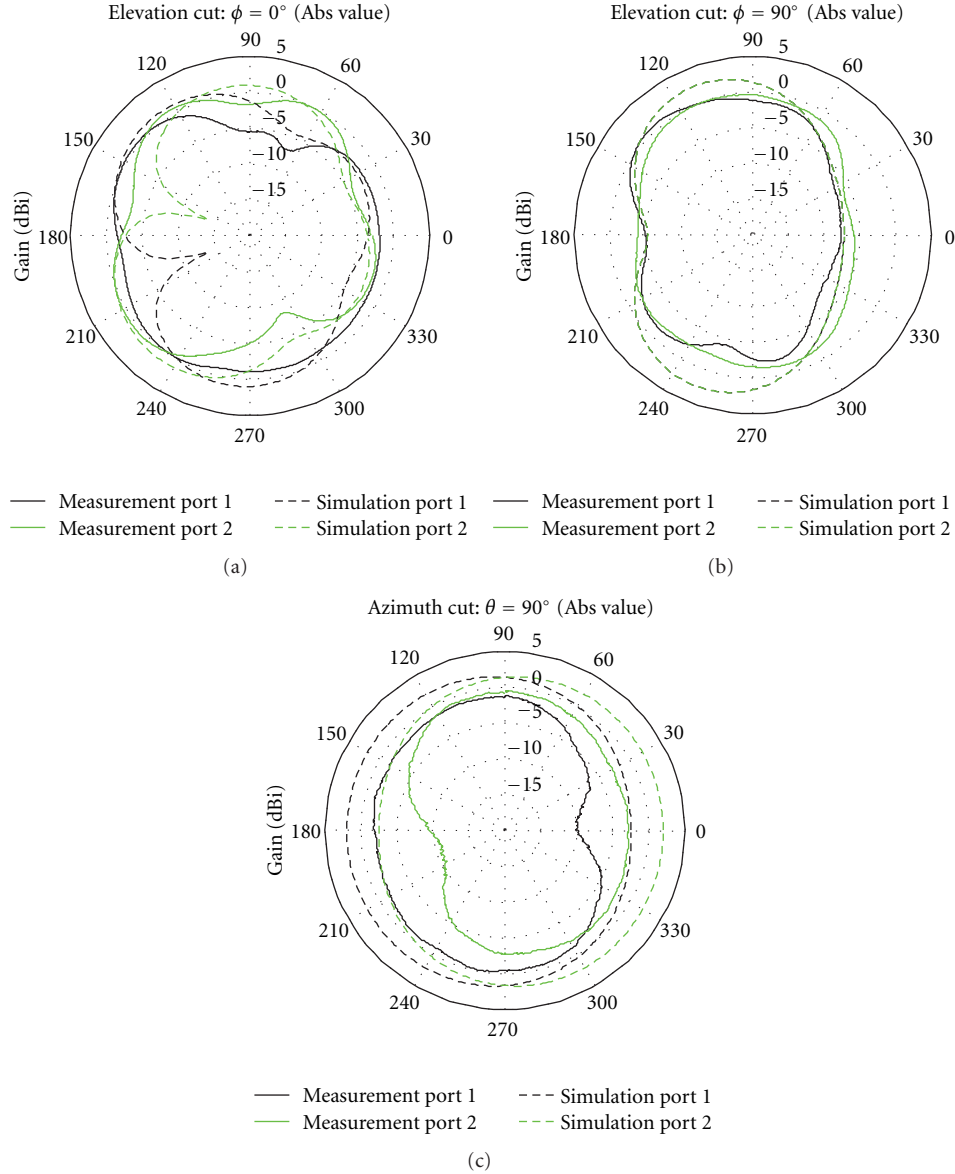


FIGURE 8: Radiation pattern cuts of the MIMO antenna system #1 (measurements versus simulations).

based on a direct connection line that is specified in the previous section (Section 3). The main difference between these two approaches consist in usage of a lumped decorrelation capacitance instead of a direct connection line.

The lumped decorrelation capacitance allows to tune the antenna coupling so that to provide high isolation. The capacitance value is optimized to achieve the low insertion loss S_{21} and S_{12} (high isolation between the antenna elements) in the required frequency band. It was found by adjusting the capacitance value that the 0.8 pF capacitance provides the highest isolation at the 2.5–2.7 GHz frequency band given that the geometry of the antenna elements is fixed. The usage of the capacitor with 0.8 pF allows improving the isolation from 3 dB to 10 dB across the required frequency band. It was observed that the usage

of the decorrelation capacitance leads to variations of the operational frequency band of the return loss S_{11} and S_{22} (the return loss level changes from -15 dB to -2.5 dB in the 2.5–2.7 GHz frequency band). In order to simultaneously adjust the return loss and the insertion loss to the same resonant frequency, a matching circuit consisting of two lumped inductors connected in shunt (L_2) and in series (L_1) to each of the antenna elements is introduced into the antenna structure (see Figure 9(a)). Since the isolation level is very high, an additional impedance network does not change the isolation. To adjust the return loss S_{11} to the required frequency band, the inductors values $L_1 = 3$ nH and $L_2 = 4.6$ nH are used.

The final results for the second designed MIMO antenna system with the lumped capacitance and the matching circuit

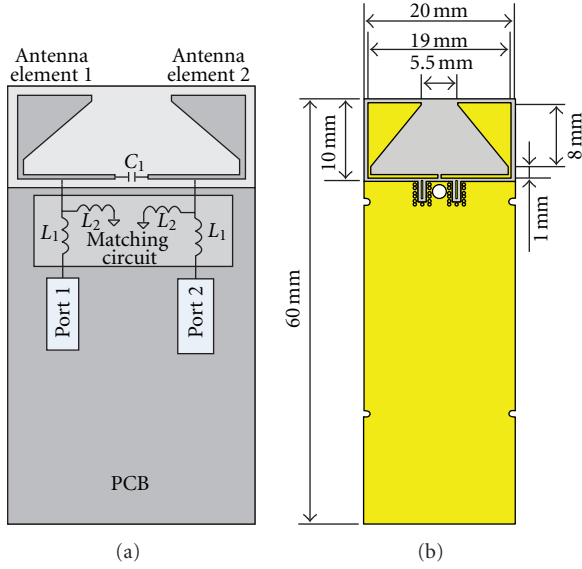


FIGURE 9: Structure (a) and CST Microwave Studio model (b) of the designed compact two-element MIMO antenna system #2.

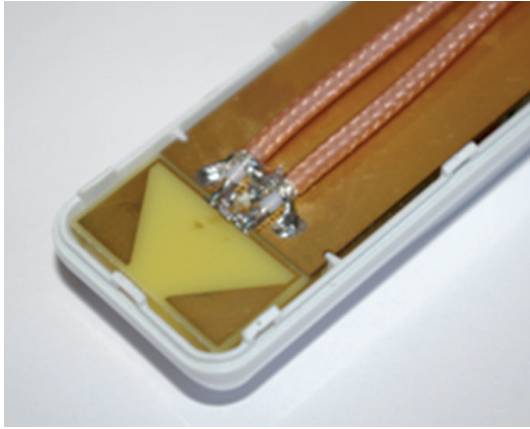


FIGURE 10: Photo of the fabricated MIMO antenna system #2 assembled with the cables.

indicate that the return loss (S_{11} and S_{22}) and the insertion loss (S_{21} and S_{12}) have -8 dB levels in the required 2.5–2.7 GHz frequency band.

4.2. Simulation and Measurement Results. The MIMO antenna system #2 that uses the diversity technique utilizing a lumped capacitance was fabricated and tested. A photo of the fabricated MIMO antenna system #2 assembled with the coaxial cables and lumped elements is shown in Figure 10.

The measured and simulated return loss (S_{11}) and insertion loss (S_{21}) are shown in Figure 11. The demonstrated results show a good agreement between the measurements and simulations. The measurement results indicate that the fabricated MIMO antenna system can operate in the 2.5–2.7 GHz frequency band with at least the -8 dB level of the return loss S_{11} and high isolation between the antenna elements (the insertion loss S_{21} is below -8.5 dB).

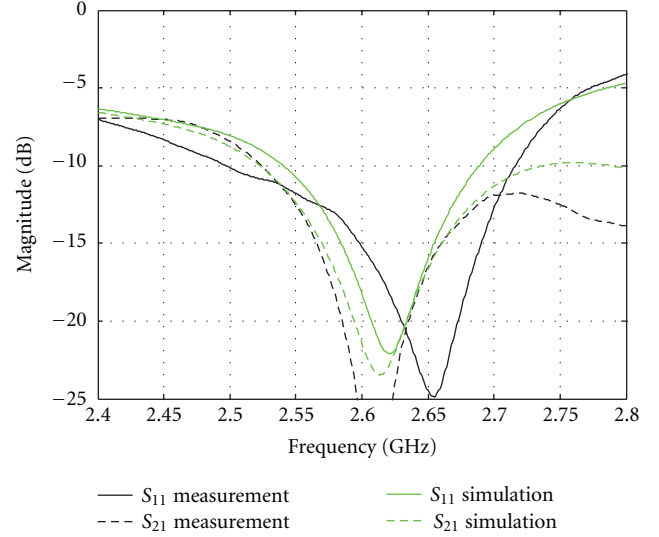


FIGURE 11: S-parameters of the MIMO antenna system #2 (measurements versus simulations).

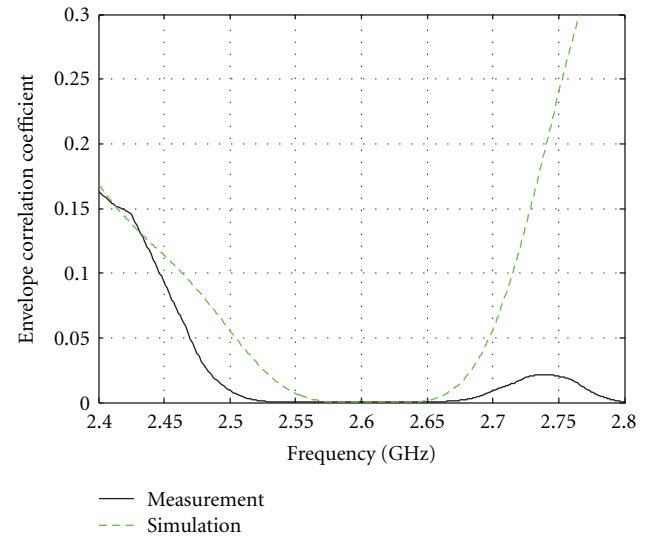


FIGURE 12: Envelope correlation coefficient of the MIMO antenna system #2 (measurements versus simulations).

The measured and simulated results for the envelope correlation coefficient are shown in Figure 12. It may be seen that the measured and simulated envelope correlation coefficients are lower than 0.06 across the required bandwidth of 2.5–2.7 GHz.

Figure 13 presents measured and simulated absolute values of the radiation pattern cuts for each antenna port in all the three planes at 2.6 GHz. During the measurements, one of the two-ports was excited, while the other was terminated with a 50Ω matching load. Thus, two different radiation patterns were obtained—one for each of the ports.

The measurement and simulation results show the radiation properties similar to the MIMO antenna system #1.

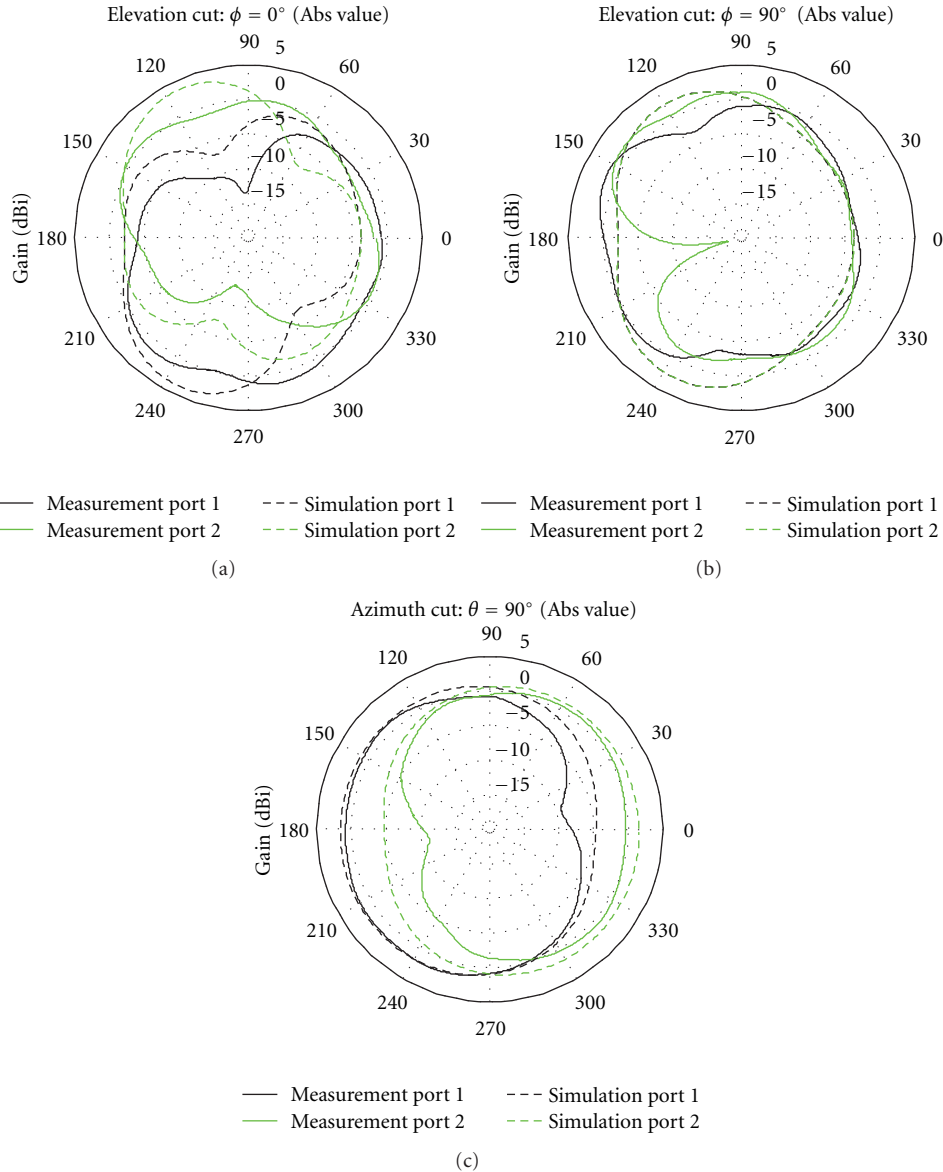


FIGURE 13: Radiation pattern cuts of the MIMO antenna system #2 (measurements versus simulations).

More specifically, the second MIMO antenna system has pattern diversity at the azimuth cut $\theta = 90^\circ$ (Figure 13(c)) and the elevation cut $\phi = 0^\circ$ (Figure 13(a)) that proves the effectiveness of the proposed MIMO antenna design approach. At the elevation cut $\phi = 90^\circ$ (Figure 13(b)), almost an omnidirectional radiation pattern is observed as expected, since the antenna elements are placed symmetrically to this cut plane. The maximum measured gain of the MIMO antenna system at the 2.6 GHz frequency is 2.5 dBi.

Comparison of the measurement and simulation results shows their good agreement. Hence, the obtained results prove sufficient return loss bandwidth with high port-to-port isolation and confirm pattern diversity of the designed compact MIMO antenna system #2. As for the first design, all the set requirements are met.

5. MIMO Antenna System Using PIFA Elements (#3)

This section describes the third designed compact two-element MIMO antenna system (#3). To achieve sufficient isolation between the antenna elements, this antenna system uses only antenna element properties and does not use special diversity techniques which application may be a subject of different limitations arising, for example, from the intellectual property rights.

5.1. MIMO Antenna System Description. The structure and the simulation model from CST Microwave Studio of the designed MIMO antenna system #3 are shown in Figures 14(a) and 14(b), respectively.

For constructing a MIMO antenna system, a planar inverted- F antenna (PIFA) was used. A PIFA is another type of a monopole antenna which allows reducing the monopole dimensions. It is achieved by using a folded stub of one part of a monopole to the ground plane. One of the inherent properties of the PIFA antenna is that its radiation is located mostly in one-half space. Therefore, two closely separated PIFAs with opposite symmetrical (mirror) orientations provide pattern and polarization diversity. In this work, it was found that two closely spaced PIFAs in strictly compact antenna area (as in USB dongle) allow achieving the convenient isolation between elements of MIMO antenna system without using the special diversity techniques.

In order to construct a MIMO antenna system, two PIFA elements were symmetrically located along the edges of the USB PCB as shown in Figure 14. To achieve the required antenna elements isolation, the distance between them was adjusted. It was observed that with an increase of the distance between the elements (i.e., ground plane size expansion), the isolation between the antenna elements increases. It was observed that the optimum distance between two PIFAs, which corresponds to the isolation level not less than 8 dB and return loss level not more than -8 dB across the required 2.5–2.7 GHz band, is equal to 12 mm or $0.1 \lambda_0$. Therefore, the total occupied antenna system area is less than $21.5 \text{ mm} \times 20 \text{ mm}$ that is equivalent to $0.19 \lambda_0 \times 0.18 \lambda_0$. However, it should be noted that the ground plane (with the $21.5 \text{ mm} \times 12 \text{ mm}$ size) between two PIFAs can be used for mounting additional IC components that further improves the PCB area utilization.

5.2. Simulation and Measurement Results. The MIMO antenna system #3 that uses PIFA elements was fabricated and tested. A photo of the fabricated MIMO antenna system #3 assembled with the coaxial cables is shown in Figure 15.

The measurement and simulation results for the return loss (S_{11}) and the insertion loss (S_{21}) are plotted in Figure 11. The demonstrated results show a good agreement between the measurements and simulations. The measurement results indicate that the fabricated MIMO antenna system can operate in the 2.5–2.7 GHz frequency band with at least the -8 dB level of the return loss S_{11} and high isolation between the antenna elements (the insertion loss S_{21} is below -8.5 dB). Note that the minimum isolation (8.5 dB) for the mirror symmetrical orientation of the two PIFAs is much better than in the case of other antenna types (like monopoles) that are located near to each other without applying any additional diversity techniques. In case when two parallel monopoles are used only 3.5 dB isolation can be achieved.

Figure 17 presents the measured and simulated results for the envelope correlation coefficient. It may be seen that the measured and simulated envelope correlation coefficients are lower than 0.1 across the required bandwidth of 2.5–2.7 GHz.

The measured and simulated absolute values of the radiation pattern cuts for each antenna port are shown in Figure 18 for all the three planes at 2.6 GHz. During the

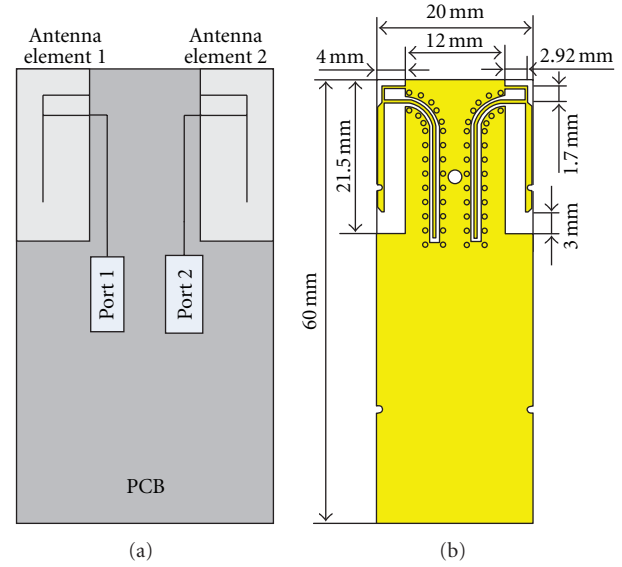


FIGURE 14: Structure (a) and CST Microwave Studio model (b) of the designed compact two-element MIMO antenna system #3.

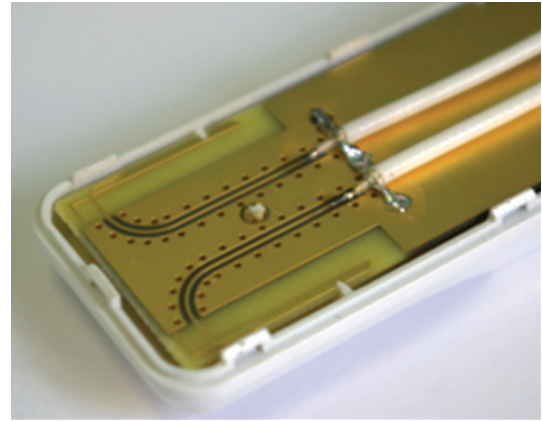


FIGURE 15: Photo of the fabricated MIMO antenna system #3 with the assembled cables.

measurements, one of the two-ports was excited, while the other was terminated with a 50Ω matching load. Thus, two different radiation patterns were obtained—one for each of the ports.

The measurement and simulation results show that the designed antenna system has an almost omnidirectional radiation pattern at the elevation cut $\phi = 90^\circ$ (Figure 18(b)) and pattern diversity at both azimuth cut $\theta = 90^\circ$ (Figure 18(c)) and the elevation cut $\phi = 0^\circ$ (Figure 18(b)). The radiation pattern diversity is achieved due to the inherent properties of the PIFA antenna. The maximum measured gain of the MIMO antenna system at the 2.6 GHz frequency is 2.5 dBi.

The measurements results satisfy all characteristics requirements that are applied to MIMO antenna system in modern USB dongles.

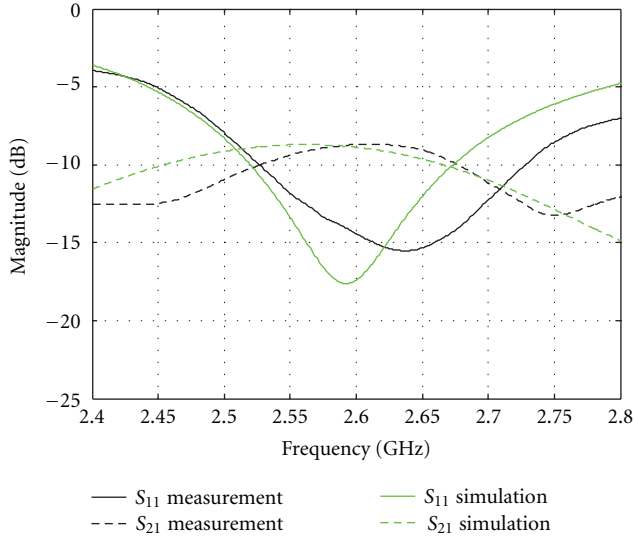


FIGURE 16: S-parameters of the MIMO antenna system of the MIMO antenna system #3 (measurements versus simulations).

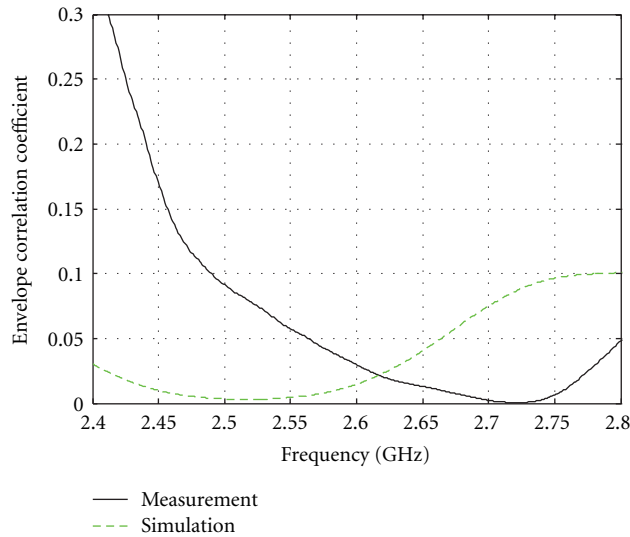


FIGURE 17: Envelope correlation coefficient of the MIMO antenna system #3 (measurements versus simulations).

6. MIMO Antenna Systems Comparison

All the three MIMO antennas systems presented in this paper achieve the characteristics required for an efficient MIMO system operation in a USB dongle as formulated in the beginning of this work.

Despite many similarities, quite important differences exist between the three designs that may impact one or another design selection in a particular case.

All the designed MIMO antennas have planar microstrip structures and use a standard PCB technology that provides a low production cost. First two antenna systems occupy

only $10 \text{ mm} \times 20 \text{ mm}$ area that is equivalent to $0.085 \lambda_0 \times 0.17 \lambda_0$. The antenna system #3 needs a larger area ($21.5 \text{ mm} \times 20 \text{ mm}$ or $0.19 \lambda_0 \times 0.18 \lambda_0$.) but keeps some space in between the PIFA elements for mounting of the IC components.

Another important differentiation is that MIMO antenna systems #1 and #2 use a special diversity technique by connecting the antenna elements while the MIMO antenna system #3 utilizes independent antenna elements (Figure 16). For MIMO antenna system #1, a direct connection line between the antenna elements was used. The geometry of the connection line allows adjusting the insertion loss S_{21} resonance to the required frequency. Hence, the final MIMO antenna system optimization should be carried out before its fabrication. In MIMO antenna system #2, the high port-to-port isolation is achieved using the same concept but instead of a direct connection line it uses a lumped capacitance introduced between the antenna elements. The introduction of the capacitor allows carrying out the final MIMO antenna system optimization after its fabrication by changing the capacitance value.

Regarding the bandwidth of the antenna system, all the three designs presented in this work achieve the formulated required characteristics for efficient MIMO system operation, namely at least -8 dB level of the return loss S_{11} and high isolation between the antenna elements (the insertion loss S_{21} below -8.5 dB) across the required $2.5\text{--}2.7 \text{ GHz}$ frequency band. However, the bandwidth requirements are met only marginally for all the three designs. The bandwidth for MIMO antenna systems #1 and #2 is limited because of application of the direct connection diversity technique—the direct connection line and the lumped capacitance significantly reduce the antenna system bandwidth relative to a single element case. The value of the bandwidth for the MIMO antenna system #3 is limited by a small size of the ground plane between the antenna elements. In order to achieve the required 200 MHz bandwidth, the rigorous parameters optimization was done for all the three MIMO antenna systems and optimal parameters were selected.

None of the three proposed systems is considered to be a preferred solution and that was one of the motivations for their joint presentation in this work. However, an introduction of new additional system constraints may shift the designer's preference towards one of the approaches.

7. Conclusion

This work presented the three different microstrip MIMO antenna system designs for LTE/WiMAX USB dongle applications operating in the $2.5\text{--}2.7 \text{ GHz}$ frequency band. These antenna systems include two antenna elements with high isolation between them and implemented in a strictly compact area. For the first antenna system design, high port-to-port isolation is achieved by using a decoupling techniques based on a direct connection of the antenna elements. For the second approach, high port-to-port isolation for the MIMO antenna system is realized by a lumped decorrelation capacitance between antenna elements feeding points. The

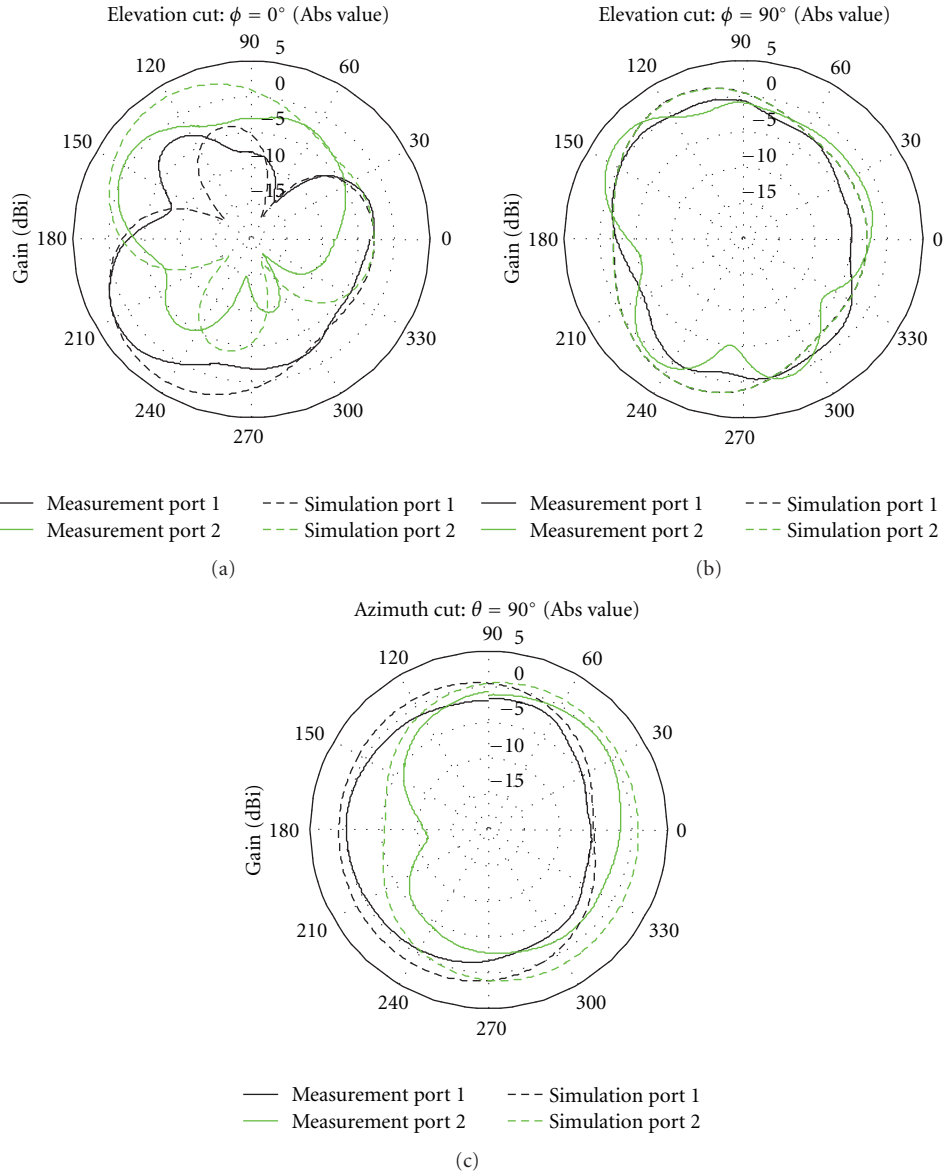


FIGURE 18: Radiation pattern cuts of the MIMO antenna system #3 (measurements versus simulations).

third proposed antenna system does not use any special techniques, and high port-to-port isolation is achieved by using only the properties of a developed printed inverted-F antenna element. The proposed MIMO antenna systems were designed in the low-cost FR4 PCB technology that is typically used for a USB dongle realization.

The performed simulation and experimental investigations of the S-parameters, envelope correlation coefficient, and radiation patterns for the designed MIMO antenna systems demonstrate low return loss (< -8 dB) and high port-to-port isolation (> 8.5 dB) in the required frequency band of 2.5–2.7 GHz and confirm their pattern diversity. The designed MIMO antenna systems can be used in different 2.5–2.7 GHz applications of USB dongles like LTE and WiMAX where effective support for MIMO transmission is required.

References

- [1] A. J. Paulraj, D. A. Gore, R. U. Nabar, and H. Bölcskei, "An overview of MIMO communications—a key to gigabit wireless," *Proceedings of the IEEE*, vol. 92, no. 2, pp. 198–218, 2004.
- [2] M. Karakoikis, C. Soras, G. Tsachtsiris, and V. Makios, "Compact dual-printed inverted-F antenna diversity systems for portable wireless devices," *IEEE Antennas and Wireless Propagation Letters*, vol. 3, no. 1, pp. 9–14, 2004.
- [3] H. Lihao, Z. Huiling, H. Zhang, and C. Quanming, "Reduction of mutual coupling between closely-packed antenna elements with split ring resonator (SRR)," in *Proceedings of the International Conference on Microwave and Millimeter Wave Technology (ICMMT '10)*, pp. 1873–1875, Chengdu, China, May 2010.
- [4] F. Yang and Y. Rahmat-Samii, "Microstrip antennas integrated with electromagnetic band-gap (EBG) structures: a

- low mutual coupling design for array applications," *IEEE Transactions on Antennas and Propagation*, vol. 51, no. 10, pp. 2936–2946, 2003.
- [5] A. C. K. Mak, C. R. Rowell, and R. D. Murch, "Isolation enhancement between two closely packed antennas," *IEEE Transactions on Antennas and Propagation*, vol. 56, no. 11, pp. 3411–3419, 2008.
 - [6] S. Zhang, S. N. Khan, and S. He, "Reducing mutual coupling for an extremely closely-packed tunable dual-element PIFA array through a resonant slot antenna formed in-between," *IEEE Transactions on Antennas and Propagation*, vol. 58, no. 8, pp. 2771–2776, 2010.
 - [7] Q. Wang, H. Zhang, D. Plettemeier, E. Ohlmer, and G. Fettweis, "Design and performance evaluation of handset MIMO antenna prototypes," in *Proceedings of the International ITG Workshop on Smart Antennas (WSA '10)*, pp. 375–382, Bremen, Germany, February 2010.
 - [8] F. M. Caimi and M. Montgomery, "Dual feed, single element antenna for WiMAX MIMO application," *Internal Journal of Antennas and Propagation*, vol. 2008, Article ID 219838, 5 pages, 2008.
 - [9] I. Dioum, A. Diallo, C. Luxey, and S. M. Farsi, "Dual-band monopole MIMO antennas for LTE mobile phones," in *Proceedings of the 20th International Conference on Applied Electromagnetics and Communications (ICECom '10)*, Dubrovnik, Croatia, September 2010.
 - [10] V. Ssorin, A. Artemenko, A. Sevastyanov, and R. Maslennikov, "Compact bandwidth-optimized two element MIMO antenna system for 2.5-2.7 GHz band," in *Proceedings of the 5th European Conference on Antennas and Propagation (EUCAP '11)*, pp. 319–323, Rome, Italy, April 2011.
 - [11] V. Ssorin, A. Artemenko, A. Sevastyanov, and R. Maslennikov, "Compact 2.5-2.7 GHz two element MIMO antenna system for modern USB dongle," in *Proceeding of the 6th European Conference on Antennas and Propagation (EuCAP '12)*, pp. 1955–1959, Prague, Czech Republic, March 2012.
 - [12] S. Blanch, J. Romeu, and I. Corbella, "Exact representation of antenna system diversity performance from input parameter description," *Electronics Letters*, vol. 39, no. 9, pp. 705–707, 2003.
 - [13] B. S. Yarman, *Design of Ultra Wideband Antenna Matching Networks*, Springer Science+Business Media B.V., 2008.
 - [14] P. J. Massey and K. R. Boyle, "Controlling the effects of feed cable in small antenna measurements," in *Proceedings of the Antennas and Propagation Society International Symposium*, vol. 2, pp. 561–564, March 2003.

Research Article

Harmonic Suppressed Slot Antennas Using Rectangular/Circular Defected Ground Structures

Mohammad Saeid Ghaffarian, Gholamreza Moradi, and Reza Zaker

Wave Propagation and Microwave Measurement Research Laboratory, Department of Electrical Engineering, Amirkabir University of Technology, Tehran 15914, Iran

Correspondence should be addressed to Mohammad Saeid Ghaffarian, msghaffarian@aut.ac.ir

Received 19 October 2011; Accepted 20 May 2012

Academic Editor: Dalia N. Elshiekh

Copyright © 2012 Mohammad Saeid Ghaffarian et al. This is an open access article distributed under the Creative Commons Attribution License, which permits unrestricted use, distribution, and reproduction in any medium, provided the original work is properly cited.

Two wide rectangle-shaped microstrip-fed 2.6-GHz slot antennas using defected ground structures (DGSs) with a low design complexity are proposed to achieve wideband harmonic suppression. To accomplish this, two rectangular DGSs (RDGSs) in the first antenna and two circular DGSs (CDGSs) in the second one with various dimensions are etched into the ground plane, which could have a wideband-stop characteristic. Simulated and measured reflection coefficients indicate that the two proposed structures effectively suppress the second and third harmonics up to 23 dB between 3.5 and 10.5 GHz with a maximum ripple of 2.4 dB. In addition, the radiation patterns and peak gains of the antennas can be suppressed at least 17 dB and 7.1 dBi, respectively, at the third harmonic frequency of 7.86 GHz.

1. Introduction

Microstrip antennas can be conventionally integrated with active RF devices, especially amplifiers. In these cases, to maximize power added efficiency (PAE) of the power amplifiers (PAs), several methods are carried out on the PA itself. Since these approaches caused RF front-end systems to have large size, complex structures, and difficulty to design, the active integrated antennas (AIAs) were proposed. AIAs are very widespread, but they suffer from undesired harmonic radiation which must be suppressed. To this purpose, in the conventional harmonic tuning circuits, additional components such as filters were employed which increase the size and cost of RF front-ends and yield an additional insertion loss [1, 2].

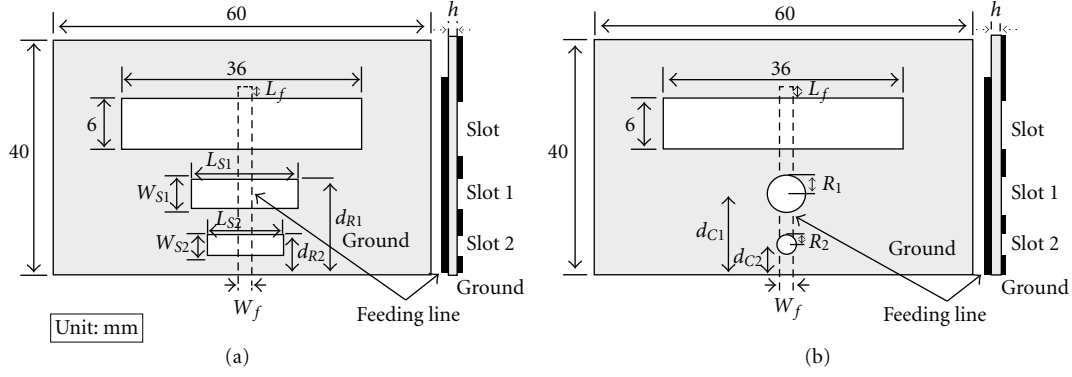
In the last decades, several methods have been researched in practice to decrease insertion loss and spurious radiation in slot and patch antennas with microstrip and CPW-fed method [3–8]. In [2], Itoh et al. have introduced a photonic bandgap structure (PBG) based on the periodic structure to tune the second harmonic in an active slot antenna. After that, there has been an increasing interest in applying PBG and electromagnetic bandgap (EBG) structures as well as defected ground structure (DGS). Afterwards, new

structures using L-C resonators as spurline conductors or other structures which act like filters that positioned on a radiator or feeding line have been proposed [4–7]. Also, harmonic suppression is done by defecting rectangular slot on tubing stub in CPW slot antenna [8]. It should be noted that the designs of mentioned periodic structures are not simple because of having several design parameters, difficulties of the modeling, and complex pattern and therefore, their fabricating is difficult.

In this paper, two harmonic suppressed slot antennas (HSAs) with rectangular and circular DGSs (i.e., RDGS & CDGS) are parametrically investigated. The antennas having low design complexity such as less-design parameters and simpler DGS patterns can be suitable options for broadband unwanted harmonic suppression. In addition, in order to get a better understanding of the suppression performance of the antennas, the current distribution and circuit model are also discussed.

2. Antenna Design and Configuration

Figure 1 shows the geometry of the two slot harmonic suppression antennas in which the first one (Figure 1(a)) consists of two unequal RDGS with parameters of WS_1 , LS_1 ,



Parameters	W_{S1}	L_{S1}	W_{S2}	L_{S2}	R_1	R_2	W_f	h	L_f	d_{R1}	d_{R2}	d_{C1}	d_{C2}
Values (mm)	3.5	11	2.5	6	3.8	1	1.1	0.508	1	14	8	11	5

FIGURE 1: Configuration of the two proposed antennas with their optimal parameters: (a) geometry of rectangular DGS slot antenna and (b) geometry of circular DGS slot antenna.

d_{R1} and W_{S2} , L_{S2} , and d_{R2} , and the other one (Figure 1(b)) has two unequal CDGS with parameters of R_1 , d_{C1} and R_2 , d_{C2} . The antennas are fabricated on the substrate RO4003C with 0.5-oz copper, whole dimension of $40 \times 60 \text{ mm}^2$, 0.508 mm height, and dielectric constant of 3.38. The width of the microstrip-fed line is $W_f = 1.1 \text{ mm}$ for a 50Ω input impedance. The optimal physical parameters of both proposed antennas are summarized in a table and illustrated in Figure 1. To eliminate unwanted radiation at harmonic frequencies, two DGS-type slots (RDGS and CDGS) are etched into the ground plane exactly below the microstrip line and near the main radiation slot with a dimension of $6 \times 36 \text{ mm}^2$. The proposed unequal slots can be represented as sequential shunt L-C resonators, which have totally wideband-stop operation over the third harmonic frequency.

In the next section, it will be shown from parametric studies that the positions and dimensions of the DGS slots are important factors to suitably suppress the third harmonic frequency and tune the matching at the main resonance and the notched band.

Some of the popular DGSs are shown in Figure 2. These structures have their own distinguish properties which can be used for harmonic suppression. The reflection coefficients of rectangular, circular, triangular, spiral, dumbbell, and H shape DGS is shown in Figure 3. To give a better understanding of the performance of DGSs and comparison between them, the position and etched square area of DGSs are identical. The etched square of DGS is critical factor for determining the depth of suppression. Therefore, this factor is parametrically investigated in the next section. As seen from Figure 3, a little frequency shifting at the fundamental frequency and depth of suppression at the third harmonic frequency are important issues which should be noted. Hence, every pair of DGSs can be suitable for harmonic suppression in slot antenna if they are placed at the appropriate position. Because of decreasing of the context, the general properties of the mentioned DGSs such as the

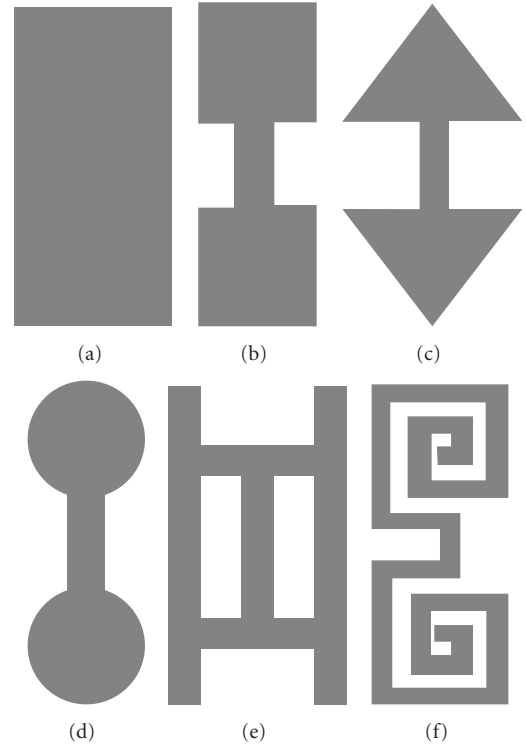


FIGURE 2: Different slots for DGS: (a) rectangular DGS, (b) square head DGS (dumbbell shape), (c) triangular DGS, (d) circular DGS, (e) H shape DGS, and (f) spiral DGS.

act of suppression and parametrically studies are examined for the rectangular and circular DGS's slot antenna, and their results can be ascribe to all of them.

In order to give a physical insight, the current distribution on the ground plane is investigated. Figure 4(a) shows the current in the absence of DGS filter, and Figures 4(b) and 4(c) demonstrate the disturbance in current distribution

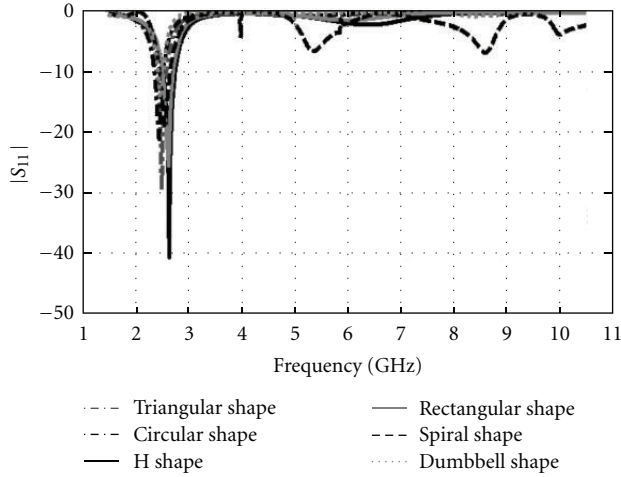


FIGURE 3: Simulated reflection coefficients of HSA with different kinds of DGS. The position and etched square area of every DGS are identical.

which caused by DGS combinations. The electromagnetic field is mostly confined under the microstrip line. The return current on the ground plane is the negative image of the current distribution on the microstrip line. The return path of the current is fully disturbed using the DGS, and this current is confined to the perimeter of the perturbation and returns to the underneath of the microstrip line once the perturbation is over. By considering the maximum concentration of the return surface current on the ground plane, the length of the slot which contributes to inductance of the DGS is determined. The width of the slots is represented by the equivalent capacitances and the inductances and capacitances, are derived from the physical dimensions using quasistatic expressions for microstrip crosses, lines, and gaps which are presented in the open literatures [9]. The same approach is ascribed to CDGS slot antenna. On the basis of this observation, an equivalent circuit model is developed. Equivalent circuit model of RDGS slot antenna can be modeled based on the transmission line model. As shown in Figure 5, the proposed circuit model consists of two parts. The first part is the lossy model of two DGS slots that composed of two parallel RLC for each slot resonator and parallel capacitor that is due to relatively large fringing field at the step discontinuity plane on metallic ground surface [10]. The second part is the model of slot antenna that made of two short-circuited slot lines parallel (with the length of $L_{cs} = 18$ mm, which is equal to the half-length L_s of rectangular slot) with conductance G_s , representing the radiated power from the slot and parallel RC which is the admittance at the input of the open-ended microstrip stub which are obtained by equations that are mentioned in [11]. The optimized ADS-simulated results of the parameters of equivalent model are also shown in Figure 5. Figure 6 shows the reflection coefficients of the circuit model of RDGS antenna in comparison with the HFSS result. Since the parallel capacitance might cause changing in the impedance of the DGS section, it should be considered

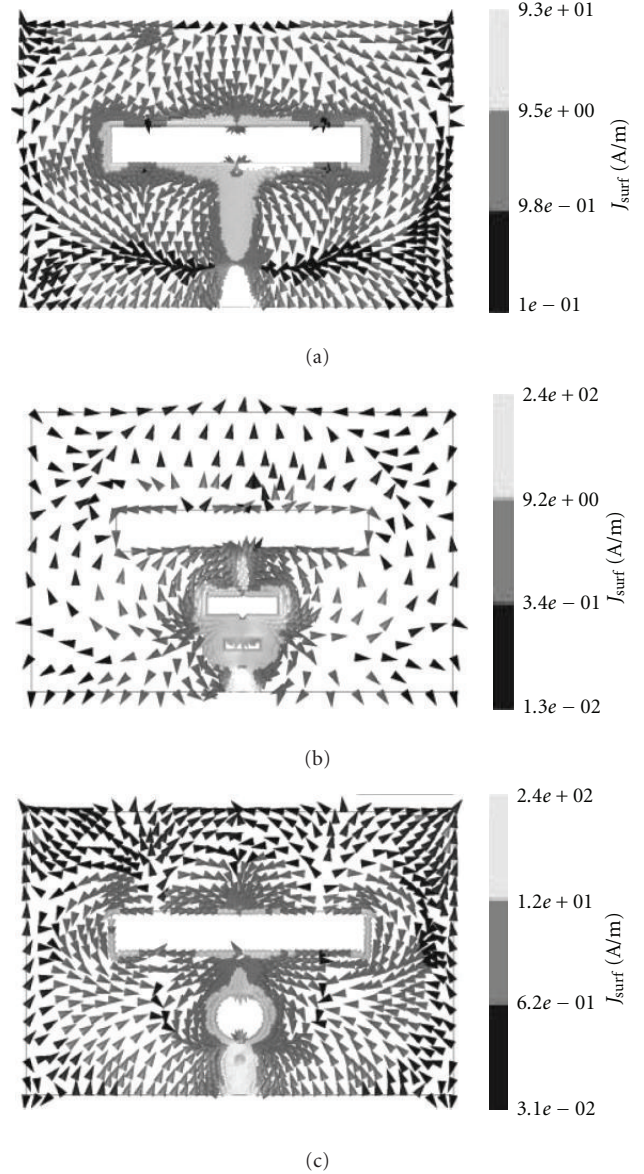


FIGURE 4: Simulated current distribution on the ground plane at the third harmonic frequency for (a) conventional slot antenna, (b) RDGS slot antenna, and (c) CDGS slot antenna.

for more precise modeling procedure. Circuit functionalities as filtering unwanted high-order harmonics can easily be accomplished by means of placing required DGS patterns without increasing circuit complexity. Each DGS provides its own distinctive characteristics depending on its geometries. It will be shown from parametric studies that the dimensions of the DGS slots are important factors to suitably suppress the third harmonic frequency.

3. Simulated and Measured Results and Discussions

The simulation is performed using high frequency structure simulator (HFSS). By using the DGS section, both the

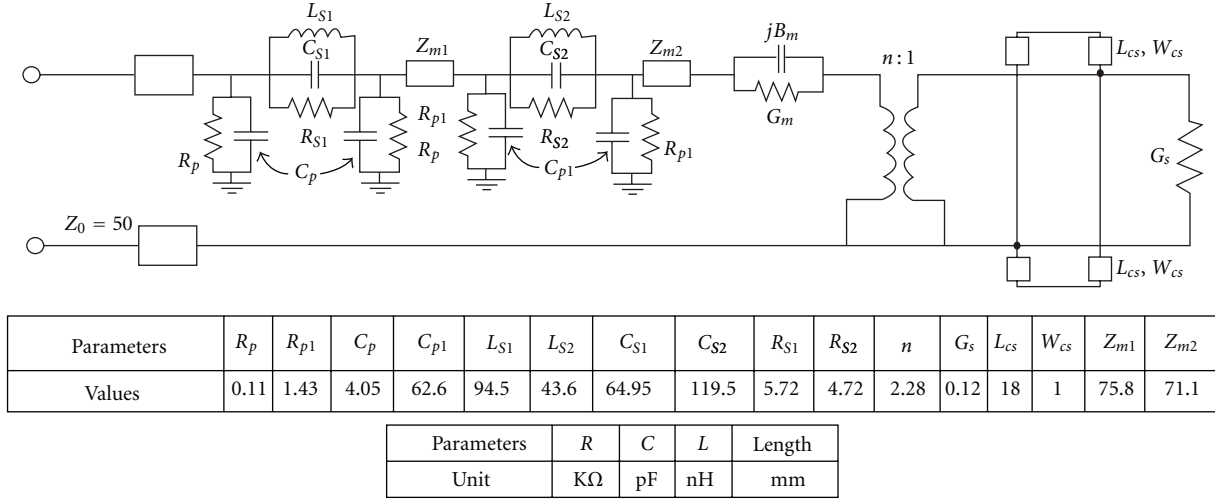


FIGURE 5: Circuit model for rectangular defected ground structure slot antenna.

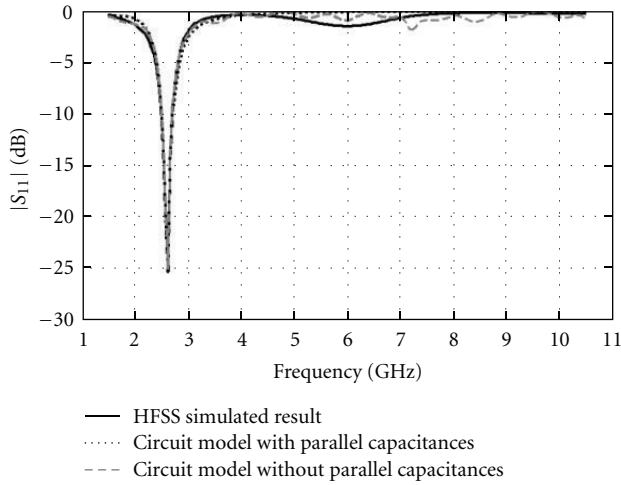


FIGURE 6: Reflection coefficients of equivalent circuit model of the harmonic suppression antenna.

effective permittivity and effective inductance of a microstrip line are increased [5]. The etched square area in the ground plane is critical factor for determining the depth of suppression. First, the parameters of the RDGS slot antenna are investigated. The change in the length in comparison with the change in the slots width is more effective for controlling the resonate frequency of RDGS slots. Figure 7(a) shows that when the length of DGS slots is altered, the depth of suppression is notably modified. The optimal ratio value of L_{S1}/L_{S2} is 1.8. The same investigation is applied to CDGS slot antenna by changing the radius of slots in which the relevant parametric results are indicated in Figure 7(b). It is clearly seen that by decreasing the ratio of R_1/R_2 , the quality of the suppression is extremely degraded especially between 5 and 9 GHz. It is interesting to point out that our studies show that the area of small DGS slots has important role in the value of input impedance at the third harmonic frequency. When the

area of the slot is reduced, the input impedance is increased at the third harmonic frequency and makes that we have not reactively termination at this harmonic.

In order to validate the designs, the optimized structures of proposed HSAs were manufactured and measured carefully. Figures 8 and 9 show the simulated and measured reflection coefficients and the measured input impedances of the proposed rectangular and circular DGS-type slot antennas, respectively. To compare the quality of harmonic suppression, a conventional wide slot antenna without DGS is fabricated and measured. Figures 8(a) and 9(a) indicate that measured and simulated reflection coefficients are matched in both cases of HSA and conventional types. These antennas resonate at 2.62 GHz and suppress the third harmonic frequency at 7.86 GHz. The measured bandwidths of the proposed RDGS and CDGS antennas at the center frequency of 2.62 GHz are about 250 MHz (9.5%) and 400 MHz (15.2%), respectively. The difference between simulation and measured bandwidths at the fundamental frequency in Figure 9(a) is due to power leakage from the used SMA connector and to the loss of energy to the surface waves.

As seen from Figures 8(a) and 9(a), the reflection coefficient between 4 and 10 GHz, especially near 7.8 GHz is about zero with a maximum ripple of 2.4 dB. Thus, the third harmonic is well suppressed up to 23 dB in RDGS and 22 dB in CDGS. In addition, it is observed from Figure 8(b) that the first mode ($53 \Omega + j5 \Omega$) of the RDGS antenna is matched while the second ($2 \Omega + j8 \Omega$) and third ($1 \Omega - j47 \Omega$) modes are suitably suppressed. Similarly, as shown in Figure 9(b), the first mode ($52 \Omega - j8 \Omega$) of the CDGS antenna is also matched while the second ($1 \Omega - j22 \Omega$) and third ($3.5 \Omega + j27 \Omega$) modes are suppressed, acceptably.

According to the results, the proposed slot antennas having a simple structure and low design complexity are suitable choices for harmonic degradation. The photographs of the two realized RDGS and CDGS wide slot antennas are illustrated in Figure 10. As an example, the constructed prototype of RDGS slot antenna was measured in an

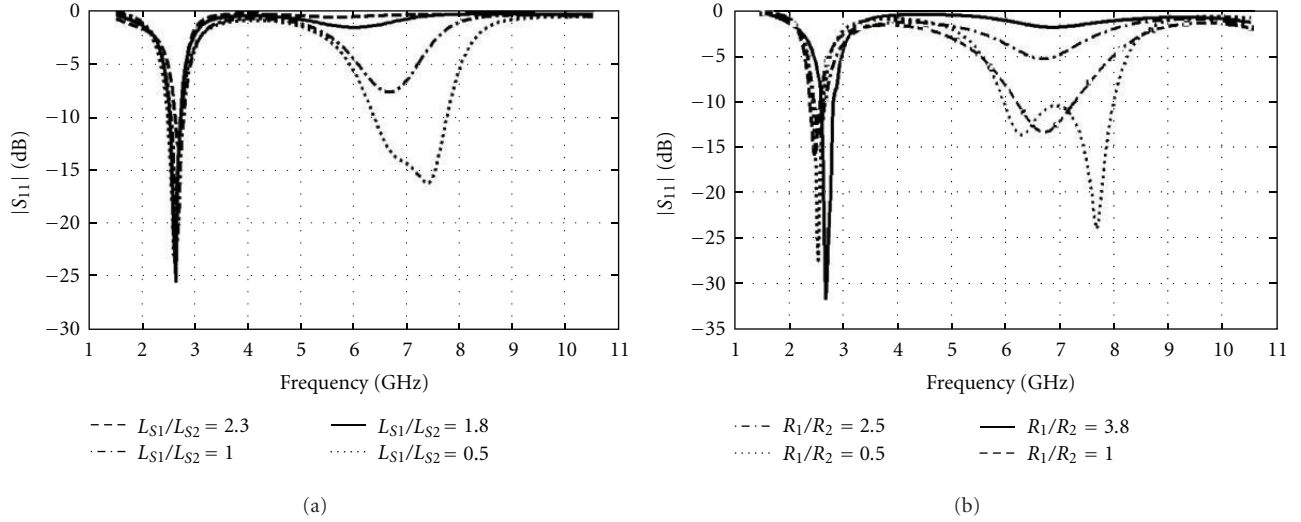


FIGURE 7: Simulated reflection coefficients of (a) RDGS slot antenna versus ratios of L_{S1}/L_{S2} and (b) CDGS slot antenna versus ratios of R_1/R_2 . The other parameters are constant and seen in Figure 1.

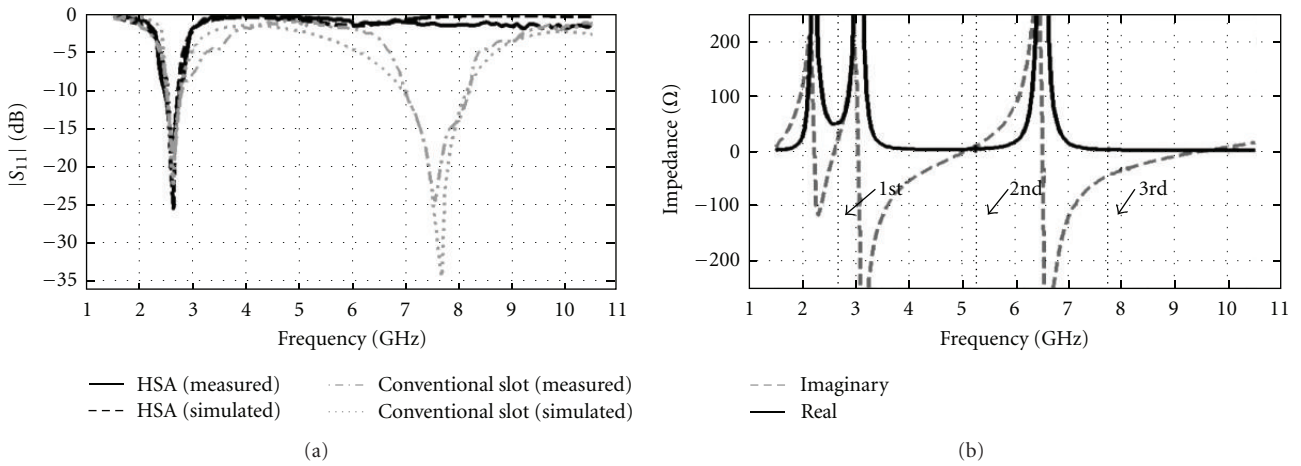


FIGURE 8: (a) Reflection coefficients of the RDGS slot antenna and (b) measured input impedance of the RDGS slot antenna.

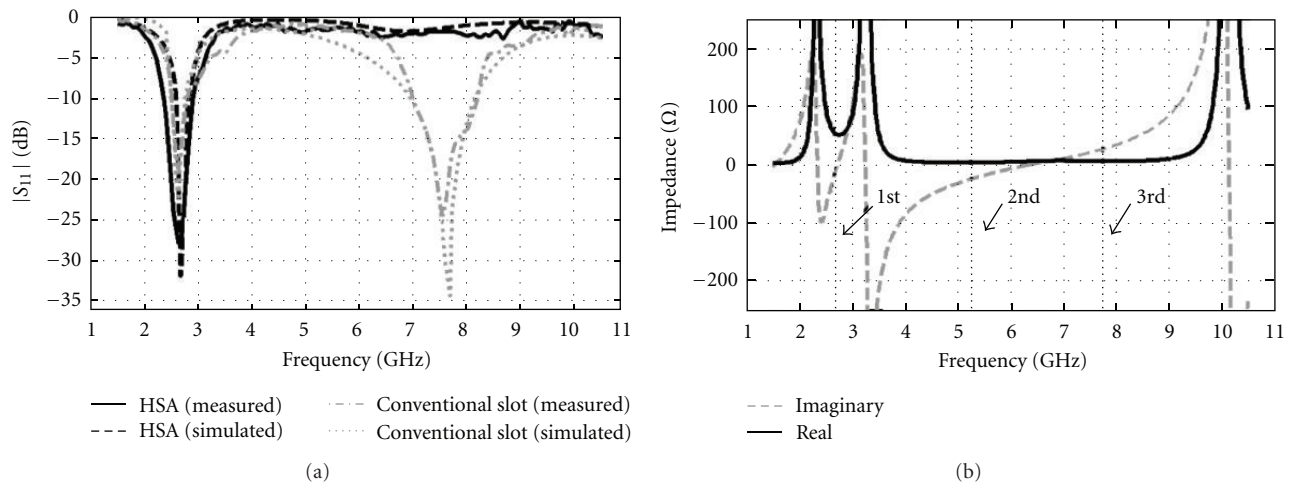


FIGURE 9: (a) Reflection coefficients of the CDGS slot antenna and (b) measured input impedance of the CDGS slot antenna.

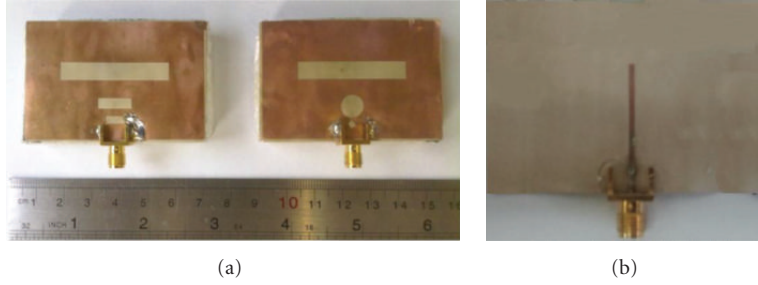


FIGURE 10: Photographs of the fabricated RDGS and CDGS wide slot antennas: (a) back and (b) front.

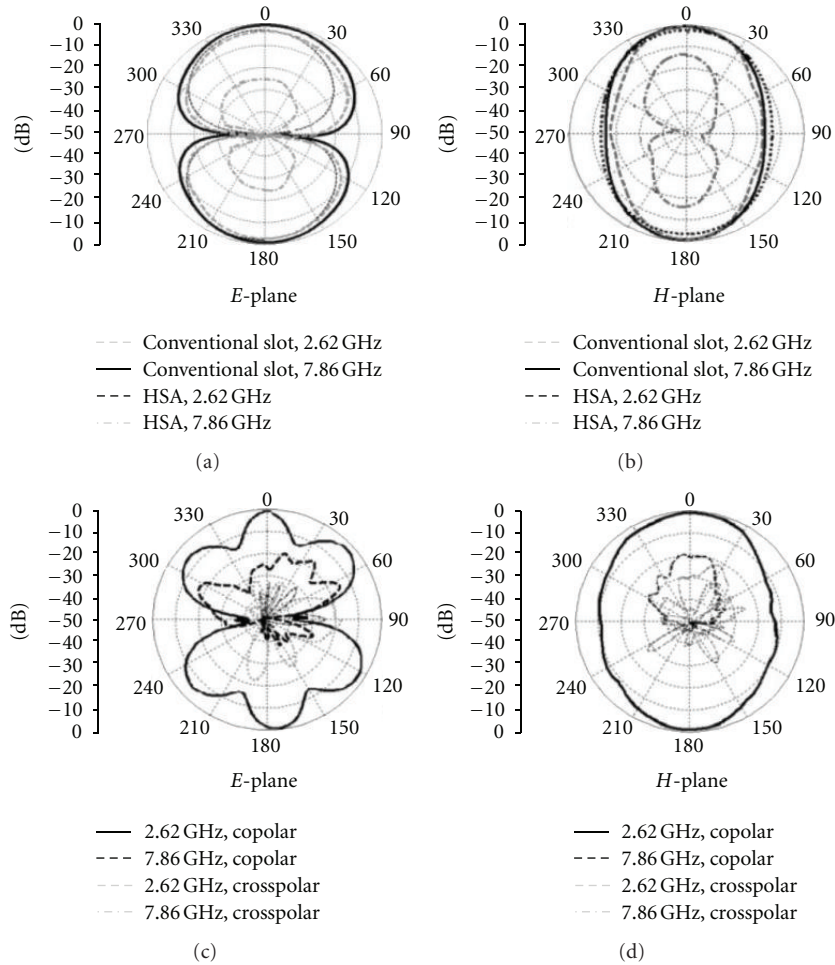


FIGURE 11: Simulated radiation patterns of both RDGS slot antenna and conventional slot antenna: (a) E-plane and (b) H-plane as well as measured patterns of only RDGS antenna: (c) E-plane and (d) H-plane.

anechoic chamber for studying and comparison of the radiation characteristics.

Figure 11 shows the measured and simulated radiation patterns of the both RDGS and conventional slot antennas at the fundamental and third harmonic frequencies. The patterns are omnidirectional in the H-plane and bidirectional in the E-plane as in a center-fed slot antenna. As seen in Figures 11(a) and 11(c), for the normalized peak power of the fundamental frequency, the simulated and measured E-plane radiation patterns of the proposed RDGS slot antenna

at the third harmonic of 7.86 GHz in the broadside direction are less than -25 and -27 dB, respectively. Similarly, Figures 11(b) and 11(d) also show that the simulated and measured H-plane patterns of the RDGS slot antenna at the third harmonic frequency are less than -17 and -20 dB, respectively. These results show that the radiation patterns at the harmonic frequency are acceptably suppressed. Moreover, the measured maximum gains of the proposed RDGS slot antenna at 2.62 and 7.86 GHz are 2.8 and 0.8 dBi, respectively, while the same values for the conventional

antenna are 3 and 7.9 dBi, respectively. It should be noticed that the 3D radiation patterns at the fundamental frequency in conventional and harmonic suppression antennas are nearly similar to each other with a stable shape which means two proposed filtering slots have not been destructed by the performance of the main radiating slot at 2.62 GHz.

4. Conclusion

In this paper, two microstrip slot antennas using rectangular and circular defected ground structures (DGSs) with harmonic suppression characteristic over harmonic frequency band have been proposed and investigated. The reflection coefficients were less than -2.4 dB at the second and third harmonic frequencies compared to those of the conventional slot antenna. The measured and simulated radiation patterns in the HSAs indicate at least 17 dB suppression at the third harmonic frequency. According to the measured results, these antennas with the simple harmonic suppression structures are quite effective for harmonic suppression. Therefore, the proposed antennas can be suitable for active integrated antennas.

Acknowledgment

The authors thank the Iran's Telecommunication Educational Research Center (ITERC) for its financial support.

References

- [1] V. Radisic, Y. Qian, and T. Itoh, "Novel architectures for high-efficiency amplifiers for wireless applications," *IEEE Transactions on Microwave Theory and Techniques*, vol. 46, no. 11, pp. 1901–1909, 1998.
- [2] V. Radisic, Y. Qian, and T. Itoh, "Broadband power amplifier integrated with slot antenna and novel harmonic tuning structure," in *Proceedings of the IEEE MTT-S International Microwave Symposium*, vol. 3, pp. 1895–1898, June 1998.
- [3] Y. Horii and M. Tsutsumi, "Harmonic control by photonic bandgap on microstrip patch antenna," *IEEE Microwave and Wireless Components Letters*, vol. 9, no. 1, pp. 13–15, 1999.
- [4] Y. J. Sung, M. Kim, and Y. S. Kim, "Harmonics reduction with defected ground structure for a microstrip patch antenna," *IEEE Antennas and Wireless Propagation Letters*, vol. 2, pp. 111–113, 2003.
- [5] Y. J. Sung and Y. S. Kim, "An improved design of microstrip patch antennas using photonic bandgap structure," *IEEE Transactions on Antennas and Propagation*, vol. 53, no. 5, pp. 1799–1804, 2005.
- [6] N. A. Nguyen, R. Ahmad, Y. T. Im, Y. S. Shin, and S. O. Park, "A T-shaped wide-slot harmonic suppression antenna," *IEEE Antennas and Wireless Propagation Letters*, vol. 6, pp. 647–650, 2007.
- [7] H. Kim and Y. J. Yoon, "Microstrip-fed slot antennas with suppressed harmonics," *IEEE Transactions on Antennas and Propagation*, vol. 53, no. 9, pp. 2809–2817, 2005.
- [8] M. S. Ghaffarian and G. Moradi, "A novel harmonic suppressed coplanar waveguide (CPW)-fed slot antenna," *IEEE Antennas and Wireless Propagation Letters*, vol. 10, Article ID 5959181, pp. 788–791, 2011.
- [9] N. C. Karmakar, S. M. Roy, and I. Balbin, "Quasi-static modeling of defected ground structure," *IEEE Transactions on Microwave Theory and Techniques*, vol. 54, no. 5, pp. 2160–2168, 2006.
- [10] M. S. Joung, J. S. Park, and H. S. Kim, "A novel modeling method for defected ground structure using adaptive frequency sampling and its application to microwave oscillator design," *IEEE Transactions on Magnetics*, vol. 41, no. 5, pp. 1656–1659, 2005.
- [11] H. G. Akhavan and D. Mirshekar-Syahkal, "Approximate model for microstrip fed slot antennas," *Electronics Letters*, vol. 30, no. 23, pp. 1902–1903, 1994.

Research Article

Hybrid Dielectric Resonator Antenna Composed of High-Permittivity Dielectric Resonator for Wireless Communications in WLAN and WiMAX

Yih-Chien Chen

Department of Electrical Engineering, Lunghwa University of Science and Technology, Shiang, Taoyuan County, 33306 Gueishan, Taiwan

Correspondence should be addressed to Yih-Chien Chen, ycchenncku@yahoo.com.tw

Received 26 January 2012; Accepted 22 May 2012

Academic Editor: Dalia N. Elshiekh

Copyright © 2012 Yih-Chien Chen. This is an open access article distributed under the Creative Commons Attribution License, which permits unrestricted use, distribution, and reproduction in any medium, provided the original work is properly cited.

The hybrid dielectric resonator antenna consisted of a cylindrical high-permittivity dielectric resonator, a rectangular slot, and two-rectangular patches were implemented. The hybrid dielectric resonator antenna had three resonant frequencies. The lower, middle, and higher resonant frequencies were associated with the rectangular slot, rectangular patches, and dielectric resonator, respectively. Parametric investigation was carried out using simulation software. The proposed hybrid dielectric resonator antenna had good agreement between the simulation results and the measurement results. The hybrid dielectric resonator antenna was implemented successfully for application in 2.4/5.2/5.8 GHz of WLAN and 2.5/3.5/5.5 GHz of WiMAX simultaneously.

1. Introduction

Many commercial applications, including mobile radio and wireless communications, use microstrip antennas. However, these microstrip antennas have a limited range of sizes, bandwidth, and efficiency. On the other hand, dielectric resonator (DR) antenna is attractive due to its small-size, high-radiation efficient, and ease of excitation [1, 2]. Many investigations of DR antenna composed of DR with relatively small permittivity around 10 have examined to enhance radiation capability [3–5]. Many works have focused on using DR with high-permittivity to promote device miniaturization when DR antenna operated at low frequency. However, these antennas composed of high-permittivity DR had a small bandwidth [6].

The use of dual band antennas in WLAN (wireless local area network) has been increasing rapidly in the last decade. Dual band antennas applied in ISM (Industrial, Scientific, Medical, 2.4–2.484 GHz) in low band of WLAN. At the same time, dual band antennas also applied in

high band of WLAN, including HIPERLAN (high-performance radio local area network, 5.15–5.35 GHz), and UNII (unlicensed national information infrastructure, 5.725–5.825 GHz). Dual band DR antennas were implemented by placing a parasitic element near the radiation part [7], or stacking many DR [8]. On the other hand, associating with the rapid development of WiMAX (worldwide interoperability for microwave access, 2.5–2.69, 3.3–3.8, and 5.25–5.85 GHz), there is an increasing demand for antennas suitable for WLAN/WiMAX simultaneously. In this paper, the hybrid DR antenna, consisting of a cylindrical high-permittivity dielectric resonator, a rectangular slot, and two-rectangular patches, operated in the ISM, HIPERLAN, UNII, and WiMAX bands simultaneously. Multiband hybrid DR antenna was implemented. However, the volume of hybrid DR antenna did not increase. The radiating resonators in the hybrid DR antenna were assembled tightly and resonated at three frequencies. The characteristics of hybrid DR antenna, such as return loss, radiation pattern, and gain were measured and discussed.

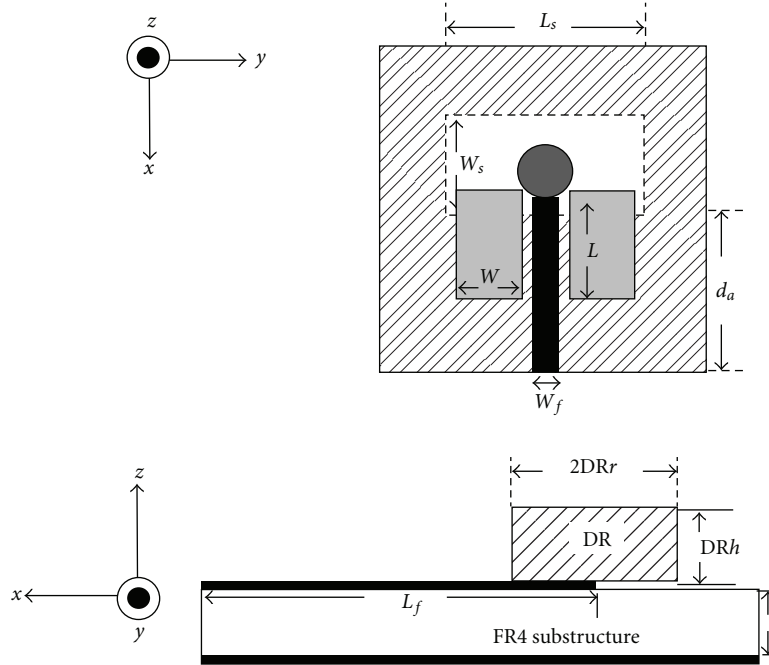


FIGURE 1: Configuration of hybrid DR antenna consisted of a rectangular slot, a cylindrical high-permittivity DR, and two-rectangular parasitic patches.

2. Design and Measurement

The resonant frequency of the cylindrical DR antenna excited at the dominant TM_{110} mode is [1]

$$f_{110}^{TM} = \frac{c}{2\pi r \sqrt{\epsilon_{ra}}} \sqrt{X_{11}'^2 + \left(\frac{\pi r}{2h}\right)^2}, \quad (1)$$

where $X_{11}' = 1.841$ is the first zero of the equation $J_1'(x) = 0$, and c is the speed of light in a vacuum. The parameters of r , h , and ϵ_{ra} is the radius, height, and permittivity of the DR, respectively. Figure 1 shows the configuration of the proposed hybrid DR antenna, consisting of a rectangular slot, a cylindrical high-permittivity DR, and two-rectangular patches. The rectangular RF4 substrate had dimensions of $50.0 \times 50.0 \text{ mm}^2$ and thickness of 1.6 mm. The cylindrical DR was fed with microstrip line. The microstrip feed line was placed below the centerline (x -axis in the figure) of the DR. Dimensions of the microstrip feed line on FR4 substrate was calculated by close-form formulas given in [9], assuming infinite ground plane and finite dielectric thickness. The microstrip feeding line had length L_f of 28.0 mm and width of W_f of 3.0 mm. The DR had a high-permittivity $\epsilon_{ra} = 25$, radius $r = 4.0 \text{ mm}$, and height $h = 3.0 \text{ mm}$. The DR was a low-loss ceramic system composed of $\text{La}(\text{MgSn})_{0.5}\text{O}_3$ and CaTiO_3 . The rectangular slot on the back side of the FR4 substrate fed with microstrip line, resonated at approximately half-guided wavelength, λ_{gs} , where λ_{gs} was the guided wavelength of the slot. The length of rectangular slot was 31 mm. Adjusted the length of the rectangular slot adjusted the lower resonant frequency. Adjusting the width of the rectangular slot enabled impedance matching. The bandwidth at lower resonant frequency could be adjusted by

adjusting the width of the rectangular slot. The rectangular patches were placed at the two sides of microstrip feed line. The electric field distributions along the top and bottom edges of the rectangular patches were in-phase, and hence these edges were referred to as radiating edges. The electric field distributions in the right and left edges of the rectangular patches were out of phase, and hence these edges were referred to as nonradiating edges (NREs) [10]. The rectangular patches were designed at a resonant frequency of 3.5 GHz. The lengths of the rectangular patches were designed to be $\lambda_{gp}/2$, where λ_{gp} was the guided wavelength of the rectangular patch [11]. The middle resonance frequency could be adjusted by adjusting the length of the rectangular patches. Impedance matching could be realized by adjusting the width of the rectangular patch. Therefore, the bandwidth at middle frequency could be adjusted by adjusting the width of the rectangular patch. In simulation, the conducting grounds and the substrates were assumed to be finite in transverse plane. Reflection coefficient was measured on a PNA-L network analyzer (N5230A). Radiation patterns were measured in a chamber. A standard-double-ridged horn antenna was used as a transmitting antenna. The hybrid DR antenna was mounted on a position which was controlled by a computer.

3. Parametric Study

Figures 2 and 3 show the simulation return loss of the hybrid DR antenna with different DR height and DR permittivity, respectively. From the results, the upper resonant frequency decreased from 5.70 to 5.55 GHz as DR height increased from 2 to 4 mm. This phenomenon can be explained by

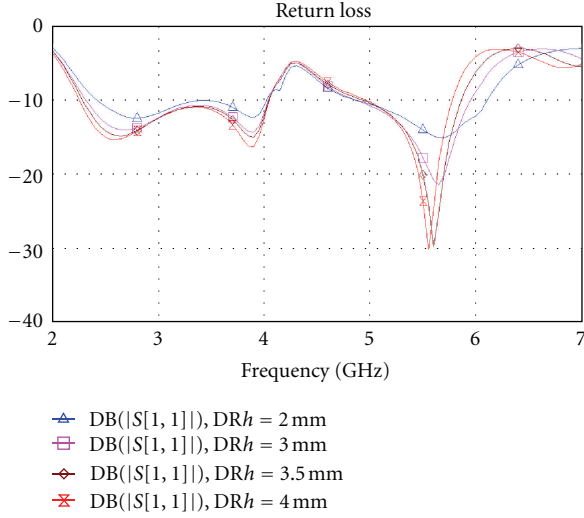


FIGURE 2: Simulation return loss of hybrid DR antenna with different DR height.

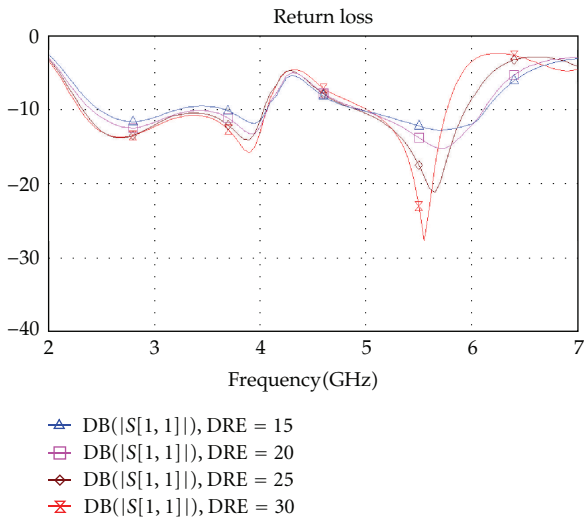


FIGURE 3: Simulation return loss of hybrid DR antenna with different DR permittivity.

using (1). The larger the DR height enabled the lower the resonant frequency of DR antenna. The upper resonant frequency decreased from 5.74 to 5.55 GHz as DR permittivity increased from 15 to 30. As shown in (1), the larger the DR permittivity enabled the lower the resonant frequency of DR antenna. The upper resonant frequency of hybrid DR antenna was demonstrated to be dominated by the DR parameters. The middle resonant frequency nearly unchanged as DR parameters varied. Additionally, the lower resonant frequency was slightly affected by the DR parameters. The variation in low resonant frequency may have been caused by the resonant length of rectangular slot was approximately half-guided wavelength. A higher the DR height and a larger the DR permittivity, is associated with a

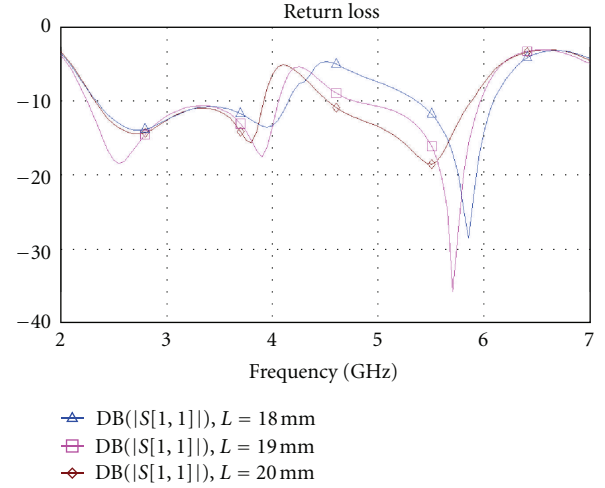


FIGURE 4: Simulation return loss of hybrid antenna with different rectangular patch length.

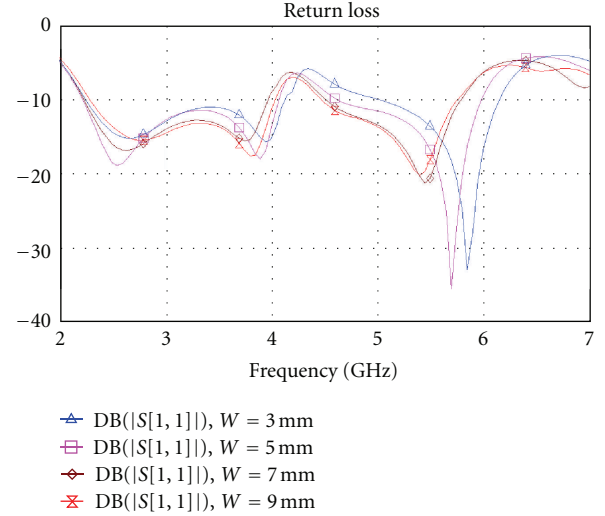


FIGURE 5: Simulation return loss of hybrid DR antenna with different rectangular patch width.

larger effective permittivity and, therefore, a lower resonant frequency.

Figures 4 and 5 show the simulation return loss of the hybrid antenna with different length and width of rectangular patch, respectively. The middle resonant frequency decreased from 3.95 to 3.80 GHz as the length of rectangular patch increased from 18 to 20 mm. Since the resonant length of rectangular patch was half-guided wavelength, the longer the length of rectangular patch enabled the lower the resonant frequency. The influence of the width of rectangular patch on the middle resonant frequency was not evident compared with that of the influence of the length of rectangular patch. The higher resonant frequency decreased as the rectangular patch length and width increased. By increasing the rectangular patch length and width, the effective permittivity of the hybrid DR antenna increased.

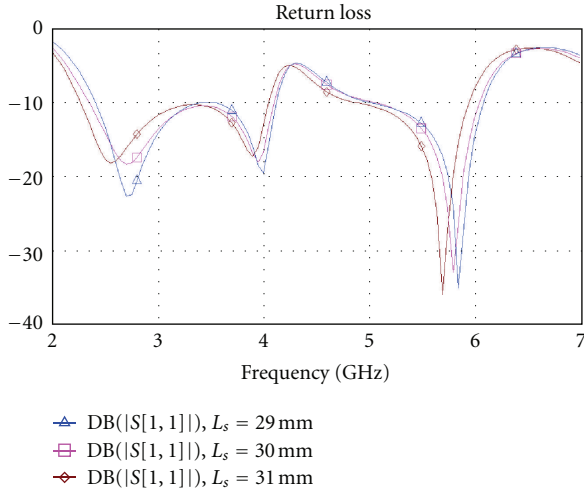


FIGURE 6: Simulation return loss of hybrid DR antenna with different rectangular slot length.

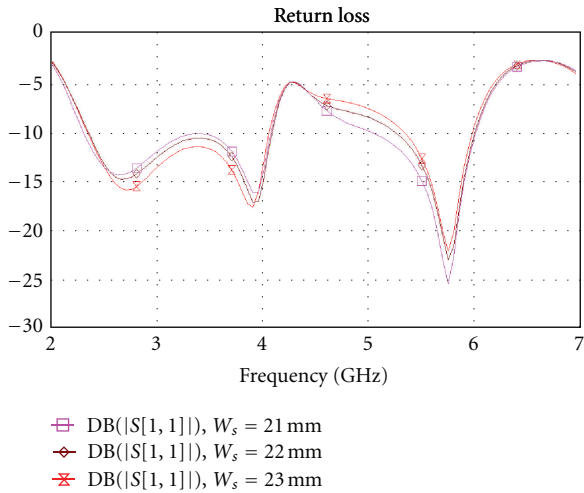


FIGURE 7: Simulation return loss of hybrid DR antenna with different rectangular slot width.

This led to reduce the resonant frequency of the DR antenna.

Figures 6 and 7 present the simulation return loss of the hybrid DR antenna with different length and width of rectangular slot, respectively. The lower resonant frequency decreased from 2.70 to 2.55 GHz as the length of rectangular slot increased from 29 to 31 mm. This was because of the resonant length of rectangular slot was half-guided wavelength. The longer the length of rectangular slot enabled the lower the resonant frequency. The higher resonant frequency of the hybrid DR antenna decreased slightly as the length of rectangular slot increased. This was associated with the effective height of DR increased as the length of rectangular slot increased. The influence of the width of rectangular slot on the resonant frequency was slight. The return loss reduced in the lower and middle resonant

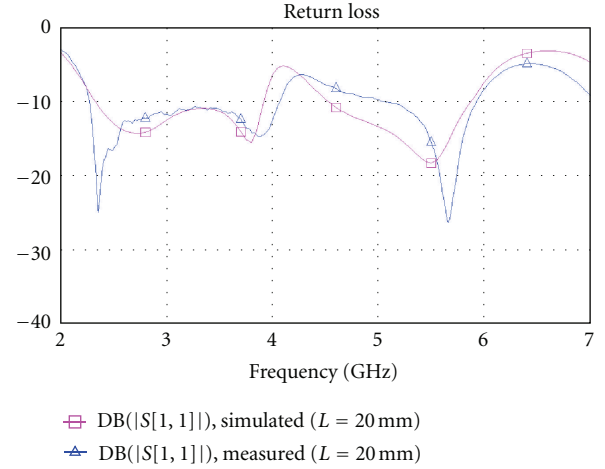


FIGURE 8: Measurement and simulation return loss of hybrid DR antenna.

frequencies as the width of rectangular slot increased. On the contrary, the return loss increased in the higher band as the width of rectangular slot increased.

4. Results and Discussion

Figure 8 shows the measurement and simulation return loss of the hybrid DR antenna. The measurement resonant frequency was close to the simulation resonant frequency. The lower, middle, and higher resonant frequencies were associated with the rectangular slot, the rectangular patches, and DR, respectively. The return losses were -25 , -15 , and -27 dB at 2.36, 3.88, and 5.66 GHz, respectively. There was a 10 dB return loss bandwidth of 1789 MHz (2273–4062 MHz) and 791 MHz (5127–5918 MHz). Alternatively, the antenna had a 10 dB S_{11} bandwidth of 56% and 14%, which covered the required bandwidth 2400–2484 MHz, 2500–2690 MHz, 3300–3800 MHz, 5150–5350 MHz, 5250–5850 MHz, and 5725–5825 MHz, simultaneously. The bandwidth was enough for many practical applications. The bandwidth at the higher resonant frequency, associating with the cylindrical DR with high-permittivity, was larger than the typical value of 6 ~ 12% of conventional DR antenna using DR with permittivity around 10 [2–5].

Figure 9 displays the radiation patterns of the hybrid DR antenna in the xz -plane and yz -plane at resonant frequencies of 2.36 GHz, 3.88 GHz, and 5.66 GHz. The radiation patterns were stable across the return loss ≤ 10 dB bands. The radiation patterns were almost omnidirectional in the xz -plane at resonant frequencies of 2.36 and 3.88 GHz. The radiation patterns in the yz -plane at resonant frequencies of 2.36 GHz, 3.88 GHz, and 5.66 GHz were symmetrical about the broadside direction and rolled-off as the elevation angle increased from broadside until about 90° . The cross-polarized patterns were about 15 dB less than the co-polarized patterns in the broadside direction ($\theta = 0^\circ$) at 2.36 and 3.88 GHz. Radiation patterns at 2.36 GHz and 3.88 GHz were similar to conventional rectangular slot

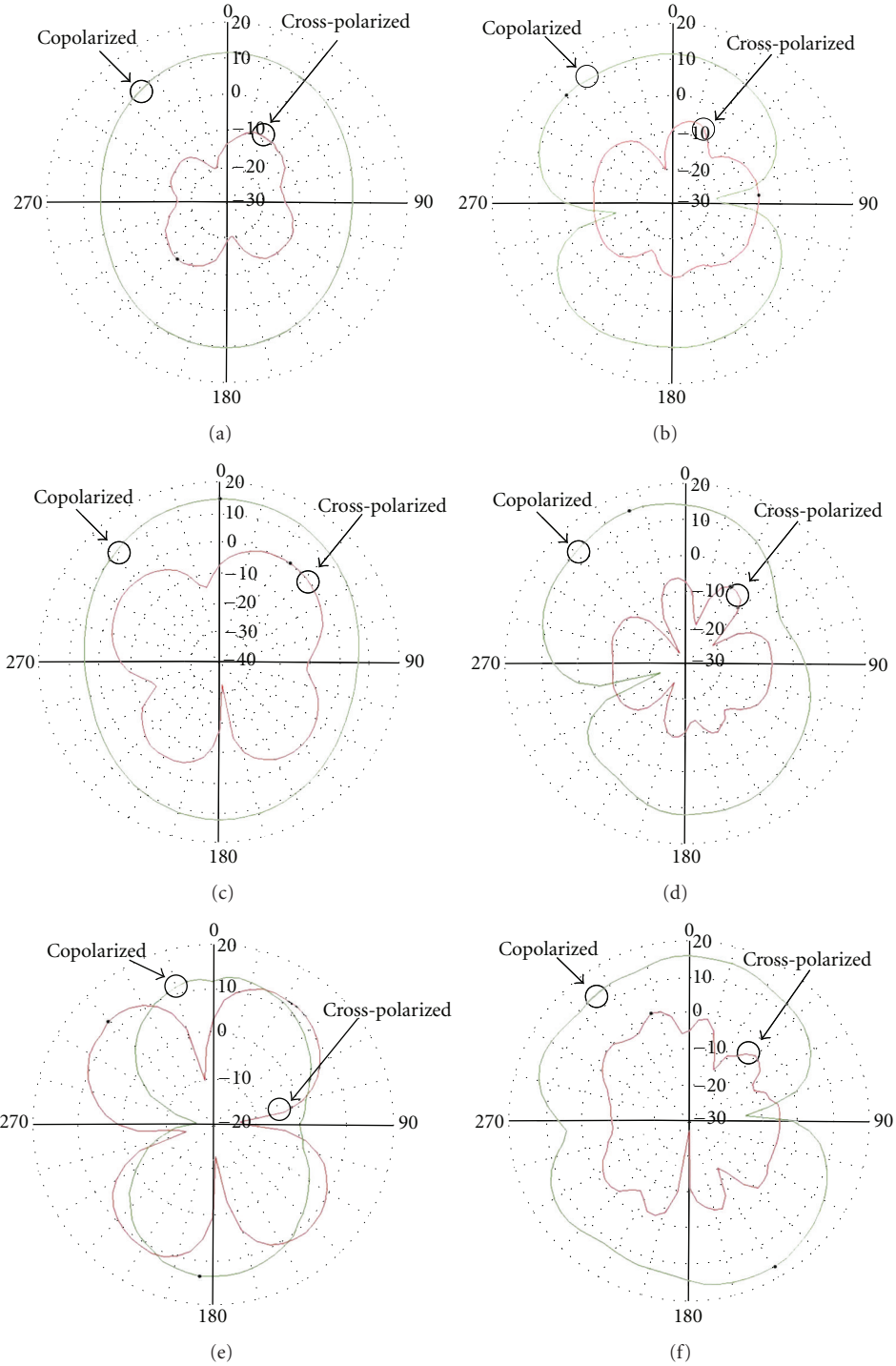


FIGURE 9: Radiation patterns of hybrid DR antenna at resonant frequency of (a) 2.36 GHz in the xz -plane, (b) 2.36 GHz in the yz -plane (c) 3.88 GHz in the xz -plane, (d) 3.88 GHz in the yz -plane, (e) 5.66 GHz in the xz -plane, and (f) 5.66 GHz in the yz -plane.

antenna and rectangular patch antenna, respectively. The radiation patterns at 5.66 GHz on the DR side were similar to those of the conventional DR antenna [12, 13], and the difference on the substrate side was associated with backlobe radiation from the slot. Large cross-polarization was observed at 5.66 GHz. However, large cross-polarization

became an advantage for practical applications. The wave propagated with multiple reflections between the transmitter and receiver in indoor applications.

Figures 10 and 11 display the gain of the proposed antenna for operating frequencies from 2.4 to 2.9 GHz and from 3.3 to 5.9 GHz, respectively. The peak gains were about

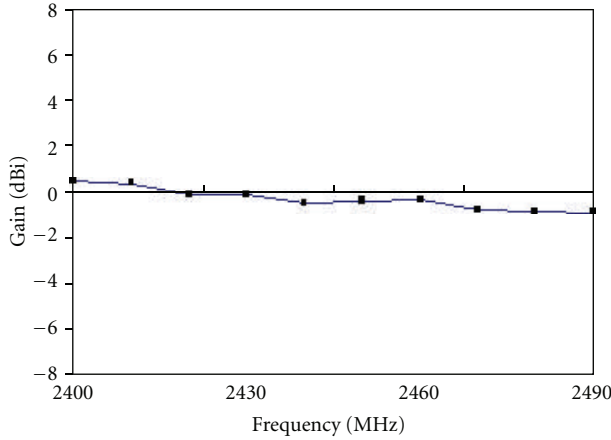


FIGURE 10: Measured gains of hybrid DR antenna for operating frequencies from 2.4 to 2.9 GHz.

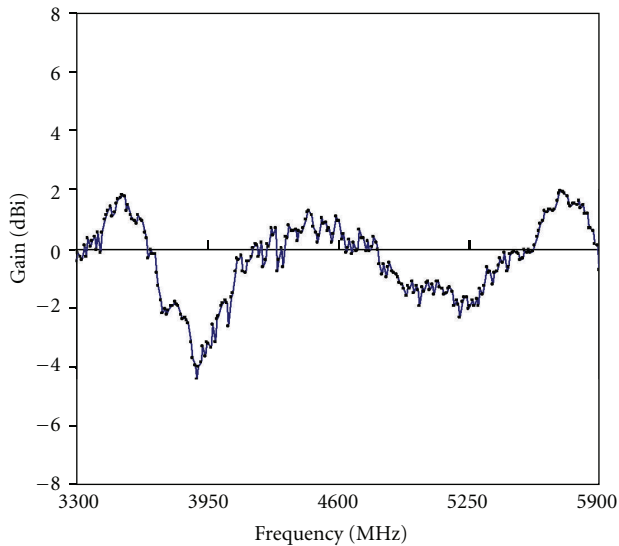


FIGURE 11: Measured gains of hybrid DR antenna gain for operating frequencies from 3.3 to 5.9 GHz.

0.5, -0.6, and 1.9 dBi in the ISM, HIPERLAN, and UNII bands, respectively. The gain variations were 1.4, 1.6, and 0.4 dBi for frequencies within the ISM, HIPERLAN, and UNII bands, respectively. The peak gains were about 1.9 and 2.0 dBi in the 3.5 and 5.5 GHz WiMAX bands, respectively. The gain variations were 4.0 and 3.9 dBi for frequencies within the 3.5 and 5.5 GHz WiMAX bands, respectively.

Acknowledgment

This work was supported by the National Science Council in Taiwan under Grant no NSC 100-2622-E-262-007-.

References

- [1] S. A. Long, M. W. McAllister, and L. C. Shen, "The resonant cylindrical dielectric cavity antenna," *IEEE Transactions on Antennas and Propagation*, vol. 31, no. 3, pp. 406–412, 1983.
- [2] R. K. Mongia, A. Ittibipoon, and M. Cuhaci, "Low profile dielectric resonator antennas using a very high permittivity material," *Electronics Letters*, vol. 30, no. 17, pp. 1362–1363, 1994.
- [3] R. A. Kranenburg, S. A. Long, and J. T. Williams, "Coplanar waveguide excitation of dielectric resonator antennas," *IEEE Transactions on Antennas and Propagation*, vol. 39, no. 1, pp. 119–122, 1991.
- [4] K. M. Luk, M. T. Lee, K. W. Leung, and E. K. N. Yung, "Technique for improving coupling between microstripline and dielectric resonator antenna," *Electronics Letters*, vol. 35, no. 5, pp. 357–358, 1999.
- [5] Y. X. Guo and K. M. Luk, "On improving coupling between a coplanar waveguide feed and a dielectric resonator antenna," *IEEE Transactions on Antennas and Propagation*, vol. 51, no. 8, pp. 2144–2146, 2003.
- [6] Y. C. Chen and K. H. Chen, "Low-profile dielectric resonator antenna with high-permittivity for application in WiMAX," *Microwave and Optical Technology Letters*, vol. 51, no. 7, pp. 1652–1654, 2009.
- [7] Y. N. Wang, Y. C. Chen, and K. H. Chen, "Dual band hybrid dielectric resonator antenna for application in ISM and UNII band," *IEICE Transactions on Communications*, vol. 93, no. 10, pp. 2662–2665, 2010.
- [8] L. H. Salman, D. Kajfez, and A. A. Kishk, "Dielectric resonator direction finding antenna," *International Journal of Antennas and Propagation*, vol. 2011, Article ID 184942, 7 pages, 2011.
- [9] G. P. Junker, A. A. Kishk, and A. W. Glisson, "Input impedance of aperture-coupled dielectric resonator antennas," *IEEE Transactions on Antennas and Propagation*, vol. 44, no. 5, pp. 600–607, 1996.
- [10] Y. C. Chen and Y. W. Zeng, "Double-layered coplanar patch antenna on CaLa4Ti5O17 high-permittivity substrate with coplanar waveguide feed line," *Microwave and Optical Technology Letters*, vol. 51, no. 1, pp. 98–100, 2009.
- [11] Y. C. Chen and J. M. Tsai, "Investigation on the use of high-permittivity substrate in stacked patch antenna fed by a coplanar waveguide," *Microwave and Optical Technology Letters*, vol. 51, no. 3, pp. 715–717, 2009.
- [12] M. S. Al Salameh, Y. M. M. Antar, and G. Séguin, "Coplanar-waveguide-fed slot-coupled rectangular dielectric resonator antenna," *IEEE Transactions on Antennas and Propagation*, vol. 50, no. 10, pp. 1415–1419, 2002.
- [13] K. W. Leung, K. M. Chow, and K. M. Luk, "Low-profile high-permittivity dielectric resonator antenna excited by a disk-loaded coaxial aperture," *IEEE Antennas and Wireless Propagation Letters*, vol. 2, no. 1, pp. 212–214, 2003.

Research Article

Design and Analysis of a Novel Compact Wideband Antenna with Two Excited Modes

Li Li, Zhi-Li Zhou, and Jing-Song Hong

Institute of Applied Physics, University of Electronic Science and Technology, Chengdu 610054, China

Correspondence should be addressed to Li Li, liliangirl@126.com

Received 23 December 2011; Accepted 25 June 2012

Academic Editor: Hala A. Elsadek

Copyright © 2012 Li Li et al. This is an open access article distributed under the Creative Commons Attribution License, which permits unrestricted use, distribution, and reproduction in any medium, provided the original work is properly cited.

A novel planar compact wideband antenna with coplanar waveguide (CPW) feeding configuration is presented in this paper. The proposed antenna is fed and coupled by the CPW feeding line at the same time. Therefore, two distinct excited modes are realized. Besides, detail investigation is presented as well to demonstrate the properties of the proposed antenna. Eventually, the prototype of the proposed antenna with optimal design is fabricated and tested. The proposed antenna, with a fairly compact size of $24\text{ mm} \times 18\text{ mm} \times 1\text{ mm}$, has a measured 10 dB impedance bandwidth spanning from 3.05 GHz to 6 GHz, about 65.2%. Moreover, stable radiation patterns over the operating band are obtained. Furthermore, time-domain characteristics of the proposed antenna are also investigated.

1. Introduction

The need of high data rates wireless communication becomes more and more urgent, and various solutions have been brought forward. Wideband antenna techniques have been paid the most attention for many advantages, such as higher data rates, immunity to multipath cancellation, increased communications operational security, and low interference to legacy systems [1]. The wideband antenna techniques will play an important role in the short-range wireless communication systems. One of the major challenges in the design of wideband antennas is how to achieve small size with desired electrical properties in the band of interest. On the other hand, planar wideband antennas have attracted much interest for applications due to their simple geometry and easier-to-integrate as well as good impedance properties. In the design of one planar wideband antenna, the shape of the antenna patch, the ground plane, and the feeding structure are of great importance. Different methods such as the truncated slot on the antenna patch or on the ground plane have been proposed for increasing the frequency range and improving the radiation pattern characteristics [2–5]. Many planar wideband antennas presented in [6–8] possess compact antenna size. However, as another important

transmission property, the time-domain characteristic of wideband antennas is investigated rarely.

This paper presents a compact wideband antenna with CPW feeding configuration. Because the antenna can be coupled and fed by CPW feeding line at the same time, two distinct excited modes were obtained. The proposed antenna demonstrated both a compact size and a wide impedance bandwidth. The size of the proposed antenna is only $24\text{ mm} \times 18\text{ mm}$, and the operating band is ranging from 3.05 GHz to 6 GHz. Details of the proposed antenna designs are presented. Measured results of the impedance bandwidth, the radiation patterns, and the simulated time-domain characteristics are given and discussed.

2. Antenna Design

Figure 1(a) shows the physical structure and dimensions of the proposed antenna. A pair of stepped structures and a coplanar waveguide feeding line are etched on the dielectric substrate (in this study, the FR4 substrate of thickness 1 mm and relative permittivity 4.4 was used). The length and the width of the dielectric substrate are 24 mm and 18 mm, respectively. The right stepped structure is directly connected to the CPW feeding line by a metal line, and the left stepped

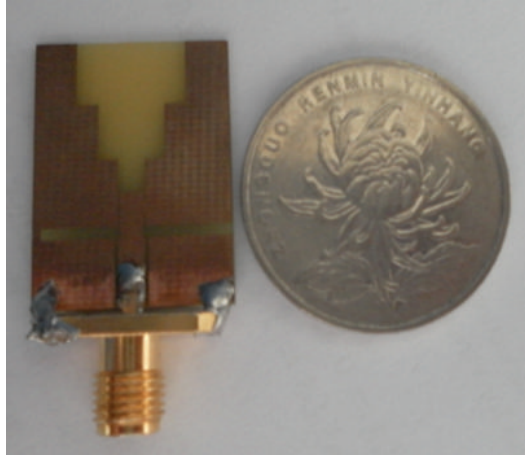
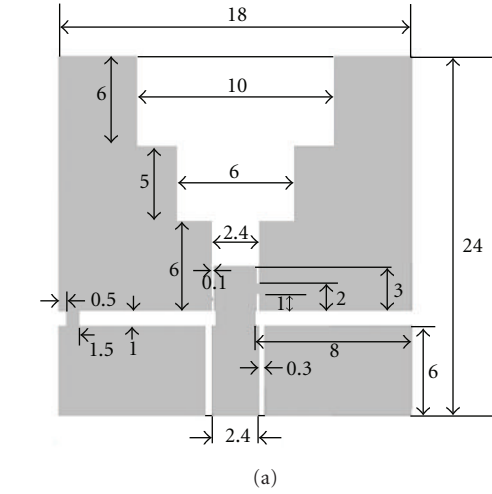


FIGURE 1: The configuration of the proposed antenna and photograph of prototype. (a) Configuration of the proposed antenna, (b) photograph of prototype.

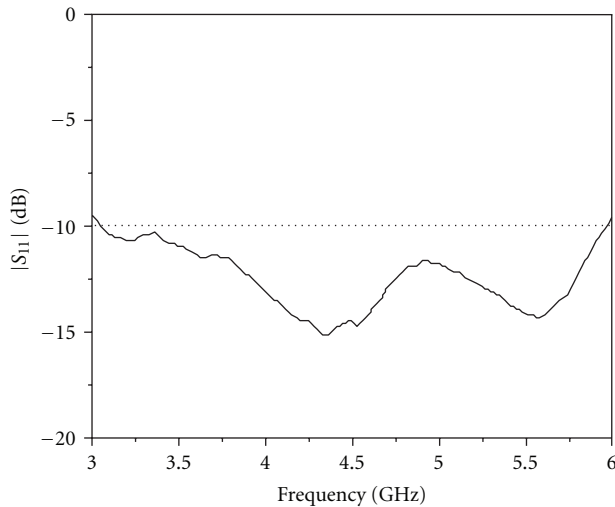


FIGURE 2: Measured reflection coefficient of the proposed antenna.

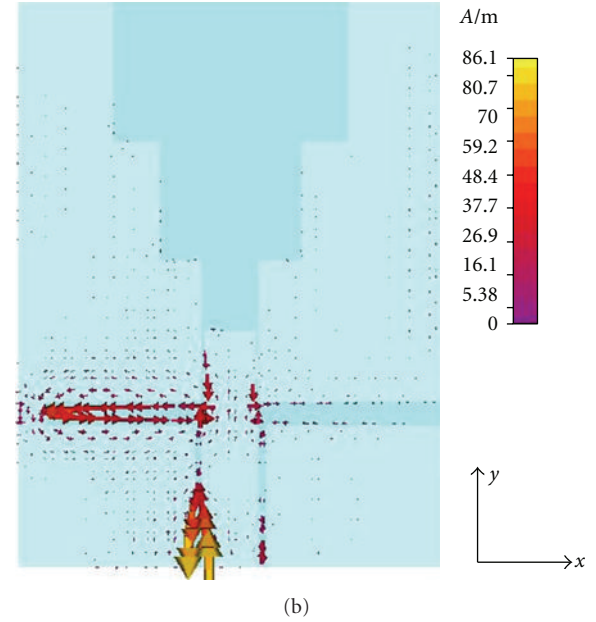
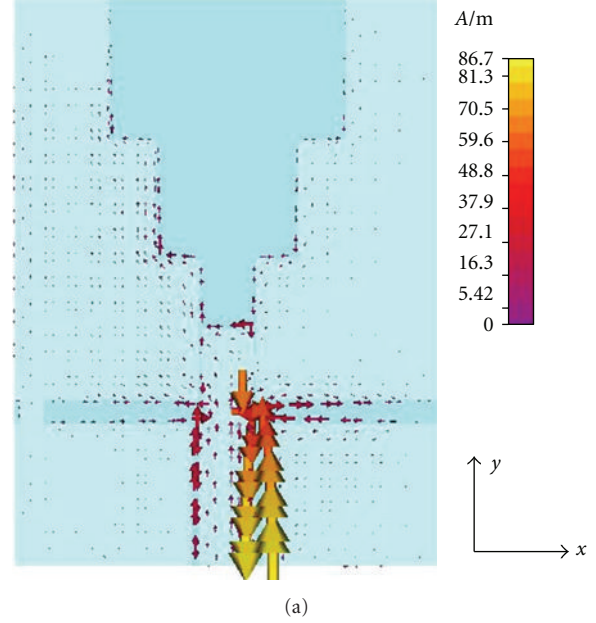


FIGURE 3: The current distributions of the proposed antenna (a) at 4.5 GHz (b) and 5.5 GHz.

structure links to the ground via the other metal line. As a result, the right stepped structure is directly fed by CPW, and the left stepped structure is coupled by the CPW feeding line.

3. Results and Discussion

The antenna prototype, as shown in Figure 1(b), was fabricated and tested. Figure 2 shows the measured reflection coefficient of the proposed antenna. It can be seen that the impedance bandwidth of the proposed antenna is from 3.05 GHz to 6 GHz, about 65.2%. The current distributions of the proposed antenna at 4.5 GHz and 5.5 GHz (simulated by CST) are illustrated in Figure 3. Because of the difference

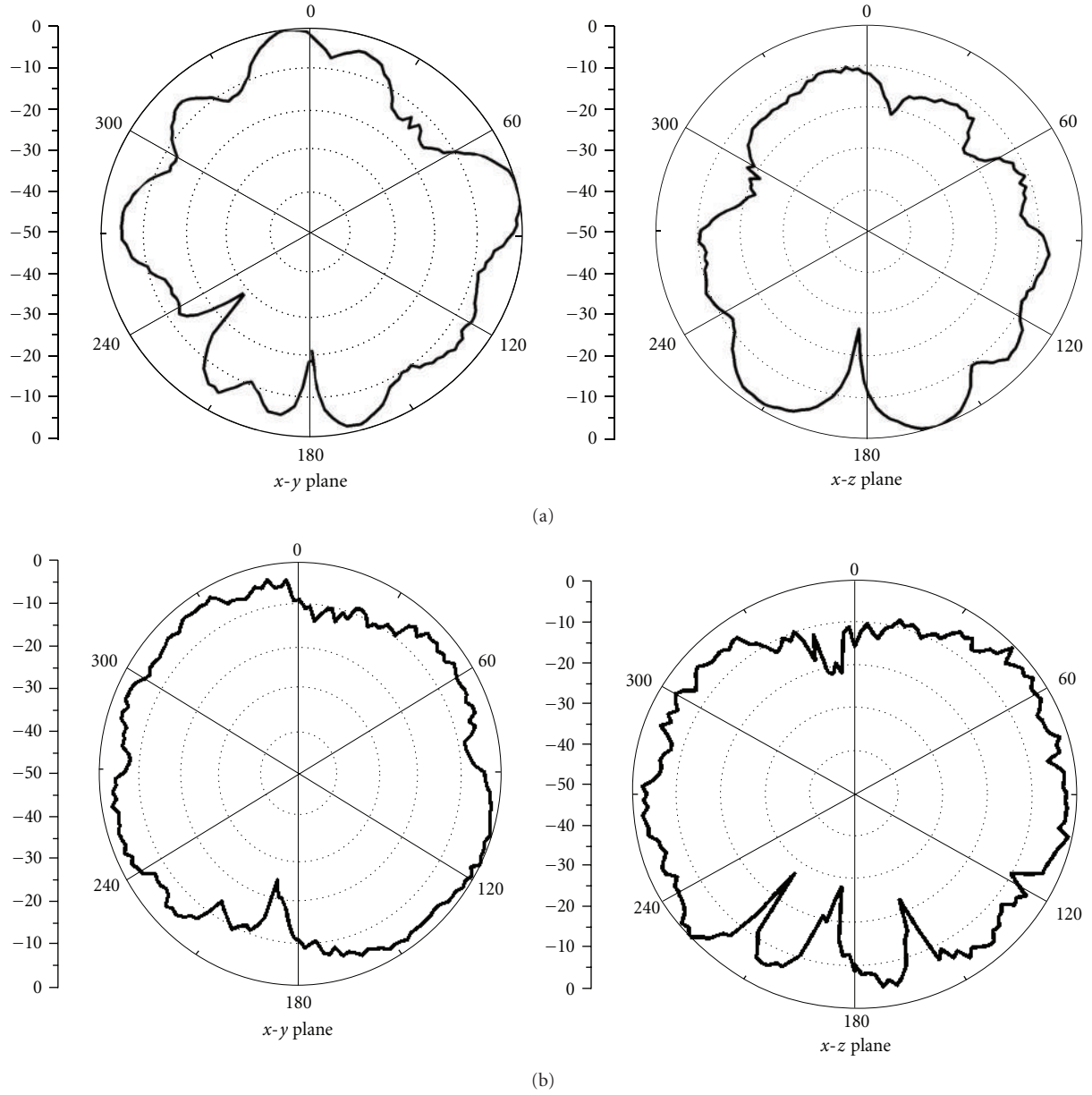


FIGURE 4: Measured radiation patterns of the proposed antenna (a) at 4.5 GHz (b) and 5.5 GHz.

of the excited methods between the left portion and the right portion of the proposed antenna, the current distributions at two frequencies are completely different. At 4.5 GHz, the current mainly distributes around the right portion and the stepped slot. However, the surface current of the proposed antenna appears mostly in the left portion at 5.5 GHz. The two excited modes can generate two resonant frequencies, and when they are close to enough, a wide bandwidth can be achieved.

Figure 4 shows the measured radiation patterns of the proposed antenna in the x - y and x - z plane for 4.5 GHz and 5.5 GHz. Clearly, the x - y plane radiation pattern is close to omnidirectional, and the x - z plane radiation pattern is monopole-like at 5.5 GHz. Meanwhile, similar radiation

patterns with only few limited distortions are observed at 4.5 GHz. Compared with at 5.5 GHz, when the antenna is mainly coupled by the CPW feeding line, the antenna is directly fed by the CPW feeding line basically at 4.5 GHz. Therefore, more energy is excited, and some extra currents distribute along the stair slots at 4.5 GHz, which leads to broadside radiation pattern.

Considering the requirements of UWB communications, both good frequency-domain and time-domain characteristics are essential to the quality of the communications. Thus, the time-domain characteristics of the proposed antennas are investigated by placing the virtual probes at a distance of 1 m from the antennas. We can assume that the probes are in the far-field region of the antenna, since the distance is more

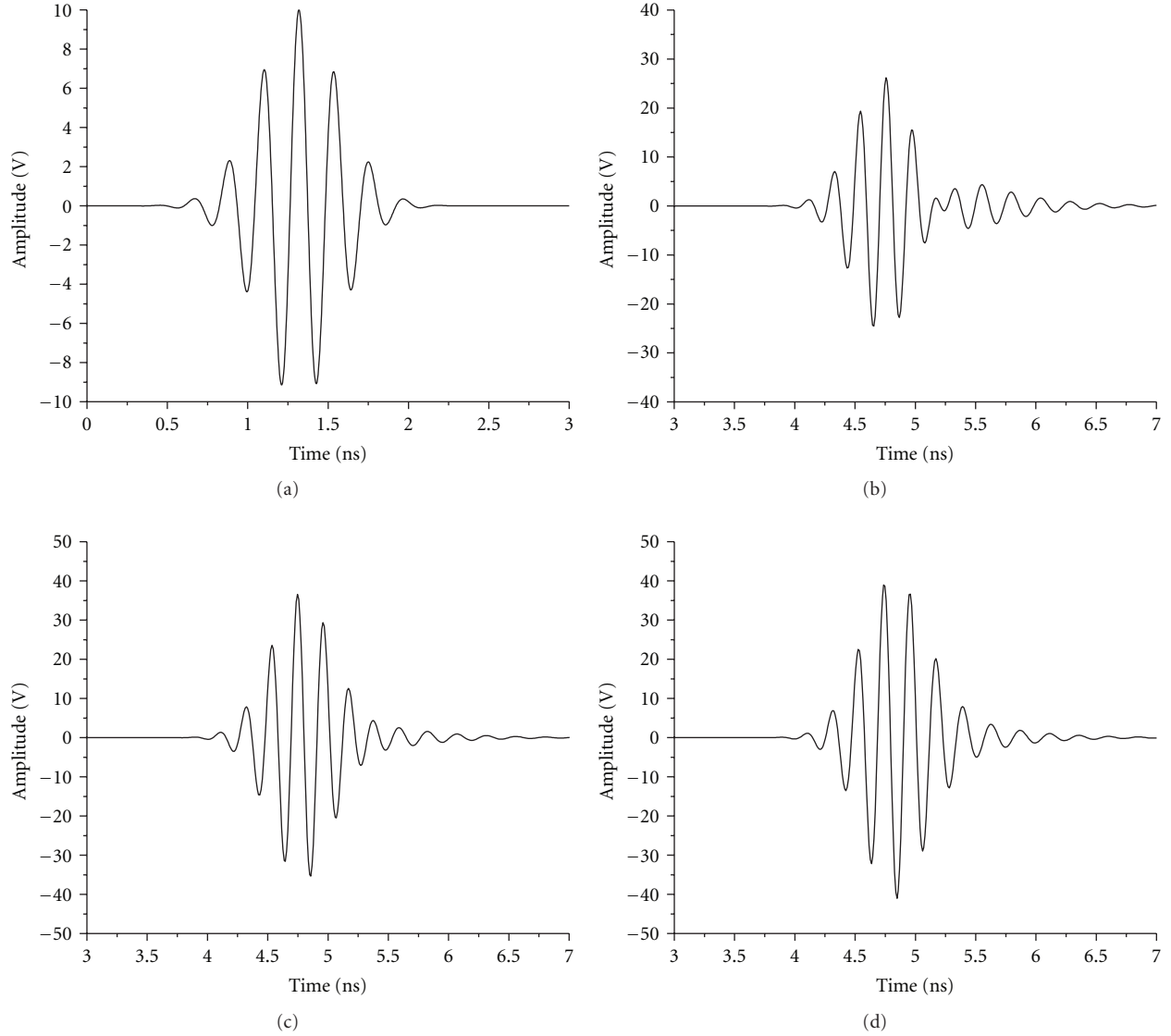


FIGURE 5: Transmitted signal and received signals of the antenna with different angles of ϕ , at $\theta = 90$ degree. (a) Transmitted signal, (b) received signal of the proposed antenna with angle $\phi = 240$ degree, (c) received signal of the proposed antenna with angle $\phi = 270$ degree, and (d) received signal of the proposed antenna with angle $\phi = 300$ degree.

than 10 wavelengths at the lowest frequency for the proposed antenna. The polarization of the probes is linear. Moreover, the copolarizations of the probes point to the copolarizations of the antennas. The whole time-domain test system operates over the frequency band ranging from 3 to 6 GHz. Figure 5 shows the transmitted signal and received signals of the proposed antenna with different angles. And considering the quasimnidirectional characteristic of the antenna and the space limitations, only three different angles are presented here. From the results, it can be seen that the received signals of the proposed antenna are similar to the transmitted signal with only few limited distortions introduced.

According to the definition in [9], the fidelity factor values of the proposed antenna with different angles of ϕ are calculated and listed in Table 1, from which it can be seen

TABLE 1: Fidelity factors of the antenna with different angles of ϕ at $\theta = 90$ degree.

Phi (degree)	Fidelity factor
240	0.9911
270	0.9945
300	0.9779

that the fidelity factor of the proposed antenna is very close to unity. However, slight tailing phenomenon of the received signal is still can be observed because of the dispersion of the antenna and the loaded slots. On the other hand, the levels of the tailing are different, since the direction of the proposed antenna is not strictly omnidirectional.

4. Conclusion

In this paper, a novel compact wideband antenna with two distinct excited modes is proposed and investigated. The measured impedance bandwidth of the proposed antenna is from 3.05 GHz to 6 GHz. Furthermore, the antenna also demonstrates a fairly compact size of $24\text{ mm} \times 18\text{ mm} \times 1\text{ mm}$. Good and stable radiation patterns are observed. Featuring of good frequency-domain characteristics and time-domain characteristics as well as easy design, the proposed wideband antenna is a very good candidate for short-range wireless communication.

Acknowledgments

This work was supported by the National Natural Science Foundation of China (no. 61172115 and no. 60872029), the High-Tech Research and Development Program of China (no. 2008AA01Z206), the Aeronautics Foundation of China (no. 20100180003), and the Fundamental Research Funds for the Central Universities (no. ZYGX 2009J037).

References

- [1] R. J. Fontana, "Recent system applications of short-pulse ultra-wideband (UWB) technology," *IEEE Transactions on Microwave Theory and Techniques*, vol. 52, no. 9 I, pp. 2087–2104, 2004.
- [2] X. Qu, S. S. Zhong, and W. Wang, "Study of the band-notch function for a UWB circular disc monopole antenna," *Microwave and Optical Technology Letters*, vol. 48, no. 8, pp. 1667–1670, 2006.
- [3] Y. J. Cho, K. H. Kim, D. H. Choi, S. S. Lee, and S. O. Park, "A miniature UWB planar monopole antenna with 5-GHz band-rejection filter and the time-domain characteristics," *IEEE Transactions on Antennas and Propagation*, vol. 54, no. 5, pp. 1453–1460, 2006.
- [4] M. Ojaroudi, C. Ghobadi, and J. Nourinia, "Small square monopole antenna with inverted T-shaped notch in the ground plane for UWB application," *IEEE Antennas and Wireless Propagation Letters*, vol. 8, pp. 728–731, 2009.
- [5] M. Ojaroudi, G. Kohneshahri, and J. Noory, "Small modified monopole antenna for UWB application," *IET Microwaves, Antennas and Propagation*, vol. 3, no. 5, pp. 863–869, 2009.
- [6] L. Y. Cai, G. Zeng, H. C. Yang, and X. W. Zhan, "Compact printed ultra-wideband antennas with band-notched characteristics," *Electronics Letters*, vol. 46, no. 12, pp. 817–819, 2010.
- [7] X. J. Liao, H. C. Yang, N. Han, and Y. Li, "Aperture UWB antenna with triple band-notched characteristics," *Electronics Letters*, vol. 47, no. 2, pp. 77–79, 2011.
- [8] L. Y. Cai, Y. Li, G. Zeng, and H. C. Yang, "Compact wideband antenna with double-fed structure having band-notched characteristics," *Electronics Letters*, vol. 46, no. 23, pp. 1534–1536, 2010.
- [9] D. H. Kwon, "Effect of antenna gain and group delay variations on pulse-preserving capabilities of ultrawideband antennas," *IEEE Transactions on Antennas and Propagation*, vol. 54, no. 8, pp. 2208–2215, 2006.

Research Article

A Novel Low RCS Design Method for X-Band Vivaldi Antenna

XiaoXiang He, Teng Chen, and Xin Wang

*College of Electronic and Information Engineering, Nanjing University of Aeronautics and Astronautics,
29 Yudao Street, Baixia District, Nanjing 210016, China*

Correspondence should be addressed to Teng Chen, ctdziwo@sina.com

Received 17 February 2012; Accepted 6 June 2012

Academic Editor: Dalia N. Elshiekh

Copyright © 2012 XiaoXiang He et al. This is an open access article distributed under the Creative Commons Attribution License, which permits unrestricted use, distribution, and reproduction in any medium, provided the original work is properly cited.

A novel low radar cross-section (RCS) design method is proposed, and its application on Vivaldi antenna that covers the entire X band is investigated. According to the difference of the current distribution on the radiator when the antenna radiates or scatters, the shape of the metal radiator is modified, so that maximally 19.2 dBsm RCS reduction is achieved which satisfied radiation performance. Simulated and measured results about gain, S_{11} , and RCS are presented. As a result, the effectiveness of the presented low RCS design method is validated.

1. Introduction

The nose cone of an aircraft is the most threatening area for radar detection, but the electromagnetic scattering of antenna array belongs to the fire control system in this area is usually very strong, which result in the importance of stealth design of antenna. Vivaldi antennas [1–3] are widely used in fire control system due to broad bandwidth and small physical dimension. Therefore, the stealth design of Vivaldi antenna is highly desirable in many prospective airborne applications.

Many methods [4–11] have been proposed to reduce the radar cross-section (RCS) of microstrip antennas. Usually, RCS reduction will increase the complexity of the antenna system or degrade the radiation performance of the antenna. Typical performance-degradation effects include gain decreasing, resonant frequency shifting, and bandwidth narrowing. Li and Liu [4, 5] proposed a stealth method with maximally 27 dBsm RCS reduction at a specific frequency with two short-circuit pins loaded on each microstrip unit and two H-shaped slots cut. However, the RCS reduction occurred only at a relatively narrow frequency band and angle range. Another effective method, investigated by Jang et al. [6, 7], uses the electromagnetic band gap (EBG) structure and achieves a 10 dBsm RCS reduction out of the working band while keeping the RCS within the operating band almost unchanged. The same effect can also be acquired with

frequency-selective surface (FSS) on radomes. Other methods [8–10] such as Fractal slots, defected ground structures (DGSs), or holly-leaf-shaped designs, also can reduce RCS in angle scope vertical to the antenna in the operating band, but all the methods are hard to be applied to Vivaldi antenna for its threatening direction is almost parallel to the antenna.

Several RCS reduction schemes have also been developed for Vivaldi antennas. Zhang et al. [11] introduced a phase-switched screen (PSS) boundary, which enables the dynamic control of RCS. Jiang fu et al. [12] investigated RCS a dual-index Vivaldi antenna which achieves a maximally of 25 dBsm RCS reduction, but the dispersion of the measured gain is decreased.

In this paper, we propose a novel low RCS design method that specifically applies to the X-band Vivaldi antenna. The design is based on the analysis of the antenna current distribution in the radiating and scattering status, respectively. Then we modify the configuration of the metal patch to achieve maximally 19.2 dBsm RCS reduction. Simulation and measurement results are provided to demonstrate the excellent radiation and stealth performance that are achieved with this design.

2. Stealth Design Scheme

A typical Vivaldi antenna [13–15] without any low RCS design is shown in Figure 1. The antenna is printed on the

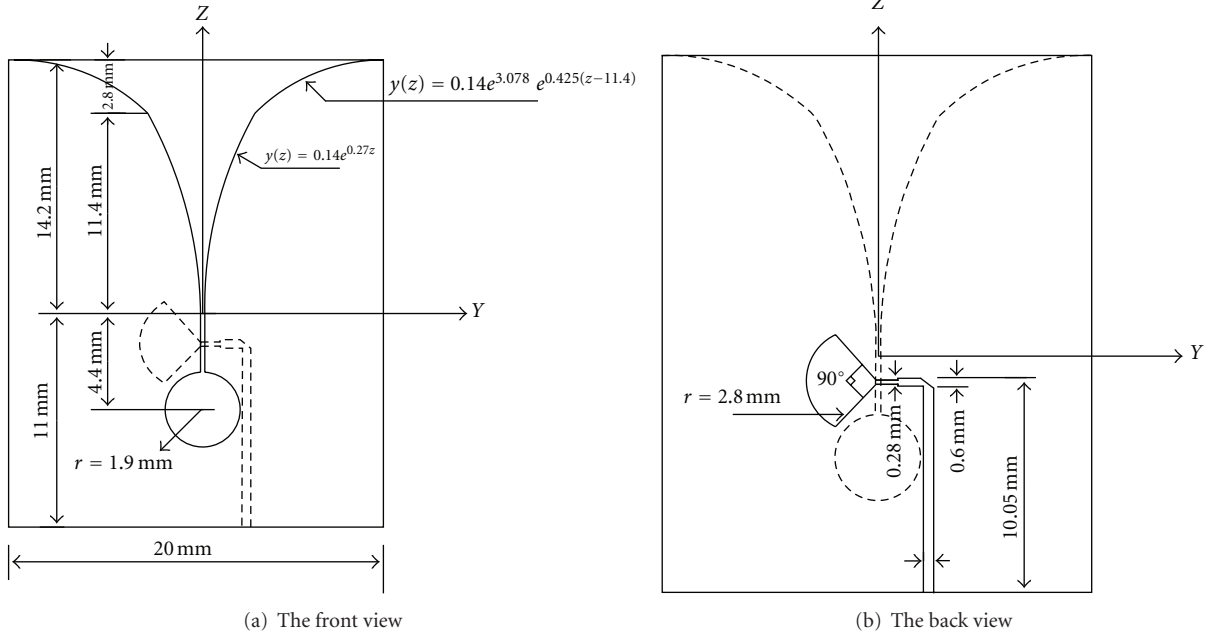


FIGURE 1: Structure of original Vivaldi antenna.

two sides of a TF-2 ($\epsilon_r = 10.2$) substrate with a thickness of 0.635 mm. On one side of the substrate is the metal patch consisting of a tapered slot line and a transmission line as illustrated by the solid lines of in Figure 1(a). On the other side, there is a feeding structure as illustrated by the solid lines of in Figure 1(b). For better illustration, dotted lines are employed in both views to indicate the position of the structures on the opposite side. The parameters marked in the figure are optimized with HFSS to match the feeding port to 50Ω . The photograph of the fabricated original antenna is shown in Figure 1(c). The measured and Generally speaking, the scattering of an antenna can be divided into two parts [16, 17]. One part is the so-called structural mode scattering that excludes the effect of the antenna's receiving channel.

This part of scattering is almost the same as the scattering of a common scatterer. The other part is the mode scattering that is caused by the reradiation of the reflected power from the receiving channel due to the impedance mismatching. Nevertheless, the mode scattering of a well-matched antenna is usually much smaller than the structural mode scattering. Take the Vivaldi antenna in Figure 1 as an example, the total RCS is about -33 dBsm at 10 GHz as simulated with HFSS while the mode scattering RCS is estimated to be about -75 dBsm [18] which is negligibly small. Therefore, in this paper, we mainly focus on the structural mode stealth design of the Vivaldi antenna.

The purpose of a stealth design is to decrease RCS of an antenna while maintaining the antenna's radiation

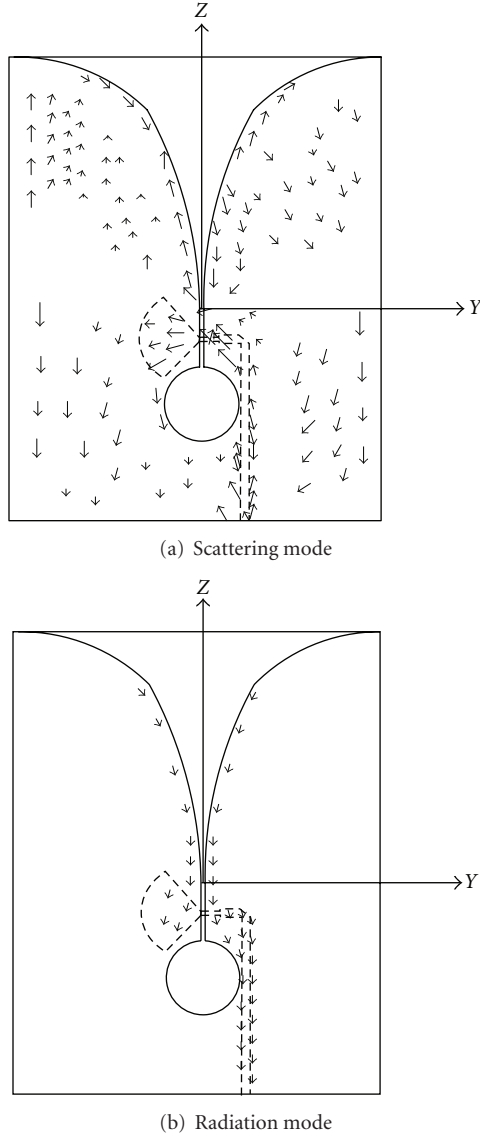


FIGURE 2: Current distribution of metal patch.

performance, which is usually conflict and should be balanced between scattering model and radiation model. In our stealth design method, the balance is well achieved by utilizing the difference between the current distributions of the antenna in the two modes. At 10 GHz, the induced current distribution due to scattering and radiation are shown in Figures 2(a) and 2(b), respectively. It can be seen from Figure 2(a) that the current distributes throughout the entire metal patch when the antenna is incident by a plane wave from $\theta^i = 0^\circ$ and $\phi^i = 0^\circ$. On the other hand, when the antenna is in the radiating mode, the current is mainly along the feeding structure and transmission line as is seen in Figure 2(b). Consequently, it can be found that there are large areas of the metal patch have no contribution to the radiation but play an important role in the scattering. The main idea of the stealth design is to, therefore, remove these metal areas in

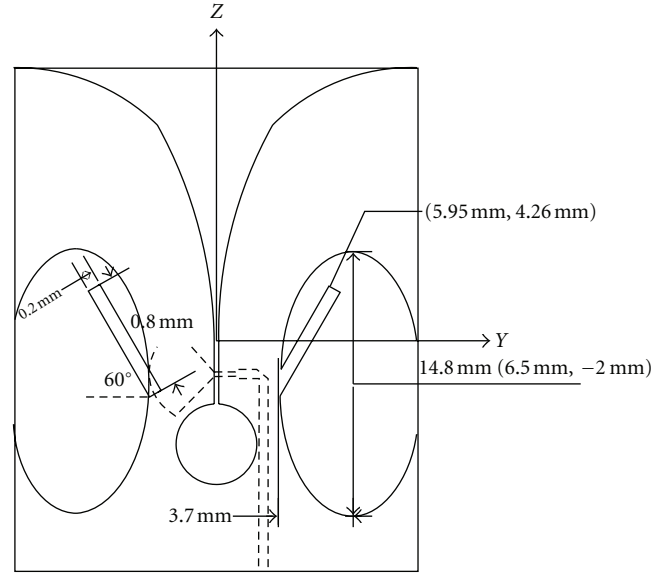


FIGURE 3: Structure of stealth design.

a way that decreases the RCS without sacrificing the radiation characteristics.

Based on the aforementioned idea, two ellipses are symmetrically cut out from the metal patch to ensure the maximum metal reduction to reduce RCS. However the large area cutdown on the metal patch will unavoidably result in slight current distribution changing in the radiation model, which will lead to high side lobe and dispersive gain in a wide frequency range. To prevent the lateral radiation, a rectangle strip is placed within the area of the two cut ellipses and connected to the remaining part of the metal patch. The rectangle strip's length is 7.8 mm and its resonant frequency is nearly 3 GHz, and then we can have two higher harmonics at 9 GHz and 12 GHz. Through HFSS simulation and optimization, we arrive at a final design of the stealth antenna as shown in Figure 3. The stealth antenna is fabricated and shown in Figure 4.

3. Result and Discussion

To validate the stealth design method presented in the previous section, we first evaluate the radiation performance of our stealth antenna compared with the original one. Figure 5 shows the measured and simulated return loss of the stealth antenna. The associated data of original Vivaldi antenna are also presented. The measured and simulated results of the stealth antenna coincide with each other from 6 to 18 GHz and for comparison are below -10 dB over the entire X-band from 8 GHz to 12 GHz. The return loss of the stealth antenna in X-band is only slightly larger than that of the original one, which is due to the impedance mismatch and can be further improved. In this paper, we will not focus on the feed matching design as long as the measured and simulated S_{11} are acceptable. There are two resonant frequency points at nearly 9 GHz and 12 GHz which coincide the previous design.



FIGURE 4: View of the fabricated stealth antenna.

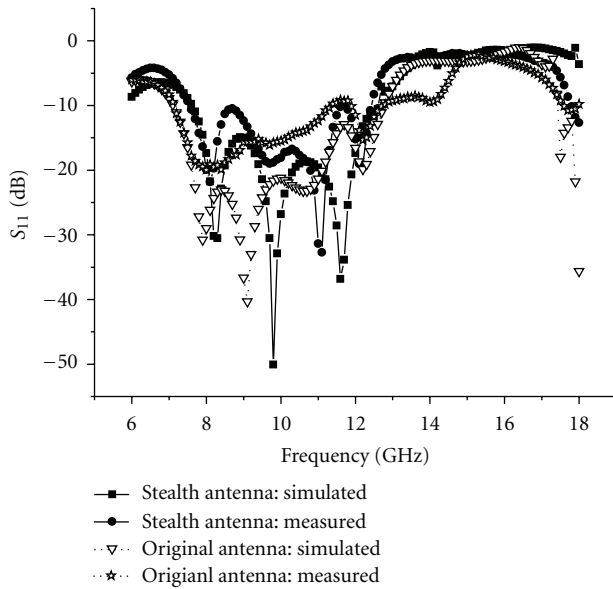


FIGURE 5: Return loss of the antenna.

By using the outdoor measurement method in [19], the gain and return loss of the stealth design is obtained with the transmitting and receiving antennas separated by 50 cm. The measured and simulated antenna gains over the X-band are given in Figure 6. About 4 dBi gain is achieved in both designs. From Figure 6 we can also observe that our stealth design method has flatter gain versus frequency as compared to the original one, which leads to a better dispersion and group delay performance.

The previous results show that our stealth design maintains good radiation performance. In the following, we will show the low observation characteristics of the stealth design. As the antenna RCSs are too low to be accurately measured in

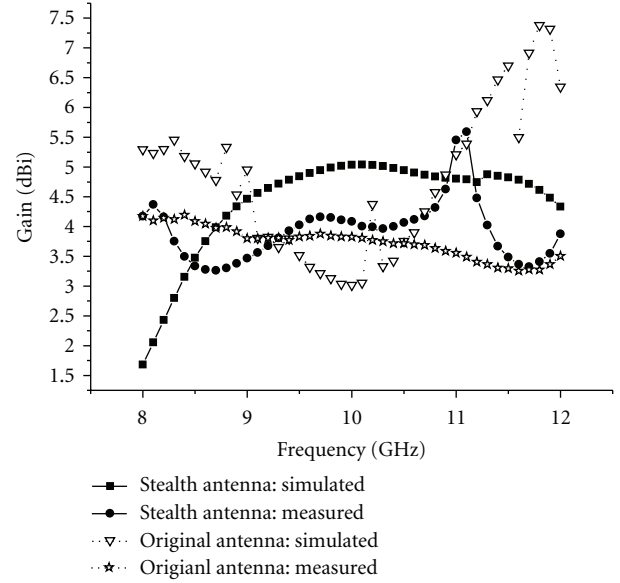


FIGURE 6: Gain of the antenna.

an ordinary chamber with common background noise, only simulation results are provided.

Consider a plane wave incident from the direction $\theta^i = 0$ and $\phi^i = 0$. As the polarization of the antenna is along the Y axis, the X-polarized RCS is very small in both antenna designs as shown in Figure 7(a). However, for the copolarization in Figure 7(b), a much higher RCS is observed. As is seen in the figure, the RCS is significantly reduced by using our stealth design. Within the X band, the maximum RCS reduction is about 19.2 dBsm at 11.3 GHz, and the minimum reduction is about 4.6 dBsm at 10.1 GHz. According to the radar range equation [20], a 19.2 dB reduction in RCS decreases the radar detection range by 68%, whereas a 4.6 dB reduction in RCS also can decrease the detection range by 24%, which is very important in stealth design of associate platform. Meanwhile, after stealth design, the mode scattering RCS is also improved and is estimated to be about -90 dBsm. So our stealth design method is very effective.

Figure 8 shows the bistatic RCS patterns versus scattering angle θ for 10.1 GHz and 11.3 GHz, respectively. In both figures, the incident angle is fixed to be $\theta^i = 0$ and $\phi^i = 0$. It can be seen that our stealth antenna maintains much lower RCS in a wide scattering range from 0° to 60° and from 300° to 360° which are most threatening scope for stealth design. Similar RCS reduction effects are also observed at other frequencies. Compared to the scattering of dual-index Vivaldi antenna studied by Jiang fu et al. [12], our method achieves a more stable gain and wider-angle range RCS reduction.

4. Conclusion

In this paper, we proposed a novel low RCS design method and applied it to Vivaldi antennas. An excellent stealth performance in the entire X-band and wide angle range

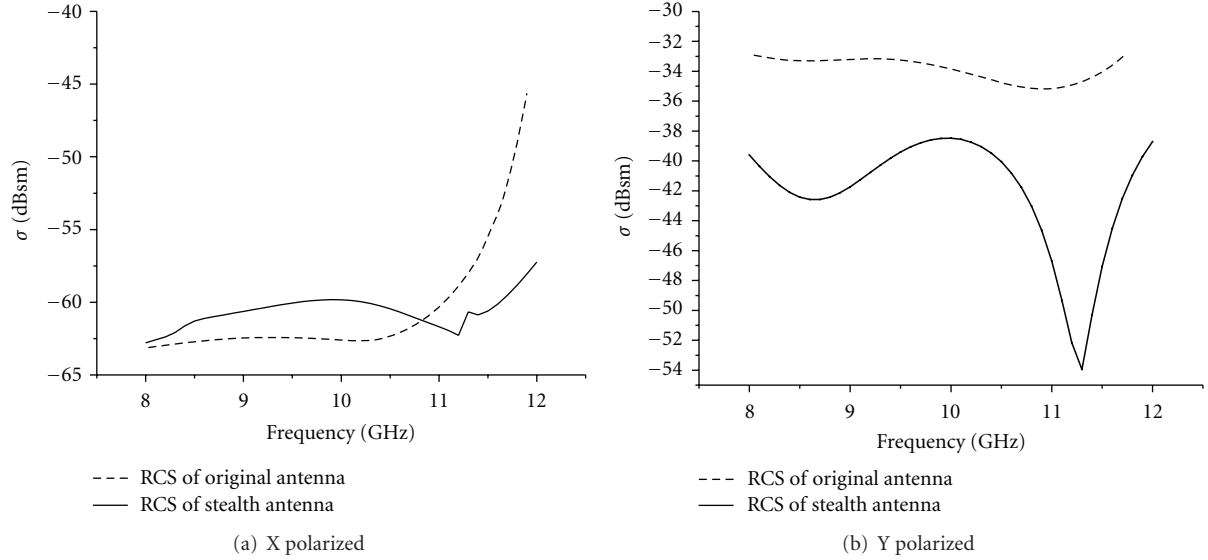


FIGURE 7: RCS with the change of frequency.

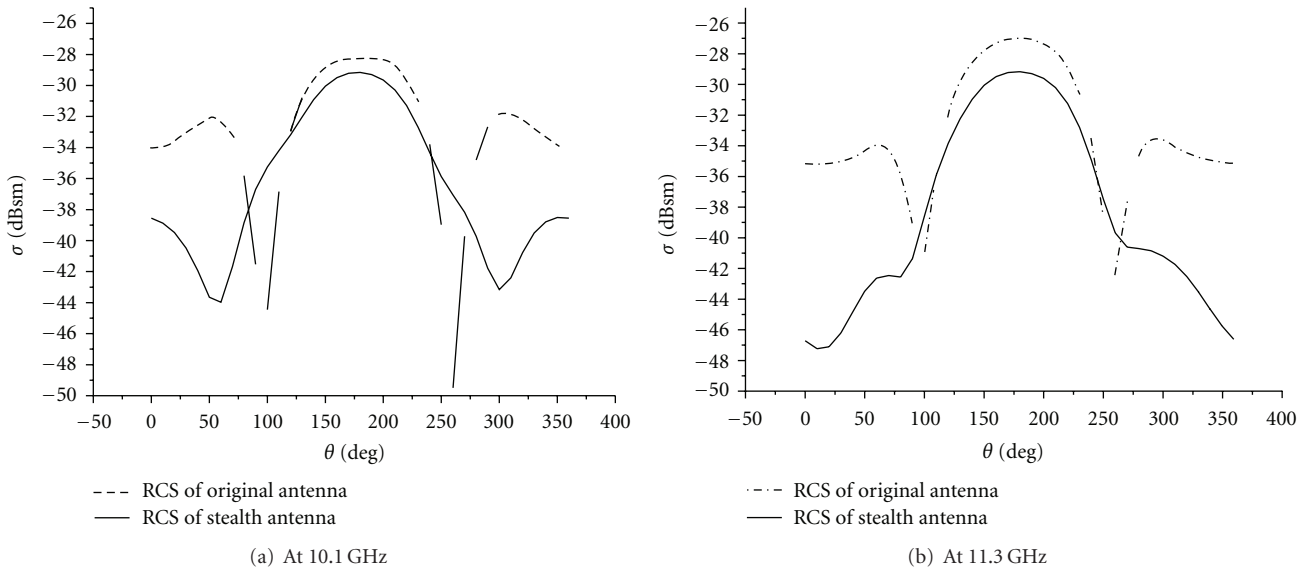


FIGURE 8: RCS with the change of angle.

is achieved. With the proposed design method, the RCS is reduced up to 19.2 dBsm with satisfactory radiation characteristic maintained, which shows that the proposed design is effective and potential for other microstrip antenna stealth design.

Acknowledgments

This paper is supported by the National Natural Science Foundation of China (no. 61102032), funding of State Key Laboratory of Millimeter Waves in China (Grant: K201005), the China Postdoctoral Science Foundation (no. 20110491423), the NUAA Research Funding (no.

NS2011014), and the NUAA Innovation Base Fund for Postgraduates.

References

- [1] P. J. Gibson, "The Vivaldi aerial," in *Proceedings of the 9th European Microwave Conference*, pp. 101–105, 1979.
- [2] D. H. Schaubert, S. Kasturi, A. O. Boryssenko, and W. M. Elsallal, "Vivaldi antenna arrays for wide bandwidth and electronic scanning," in *Proceedings of the 2nd European Conference on Antennas and Propagation (EuCAP'07)*, pp. 1–6, November 2007.
- [3] C. Deng and Y. J. Xie, "Design of resistive loading Vivaldi antenna," *IEEE Antennas and Wireless Propagation Letters*, vol. 8, pp. 240–243, 2009.

- [4] Y. Li and H. Liu, "RCS reduction of missile-borne quasi-traveling wave microstrip antenna," in *Proceedings of the 9th International Conference on Electronic Measurement and Instruments (ICEMI '09)*, pp. 3246–3249, August 2009.
- [5] D. Jun, C. Chunxia, and G. ChenJiang, "A method for microstrip antenna RCS reduction," *Computer Simulation*, pp. 130–133, 2008.
- [6] H. K. Jang, W. J. Lee, and C. G. Kim, "Design and fabrication of a microstrip patch antenna with a low radar cross section in the X-band," *Smart Materials and Structures*, vol. 20, no. 1, Article ID 015007, 8 pages, 2011.
- [7] Y. Tan, N. Yuan, Y. Yang, and Y. Fu, "Improved RCS and efficient waveguide slot antenna," *Electronics Letters*, vol. 47, pp. 582–583, 2011.
- [8] Y. Liu, S. X. Gong, and D. M. Fu, "A novel model for analyzing the RCS of microstrip antenna," in *Proceedings of the IEEE International Antennas and Propagation Symposium and USNC/CNC/URSI North American Radio Science Meeting*, pp. 835–838, June 2003.
- [9] S. C. Zhao, B. Z. Wang, and Q. Q. He, "Broadband radar cross section reduction of a rectangular patch antenna," *Progress in Electromagnetics Research*, vol. 79, pp. 263–275, 2008.
- [10] H. Y. Xu, H. Zhang, K. Lu, and X. F. Zeng, "A holly-leaf-shaped monopole antenna with low RCS for UWB application," *Progress in Electromagnetics Research*, vol. 117, pp. 35–50, 2011.
- [11] G. Zhang, L. Xu, and A. Chen, "RCS reduction of Vivaldi antenna array using a PSS boundary," in *Proceedings of the 8th International Symposium on Antennas, Propagation and EM Theory (ISAPE '08)*, pp. 345–347, November 2008.
- [12] L. Jiang fu, G. Shu xi, Y. xue, and Z. Xiao lu, "Study of RCS on the dual-index Vivaldi antenna," *Space Electronic Technology*, vol. 2, pp. 26–29, 2011.
- [13] L. Yang, H. Guo, X. Liu, H. Du, and G. Ji, "An antipodal Vivaldi antenna for ultra-wideband system," in *Proceedings of the IEEE International Conference on Ultra-Wideband (ICUWB '10)*, vol. 1, pp. 301–304, September 2010.
- [14] T. Li, Y. Rao, and Z. Niu, "Analysis and design of UWB Vivaldi antenna," in *Proceedings of the IEEE International Symposium on Microwave, Antenna, Propagation, and EMC Technologies for Wireless Communications (MAPE '07)*, pp. 579–581, August 2007.
- [15] M. R. Hamid, P. Gardner, P. S. Hall, and F. Ghanem, "Multi-mode Vivaldi antenna," *Electronics Letters*, vol. 46, no. 21, pp. 1424–1425, 2010.
- [16] S. Gong and Y. Liu, *Prediction and Reduction of Antenna Radar Cross Section*, Xi'an University of Electronic Science and Technology Press, 2010.
- [17] Y. T. Lo and S. W. Lee, *Antenna Handbook: Theory, Applications and Design*, Artech House, New York, NY, USA, 1993.
- [18] B. A. Munk, *Finite Antenna Arrays and FSS*, Wiley-IEEE Press, 2003.
- [19] G. Felic, "Antenna gain measurements in the V-band: a single-antenna method," in *Proceedings of the Electromagnetic Compatibility Symposium Adelaide (EMCSA '09)*, pp. 98–101, September 2009.
- [20] D. Lynch Jr., *Introduction to RF Stealth*, SciTech Publishing, 2004.

Research Article

Novel Compact CPW-Fed Antennas with Harmonic Suppression and Bandwidth Enhancement

Zhi-Li Zhou, Li Li, and Jing-Song Hong

Institute of Applied Physics, University of Electronic Science and Technology, Chengdu 610054, China

Correspondence should be addressed to Zhi-Li Zhou, zhouzhili003@163.com

Received 9 December 2011; Accepted 4 July 2012

Academic Editor: Hala A. Elsadek

Copyright © 2012 Zhi-Li Zhou et al. This is an open access article distributed under the Creative Commons Attribution License, which permits unrestricted use, distribution, and reproduction in any medium, provided the original work is properly cited.

Novel compact CPW-fed antennas with harmonic suppression are presented and investigated in detail. By inserting symmetrical slots connected to the end of CPW transmission line in the ground plane, and exploiting parasitic technique, harmonic suppression, compact size, as well as wide bandwidth are obtained. General performances of the proposed antennas are studied by equivalent transmission line circuits. Moreover, the steps of constructing such harmonic suppression antennas are derived. Eventually, the experiment results verified the validation of the proposed harmonic suppression antennas.

1. Introduction

The harmonic suppression antenna (HSA) has become very attractive due to its great advantages such as low cost, small size, and easy integration in wireless communication and microwave power transmission (MPT) systems [1, 2]. Conventionally, a harmonic suppression filter is chosen in these systems to avoid harmonic interference and achieve good system performances. However, it is bulky, expensive, and hard to be integrated in monolithic microwave integrated (MMIC) devices. To overcome these defects, harmonic suppression technologies for antenna have been widely investigated recently [3–9]. Defected ground plane structure (DGS) and photonic band gap (PBG) structure are widely used to achieve harmonic suppression function [10, 11]. However, most of them are focus on microstrip-fed antennas. Compared with the microwave-fed antennas, CPW-fed antennas exhibit even more promising merits, such as wider bandwidth, simpler structure, and easier integration with active devices and MMIC devices. It reveals us that the CPW-fed antennas with harmonic suppression will be more attractive and applicable. Nevertheless, there are only a few researches on that [12–14], and much more works is required to fulfill its potential. In [12], a CPW-fed broadband HSA (1.56 GHz–2.88 GHz) was achieved by exploiting PBG structures with cross-shaped lattices. Besides, by inserting

symmetrical slots in the ground plane of an open-ended CPW-fed transmission line, an HSA with fairly compact size (26 mm × 15 mm) was obtained in [13]. However, the broadband HSA in [12] is limited by its rather big size, and the compact HSA in [13] suffered a quite narrow bandwidth.

In this paper, several novel compact CPW-fed antennas with harmonic suppression are presented. In order to suppress the harmonic frequencies, symmetrical slots connected to the end of CPW-fed transmission line are etched on the ground plane. Moreover, by employing parasitic technique, bandwidth enhancement is also achieved. General performances of the proposed antennas are investigated by equivalent transmission line circuits. Furthermore, the steps of constructing such HSAs are derived. Eventually, the experiment results verified the validation of the proposed HSAs.

2. Antenna Geometry and Mechanism

2.1. Simple Slot-Type HSA. A normal open-ended CPW-fed transmission line, as shown in Figure 1(a), will not radiate electromagnetic energy. However, radiation behavior can be brought by creating discontinuities in the CPW-fed transmission line, and by etching slots on the ground plane. In order to excite desired resonant frequency, two simple symmetrical short-ended slots connected with the end of

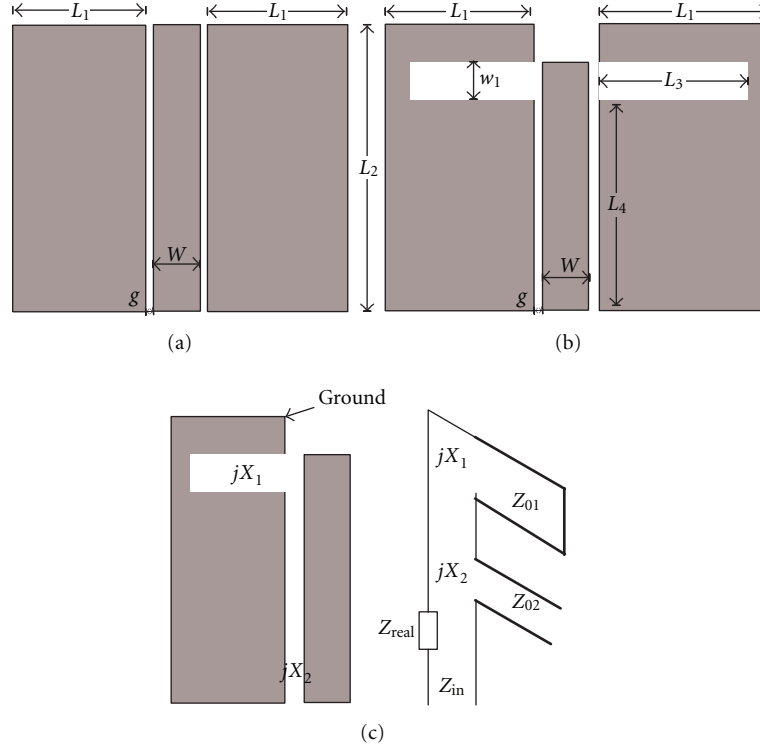


FIGURE 1: (a) A normal open-ended CPW-fed transmission line. (b) The geometry of antenna 1 and (c) The equivalent transmission line circuits for antenna 1.

the CPW transmission line were etched on the ground plane, as shown in Figure 1(b), named antenna 1. The short-ended slots are the radiator and impedance controller. They can be expressed as series pure imaginary impedance load at the end of the CPW-fed transmission line, according to the equivalent transmission line circuits, as shown in Figure 1(c). The imaginary part of the input impedance for antenna 1 can be expressed as.

jX_1 , jX_2 are the imaginary part of the input impedances of the equivalent transmission line for the short-ended slot and the CPW feeding line, respectively,

$$Z_{imag} = jX_1 + jX_2 = jZ_{01}tg\beta L_3 + jZ_{02}ctg\beta L_4, \quad (1)$$

where Z_{01} , Z_{02} are the characteristic impedances of the equivalent transmission line. And they depend on the width of the symmetrical slot, the height of substrate, as well as the dielectric constant of the substrate.

To achieve the desired resonant frequency, we can take (1), which is derived from the equivalent T.L. circuit model, into account in obtaining the parameters of the short-ended slots at the beginning design. And then, the full-wave solver CST has been used to finalize and optimize the structure. By changing the length of the slots, the imaginary part of the input impedance for antenna 1 can be close to null, thus pure resistive input impedance can be produced. As a result, resonant can be excited at the desired frequency.

Antenna 1 was printed on a dielectric substrate with thickness of 1.6 mm, and relative permittivity of 4.5. Simulation and optimization were performed with the commercial

TABLE 1: Antenna dimensions.

Antenna 1	Antenna 2	Antenna 3
$L_1 = 17.3$ mm	$L_1 = 9.1$ mm	$L_1 = 20$ mm
$L_2 = 20$ mm	$L_2 = 3$ mm	$R_1 = 15$ mm
$L_3 = 16.5$ mm	$L_3 = 9$ mm	$R_2 = 14$ mm
$L_4 = 16$ mm	$L_4 = 18$ mm	$a_1 = 15$ degree
$W_1 = 2$ mm	$W_1 = W_2 = 2$ mm	$a_2 = 20$ degree
$g = 0.2$ mm	$g = 0.2$ mm	$g = 0.2$ mm
$W = 3$ mm	$W = 3$ mm	$W = 3$ mm

software CST. And the final results, with the optimized parameters listed in Table 1, are demonstrated in Figure 2.

To obtain the harmonic suppression, additional antenna structures which act as a wide-band stop filter are usually required for microwave-fed antennas [15]. Generally, such structures are not necessary for the proposed CPW-fed HSAs since the open-ended CPW-fed transmission line can be expressed a wide-band stop filter. However, it can be seen from the results in Figure 2, the simple symmetrical slots in antenna 1 cannot suppress the third harmonic frequency effectively, though it can suppress the second harmonic frequency well. In order to excite the fundamental frequency and suppress both the second and third harmonic frequencies, further studies were carried out.

The fundamental resonant frequency is supposed to be f_0 . According to what have mentioned above, the length of the symmetrical slots should be about $\lambda/4$ (λ is the wavelength of the desired resonant frequency in the substrate).

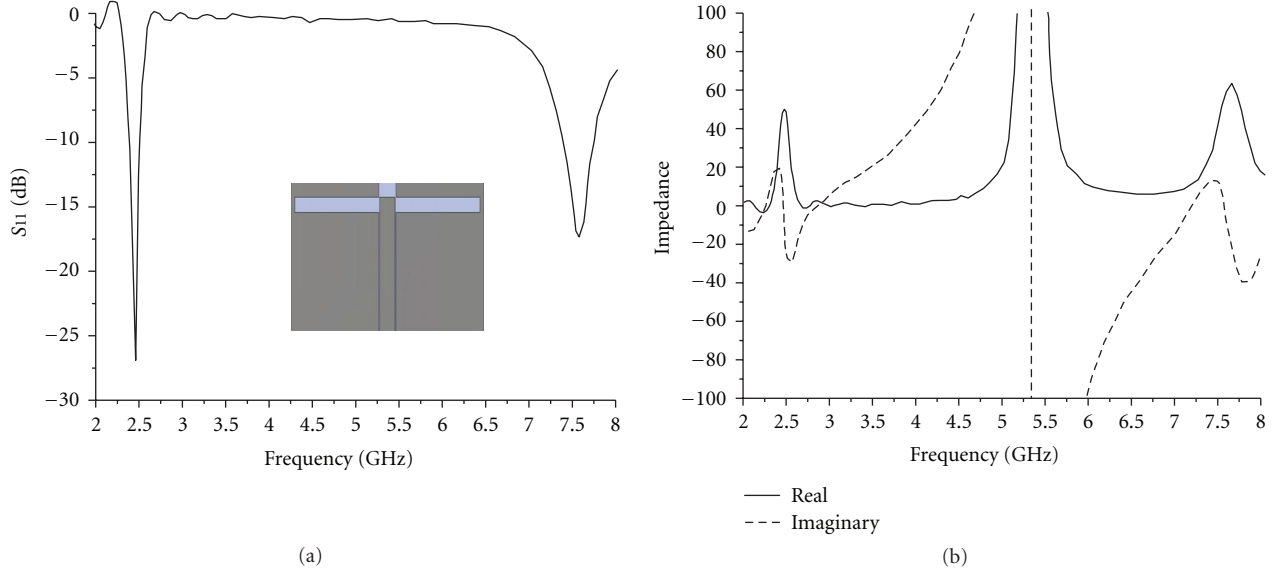


FIGURE 2: (a) The simulated return losses of antenna 1 and (b) The simulated input impedance of antenna 1.

As a result, the length of the symmetrical slots is also equal to $3\lambda_{3th}/4$ (λ_{3th} is the wavelength of the third harmonic frequency in the substrate). Therefore, pure resistive input impedance is also achieved at the third harmonic frequency, which means that a spurious resonant is also excited at the third harmonic frequency. Accordingly, necessary modification must be done on the basis of antenna 1, so as to excite the fundamental resonant and suppress both the second and third harmonic frequencies. Thus, the transmission line which connected with pure reactive load is considered, as shown in Figure 3(a).

Antenna 2 is printed on a dielectric substrate with thickness of 1.6 mm, and relative permittivity of 4.5. Two symmetrical short-ended transmission lines were connected with the end of the symmetrical slots, respectively, as shown in Figure 3(b). The equivalent transmission line circuit of antenna 2 is also presented in Figure 3(c). According to the transmission line impedance equation, the imaginary part of the input impedance of antenna 2 is

$$Z_{imag} = jX_1 + jX_2 = Z_{01} \frac{Z_L + jZ_{01}tg\beta L_2}{Z_{01} + jZ_Ltg\beta L_2} - jZ_{02}ctg\beta L_4, \quad (2)$$

where Z_{01} , Z_{02} are the characteristic impedances of the equivalent transmission lines:

$$Z_L = Z_{stub1} + Z_{stub2} = jZ_{01}tg\beta L_1 + jZ_{03}tg\beta L_3. \quad (3)$$

We can also take (2) and (3), which are derived from the equivalent T.L. circuit models, into account in obtaining the parameters of the slots at the beginning design, and then finalize and optimize the structures by the full-wave solver. Optimized parameters of the proposed antenna 2 are listed in Table 1. Figure 4 depicts the final results.

2.2. Bandwidth Enhancement of the CPW-Fed Capacitive Slot Type HSA for Wideband Applications. The bandwidth

limitation of antenna is probably the most serious problem in the practical applications of engineering. In order to improve the bandwidth of the proposed HSA, parasitic technique is applied, as shown in Figure 5(a). Two pairs of symmetrical slots connected with the end of the CPW-fed transmission line are etching on the ground plane. Each pair of symmetrical slots can excite a resonant mode. So, both broadband characteristic and harmonic suppression function can be obtained when the two resonant frequencies are close enough. The transmission line equivalent circuit of the proposed antenna 3 is also presented in Figure 5(b). According to the transmission line impedance equation, the imaginary part of the input impedance for antenna 3 is

$$Z_{imag} = jX_1 + jX_2 + jX_3, \quad (4)$$

jX_1 , jX_2 are the impedances of the equivalent transmission line of the two pairs of symmetrical slots connected with the CPW-fed transmission line, which can be seen as two pairs of tapered transmission line (Figure 6), respectively. $Z_{01}, Z_{02}, \dots, Z_{0N}$, are the characteristic impedances of the equivalent transmission lines. Considering the fact that the T.L model is used to provide only the initial estimates for the antenna designed parameters and in order to simplify the design, N is chosen to be 2 in this design, that is

$$jX_1(jX_2) = Z_{01} \frac{jZ_{02}tg\beta((R1(R2))/2) + jZ_{01}tg\beta((R1(R2))/2)}{Z_{01} - Z_{02}tg\beta((R1(R2))/2)tg\beta((R1(R2))/2)},$$

$$jX_3 = -jZ_{03}ctg\beta L_1, \quad (5)$$

Z_{03} is the characteristic impedance of the equivalent CPW-fed transmission line. Similarly, we can take (5) into account in obtaining the lengths of the slots at the beginning design and tune the geometry for the final design. Make sure that the pure resistive input impedance is obtained only at the

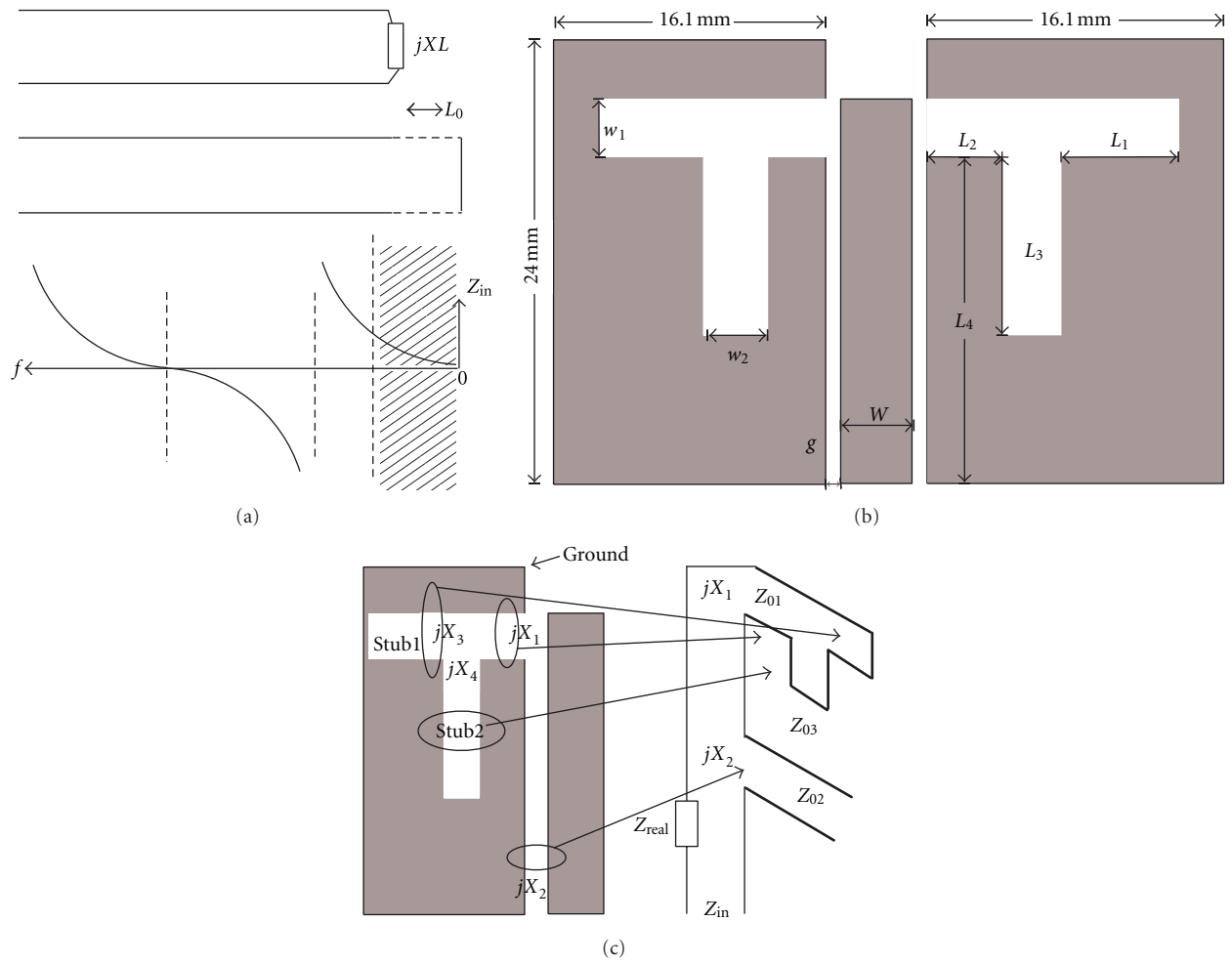


FIGURE 3: (a) The impedance of purely reactive loaded transmission line. (b) The geometry of antenna 2 and (c) The equivalent transmission line circuits for antenna 2.

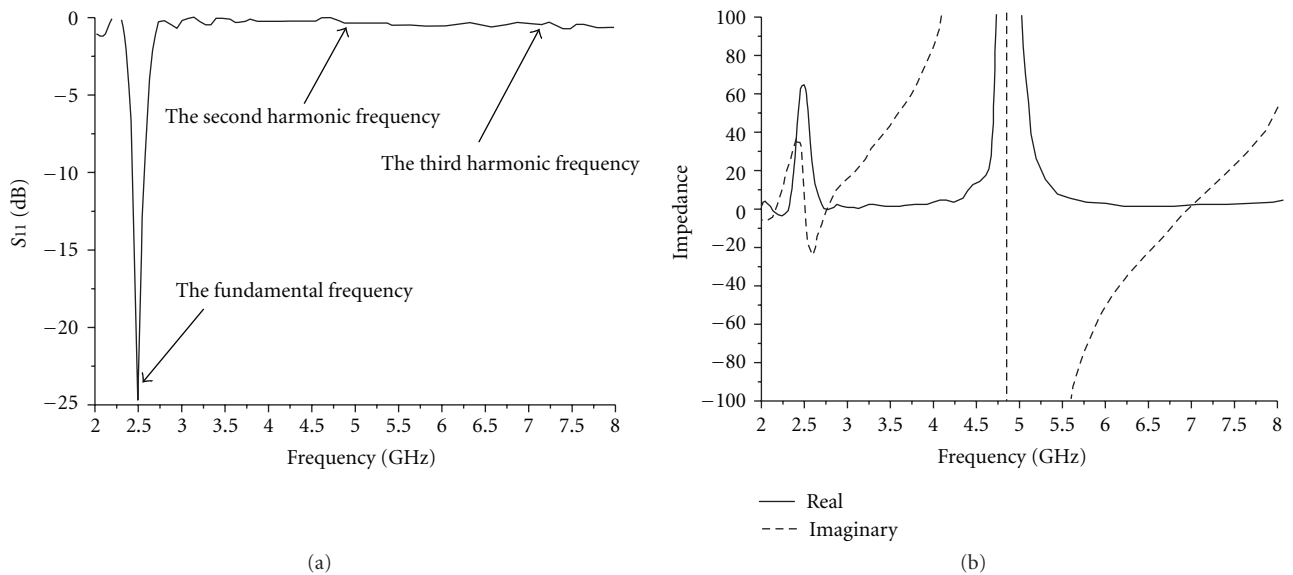


FIGURE 4: (a) The simulated return losses of antenna 2 and (b) The simulated input impedance of antenna 2.

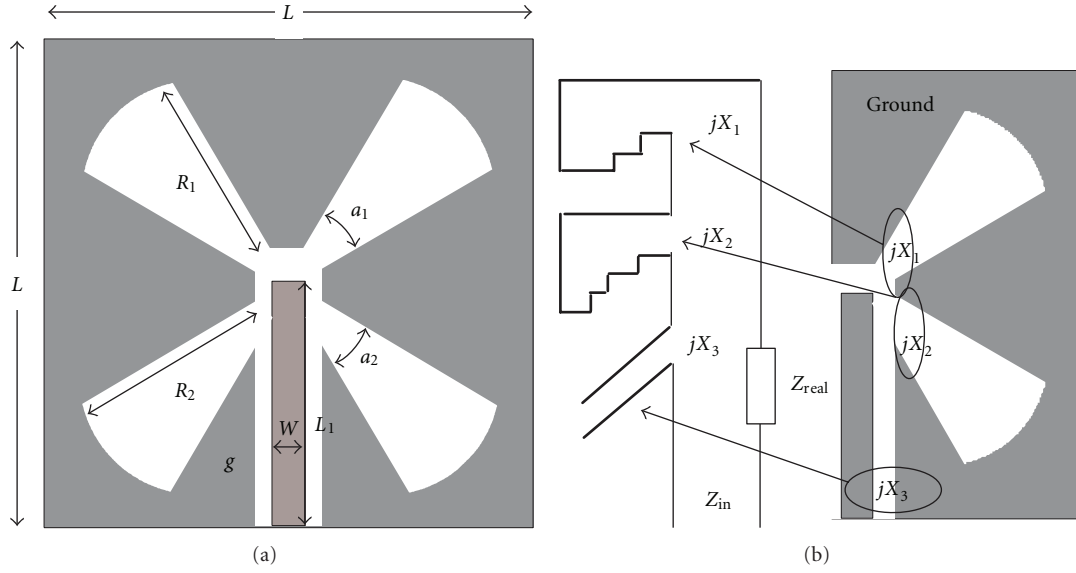


FIGURE 5: (a) The geometry of antenna 3 and (b) The equivalent transmission line circuits for antenna 3.

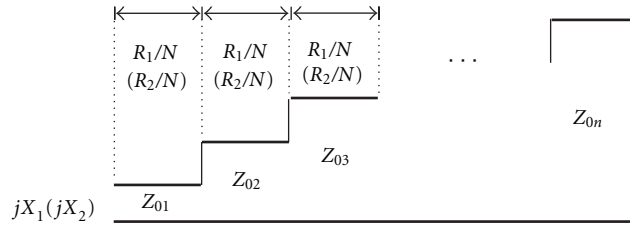


FIGURE 6: The equivalent transmission line model of the two pairs of symmetrical slots.

two desired fundamental frequencies. Thus, both harmonic suppression and wide bandwidth can be achieved when the two fundamental frequencies are close enough. The final optimized parameters are listed in Table 1, and Figure 7 demonstrates the final results.

2.3. General Approach of Constructing Capacitive CPW-Fed Slot-Type HSA. General approach of constructing capacitive CPW-fed slot type HSA can be summarized from what have mentioned above. Briefly, the design procedures are as follows:

- (1) etching symmetrical slots connected with the end of the CPW-fed transmission line in the ground plane,
- (2) calculate the slot length according to the equivalent transmission line circuits, and try to make the pure resistive input impedance obtained only at the desired fundamental resonant frequency,
- (3) carefully adjust the parameters until optimized results are achieved,
- (4) if wideband is required, extra slots can be connected with the end of the CPW transmission line,
- (5) repeat step 1 to make sure the pure resistive input impedance only achieved at the desired resonant frequency, and it is close enough to the earlier one,
- (6) carefully adjust the parameters until best results are obtained.

3. Results and Discussion

In order to verify the validation of the proposed antennas, experiments were carried out, and the measured results are plotted in Figures 8(a) and 8(b), respectively. The measured -10 dB impedance bandwidth of the proposed simple compact HSA (antenna 2) is 90 MHz (2.4–2.49 GHz, 3.6%) with compact size of 36 mm \times 24 mm. The proposed compact broadband HSA (antenna 3) achieved a wide -10 dB impedance bandwidth (530 MHz) spanning from 2.25 GHz to 2.78 GHz, which is about 150% broader than that proposed in [13]. Furthermore, the proposed compact broadband HSA (antenna 3) also exhibits compact size of 40 mm \times 40 mm, which is about 47% smaller in size compared with the above-mentioned broadband HSA in [12].

The radiation patterns at different frequencies (at 2.45 GHz, 4.9 GHz and 7.35 GHz) for antenna 1, antenna 2

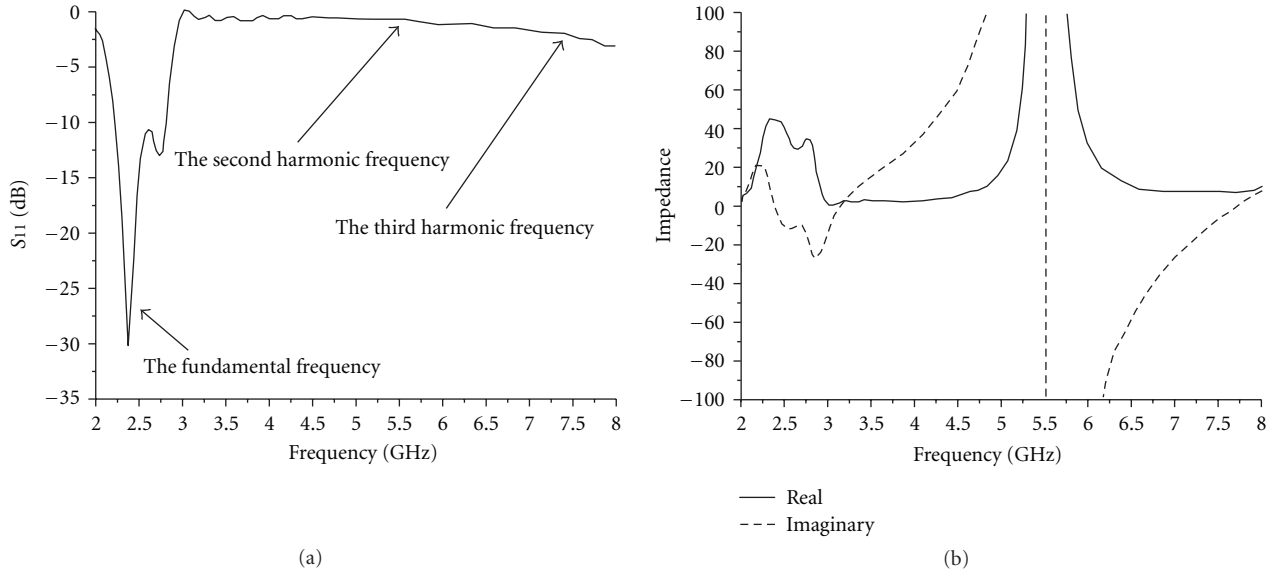


FIGURE 7: (a) The simulated return losses of antenna 3 and (b) The simulated input impedance of antenna 3.

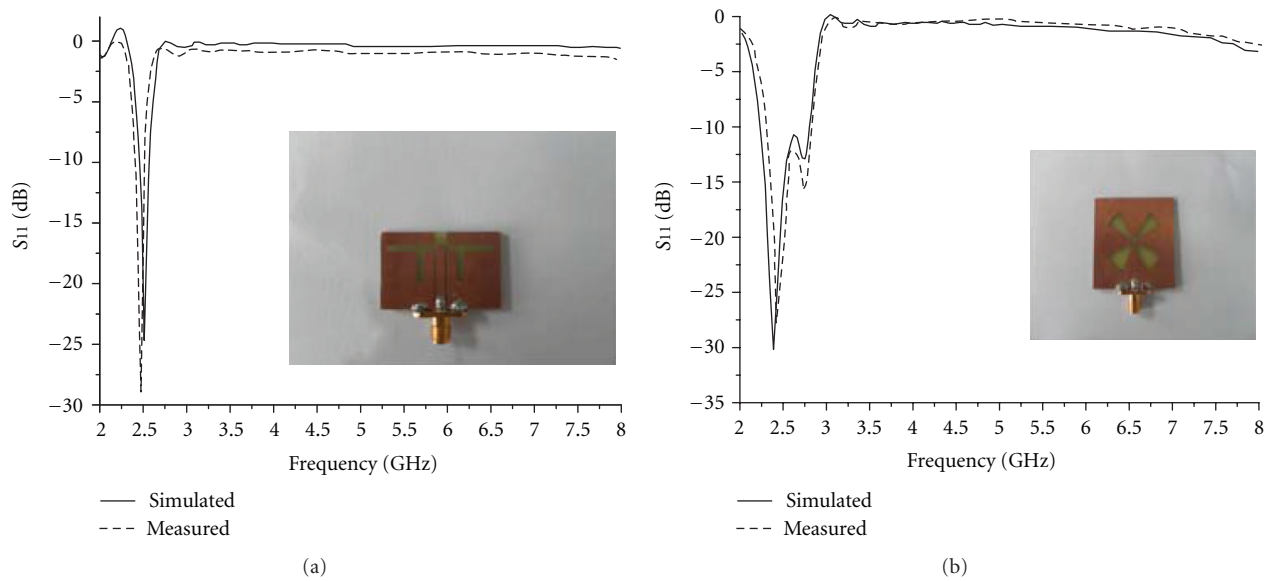


FIGURE 8: The simulated and measured return losses for (a) antenna 2 and (b) antenna 3.

and antenna 3 are also demonstrated in Figures 9(a), 9(b), and 9(c), respectively. It can be seen that antenna 1 can only suppress the second harmonic frequency, while both antenna 2 and antenna 3 can suppress the second and third harmonic frequencies well.

4. Conclusion

In this paper, CPW-fed antennas with harmonic suppression including the second and third harmonic frequencies are demonstrated and investigated. By etching symmetrical slots connected to the end of the CPW-fed transmission line in the ground plane, and exploiting parasitic technology,

both compact size and wide bandwidth are achieved. The proposed antenna has been verified through the equivalent circuit analysis and experimental results. General construction approach of such kind of HSA has also been derived. Given the merits such as compact size, good harmonic suppression, as well as wide bandwidth, the proposed HSA is very attractive for wireless communication and microwave power transmission applications.

Acknowledgments

This work was supported by the National Natural Science Foundation of China (nos. 61172115 and 60872029),

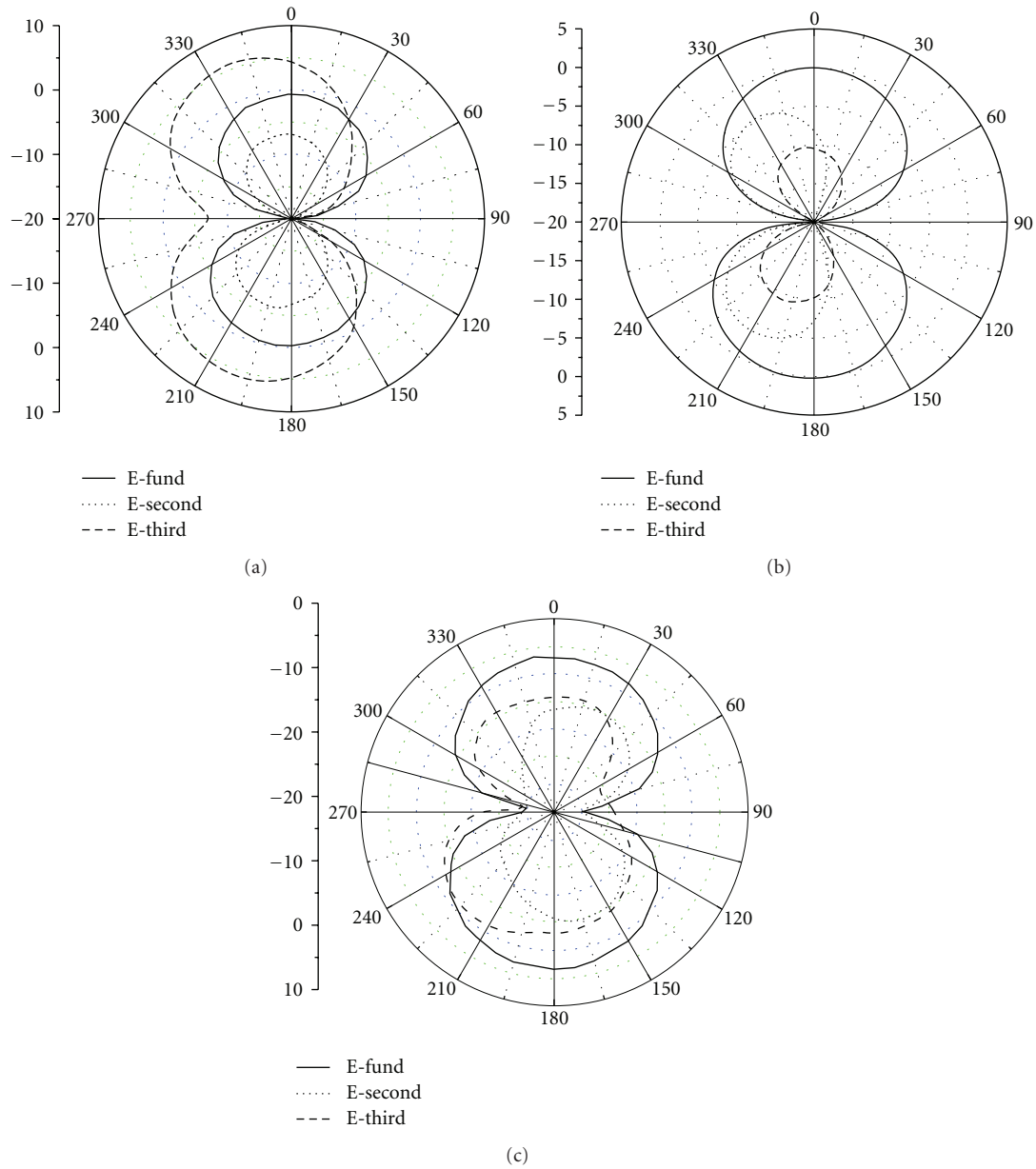


FIGURE 9: The radiation patterns at different frequencies for: (a) antenna 1, (b) antenna 2, and (c) antenna 3.

the High-Tech Research and Development Program of China (no. 2008AA01Z206), the Aeronautics Foundation of China (no. 20100180003), and the Fundamental Research Funds for the Central Universities (no. ZYGX 2009J037).

References

- [1] V. Radisic, Y. Qian, and T. Itoh, "Novel architectures for high-efficiency amplifiers for wireless applications," *IEEE Transactions on Microwave Theory and Techniques*, vol. 46, no. 11, pp. 1901–1909, 1998.
- [2] R. Dehbashi, Z. Atlasbaf, and K. Forooghi, "New compact size microstrip antennas with harmonic rejection," *IEEE Antennas and Wireless Propagation Letters*, vol. 5, no. 1, pp. 395–398, 2006.
- [3] H. Kim and Y. J. Yoon, "Microstrip-fed slot antennas with suppressed harmonics," *IEEE Transactions on Antennas and Propagation*, vol. 53, no. 9, pp. 2809–2817, 2005.
- [4] D. H. Choi, Y. J. Cho, and S. O. Park, "A broadband T-shaped microstrip-line-fed slot antenna with harmonic suppression," in *Proceedings of the Asia-Pacific Microwave Conference (APMC'05)*, vol. 4, December 2005.
- [5] Y. Horii, "A harmonically controlled microstrip patch antenna using grounded-pads embedded in an antenna substrate," in *Proceedings of the IEEE International Antennas and Propagation Symposium and USNC/CNC/URSI North American Radio Science Meeting*, pp. 724–727, June 2003.
- [6] S. Kwon, B. M. Lee, Y. J. Yoon, W. Y. Song, and J. G. Yook, "A harmonic suppression antenna for an active integrated antenna," *IEEE Microwave and Wireless Components Letters*, vol. 13, no. 2, pp. 54–56, 2003.

- [7] J. Ding, "A harmonic suppression antenna using split ring resonators coupled with microstrip line," in *Proceedings of the 7th International Symposium on Antennas, Propagation and EM Theory (ISAPE'06)*, pp. 1–3, October 2006.
- [8] J. Y. Park, S. M. Han, and T. Itoh, "A rectenna design with harmonic-rejecting circular-sector antenna," *IEEE Antennas and Wireless Propagation Letters*, vol. 3, no. 1, pp. 52–54, 2004.
- [9] J. Y. Park, S. M. Han, and T. Itoh, "Antenna with harmonic rejecting circular sector antenna," *IEEE Antennas and Wireless Propagation Letters*, vol. 5, pp. 395–398, 2006.
- [10] I. Chang and B. Lee, "Design of defected ground structures for harmonic control of active microstrip antenna," in *Proceedings of the IEEE Antennas and Propagation Society International Symposium*, pp. 852–855, June 2002.
- [11] H. Liu, Z. Li, X. Sun, and J. Mao, "Harmonic suppression with photonic bandgap And defected ground structure for a microstrip patch antenna," *IEEE Microwave and Wireless Components Letters*, vol. 15, no. 2, pp. 55–56, 2005.
- [12] X. C. Lin and L. T. Wang, "A broadband CPW-fed loop slot antenna with harmonic control," *IEEE Antennas and Wireless Propagation Letters*, vol. 2, pp. 323–325, 2003.
- [13] R. Sujith, S. Mridula, P. Binu, D. Laila, R. Dinesh, and P. Mohanan, "Compact CPW-fed ground defected H-shaped slot antenna with harmonic suppression and stable radiation characteristics," *Electronics Letters*, vol. 46, no. 12, pp. 812–814, 2010.
- [14] W. H. Tu, "Compact harmonic-suppressed coplanar waveguide-fed inductively coupled slot antenna," *IEEE Antennas and Wireless Propagation Letters*, vol. 7, pp. 535–545, 2008.
- [15] N. A. Nguyen, R. Ahmad, Y. T. Im, Y. S. Shin, and S. O. Park, "A T-shaped wide-slot harmonic suppression antenna," *IEEE Antennas and Wireless Propagation Letters*, vol. 6, pp. 647–650, 2007.

Research Article

Study on Glass-Epoxy-Based Low-Cost and Compact Tip-Truncated Triangular Printed Antenna

Rajeev Kumar Kanth,¹ Pasi Liljeberg,¹ Hannu Tenhunen,¹ Qiang Chen,² Lirong Zheng,² and Harish Kumar³

¹ *Turku Centre for Computer Science (TUCS) and Department of Information Technology, University of Turku, 20520 Turku, Finland*

² *School of Information and Communication Technologies, Royal Institute of Technology (KTH), 10044 Stockholm, Sweden*

³ *Department of Electronics and Communication Engineering, BIT, Muzaffarnagar 251315 (U.P.), India*

Correspondence should be addressed to Rajeev Kumar Kanth, rajkan@utu.fi

Received 11 February 2012; Revised 1 June 2012; Accepted 1 June 2012

Academic Editor: Dalia N. Elshiekh

Copyright © 2012 Rajeev Kumar Kanth et al. This is an open access article distributed under the Creative Commons Attribution License, which permits unrestricted use, distribution, and reproduction in any medium, provided the original work is properly cited.

Printed antennas based on glass epoxy substrate have been developed. On the basis of required specifications and assigned frequencies, tip-truncated triangular printed antennas have been designed, analyzed, and fabricated. The performances of the antennas have been measured in terms of return loss, frequency of operation, bandwidth, and radiation pattern. Triangular microstrip antenna (TMSA) configuration consisting of copper as active radiating patch and glass epoxy as dielectric substrate has been screened out to achieve the essential characteristics and satisfying recommended low-cost antenna. The Method of Moment (MOM) analyzing techniques have been employed to realize the required specific properties, whereas optimized tip truncation technique and varying feed point location give rise to suitable LHCP or RHCP configuration of the printed antenna. The coaxial probe signal feed arrangement have been considered for this work. The proposed printed antennas are suitable for communication links between ships or buoys and satellites specially for navigation purpose.

1. Introduction

The rapid progress in telecommunications has to deal with a great variety of communication systems, like cellular communications, global positioning, and satellite communications, each of these systems operate at several frequency bands. To provide an efficient and seamless services to the users, each of these systems must have an antenna that has to operate in the allocated frequency band for each specific system. Dielectric material plays an important role to characterize the performance of a microstrip antenna [1–4]. Usually, it is difficult to configure and optimize the parameters of an antenna with known value of dielectric constant. In this work, we have selected a widely available and low-cost dielectric material for design and fabrication of the antennas. Glass-epoxy dielectric material has several advantages such as rigid, low cost, uniform permittivity, and fine dielectric loss tangent characteristics over other substrates. A glass-epoxy substrate, which is generally used

as printed circuit board for analog and digital circuits, can also be used for low-cost applications. The relative dielectric constant (ϵ_r) of the substrate varies typically from 3.8 to 4.7 and tangent loss varies from 0.01 to 0.03 in the microwave frequency band.

Another major constraint resource is the frequency of operation. International Telecommunication Union Radio Communication Sector (ITU-R) has assigned two frequencies 1.176 GHz and 2.487 GHz for Regional Navigation Satellite System (RNSS) for the purpose of satellite navigational aids. The objective of this paper is to design and develop two separate antennas resonating at those specific frequencies accomplishing the required bandwidths, axial ratios, and gain radiation patterns.

A microstrip printed antenna consists of a very thin radiating patch on one side of a dielectric substrate and a conducting ground plane on the other side. The patch and the ground plane are separated by a dielectric. In this work, copper has been taken into consideration as a radiating patch

conductor and it can have any regular geometry. The patches are usually photoetched on the dielectric substrate and the substrate is usually nonmagnetic. The relative permittivity of the substrate is an important parameter to consider because it will enhance the fringing fields that accounts for radiation. To achieve the design specification for these separate 1.176 GHz and 2.487 GHz antennas, substrate is considered as glass epoxy whose relative dielectric constant (ϵ_r) is 4.4 and dimensions of the antenna is set up by the empirical relationship [5] as illustrated in (1), (2), (3), and (4) for Equilateral Triangle Micro Strip Antenna (ETMSA). MathCAD 2000 tool has been used to find the exact dimensions of both antennas.

This work is an extension of our previous studies on low profile microstrip antenna [6–11]. In recent years, several microstrip patch geometries have been introduced for antenna applications with varying degrees of success in improving antenna characteristics [12–18]. Some of these geometries have been particularly useful in reducing the size of the antenna. However, the proposed models are appropriate for the specified frequencies, respectively, in L and S band having the gain of -4 dBi up to $\pm 50^\circ$ and can be employed in the application of satellite navigation.

This paper is structured as follows. Sections 2 and 3 provide the description about related antenna theory and specifications of the antennas, respectively. Section 4 will present the design layout, physical dimensions, and probe positions of the proposed antennas. Section 5 is dedicated to exemplify the outcomes obtained and their analysis in each antenna configuration. This paper also includes the fabrication process and measurement techniques which are discussed in Sections 6 and 7, respectively. Conclusion, Acknowledgment, and References are the latter appendages of this paper.

2. Related Theory

Related antenna theory has been discussed in this section. The aim of this section is to clarify the readers about mathematical computation of specified parameters during antenna design. Figure 1 characterizes the dominant mode of ETMSA, TM_{10} and TM_{01} are required to configure circular polarization, and this figure also elucidates voltage distribution and field vector representation around ETMSA. The set of four equations help to determine the dimensions of both antennas

$$f_{mn} = \frac{2c(m^2 + mn + n^2)^{1/2}}{3S_e\sqrt{\epsilon_e}}, \quad (1)$$

$$S_e = S + \frac{4h}{\epsilon_e}, \quad (2)$$

$$\epsilon_e = \frac{(\epsilon_r + 1)}{2} + \frac{(\epsilon_r - 1)}{2} \left[1 + \frac{20h}{S} \right]^{-1/2}, \quad (3)$$

$$y = \sqrt{S^2 - \left(\frac{S}{2}\right)^2}. \quad (4)$$

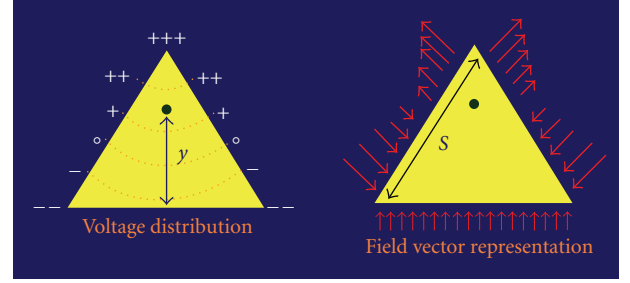


FIGURE 1: ETMSA voltage distribution and its vector representation.



FIGURE 2: Methods obtaining circular polarization.

The resonant frequency (f_{mn}) can be expressed in terms of effective side length (S_e), mode of triangular patch antenna ($m = 1, n = 0$), speed of light (c), and the effective dielectric constant (ϵ_e). Similarly, the effective side length can be estimated with (2) where effective dielectric constant (ϵ_e) can be obtained in (3) with the use of associated parameters like relative dielectric constant (ϵ_r), height, or thickness of the ground plane to patch (h) and side of equilateral triangle (S). The empirical mathematical statements shown in (1), (2), (3), and (4) assist to compute the dimensions of the active patches. MathCAD 2000 tool has been employed to achieve the optimized parameters.

Modified triangular MSA configuration with a single feed generates circular polarization. Some of the well-known techniques for generating circular polarization in ETMSA are nearly ETMSA (isosceles triangle with $S_1/S_2 = 1.01$ to 1.1), tip-truncated ETMSA, ETMSA with a rectangular slot and notched ETMSA as shown in Figure 2. LHCP or RHCP can be obtained by variation of feed point location and dimensions of the antenna. For the sake of convenience and easy realization, tip-truncated ETMSA has been employed for these designs. For these developed antennas, coaxial probe feeding technique has been exploited. The coaxial feed or probe feed is a very common technique used for feeding microstrip patch antennas. In this technique, inner conductor of the coaxial connector extends through the dielectric and is soldered to the radiating patch, while the outer conductor is connected to the ground plane. For the present design, the substrate chosen is glass epoxy and the reasons for selection of glass epoxy are low cost, compact size and easily available for mass production.

3. Specifications

A specification is an explicit set of requirements to be satisfied by the antenna. The technical specifications for

TABLE 1: Specifications of 1.176 GHz and 2.487 GHz antennas.

Serial number	Parameters	1.176 GHz antenna	2.487 GHz antenna	Unit
(1)	Frequency band	1.16–1.19	2.46–2.50	GHz
(2)	Gain	−4 (Minimum)	−4 (Minimum)	dBi up to $\pm 50^\circ$
(3)	Axial ratio	3	3	dB
(4)	Polarization	LHCP	LHCP	
(5)	3 dB beam width	$\pm 50^\circ$	$\pm 50^\circ$	

both the antennas have been shown in Table 1. Based on communication link between associated application and the satellite, this technical specification came in to the picture. It is evident from Table 1 that antennas bandwidth must large enough such that frequency of operation has to be included within the band. The numerical values of the bandwidths are 30 MHz and 40 MHz, respectively, for both the antennas respectively. Apart from bandwidth consideration, the gain must exceed −4 dBi and feed point must be set up such that left-hand circular polarization (LHCP) is obtained.

4. Design Layout

This section deals with the layout for both antennas. We will discuss design criteria regarding physical dimensions as well as probe position.

The layout of the 1.176 GHz microstrip antenna is shown in Figure 3. In this layout, tip-truncated ETMSA has been devised to get the circular polarization. Truncated portion creates two dominant modes with equal amplitude and 90° phase difference. Both modes are applied on orthogonal plane to generate circular polarization. This method is employed because of good axial ratio and bandwidth. The sides of the patch have been optimized as 72.43 mm, 78.55 mm, and 72.45 mm, respectively, for three sides of the triangle. These lengths of the patch side offer the required specification of the antenna operating at 1.176 GHz. The probe position plays a significant role in designing the patch antenna. Several iterations have been performed to achieve the exact impedance matching. At the same time, the resonant frequency is controlled by changes in dimensions of the patch. For the design of 1.176 GHz patch, it has been noticed that port *P* of coordinate (1.9, 35.4) in Figure 3 is required position of the probe for maximum impedance matching where the lower vertex of the antenna is assumed at the position (0, 0).

The layout of the 2.487 GHz microstrip antenna is also similar to Figure 3. As shown in Figure 3, the sides of the patch have been optimized as 31.1 mm, 36.5 mm, and 31.1 mm, respectively, for three sides of the triangle. These lengths of the patch sides offer the required specification of the antenna operating at 2.487 GHz. For the design of 2.487 GHz patch, we have noticed that port *P* of coordinate

(0.78, 15) in Figure 3 is required position of the probe for maximum impedance matching where the lower vertex of the antenna is assumed at the position (0, 0).

5. Outcomes of 1.176 GHz and 2.487 GHz Antenna

This section discusses simulated and measured results. We have attempted to analyze the specific design parameters in Section 3 for 1.176 GHz antenna. An electromagnetic modeling tool, Ansoft designer, has been employed to simulate the required specifications of the antenna. The following subsection deals with the results in terms of return loss, bandwidth, smith plot, axial ratio, and gain radiation pattern.

5.1. Outcomes of 1.176 GHz Antenna

5.1.1. Outcomes. Figure 4 is return loss diagram analyzed using Ansoft designer version 2 software tool. It points out that the antenna is resonating at 1.176 GHz frequency and providing a large enough bandwidth of 30 MHz ranging from 1.17 GHz to 1.20 GHz at the level of 10 dB return loss. This value of bandwidth has been achieved after several iterations optimizing several parameters in the design. The measured return loss curves have been also presented in Figure 4. The desired frequency of operation has been attained on 4.8 mm thickness of the substrate. As glass-epoxy substrate sheet was available with 1.6 mm thickness, and the required thickness of the substrate was 4.8 mm (according to design), therefore, three layers of the substrate were stacked together to get the desired thickness for the specific design. These three layers have been stacked by two ways; firstly, they have been stacked with air gapping and secondly, they have been stacked using the adhesive. In both the cases measurements have been carried out. Simulated and measured impedance matching plots have been performed using Ansoft tool and Vector Network Analyzer (VNA), respectively. The reflection coefficient and impedance matching were found exactly as desired. Gain radiation pattern and axial ratio diagrams are shown in Figures 5 and 6, respectively.

5.1.2. Results Analysis. For 1.176 GHz antenna, Figure 4 is showing that the antenna is resonating at 1.176 GHz corresponding to lower data cursor in simulated labeled return loss curve. This depicts that at 10 dB S_{11} , bandwidth of 30 MHz is achieved ranging from 1.17 GHz to 1.20 GHz. The measured return loss with adhesive and air gap have been shown with corresponding lower cursor points in the same Figure 4. In our design, the center frequency is 1.176 GHz but the measured center frequency using Vector Network Analyzer (VNA) becomes 1.226 GHz in case of air gap and 1.221 GHz in case of adhesive, both of them are shifted toward the right. The possible reasons for center frequency shift and bandwidth are as follows.

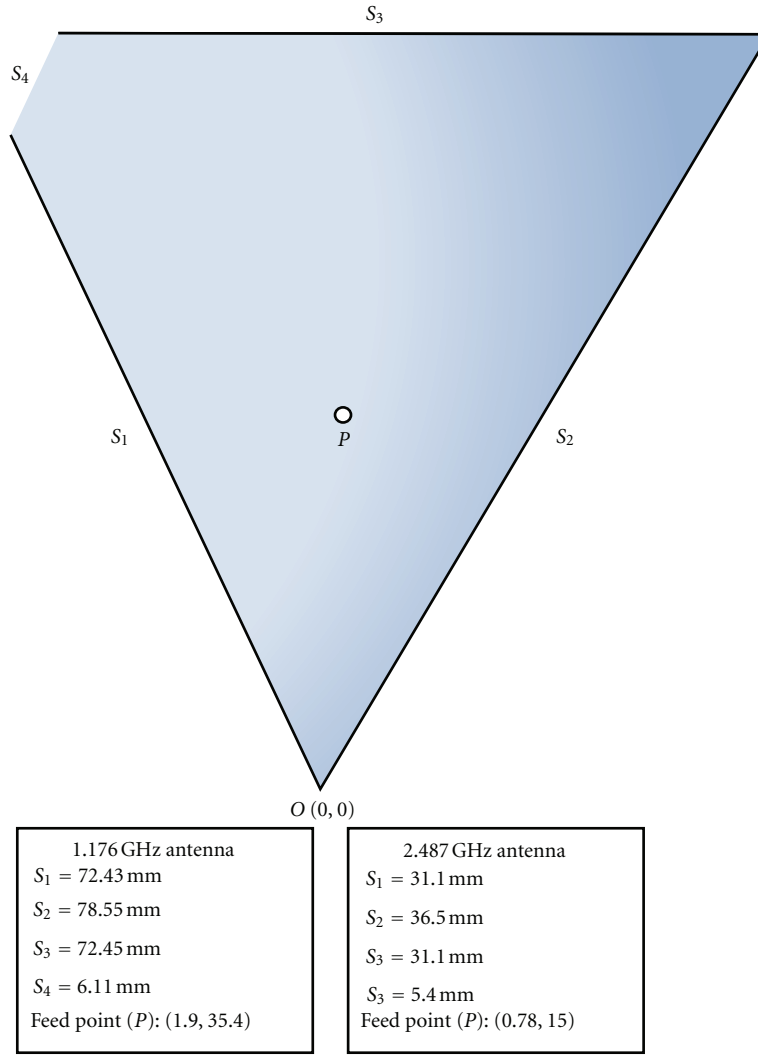


FIGURE 3: Layout of 1.176 GHz and 2.487 GHz Antennas.

- (i) We have considered the dielectric material of thickness 4.8 mm, but it is not available with this thickness. Therefore, three 1.6 mm sheets of glass epoxy are stacked together to get the desired specification.
- (ii) Another reason for frequency shift is that the effective dielectric constant must decrease due to insertion of some gaps among these three layers of glass epoxy.

In a similar way, the return loss of the antenna is measured with the air gap in between the sheets of the glass epoxy, which is also shifted due to the change in the effective dielectric material of the antenna.

The simulated impedance plot shows that there is a loop formation near 1.0, which indicates that the antenna is circularly polarized, and inductive reactance is created by a change in thickness of actual hardware. The resonant frequency, that is, 1.176 GHz, is at the nearest point in the loop that shows the perfect behavior of the patch antenna. The measuring Smith plot for both adhesive and air gap

1.176 GHz antenna have been performed. The measured and simulated impedance plots are very close to each other.

From gain radiation pattern, shown in Figure 5, it can be stated that the gain along the bore sight is around 5.14 dBi. The radiation pattern has been constructed for three different angles of Φ , that is, 0° , 45° , and 90° , which gives the pattern appropriate to the specification. For the angle theta (θ) of $\pm 70^\circ$, the gain pattern is reasonable. The axial ratio for the specified patch antenna is shown in Figure 6. It has been shown that the axial ratio is 2.17 dB and in practical case it should be less than 3 dB. Hence, this also fulfills the requirement of the design. Figure 7 is the actual 1.176 GHz antenna developed fulfilling the required specification showing its patch side where as the other side of the antenna has a coaxial probe, soldered with the patch through 3 mm Via.

5.2. Outcomes of 2.487 GHz Antenna. This section discusses simulated and measured results. We have attempted to analyze the appropriate designing parameters in Section 3

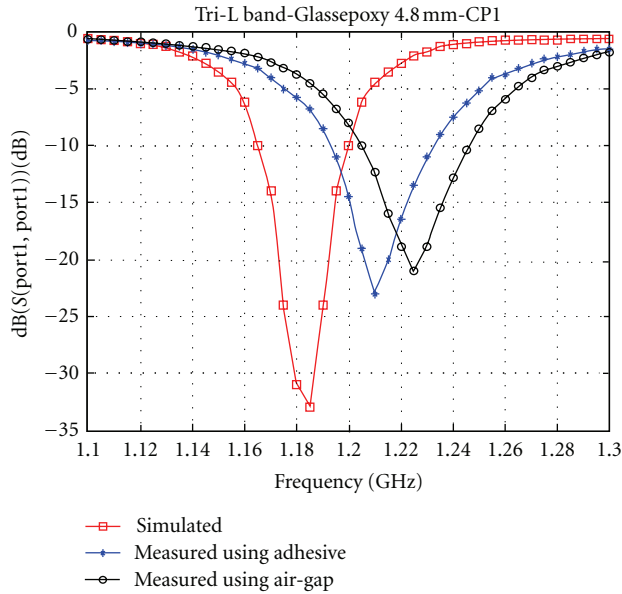


FIGURE 4: Return loss diagram.

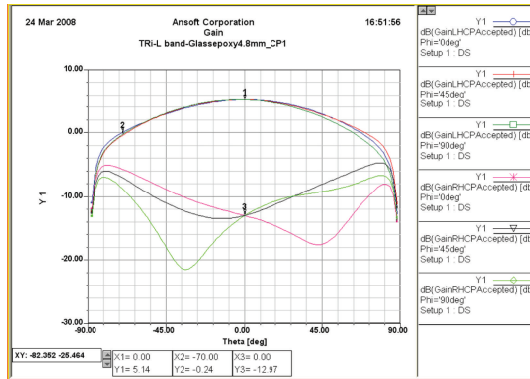


FIGURE 5: Gain radiation pattern.

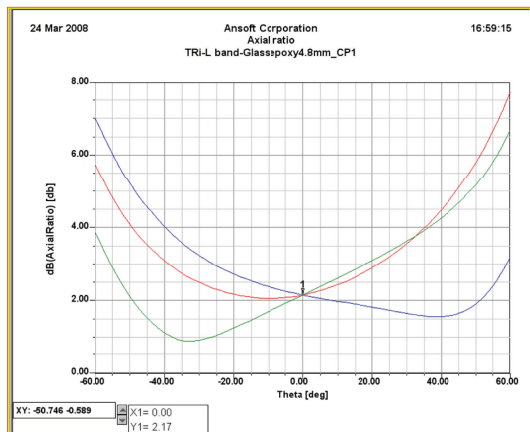


FIGURE 6: Axial ratio.

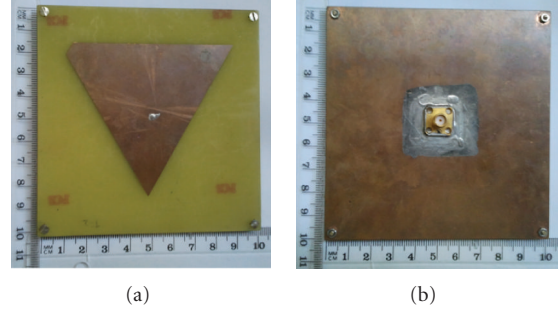


FIGURE 7: Developed 1.176 GHz antenna: left-radiation face, right-ground face with 3 mm Via.

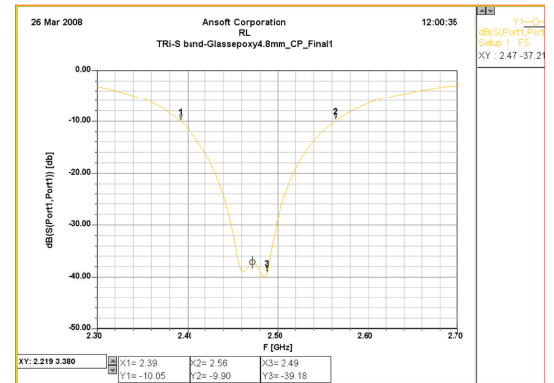


FIGURE 8: Simulated return loss.

for 2.487 GHz antenna. Ansoft designer has been employed to simulate the required specifications of the antenna. The following subsection deals with the results in terms of return loss, bandwidth, smith plot, axial ratio, and gain radiation pattern for this antenna.

5.2.1. Outcomes. Simulated return loss diagram has been presented in Figure 8 using RF design tool, Ansoft designer version 2 software. It shows that the antenna is resonating at 2.487 GHz frequency and providing the superior bandwidth of 170 MHz ranging from 2.39 GHz to 2.56 GHz at the level of 10 dB return loss. This value of bandwidth is obtained after several iterations with optimized parameters in design. The measured return loss diagrams are shown in Figures 9 and 10 in presence of adhesive and the air gap, respectively. Again, there is same problem for stacking the sheets of glass epoxy due to unavailability of 4.48 mm single sheet. This problem has been sorted out by stacking three sheets of 1.16 mm together using adhesive and using air gap in between the sheets. In both instances, the measurements have been carried out.

5.2.2. Results Analysis. For 2.487 GHz antenna, Figure 8 is showing that the antenna is resonating at 2.487 GHz corresponding to data cursor 3 where as data cursor 1 and 2 at the level of 10 dB providing a good bandwidth of approximately 170 MHz ranging from 2.39 GHz to 2.56 GHz. The measured return loss with adhesive and air gap has

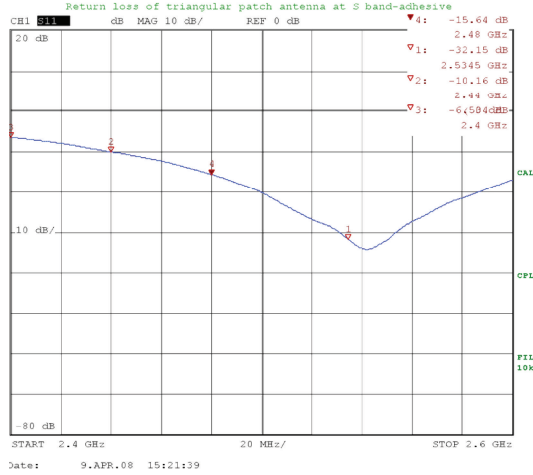


FIGURE 9: Measured return loss using adhesive.

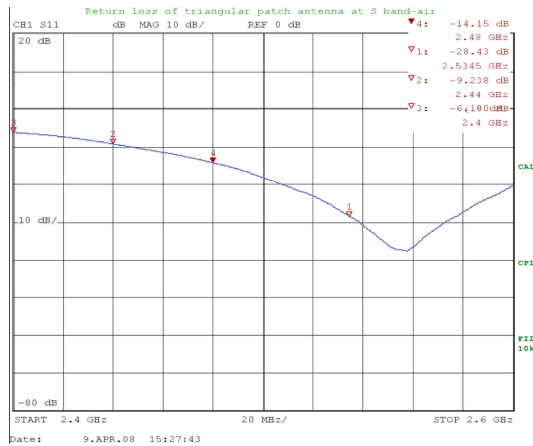


FIGURE 10: Measured return loss using air gap.

been shown in Figures 9 and 10, respectively. In our design the center frequency is 2.487 GHz but the measured center frequency using Vector Network Analyzer is 2.5345 GHz, which is shifted toward the right. The possible reasons for center frequency shift and bandwidth are the same as in the case of 1.176 GHz antenna. Similarly the return loss of the antenna is measured with the air gap in between the sheets of the glass epoxy, which is also shifted due to the change in the effective dielectric material of the antenna.

The impedance plot for this antenna had shown that there was a loop formation near 1.0, which indicates that the antenna is circularly polarized, and inductive reactance is created by a change in thickness of actual hardware. The resonant frequency, that is, 2.487 GHz, is at the nearest point in the loop that shows the perfect behavior of the patch antenna. The measuring smith chart for both adhesive and air gap 2.487 GHz antenna have been performed. Here also the measured and simulated smith plots are nearly similar.

From gain radiation pattern, shown in Figure 11, it can be stated that the gain along the bore sight is around 5.07 dBi. The radiation pattern has been manipulated for

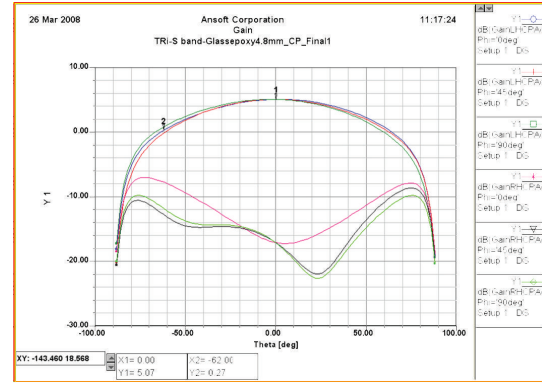


FIGURE 11: Gain radiation pattern.

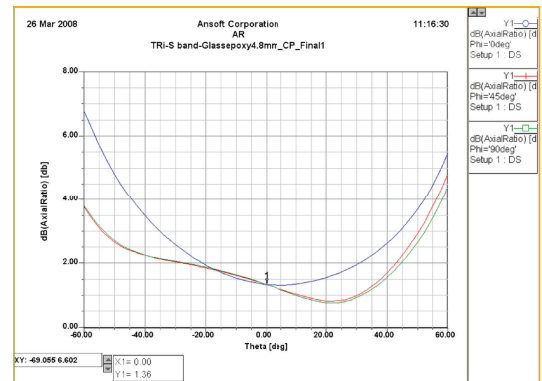


FIGURE 12: Axial Ratio.

three different angles of Φ that is, 0° , 45° and 90° , which gives the pattern appropriate to the specification. For the angle theta (θ) of $\pm 62^\circ$ the gain pattern is reasonable. The axial ratio for the specified patch antenna is shown in Figure 12. It has been shown that the axial ratio is 1.36 dB and in practical case it should be less than 3 dB. Hence this also fulfills the requirement of the design. Figure 13 is the actual 2.487 GHz antenna developed fulfilling the required specification showing its patch side where as the other side of the antenna has a coaxial probe, soldered with the patch through 3 mm Via.

6. Fabrication Process

The antenna artwork has been composed using a software tool, AutoCAD 2000. Here, the whole fabrication process flow is presented briefly. The photoetching process utilizes the final schematic constructed in AutoCAD 2000. Following steps have been carried to perform the etching process.

- (i) Cutting and lamination as per antenna layout
- (ii) Scanning and making film for desired pattern of the layout on the laminate.
- (iii) Etching process where the scanned laminate use chemical liquid to wipe off the unwanted copper area.

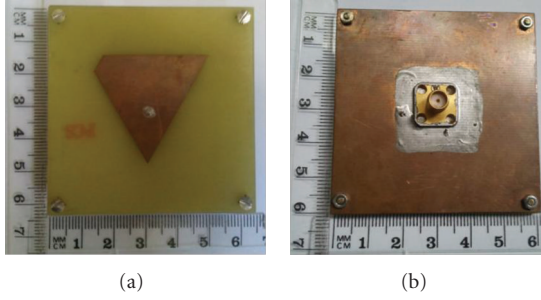


FIGURE 13: Developed 2.487 GHz antenna: left-radiation face, right-ground face with 3 mm Via.

TABLE 2: Measurement of 1.176 GHz antenna.

Serial number	Parameters	Value	Unit
(1)	Measured center frequency	1.21	GHz
(2)	Return loss (adhesive)	Better than 10 dB	
(3)	Return loss at 1.176	3.3	dB

The Fabrication process begins with the final drawing layout of 1.176 GHz triangular patch, 2.487 GHz triangular patch designed using simulation software tool. This layout is exported to the AutoCAD 2000 and saving it in DXF format, as this format of layout has easily been readable by film making machine. This machine changes the DXF format into the gbx (Gerber) format and the resolution of the machine was set to 10000 dpi. The machine is capable of producing the film up to 20000 dpi and it utilizes the transparent photo plotter film of size 24 inch by 28 inch. The machine is capable of printing copper patch on the glass epoxy substrate using subtractive printing methodology. Presently, several additive printing technology and equipments are available in market.

Then the film was sent to fabrication where etching, rinsing, scrapping, and drying processes were carried out. The 50 ohm SMA is the soldered at the feeding point of the fabricated antenna.

7. Measurement

After developing the antennas, their required performances have been measured. The return loss of the antennas has been measured with Vector Network Analyzer (VNA). The observed measurement values for the 1.176 GHz antenna are shown in Table 2. In our design, the center frequency is 1.176 GHz but the measured center frequency using Vector Network Analyzer is 1.226 GHz, which is shifted toward the right.

In the similar manner, 2.487 GHz antenna has been developed and measured its required characteristics. Here again the return loss of the antenna has been measured with Vector Network Analyzer (VNA). Table 3 demonstrates the observed measurement values for the 2.487 GHz antenna. In the similar way, return loss of the antenna has been measured in presence of air gap in between the sheets of the glass epoxy.

TABLE 3: Measurement of 2.487 GHz antenna.

Serial number	Parameters	Value	Unit
(1)	Measured center frequency	2.53	GHz
(2)	Return loss (adhesive)	Better than 10 dB	
(3)	Return loss at 2.487	3.1	dB

8. Conclusion and Future Works

Our research makes significant contributions in the field of electromagnetic modeling and antenna design. Obvious practical implications of our results reveals that successive and iterative optimization on the parameters of microstrip antenna leads to achieve the required performances suitable for specific applications. We performed the modelings based on glass epoxy as a substrate material and copper as a radiating patch. The measured performances such as return loss, frequency of operation, bandwidth, and axial ratio have the similar characteristics as of obtained theoretically using simulating tool. We have found slight shift in the frequencies due to stacking of the glass epoxy sheets. The gain radiation pattern has been measured and found better than expected. This research has made possible to fabricate an antenna satisfying the required specifications and allowing us to create a compact and low-cost tip-truncated triangular antenna.

There are several avenues for further research. The first important future work is to reflect on optimization of technology. In our earlier studies [19–24], we have analyzed additive printing methodologies for RFID-based applications and investigated environmental friendly designs for printed antenna. Therefore, first important future work is to analyze several printing methodology for such antenna technology and evaluate their environmental impacts and resources utilized in both technologies. Another imperative future work is to improve the efficiency of the designed antenna using latest numerical techniques and recent electromagnetic modeling tool. Finally, it would be worthwhile to examine the role of copper traced printed antennas and to explore its environmental emissions during manufacturing process.

Acknowledgment

The authors would like to thank iPack Centre, Royal Institute of Technology, KTH, for providing software tools and necessary supports to carry out these investigations.

References

- [1] A. O. Karilainen, P. M. T. Ikonen, C. R. Simovski et al., "Experimental studies on antenna miniaturisation using magneto-dielectric and dielectric materials," *IET Microwaves, Antennas & Propagation*, vol. 5, no. 4, pp. 495–502, 2011.
- [2] S. Fargeot, A. Julien-Vergonjanne, and P. Guillon, "Dielectric resonator antenna for material characterization," in *Proceedings of the International Conference on Precision Electromagnetic Measurements Digest*, pp. 70–71, June 1996.

- [3] A. Louzir, P. Minard, and J. F. Pintos, "Parametric study on the use of magneto-dielectric materials for antenna miniaturization," in *Proceedings of the IEEE International Symposium (APSURSI) on Antennas and Propagation Society*, pp. 1–4, July 2010.
- [4] K. D. Jang, J. H. Kim, D. H. Lee, G. H. Kim, W. M. Seong, and W. S. Park, "A small CRLH-TL metamaterial antenna with a magneto-dielectric material," in *Proceedings of the International Symposium on Antennas and Propagation Society (AP-S '08)*, pp. 1–4, July 2008.
- [5] G. Kumar and K. P. Ray, "Chapter-2: regularly shaped broadband MSAs," in *A Book on Broadband Microstrip Antenna*, Artech House Antennas and Propagation Library, pp. 32–81, 2002.
- [6] R. K. Kanth, A. K. Singhal, P. Liljeberg, and H. Tenhunen, "Design of multiband fractal antenna for mobile and handheld terminals," in *Proceedings of the 1st Asian Himalayas International Conference on Internet (AH-ICI '09)*, pp. 1–4, November 2009.
- [7] R. K. Kanth, W. Ahmad, Y. Amin, P. Liljeberg, L.-R. Zheng, and H. Tenhunen, "Analysis, design and development of novel, low profile microstrip antenna for satellite navigation," in *Proceedings of the 14th International Symposium on Antenna Technology and Applied Electromagnetics & the American Electromagnetics Conference (ANTEM-AMEREM '10)*, pp. 1–4, July 2010.
- [8] R. K. Kanth, W. Ahmad, Y. Amin, P. Liljeberg, L. R. Zheng, and H. Tenhunen, "Analysis, design and development of novel, low profile 2.487 GHz microstrip antenna," in *Proceedings of the 14th International Symposium on Antenna Technology and Applied Electromagnetics and the American Electromagnetics Conference (ANTEM/AMEREM '10)*, July 2010.
- [9] R. K. Kanth, W. Ahmad, S. Shakya, P. Liljeberg, L.-R. Zheng, and H. Tenhunen, "Autonomous use of fractal structure in low cost, multiband and compact navigational antenna," in *Proceedings of the 10th Mediterranean Microwave Symposium (MMS '10)*, pp. 135–138, August 2010.
- [10] H. Kumar, R. Kumar Kanth, P. Liljeberg, and H. Tenhunen, "Metamaterial based slotted patch antenna," in *Proceedings of the 10th International Conference on Telecommunication in Modern Satellite Cable and Broadcasting Services (TELSIKS '11)*, vol. 1, pp. 43–46, 2011.
- [11] H. Kumar, M. D. Upadhyay, R. K. Kanth, and P. Liljeberg, "Study of electronically tunable circular patch antenna," in *Proceedings of the 10th International Conference on Telecommunication in Modern Satellite Cable and Broadcasting Services (TELSIKS '11)*, vol. 2, pp. 536–539, 2011.
- [12] A. Thabet, A. Z. El Dein, and A. Hassan, "Design of compact microstrip antenna by using new nanocomposite materials," in *Proceedings of the IEEE 4th International Conference on Nanoelectronics (INEC '11)*, pp. 1–2, 2011.
- [13] Y. Ushijima, E. Nishiyama, and M. Aikawa, "Dualpolarized microstrip array antenna with orthogonal feed circuit," in *Proceedings of the IEEE International Symposium on Antennas and Propagation (APSURSI '11)*, pp. 561–564, 2011.
- [14] J. H. Kim, C. K. Hyeon, and K. Chun, "Performance enhancements of a microstrip antenna with multiple layer substrates," in *Proceedings of the International Symposium on Signals, Systems and Electronics (ISSSE '07)*, pp. 319–322, August 2007.
- [15] T. Seki, N. Honma, K. Nishikawa, and K. Tsunekawa, "Millimeter-wave high-efficiency multilayer parasitic microstrip antenna array on teflon substrate," *IEEE Transactions on Microwave Theory and Techniques*, vol. 53, no. 6, pp. 2101–2106, 2005.
- [16] T. J. Ellis, J.-P. Raskin, G. M. Rebeiz, and L. P. Katehi, "A wide-band CPW-fed microstrip antenna at millimeter-wave frequencies," in *Proceedings of the International Symposium on Antennas and Propagation Society IEEE*, vol. 2, pp. 1220–1223, 1999.
- [17] C. Y. Huang and C. W. Ling, "CPW feed circularly polarised microstrip antenna using asymmetric coupling slot," *Electronics Letters*, vol. 39, no. 23, pp. 1627–1628, 2003.
- [18] K. Kumar and N. Gunasekaran, "A novel wideband slotted mm wave microstrip patch antenna," in *Proceedings of the International Conference on Signal Processing, Communication, Computing and Networking Technologies (ICSCCN '11)*, pp. 10–14, 2011.
- [19] R. K. Kanth, Q. Wan, H. Kumar, P. Liljeberg, L. Zheng, and H. Tenhunen, "Life cycle assessment of printed antenna: comparative analysis and environmental impacts evaluation," in *Proceedings of the IEEE International Symposium on Sustainable Systems and Technology (ISSST '11)*, May 2011.
- [20] R. K. Kanth, Q. Wan, P. Liljeberg, L. Zheng, and H. Tenhunen, "Insight into quantitative environmental emission analysis of printed circuit board," in *Proceedings of the 10th International Conference on Environment and Electrical Engineering (EEEIC.EU '11)*, pp. 1–4, May 2011.
- [21] R. K. Kanth, P. Liljeberg, H. Tenhunen et al., "Evaluating sustainability, environmental assessment and toxic emissions during manufacturing process of RFID based systems," in *Proceedings of the IEEE 9th International Conference on Dependable, Autonomic and Secure Computing (DASC '11)*, pp. 1066–1071, 2011.
- [22] R. K. Kanth, P. Liljeberg, H. Tenhunen et al., "Comparative end-of-life study of polymer and paper based radio frequency devices," *International Journal of Environmental Protection*, vol. 2, no. 8, pp. 23–27, 2012.
- [23] R. K. Kanth, Q. Wan, H. Kumar et al., "Evaluating sustainability, environment assessment and toxic emissions in life cycle stages of printed antenna," *Procedia Engineering*, vol. 30, pp. 508–513, 2012.
- [24] R. K. Kanth, Q. Wan, P. Liljeberg, A. Tuominen, L. Zheng, and H. Tenhunen, "Investigation and evaluation of life cycle assessment of printed electronics and its environmental impacts analysis," in *Proceedings of the NEXT Conference (NEXT '10)*, pp. 52–67, October 2010.

Research Article

Design of Multilevel Sequential Rotation Feeding Networks Used for Circularly Polarized Microstrip Antenna Arrays

Aixin Chen,¹ Chuo Yang,¹ Zhizhang Chen,² Yanjun Zhang,¹ and Yingyi He³

¹ School of Electronic and Information Engineering, Beihang University, Beijing 100191, China

² Department of Electrical and Computer Engineering, Dalhousie University, Halifax, NS, Canada B3J 2X4

³ Institute of Electronic Engineering, China Academy of Engineering Physics, Mianyang, Sichuan 621900, China

Correspondence should be addressed to Aixin Chen, axchen@buaa.edu.cn

Received 8 March 2012; Accepted 11 July 2012

Academic Editor: Hala A. Elsadek

Copyright © 2012 Aixin Chen et al. This is an open access article distributed under the Creative Commons Attribution License, which permits unrestricted use, distribution, and reproduction in any medium, provided the original work is properly cited.

Sequential rotation feeding networks can significantly improve performance of the circularly polarized microstrip antenna array. In this paper, single, double, and multiple series-parallel sequential rotation feeding networks are examined. Compared with conventional parallel feeding structures, these multilevel feeding techniques present reduction of loss, increase of bandwidth, and improvement of radiation pattern and polarization purity. By using corner-truncated square patch as the array element and adopting appropriate level of sequential rotation series-parallel feeding structures as feeding networks, microstrip arrays can generate excellent circular polarization (CP) over a relatively wide frequency band. They can find wide applications in phased array radar and satellite communication systems.

1. Introduction

Circularly polarized (CP) microstrip antenna array is more often used in wireless communication systems as they can be easily mounted on mobile devices and provide more focused radiation beams for better weather penetration and mitigation of multipath reflections [1]. Generally, CP patch antennas can be designed by using single-feed and dual-feed configurations. Both configurations can excite orthogonal modes with a quadrature phase shift [2, 3]. For instance, in [2], by using a simple feed structure and a corner-truncated square patch with a thick air-layer substrate, a single-element antenna can have a CP bandwidth larger than 10%. In [3], dual-feed configuration and sequential rotation feeding technique are applied to achieve a 30% CP bandwidth.

However, problems and issues still exist with a CP array in particular related to the feed network, such as ohmic and dielectric losses, parasitic radiation, and the excitation of surface waves in dielectric substrates. Especially, in *Ka*-band or at millimeter-wave frequency [4, 5], the problems become more severe and have more serious adverse effects on gain and impedance bandwidth than those in lower

frequency bands. One way to improve the performance is to increase size. Another way is to develop efficient feed network configuration [6–10]. In [6], a microstrip antenna array with a relative gain bandwidth of 4.4% with less than 1 dB of gain ripple is developed with the use of a low-loss parallel-series feed topology. The work in [8] proposes a novel 2×2 patch antenna array with a serial feed arrangement which can be easily employed as subarrays in larger arrays.

In this paper, we propose single, double, and multiple series-parallel sequential rotation feeding networks in *Ka*-band for use with 4-element [11], 64-element [12], and 256-element CP microstrip antenna arrays, respectively. In order to show effectiveness of these multilevel feeding networks, they are compared with the conventional parallel feeding networks.

This paper is organized in the following manner. First, the structures of single, double and multiple series-parallel sequential rotation feeding networks and their comparisons with the conventional parallel feeding networks are presented in Section 2. Then, in Section 3, the simulated and/or measured results of the arrays with the proposed feeding networks are shown, compared, and discussed. Finally, in Section 4, the conclusion is drawn.

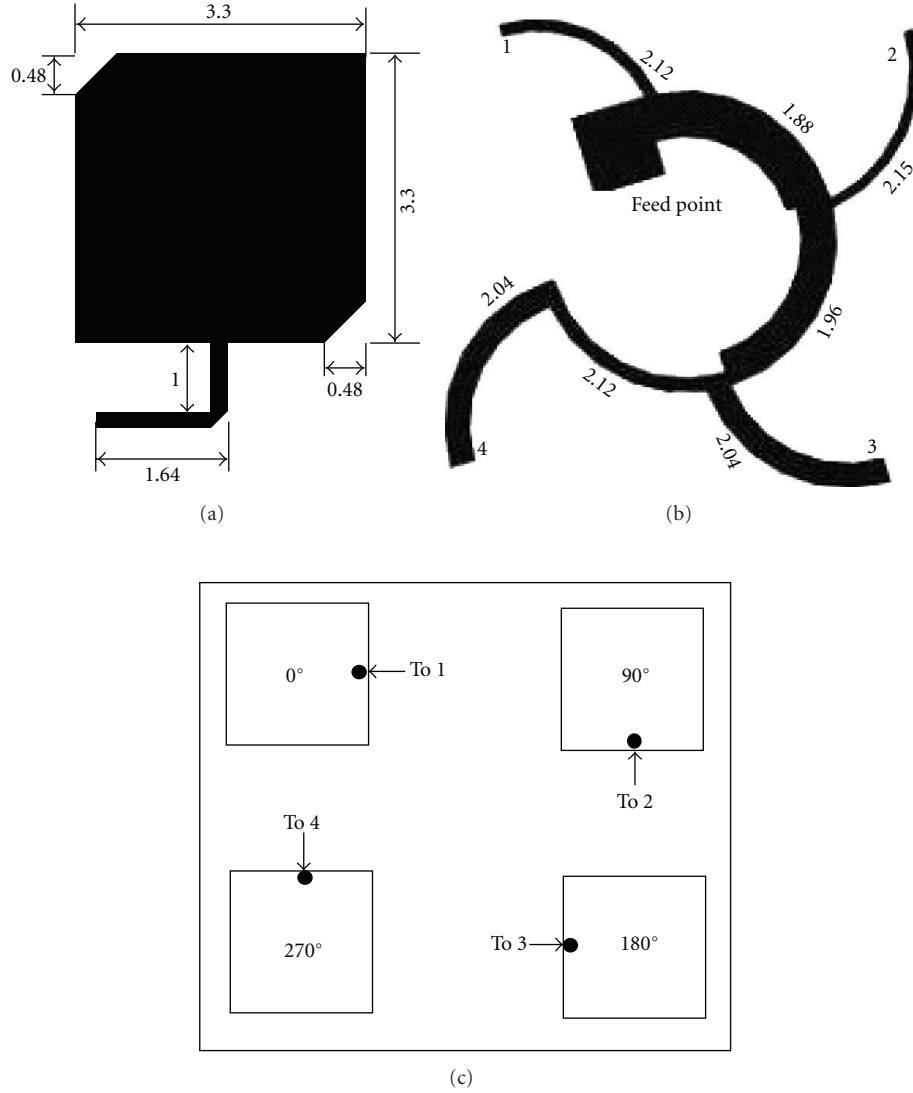


FIGURE 1: (a) Configuration of the single patch element, (b) the proposed single series-parallel sequential rotation feeding network, and (c) four patch elements (unit: millimeters).

2. The Proposed Feeding Networks and Antenna Arrays

Figure 1 shows the configuration of the single patch element, the proposed single series-parallel sequential rotation feeding network and the way four patch elements is connected to the feeding network. These four elements are arranged in a 2×2 square position with element angular orientation and feed phase arranged in a 0° , 90° , 180° , and 270° fashion. The phase arrangement, as well as power distribution, is achieved by the feed lines of quarter-wavelength transformers and power dividers in the feeding network. The series-parallel sequential rotation feeding network and the four radiating elements together can form a 4-element CP antenna array. The reason that a sequential rotation feeding network can significantly improve the performance of circularly polarized antenna arrays is primarily attributed to its capability of phase arrangement and equal power split.

The array element is a corner-truncated microstrip patch [11, 12]. The dimensions of the patch element and the feeding network are shown in Figures 1(a) and 1(b), respectively. With the application of single series-parallel sequential rotation feeding network, the 4-element CP microstrip antenna array can be obtained. Taking 4-element microstrip antenna array as a subarray, and applying double and multiple sequential rotation feeding networks, respectively, the 64-element and 256-element CP antenna arrays can then be obtained. In all cases, the spacing between adjacent elements is 0.77λ , where λ is the free-space wavelength of the central frequency of 29 GHz. The substrate material is RT/duriod5880. It has a thickness of 0.254 mm with a relative dielectric constant of 2.2 and a dielectric loss tangent of 0.0009.

Figure 2 shows the final layout of the arrays. Figure 2(a) is with the single series-parallel sequential rotation feeding network. Figure 2(b) is the conventional parallel feeding

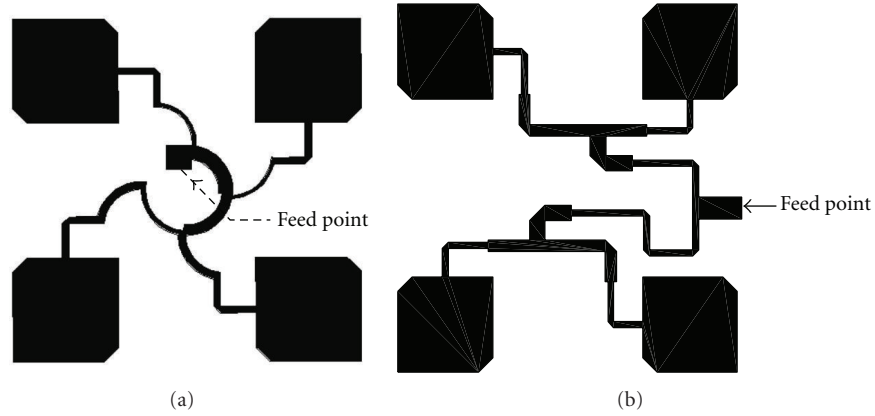


FIGURE 2: 4-element CP antenna arrays; (a) with the single series-parallel sequential rotation feeding network; (b) with the conventional parallel feeding network.

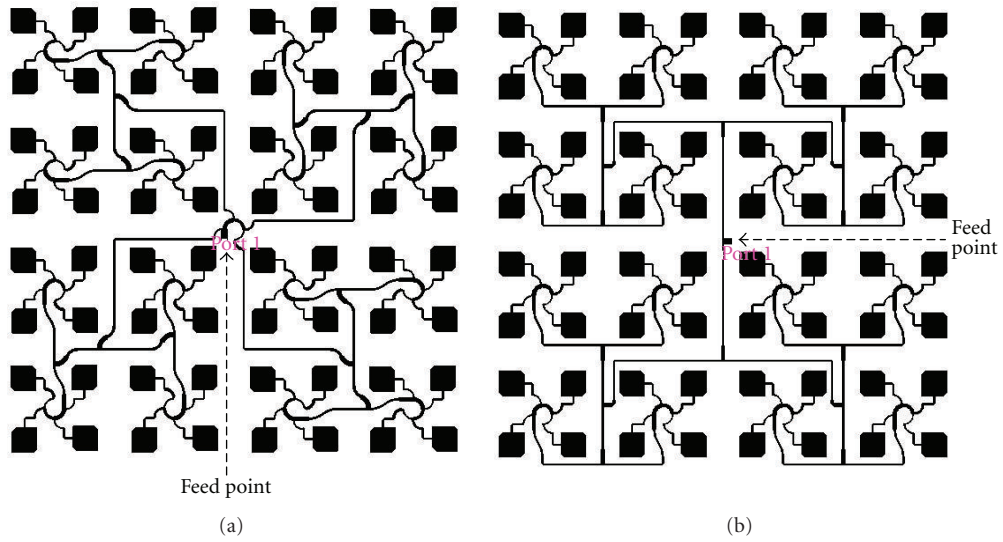


FIGURE 3: 64-element CP antenna arrays; (a) with the proposed double series-parallel sequential rotation feeding network; (b) with the conventional parallel feeding network.

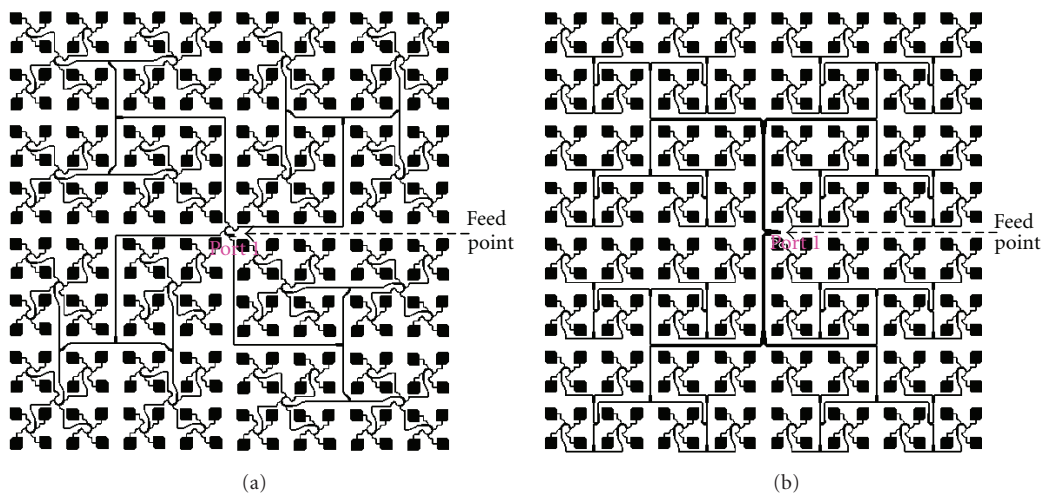


FIGURE 4: 256-element CP antenna arrays; (a) with the proposed multiple series-parallel sequential rotation feeding network; (b) with the conventional parallel feeding network.

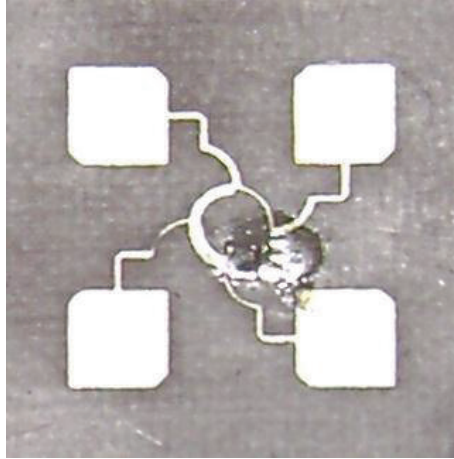


FIGURE 5: Photograph of 4-element CP antenna array with the proposed single sequential rotation feeding network [11].

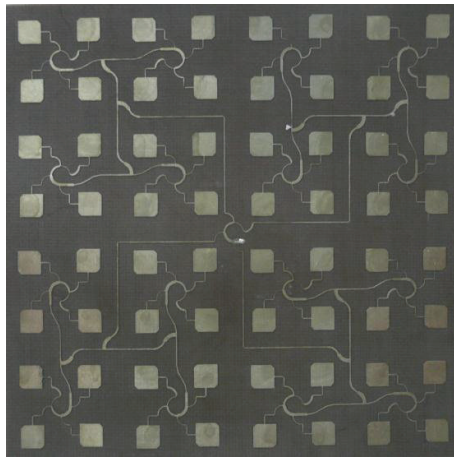


FIGURE 6: Photograph of 64-element CP antenna array with the proposed double sequential rotation feeding network [12].

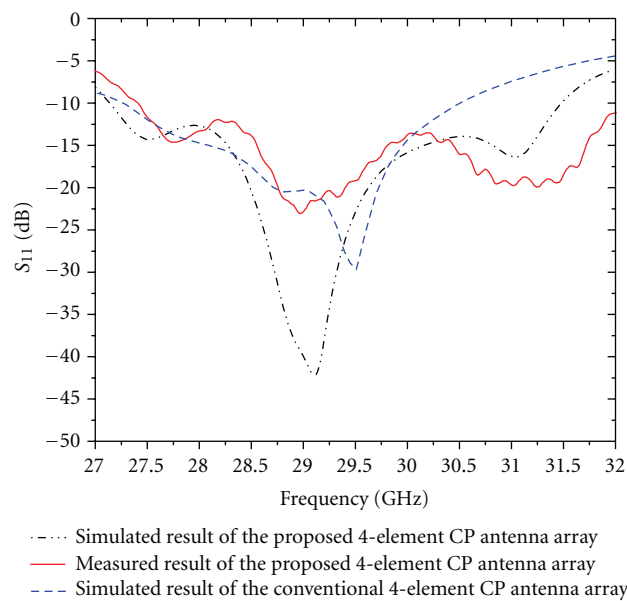


FIGURE 7: Measured and simulated S_{11} of the 4-element CP antenna arrays.

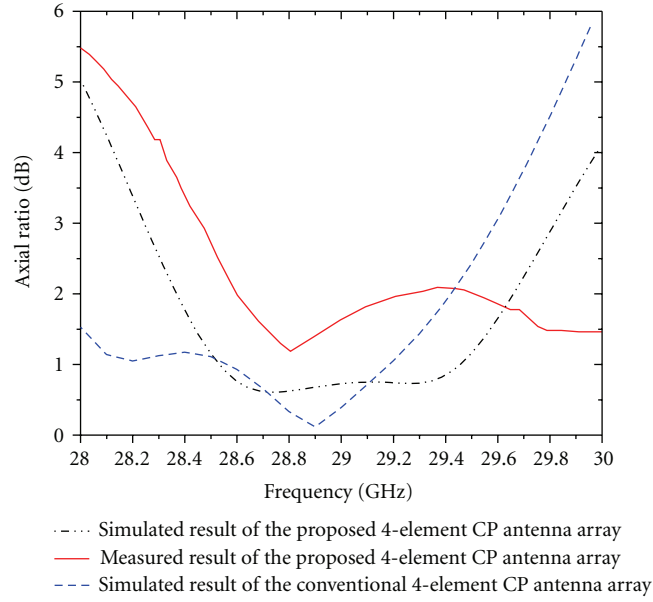


FIGURE 8: Measured and simulated axial ratio of the 4-element CP antenna arrays.

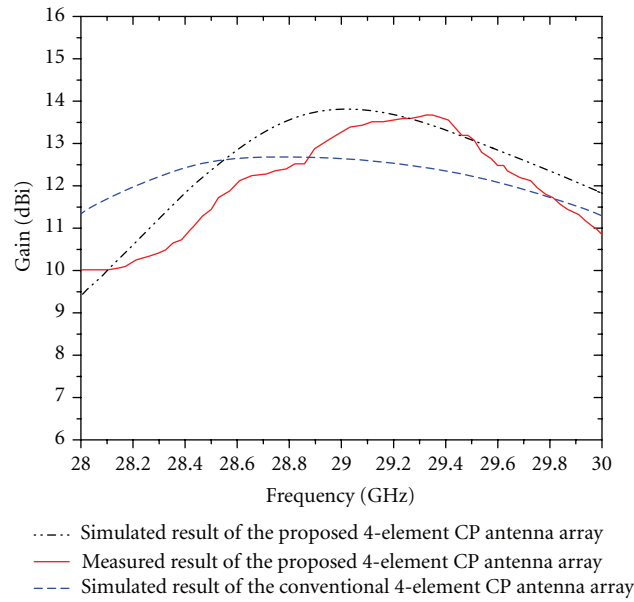


FIGURE 9: Measured and simulated gain of the 4-element CP antenna arrays.

network for the comparison and reference purpose. The phase shift with the reference array is also arranged in a 0° , 90° , 180° , and 270° fashion, just the same as that with the proposed single series-parallel sequential rotation feeding network.

Figure 3 shows the geometry of the 64-element antenna arrays. It can be seen that the 4-element antenna array with single series-parallel sequential rotation feeding network is used as a subarray to construct the larger arrays. Figure 3(a) shows the double applications of the sequential rotation technique: first to four patches to form

a 4-element subarray, and then all the 4-element subarrays to form a 64-element array. Figure 3(b) shows the conventional antenna array with the conventional parallel feeding network.

To investigate the performance of the series-parallel sequential rotation feeding network further, we also designed two 256-element antenna arrays, as depicted in Figure 4. Figure 4(a) shows the antenna array with the sequential rotation technique applied twice. The reference antenna array, shown in Figure 4(b), uses the conventional parallel feeding technique.

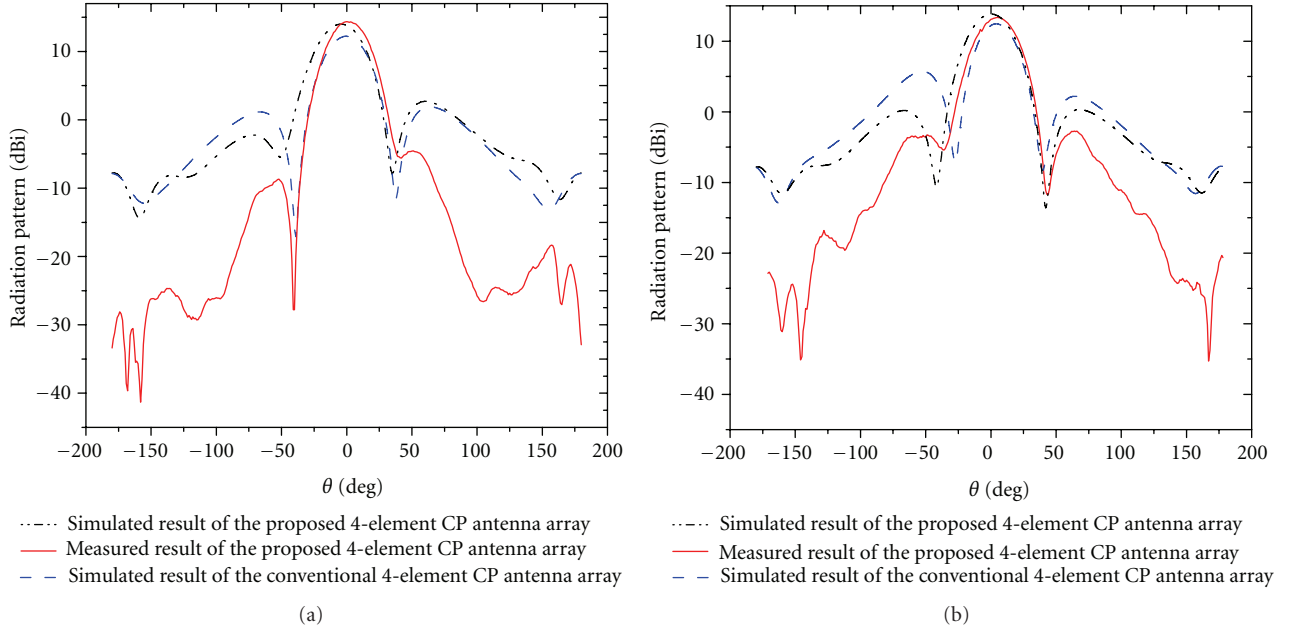


FIGURE 10: Measured and simulated radiation patterns of the 4-element CP antenna arrays at 29 GHz: (a) $\phi = 0^\circ$, (b) $\phi = 90^\circ$.

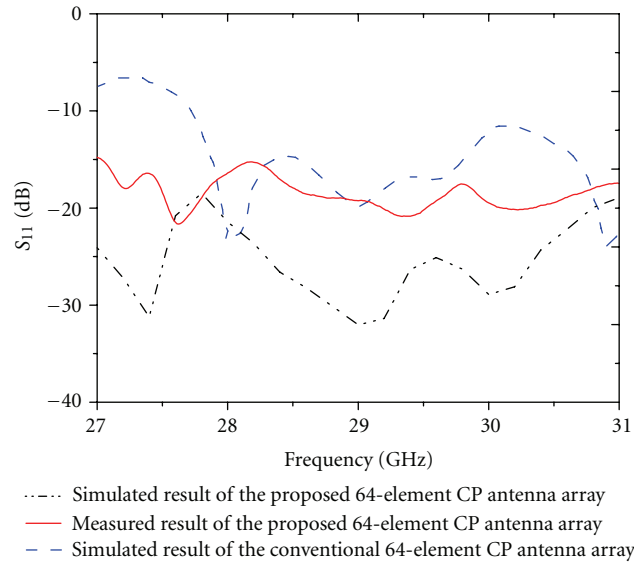


FIGURE 11: Measured and simulated S_{11} of the 64-element CP antenna arrays.

3. Simulated and Measured Results

After simulation and optimization with Ansoft Designer and HFSS, the 4-element and 64-element CP antenna arrays with the parallel-series sequential rotation feeding networks are fabricated and tested. Their photographs are shown in Figures 5 and 6. The measurement results are shown in Figures 7 and 8, along with the simulated results. For the 256-element CP antenna arrays, only simulated results of the arrays with parallel-series sequential rotation feeding networks and with parallel feeding networks are compared.

3.1. 4-Element CP Antenna Arrays. As seen from Figure 7, the measured and simulated results of the 4-element CP antenna array with the single series-parallel sequential rotation feeding network corroborate well for S_{11} . The measured bandwidth of the fabricated 4-element CP antenna array is about 4.33 GHz, or 14.75%, from 27.19 to 31.52 GHz [11]. The simulated result of the conventional 4-element CP antenna array with the parallel feeding network shows the bandwidth of about 3.0 GHz, or 10.34%, from 27.25 to 30.25 GHz.

Figure 8 shows the measured and simulated axial ratio. The figure shows the fabricated 4-element CP antenna array

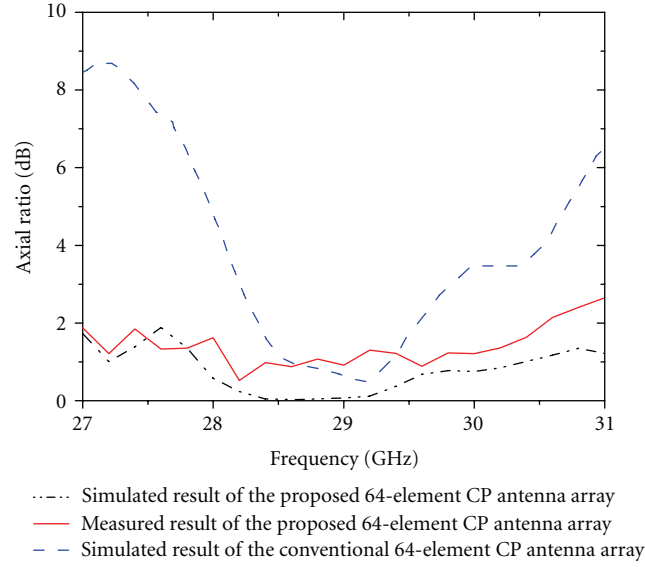


FIGURE 12: Measured and simulated axial ratio of the 64-element CP antenna arrays.

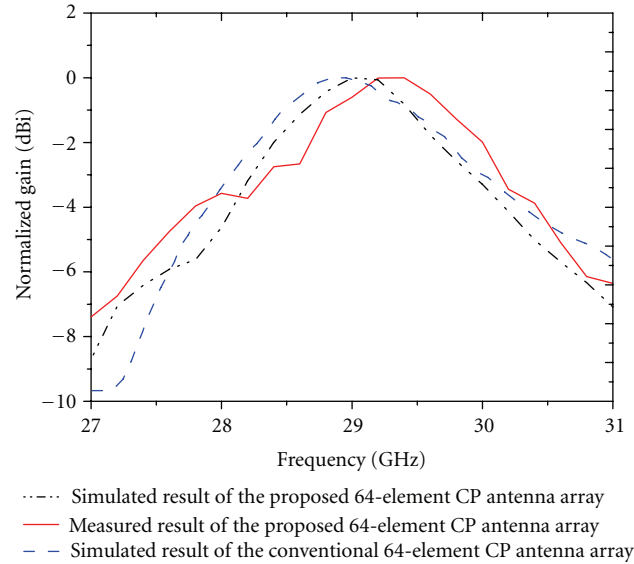


FIGURE 13: Measured and simulated gain of the 64-element CP antenna arrays.

has a 3-dB bandwidth from 28.45 GHz to over 30 GHz [11], and the conventional 4-element CP antenna array's 3-dB bandwidth is from 28 GHz to 29.61 GHz.

Figures 9 and 10 shows the measured and simulated gain and radiation patterns at 29 GHz, respectively. It can be seen that the measured sidelobes of the fabricated 4-element CP antenna array are lower than that of the simulated ones, and the gain of the conventional 4-element antenna array is about 1.5 dBi lower than that of the proposed 4-element CP antenna array with the single series-parallel sequential rotation feeding network. This is mainly due to the fact that the parallel feeding network does not maintain the symmetry of the antenna array.

3.2. 64-Element CP Antenna Arrays. Figure 11 presents the measured and simulated reflection coefficients of the 64-element CP antenna arrays with the double series-parallel sequential rotation feeding network and with the conventional parallel feeding network. It can be seen that the fabricated antenna array has a bandwidth from 27 GHz to 31 GHz [12]. Although the measured reflection coefficient of the proposed array is bigger than its simulated one, it is lower than the simulated coefficient of the conventional antenna array. Moreover, as seen from Figure 7, the double series-parallel sequential rotation feeding network has the lower reflection coefficients than the conventional one; therefore, it reduces the RF power loss.

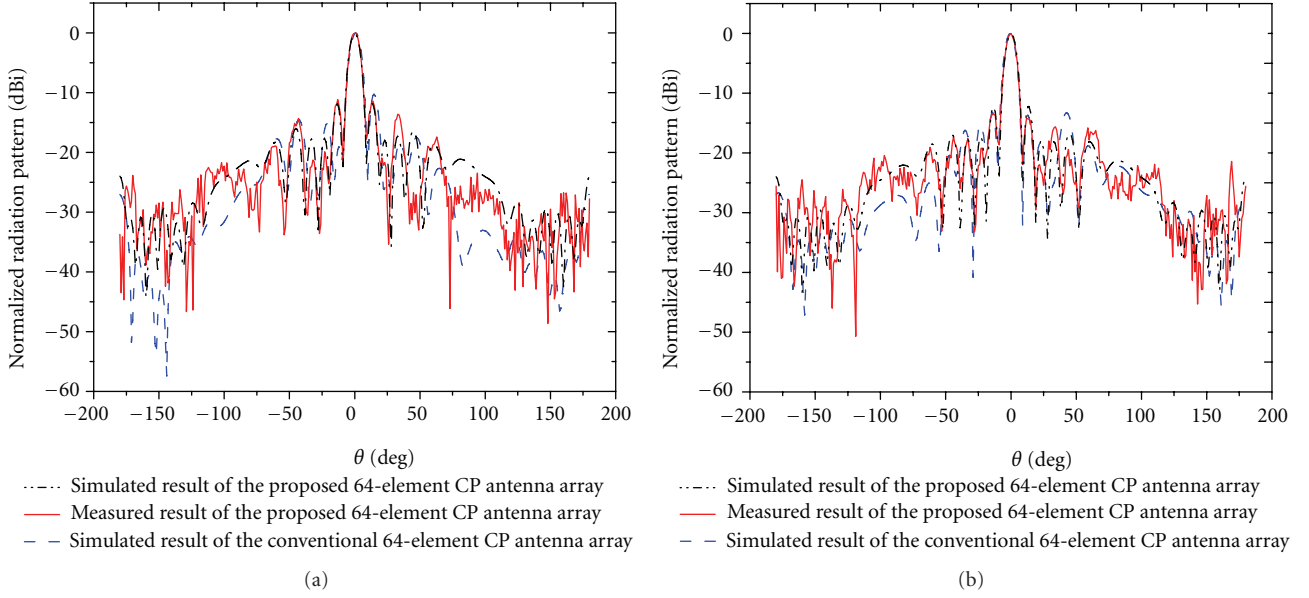


FIGURE 14: Measured and simulated radiation patterns of the 64-element CP antenna arrays at 29 GHz: (a) $\phi = 0^\circ$, (b) $\phi = 90^\circ$.

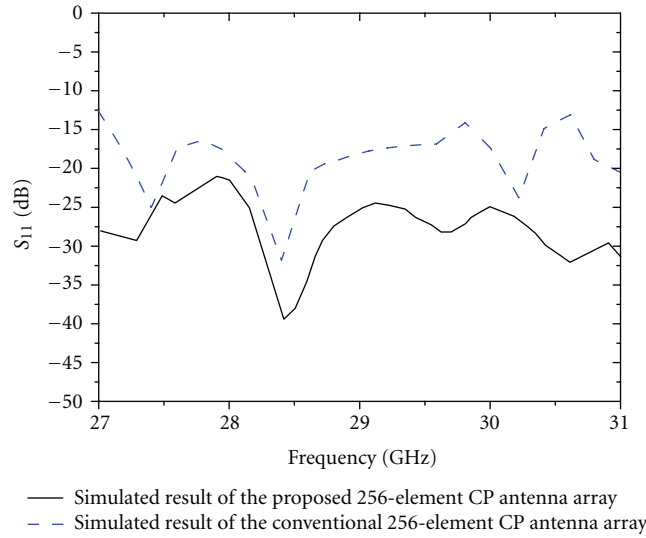


FIGURE 15: Simulated S_{11} of the 256-element CP antenna arrays.

The measured and simulated axial ratio of the proposed 64-element CP antenna arrays is shown in Figure 12. The measured and simulated results are almost at the same level. The 3 dB axial ratio bandwidth covers from 27 GHz to 31 GHz [12]. However, the conventional array has only the bandwidth of about 1.7 GHz, from 28.2–29.9 GHz.

Figures 13 and 14 represent the normalized peak gain versus frequency and the normalized radiation pattern at 29 GHz. The peak gain of the fabricated antenna array is found to be between 16 and 25 dBi [12].

3.3. 256-Element CP Antenna Arrays. Figures 15, 16, 17 and 18 show the results with the 256-element CP antenna array in the frequency range from 27 to 31 GHz. The reflection

coefficient is less than -20 dB, the axial ratio is less than 0.5 dB at most frequencies, and the peak gain is found to be between 20 and 30 dBi (unfortunately, the authors are not allowed to disclose the exact values due to the proprietary requirement by the industrial sponsor of the work). All these results are better than that of the conventional array with the parallel feeding network; this once again proves that the series-parallel sequential rotation feeding network can improve the performance of the CP microstrip antenna arrays, especially when be used in large antenna arrays.

4. Conclusion

In this paper, we investigate the performance of *Ka*-band CP microstrip antenna arrays with single, double and multiple

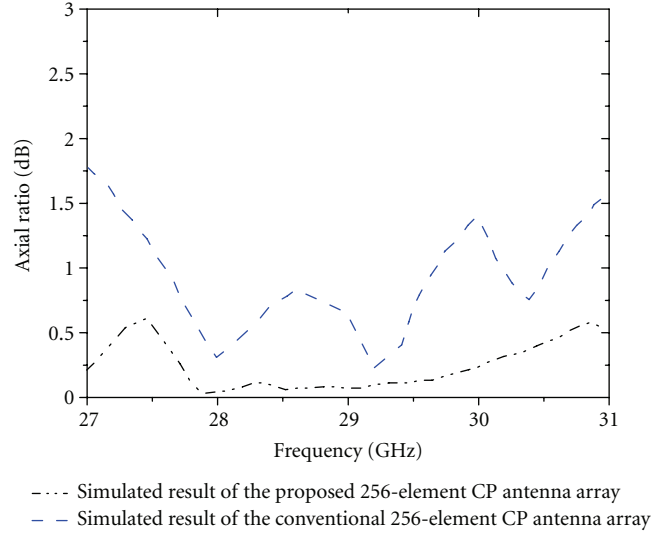


FIGURE 16: Simulated axial ratio of the 256-element CP antenna arrays.

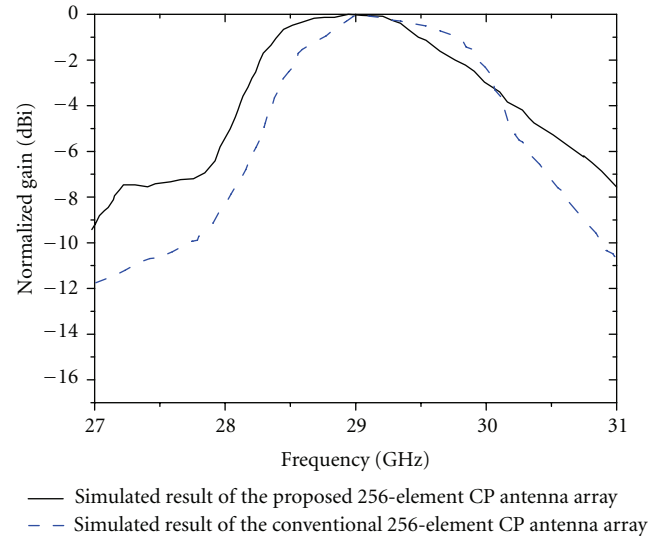
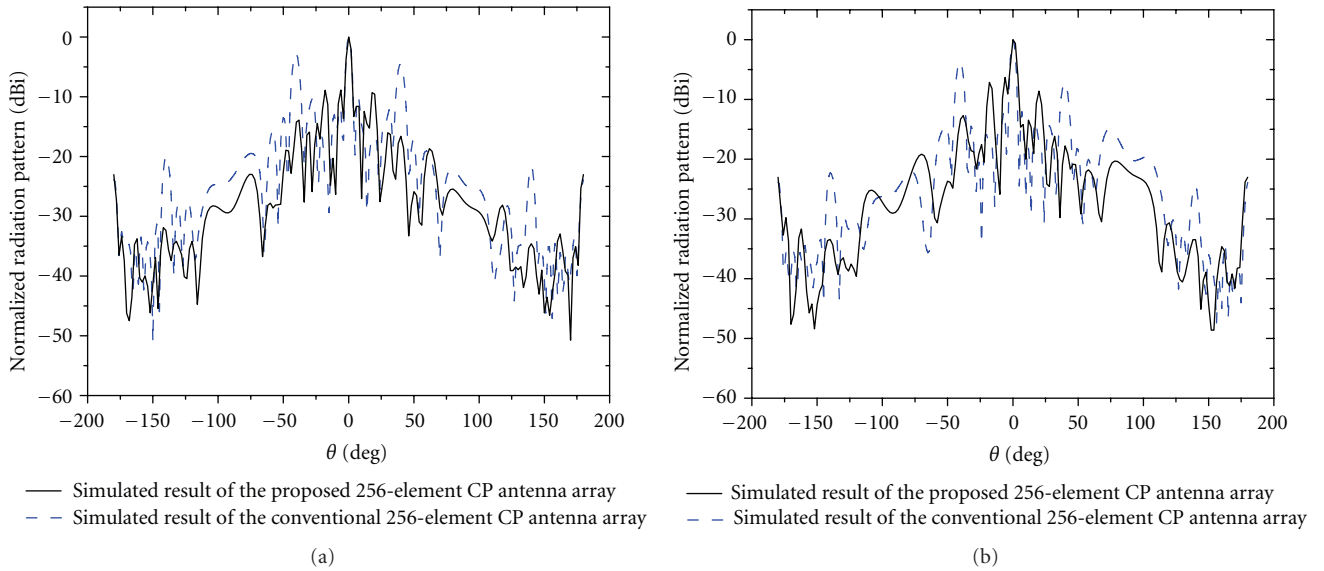


FIGURE 17: Simulated gain of the 256-element CP antenna arrays.

FIGURE 18: Simulated radiation patterns of the 256-element CP antenna arrays at 29 GHz: (a) $\varphi = 0^\circ$, (b) $\varphi = 90^\circ$.

series-parallel sequential rotation feeding network. The 4-element, 64-element and 256-element CP antenna arrays are designed, simulated, fabricated, and tested. By comparing with the performance of the CP antenna arrays with the conventional parallel feeding network, it can be concluded that the multilevel series-parallel sequential rotation feeding technique can significantly reduce the RF loss, broaden the bandwidth, improve the CP purity, and achieve high gain. And the larger the arrays, the better the feeding networks perform. This feeding technique can be widely used in the design of antenna arrays in radar and satellite communication systems.

Acknowledgment

This work was supported in part by the National Science Foundation of China and NSAF under their joint Grant (no. 11076031).

References

- [1] R. Garg, I. Bhartia, I. Bahl, and A. Ittipiboon, *Microstrip Antenna Design Handbook*, Artech House, Boston, Mass, USA, 2001.
- [2] F. S. Chang, K. L. Wong, and T. W. Chiou, "Low-cost broadband circularly polarized patch antenna," *IEEE Transactions on Antennas and Propagation*, vol. 51, no. 10, pp. 3006–3009, 2003.
- [3] R. Caso, A. Buffi, M. Rodriguez Pino, P. Nepa, and G. Manara, "A novel dual-feed slot-coupling feeding technique for circularly polarized patch arrays," *IEEE Antennas and Wireless Propagation Letters*, vol. 9, pp. 183–186, 2010.
- [4] J. Huang, "Ka-band circularly polarized high-gain microstrip array antenna," *IEEE Transactions on Antennas and Propagation*, vol. 43, no. 1, pp. 113–116, 1995.
- [5] B. Biglarbegian, M. Fakharzadeh, D. Busuioc, M. R. Nezhad-Ahmadi, and S. Safavi-Naeini, "Optimized microstrip antenna arrays for emerging millimeter-wave wireless applications," *IEEE Transactions on Antennas and Propagation*, vol. 59, no. 5, pp. 1742–1747, 2011.
- [6] M. Yousefbeigi, A. Enayati, M. Shahabadi, and D. Busuioc, "Parallel-series feed network with improved G/T performance for high-gain microstrip antenna arrays," *Electronics Letters*, vol. 44, no. 3, pp. 180–182, 2008.
- [7] H. Legay and L. Shafai, "A self-matching wideband feed network for micro strip arrays," *IEEE Transactions on Antennas and Propagation*, vol. 45, no. 4, pp. 715–722, 1997.
- [8] H. Evans, P. Gale, B. Aljibouri, E. G. Lim, E. Korolkeiwicz, and A. Sambell, "Application of simulated annealing to design of serial feed sequentially rotated 2×2 antenna array," *Electronics Letters*, vol. 36, no. 24, pp. 1987–1988, 2000.
- [9] T. Yuan, N. Yuan, and L. W. Li, "A novel series-fed taper antenna array design," *IEEE Antennas and Wireless Propagation Letters*, vol. 7, pp. 362–365, 2008.
- [10] E. Levine, G. Malamud, S. Shtrikman, and D. Treves, "Study of microstrip array antennas with the feed network," *IEEE Transactions on Antennas and Propagation*, vol. 37, no. 4, pp. 426–434, 1992.
- [11] A. Chen, Y. Zhang, Z. Chen, and S. Cao, "A Ka-band high-gain circularly polarized microstrip antenna array," *IEEE Antennas and Wireless Propagation Letters*, vol. 9, pp. 1115–1118, 2010.
- [12] A. Chen, Y. Zhang, Z. Chen, and C. Yang, "Development of a Ka-band wideband circularly polarized 64-element microstrip antenna array with double application of the sequential rotation feeding technique," *IEEE Antennas and Wireless Propagation Letters*, vol. 10, pp. 1270–1273, 2011.

Application Article

A Small UWB Antenna with Dual Band-Notched Characteristics

J. Xu,¹ D.-Y. Shen,¹ G.-T. Wang,¹ X.-H. Zhang,¹ X.-P. Zhang,² and K. Wu³

¹ School of Information Science and Engineering, Yunnan University, Kunming 650091, China

² Department of Electrical and Computer Engineering, Concordia University, Montreal, QC, Canada

³ Department of Electrical Engineering, Université de Montréal, Montreal, QC, Canada

Correspondence should be addressed to D.-Y. Shen, shendy@ynu.edu.cn

Received 15 February 2012; Accepted 21 June 2012

Academic Editor: Hala A. Elsadek

Copyright © 2012 J. Xu et al. This is an open access article distributed under the Creative Commons Attribution License, which permits unrestricted use, distribution, and reproduction in any medium, provided the original work is properly cited.

A small novel ultrawideband (UWB) antenna with dual band-notched functions is proposed. The dual band rejection is achieved by etching two C-shaped slots on the radiation patch with limited area. A single band-notched antenna is firstly presented, and then an optimized dual band-notched antenna is presented and analyzed. The measured VSWR shows that the proposed antenna could operate from 3.05 to 10.7 GHz with VSWR less than 2, except two stopbands at 3.38 to 3.82 GHz and 5.3 to 5.8 GHz for filtering the WiMAX and WLAN signals. Radiation patterns are simulated by HFSS and verified by CST, and quasisymmetrical radiation patterns in the H-plane could be observed. Moreover, the proposed antenna has a very compact size and could be easily integrated into portable UWB devices.

1. Introduction

Since the Federal Communication Commission (FCC) allocated the frequency band 3.1–10.6 GHz for commercial ultrawideband (UWB) systems, considerable research efforts have been put into UWB radio technology in industry and academia. Several UWB antennas with compact size have been reported in [1–3] recently. However, UWB systems have encountered a hostile radio environment which may cause potential interferences to the UWB band. For instance, IEEE 802.16 WiMAX system operates at 3.3–3.7 GHz and IEEE 802.11a WLAN system operates at 5.15–5.825 GHz. In some cases, UWB antennas use filters to avoid interferences. However, the use of filters increases the complexity and cost of the UWB system. Thus, antenna-filtering technique may be one of the simple, effective, and inexpensive methods, and antennas with small size and band rejection functions are desirable. In order to design UWB antennas with band-notched functions, several methods have been proposed, including etching C-shaped, L-shaped, T-shaped, H-shaped, U-shaped, E-shaped, and half-circle slots on the radiation patch or on the ground plane [4–14]. Besides, by employing T-shaped, L-shaped, and spiral parasitic strips, band-rejection functions could be obtained [15–20]. By etching slots and employing parasitic strips at the same time [21, 22], dual band-notched functions could be achieved.

In this paper, a small novel ultrawideband antenna with dual band-notched characteristics is proposed and investigated in detail. The primitive UWB antenna has a compact size of $22\text{ mm} \times 18\text{ mm} \times 1.5\text{ mm}$. By etching a C-shaped slot on the radiation patch, a single band-notched UWB antenna is first designed. By adding another C-shaped slot on the radiation patch, a small dual band-notched antenna has been successfully designed. It is observed from the simulated and measured VSWR that the proposed dual band-notched antenna could operate from 3.05 to 10.7 GHz with VSWR less than 2, except two stopbands at 3.38 to 3.82 GHz and 5.3 to 5.8 GHz for filtering the WiMAX and WLAN signals. In addition, the proposed antenna has a nearly omnidirectional radiation patterns at the H-plane across the operating frequency band, which makes it a good candidate for UWB devices.

2. Single Band-Notched UWB Antenna Design and Results

A 3.5 GHz single band-notched UWB antenna is firstly designed, and the specific geometry is shown in Figure 1. The substrate of the antenna is FR4 with a thickness of $h_{\text{sub}} = 1.5\text{ mm}$ and relative dielectric constant of 4.5. An SMA connector is connected to the $50\ \Omega$ microstrip feed line to feed the antenna. The radiation patch has a

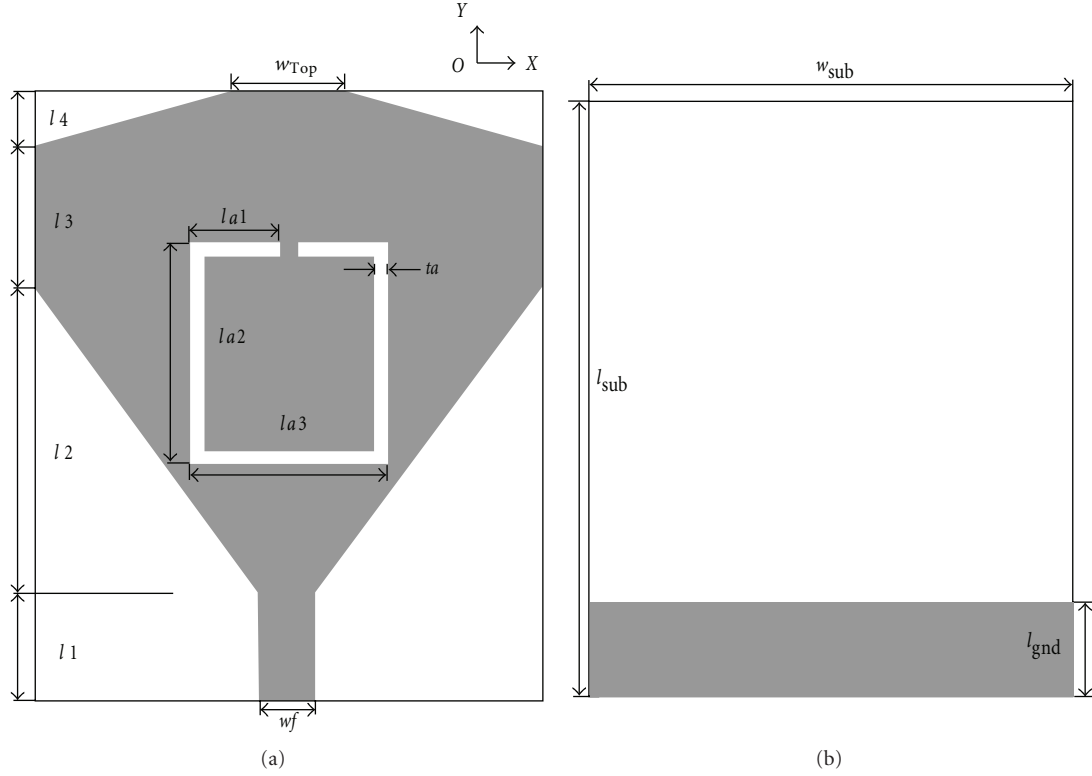


FIGURE 1: Geometry of single band-notched antenna. (a) Top view, (b) bottom view.

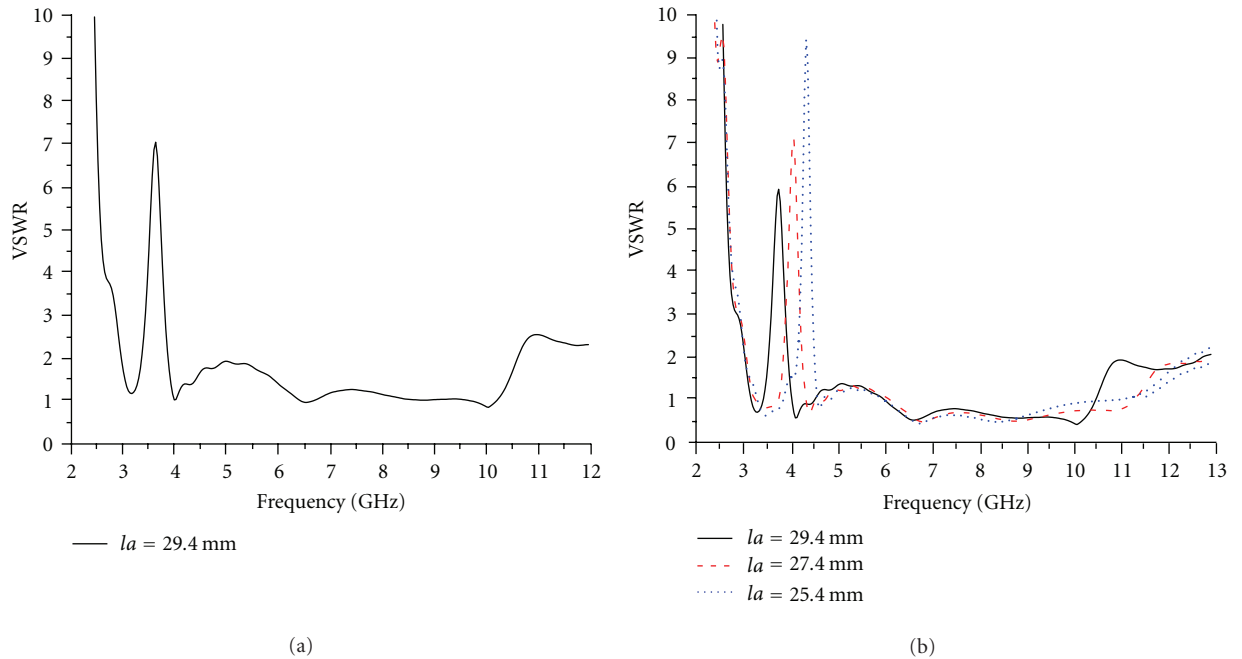


FIGURE 2: Simulated VSWR of single band-notched antenna with (a) optimized l_a , (b) different l_a .

shovel-shaped structure, and the dimensions are optimized using commercial software CST and HFSS. In order to eliminate interferences from IEEE 802.16 WiMAX system linebreak operating at 3.3–3.7 GHz, a C-shaped slot is etched on the patch to generate band rejection function. The

notched frequency generated by the C-shaped slot can be postulated as

$$f_{\text{notch}} = \frac{c}{2L \cdot \sqrt{\epsilon_{\text{eff}}}}, \quad (1)$$

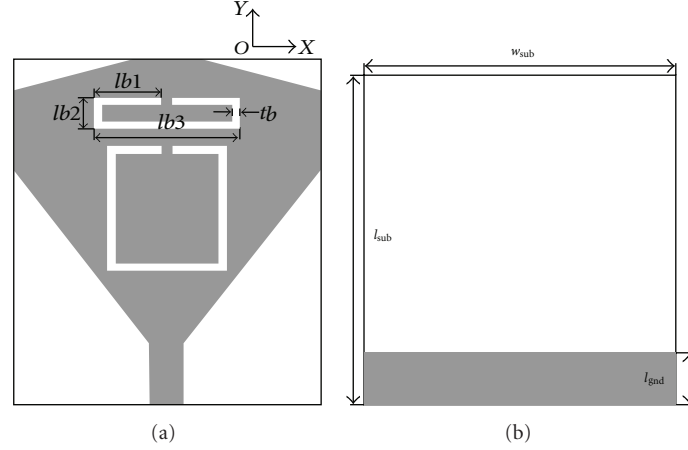


FIGURE 3: Geometry of dual band-notched antenna. (a) Top view, (b) bottom view.

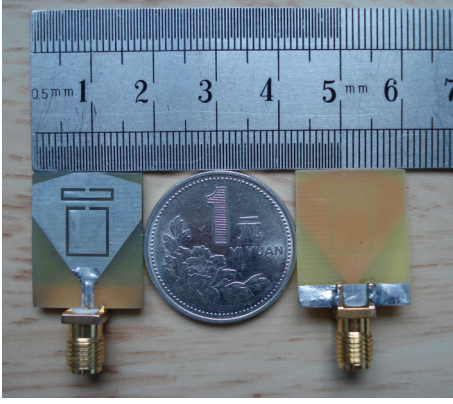


FIGURE 4: Photograph of the proposed dual band-notched antenna.

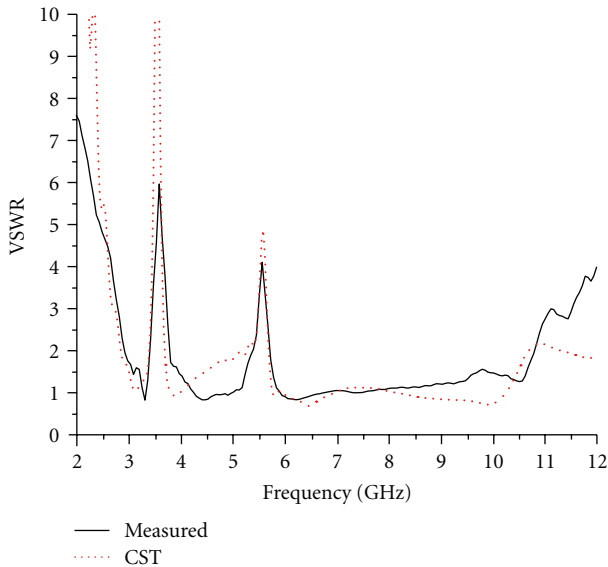


FIGURE 5: Simulated and measured VSWR of the proposed dual band-notched antenna.

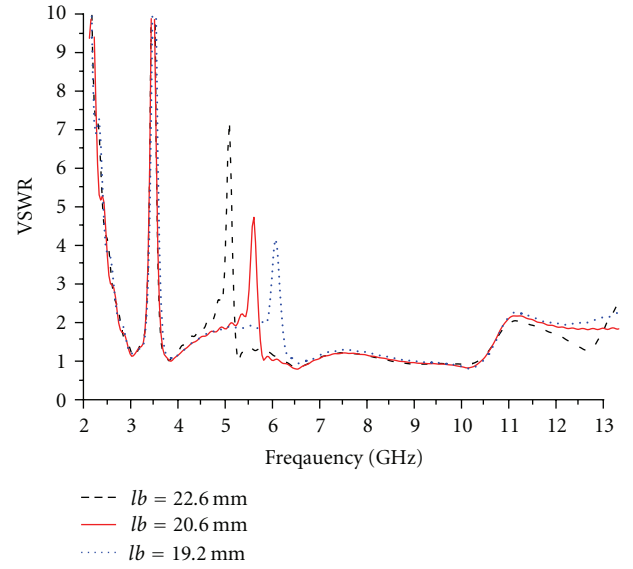
FIGURE 6: Effects of parameter lb on the 5.5 GHz band-notch function.

TABLE 1: Optimized parameters of the single band-notched antenna.

Parameters	w_{sub}	l_{sub}	l_{gnd}	h_{sub}	$l1$	$l2$	$l3$
Value (mm)	18	22	3.5	1.5	4	11	5
Parameters	$l4$	$la1$	$la2$	$la3$	ta	w_{Top}	w_f
Value (mm)	2	3.2	8	7	0.5	4	2

where L is the total length of the C-shaped slot, ϵ_{eff} is the effective dielectric constant, and c is the speed of light. The position, length, and width of the slot have great effects on the band rejection performance and should be tuned carefully. Note that when the C-shaped slot is etched on the radiation patch, there is no retuning work needed for the primitive antenna structure. The optimized parameters of the antenna geometry are listed in Table 1.

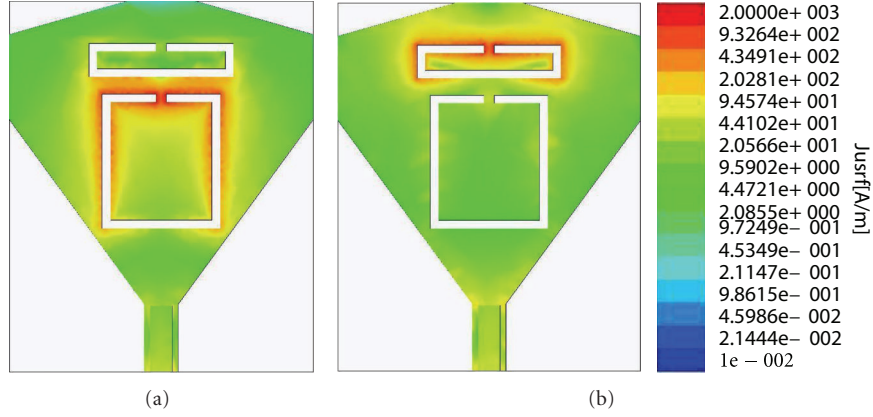


FIGURE 7: Simulated current distribution of the proposed antenna. (a) 3.5 GHz, (b) 5.5 GHz.

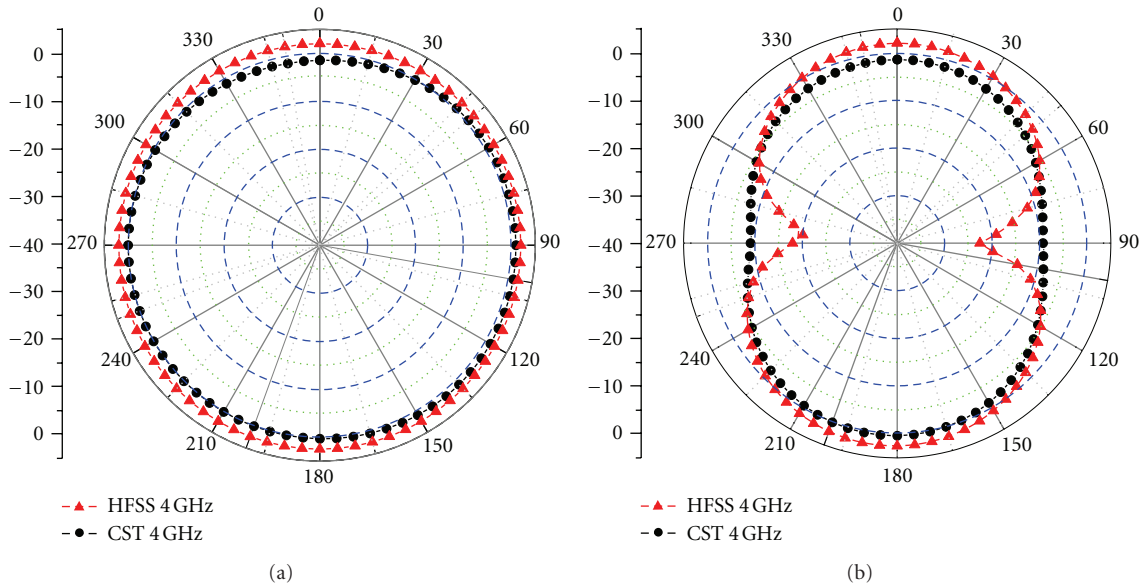


FIGURE 8: Radiation patterns of the proposed antenna at 4 GHz; (a) xoz-plane, (b) yoz-plane.

The simulated VSWR of the single band-notched antenna is shown in Figure 2. It could be observed that this antenna could operate from 2.95 to 10.68 GHz with VSWR less than 2, except one stopband from 3.35 to 3.85 GHz. Let $la = 2 \times la1 + 2 \times la2 + la3$; the simulated VSWR for different la is given in Figure 2(b). By decreasing la from 29.4 to 25.4 mm, the notched frequency is shifted up from 3.6 to 4.2 GHz.

3. Dual Band-Notched UWB Antenna

3.1. Antenna Design and Configuration. Besides WiMAX systems, WLAN operating from 5.15 to 5.825 GHz may cause interferences to the UWB system too. By etching another smaller C-shaped slot on the radiation patch, 5.5 GHz band-notched function is realized. The notched frequency generated by the C-shaped slot can be postulated by (1). The specific geometry of the dual band-notched antenna is shown in Figure 3. All the dimensions are the same as that in Figure 1, except the adding of another smaller C-shaped

slot. The geometry of the smaller slot is given in Table 2. An alternative method to generate dual band-notched function is using two nested C-shaped slots [4], but the tuning process may be complicated due to mutual coupling of the slots. Thus, two independent C-shaped slots are used to generate dual band-notched functions and the tuning process could be simplified.

3.2. Simulated and Measured Results and Discussions. In order to verify the design concept, a prototype of the dual band-notched antenna is fabricated and measured. The photograph of the fabricated dual band-notched antenna is given in Figure 4. The VSWR of the dual band-notched antenna is measured by Agilent E8364B Vector Network Analyzer and is given in Figure 5. Relatively good agreement between the simulated and measured VSWR could be observed. The discrepancy is mainly due to the fabrication tolerance and hand welding inaccuracy. It could be observed that the designed antenna has a wideband performance of

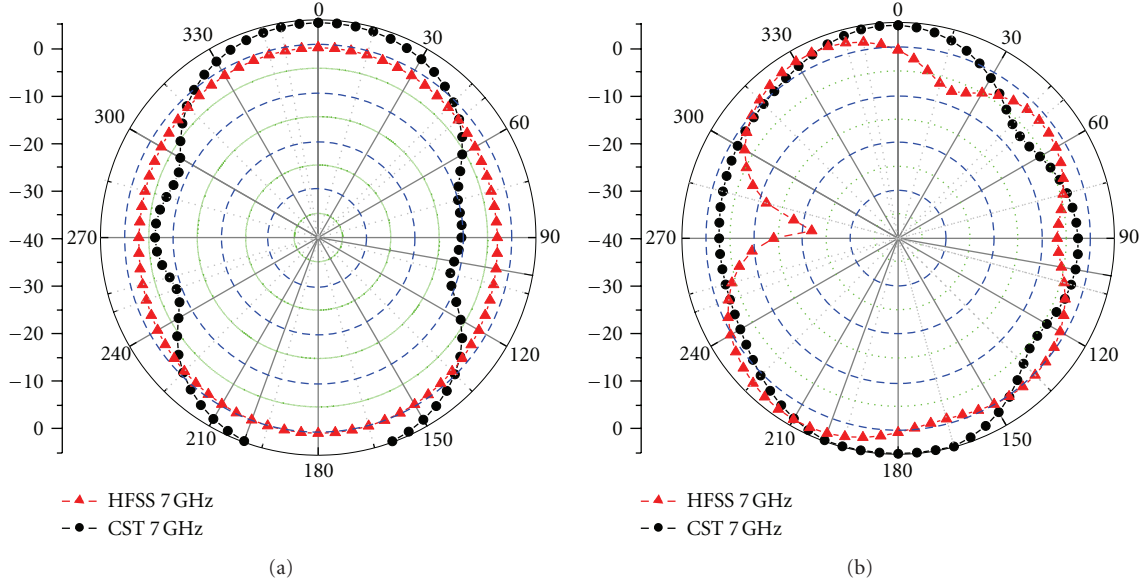


FIGURE 9: Radiation patterns of the proposed antenna at 7 GHz; (a) xoz-plane, (b) yoz-plane.

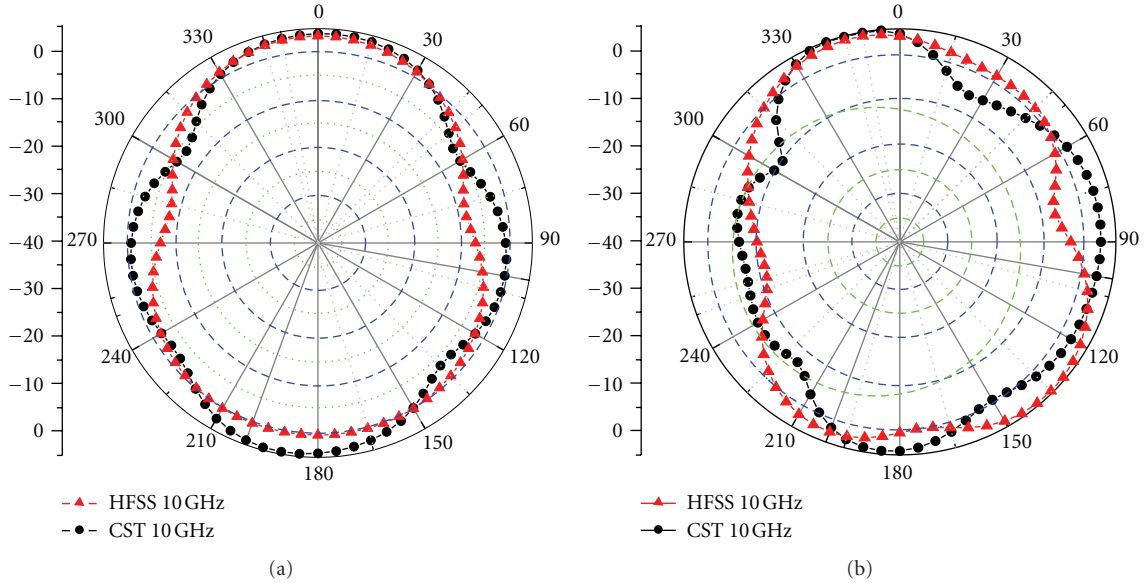


FIGURE 10: Radiation patterns of the proposed antenna at 10 GHz; (a) xoz-plane, (b) yoz-plane.

TABLE 2: Optimized geometry of the smaller C-shaped slot.

Parameters	$lb1$	$lb2$	$lb3$	tb
Value (mm)	4	2	8.6	0.5

3.05–10.7 GHz for VSWR less than 2, covering the entire UWB frequency band, with two stopbands at 3.38–3.82 GHz and 5.3–5.8 GHz for filtering the WiMAX and WLAN signals.

Let $lb = 2 \times lb1 + 2 \times lb2 + lb3$; effects of parameter lb on the 5.5 GHz band-notched function is simulated and is shown in Figure 6. Note that the tuning of parameter lb

has little affection on the VSWR of the dual band-notched antenna throughout the whole UWB frequency range, except the 5.5 GHz stopband. Thus, the 5.5 GHz band-notched characteristic could be tuned independently and no retuning work is needed for the antenna structure. It is observed that by decreasing lb from 22.6 to 19.2 mm, the notched frequency is shifted up from 5.1 to 6.0 GHz.

The simulated surface current distributions at 3.5 GHz and 5.5 GHz are given in Figure 7. The large current distribution is indicated in red, and small one is in blue. It is observed that the surface current is highly concentrated at each C-shaped slot, which means that a large portion of

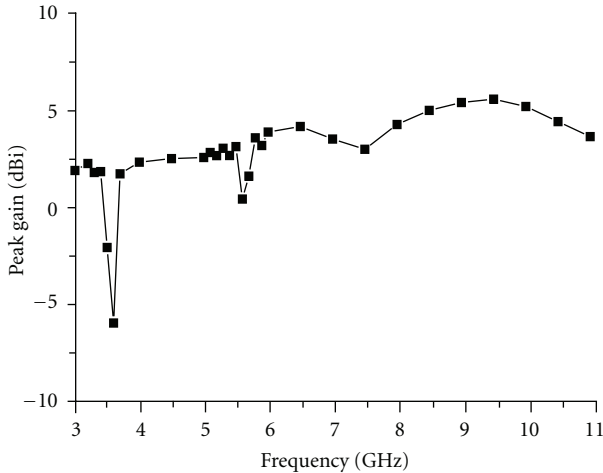


FIGURE 11: Peak gain of the proposed antenna.

electromagnetic energy has been stored around the slots and the radiation efficiency decreases at the rejected band.

The simulated radiation patterns at xoz-plane (H-plane) and yoz-plane (E-plane) of the proposed antenna at 4 GHz, 7 GHz, and 10 GHz are illustrated in Figures 8, 9, and 10, respectively. It is observed that the radiation patterns at xoz-plane are nearly omnidirectional, which makes it a good candidate for UWB devices.

Furthermore, Figure 11 shows the peak gain of the proposed dual band-notched antenna. The simulated peak gain ranges from 2 to 5.5 dBi throughout the whole UWB frequency band, except two stopbands. As discussed above, the energy at the notched frequency bands is not radiated so that the radiation efficiency drops at the notched frequency bands. Thus, the peak gain decreases sharply at 3.5 GHz and 5.5 GHz, which clearly indicates the dual band rejection functions of the proposed antenna.

4. Conclusions

In this paper, a small novel UWB antenna with dual band-notched characteristics has been proposed and analyzed. The primitive UWB antenna is fabricated on FR4 substrate and has a shovel-shaped radiation patch, which results in a compact size of 22 mm × 18 mm × 1.5 mm. Two C-shaped slots are etched on the small patch to achieve 3.5 GHz and 5.5 GHz dual band-notched functions. Nearly omnidirectional radiation patterns could be observed at the H-plane throughout the whole operating frequency band. Accordingly, the proposed dual band-notched UWB antenna might be useful for compact portable UWB devices to eliminate abundant electromagnetic interferences.

Acknowledgments

This work was supported in part by the National Science and Technology Major Project (no. 2010ZX03007-001) and the Key Project of International Cooperation of Yunnan Province (no. 2009AC010).

References

- [1] Z.-A. Zheng and Q.-X. Chu, "CPW-fed ultra-wideband antenna with compact size," *Electronics Letters*, vol. 45, no. 12, pp. 593–594, 2009.
- [2] A. A. Shaalan and M. I. Ramadan, "Design of a compact hexagonal monopole antenna for ultra-wideband applications," *Journal of Infrared, Millimeter, and Terahertz Waves*, vol. 31, no. 8, pp. 958–968, 2010.
- [3] Z.-N. Chen, T. S. P. See, and X.-M. Qing, "Small printed ultrawideband antenna with reduced ground plane effect," *IEEE Transactions on Antennas and Propagation*, vol. 55, no. 2, pp. 383–388, 2007.
- [4] Q.-X. Chu and Y.-Y. Yang, "A compact ultrawideband antenna with 3.4/5.5 GHz dual band-notched characteristics," *IEEE Transactions on Antennas and Propagation*, vol. 56, no. 12, pp. 3637–3644, 2008.
- [5] A. Edalati and T. A. Denidni, "A compact uwb antenna with dual band-notched characteristics," *Microwave and Optical Technology Letters*, vol. 52, no. 5, pp. 1183–1186, 2010.
- [6] M. T. Islam, A. T. Mobashsher, and N. Misran, "Coplanar waveguide fed printed antenna with compact size for broadband wireless applications," *Journal of Infrared, Millimeter, and Terahertz Waves*, vol. 31, no. 12, pp. 1427–1437, 2010.
- [7] O. M. H. Ahmed and A. R. Sebak, "A novel maple-leaf shaped UWB antenna with a 5.0-6.0 GHz band-notch characteristic," *Progress in Electromagnetics Research C*, vol. 11, pp. 39–49, 2009.
- [8] R. Movahedinia and M. N. Azarmanesh, "A novel planar UWB monopole antenna with variable frequency band-notch function based on etched slot-type ELC on the patch," *Microwave and Optical Technology Letters*, vol. 52, no. 1, pp. 229–232, 2010.
- [9] S.-F. Niu, G.-P. Gao, M. Li, Y.-S. Hu, and B.-N. Li, "Design of a novel elliptical monopole UWB antenna with dual band-notched function," *Microwave and Optical Technology Letters*, vol. 52, no. 6, pp. 1306–1310, 2010.
- [10] H.-L. Zhang, R.-G. Zhou, Z.-R. Wu, H. Xin, and R. W. Ziolkowski, "Designs of ultra wideband (UWB) printed elliptical monopole antennas with slots," *Microwave and Optical Technology Letters*, vol. 52, no. 2, pp. 466–471, 2010.
- [11] M. Ojaroudi, G. Ghanbari, N. Ojaroudi, and C. Ghobadi, "Small square monopole antenna for UWB applications with variable frequency band-notch function," *IEEE Antennas and Wireless Propagation Letters*, vol. 8, pp. 1061–1064, 2009.
- [12] X.-F. Zhu and D.-L. Su, "Symmetric E-shaped slot for UWB antenna with band-notched characteristic," *Microwave and Optical Technology Letters*, vol. 52, no. 7, pp. 1594–1597, 2010.
- [13] M. A. Habib, A. Bostani, A. Djaiz, M. Nedil, M. C. E. Yagoub, and T. A. Denidni, "Ultra wideband cpw-fed aperture antenna with wlan band rejection," *Progress in Electromagnetics Research*, vol. 106, pp. 17–31, 2010.
- [14] S. Barbarino and F. Consoli, "UWB circular slot antenna provided with an inverted-L notch filter for the 5 GHz WLAN band," *Progress in Electromagnetics Research*, vol. 104, pp. 1–13, 2010.
- [15] R. Fallahi, A.-A. Kalteh, and M.-G. Roozbahani, "A novel UWB elliptical slot antenna with band-notched characteristics," *Progress in Electromagnetics Research*, vol. 82, pp. 127–136, 2008.
- [16] T.-F. Xia, S.-W. Yang, and Z.-P. Nie, "Band-notched UWB planar antenna with parasitic spiral strips," *Microwave and Optical Technology Letters*, vol. 53, no. 7, pp. 1532–1535, 2011.

- [17] W.-X. Liu and Y.-Z. Yin, "Dual band-notched antenna with the parasitic strip for UWB," *Progress in Electromagnetics Research Letters*, vol. 25, pp. 21–30, 2011.
- [18] R. Rouhi, C. Ghobadi, J. Nourinia, and M. Ojaroudi, "Microstrip-fed small square monopole antenna for UWB application with variable band-notched function," *Microwave and Optical Technology Letters*, vol. 52, no. 9, pp. 2065–2069, 2010.
- [19] G.-P. Gao, M. Li, S.-F. Niu, X.-J. Li, B.-N. Li, and J.-S. Zhang, "Study of a novel wideband circular slot antenna having frequency band-notched function," *Progress in Electromagnetics Research*, vol. 96, pp. 141–154, 2009.
- [20] K. S. Ryu and A. A. Kishk, "UWB antenna with single or dual band-notches for lower WLAN band and upper WLAN band," *IEEE Transactions on Antennas and Propagation*, vol. 57, no. 12, pp. 3942–3950, 2009.
- [21] C.-M. Li and L.-H. Ye, "Improved dual band-notched uwb slot antenna with controllable notched band-widths," *Progress in Electromagnetics Research*, vol. 115, pp. 477–493, 2011.
- [22] W.-T. Li, X.-W. Shi, T.-L. Zhang, and Y. Song, "Novel UWB planar monopole antenna with dual band-notched characteristics," *Microwave and Optical Technology Letters*, vol. 52, no. 1, pp. 48–51, 2010.

Research Article

Compact Multiband Planar Fractal Cantor Antenna for Wireless Applications: An Approach

Gopalakrishnan Srivatsun and Sundaresan Subha Rani

Department of Electronics and Communication Engineering, PSG College of Technology, Tamil Nadu, Coimbatore 641004, India

Correspondence should be addressed to Gopalakrishnan Srivatsun, srivatsunece@yahoo.co.in

Received 16 February 2012; Accepted 20 May 2012

Academic Editor: Dalia N. Elshiekh

Copyright © 2012 G. Srivatsun and S. Subha Rani. This is an open access article distributed under the Creative Commons Attribution License, which permits unrestricted use, distribution, and reproduction in any medium, provided the original work is properly cited.

A compact multiband fractal antenna which is a new criterion in communication is proposed. The optimized prototype measures $35\text{ mm} \times 31\text{ mm} \times 1.6\text{ mm}$. The proposed antenna covers WLAN IEEE 802.11b, 802.15, PCS, GSM lower and higher bands, DCS, IMT, UMTS, Wi-Fi, and WLAN wireless applications. The proposed antenna exhibits multiband characteristics with an S_{11} of -30.69 dB at design frequency and it is found that $\sim 70\%$ of the S_{11} graph below -10 dB reference is achieved. Experimental S_{11} has been compared with the one which is obtained using method of moments. The aim of implementing self-affine fractal concept in antenna design makes it flexible in controlling the resonance and bandwidth. This paper investigates self-affine fractal geometry to miniaturize and to resonate multiband frequencies. The prototype model with a good agreement of S_{11} is reported.

1. Introduction

The immense increase in wireless devices and systems to establish wireless connectivity, results in congested wireless band. Wireless market needs a low profile and compact antenna to fit the wireless devices with multiband characteristics. Currently, developed compact broadband antennas are designed for mobile devices [1–10] which involve tuning of non planar, metallic strips and photolithographic concepts partially. This was a motivation to develop a compact multiband antenna, which is essential for wireless applications to solve the needs. The prototype tends to fit IEEE 802.11 series, WLAN, GSM, Wi-Fi, PCS, and DCS frequencies. Microstrip antenna is capable of providing narrowband width, to resonate for multiband, fractal geometry is preferred, and it also occupies less space on wireless boards.

Mandelbrot found the name “fractals” to all that is occurring in nature. Fractal dimensions were not whole numbers, regular, and irregular structures seen in nature [11–23], and latter, John Gianvittoria and many others have devoted to this geometry in particular. A few examples of these geometries are coastlines, mountains, snow structure, fern leaves, bark of trees, and pebbles. Fractal geometry finds

a variety of application in engineering and nonengineering fields.

This paper aims at regular self-affine cantor. The visual examinations of self-affine cantor are same in all successive iterations and portray the self-affinity property. As the fractal iteration increases, then the volume of the initiator reduces by 45% in size, thereby maintaining a radiation pattern compared to that of a normal patch [23]. A self-affine [12] cantor length (L) and the width (W) are reduced to a maximum number of possible iterations (n), through iterative coefficients to shrink the volume of the geometry through which individuality is maintained. This approach provides flexibility in designing a miniaturized antenna. The antenna exhibits multiband resonance by selecting proper scaling factor and optimization of the feed position. Sinha and Jain [24] examined self-affine property of fractals and evaluated the multiband characteristics and implemented the microstrip feed line on a RT-Duroid substrate, and the antenna is found to have finite ground plane of length $85\text{ mm} \times 85\text{ mm}$ with aperture coupling to cover the frequency bands at 2.5 GHz, 5 GHz, and 10 GHz with 130 MHz, 580 MHz, and 690 MHz bandwidths. The above bandwidth is achieved through 3 mm between the substrate and the

ground plane. Also, the cost of RT-Duroid is too high when compared to FR4 substrate. [25] Xiaoxiang He designed a dual band antenna for WLAN applications of $109.03 \text{ mm} \times 77.88 \text{ mm} \times 102.8 \text{ mm}$ with three parts namely monopole which is in the shape of a fork, rectangular slot and patch. All the three parameters vary and the gain is achieved by adjusting the length and gap using reflector. [26] Liu et al. designed a triple frequency meander monopole antenna on one side and three parasitic strips 1, 2 and 3 on the other side measures of $35 \text{ mm} \times 31 \text{ mm}$.

The antenna is etched on a RT Duroid substrate at 2.45 GHz [27] and the antenna that is designed measures $18 \text{ mm} \times 7.2 \text{ mm} \times 0.254 \text{ mm}$. But the antenna is tuned for GPS, DCS-1800, IMT-2000 and WLAN handsets by varying the “s” strip and the height. [28] designed a three band planar antenna covering GSM and Wi-Fi frequency bands along with Sierpinski and meander slits on Arlon substrate. The compact dual band antenna [29] designed for DCS application measuring $30 \text{ mm} \times 30 \text{ mm}$ with both the layers of the substrate with CPW feed is reported in the literature. Hence, a self-affine structure with fractal geometry has been proposed to avoid such complications in designing and tuning to fulfill a variety of wireless applications with a low cost FR4 substrate.

2. Proposed Design Methodologies

2.1. Proposed Self-Affine Technique. The proposed self-affine cantor is a rectangle and is called an initiator S1 shown in Figure 1(a). Based on iterative function (IF), the initiator S1 is scaled at center by a factor of two along its length and width of equal dimension, which leads to four rectangles. The topmost corner region is removed thereby retaining the remaining regions as shown in Figure 1(b). Initially, S1 is made to resonate at design frequency by selecting coaxial feed technique. This process is a repetitive procedure and is continued up to n th iteration. Iterative function (IF) for self-affine set is described using (1) and the corresponding values are shown in Figure 2.

2.2. Antenna Design Procedure. The self-affine antenna is developed on a FR4 substrate whose thickness is 1.6 mm , $\epsilon_r = 4.4$, and $\tan \delta = 0.01$ with ground plane at the bottom. The initiator (S1) measures $38.6 \text{ mm} \times 28.75 \text{ mm} \times 1.6 \text{ mm}$ which resonates near 2.4 GHz . Then, S1 is iterated to obtain (S2) up to (S4) as guided by iterative function, in order to achieve multiband characteristics and the optimized size as shown in Figures 2(a) and 2(b). The set and subsets are assumed in anticlockwise direction for convenience.

The iterative function (IF) of the antenna is derived as follows:

$w(X)$ is a set which is spanned by

$$w\{X_1, X_2, \dots, X_n\}, \quad n = 4, \quad (1)$$

$$w(X_1) = w\{X_{11}, \dots, X_{1n}\} \text{ is a subset of } w(X_1). \quad (2)$$

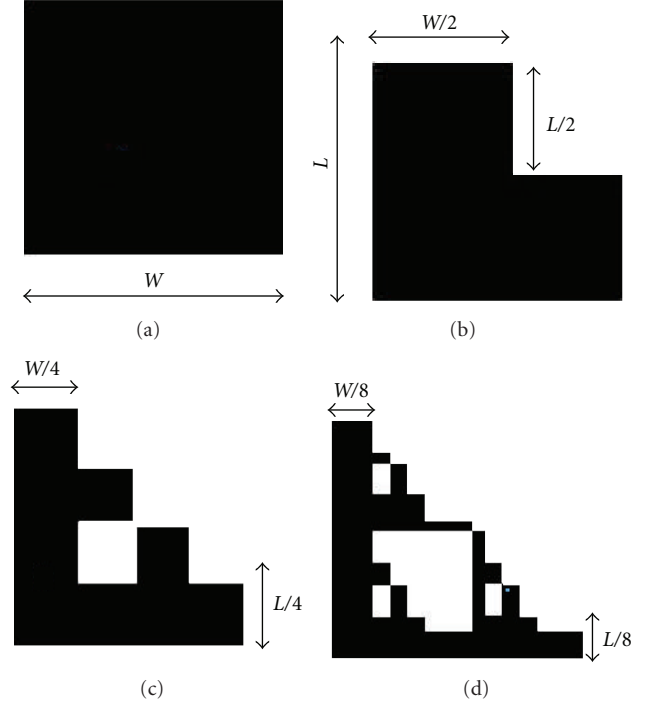


FIGURE 1: Self-affine fractal structure. (a) initiator S1; (b) first iteration S2; (c) second iteration S3; (d) third iteration S4.

Equation (2) holds true for remaining subsets $w(X_{22}, \dots, X_{2n})$

$$w(X) = \bigcup_{i=1}^4 X_i \quad (3)$$

$$w(X_1) = \bigcup_{i=1}^4 X_i - X_3,$$

Repetition holds true \forall values of X_1, \dots, X_n (except) X_3 ,

$$w(X_2) = \left[\left(\frac{x}{2}, 0 \right) (x, 0) \left(x, \frac{y}{2} \right) \left(\frac{x}{2}, \frac{y}{2} \right) \right]$$

$$w(X_4) = \left[\left(0, \frac{y}{2} \right) \left(\frac{x}{2}, \frac{y}{2} \right) \left(\frac{x}{2}, y \right) (0, y) \right]$$

$$w(X_{11}) = \left[(0, 0) \left(\frac{x}{4}, 0 \right) \left(\frac{x}{4}, \frac{y}{4} \right) \left(0, \frac{y}{4} \right) \right] \quad (4)$$

$$w(X_{12}) = \left[\left(\frac{x}{4}, 0 \right) \left(\frac{x}{2}, 0 \right) \left(\frac{x}{2}, \frac{y}{4} \right) \left(\frac{y}{4}, \frac{y}{4} \right) \right]$$

$$w(X_{41}) = \left[\left(0, \frac{y}{4} \right) \left(\frac{x}{4}, \frac{y}{4} \right) \left(\frac{x}{4}, \frac{y}{2} \right) \left(0, \frac{y}{2} \right) \right].$$

Similarly the process can be repeated. But, total volume reduces compared to the original size. The performance of the antenna at different iteration has been investigated using advanced design systems momentum.

The performance for coaxial feed of the self-affine cantor is plotted against frequency and S_{11} is shown in Figures 3, 4 and 5 and the corresponding values are tabulated in Table 1.

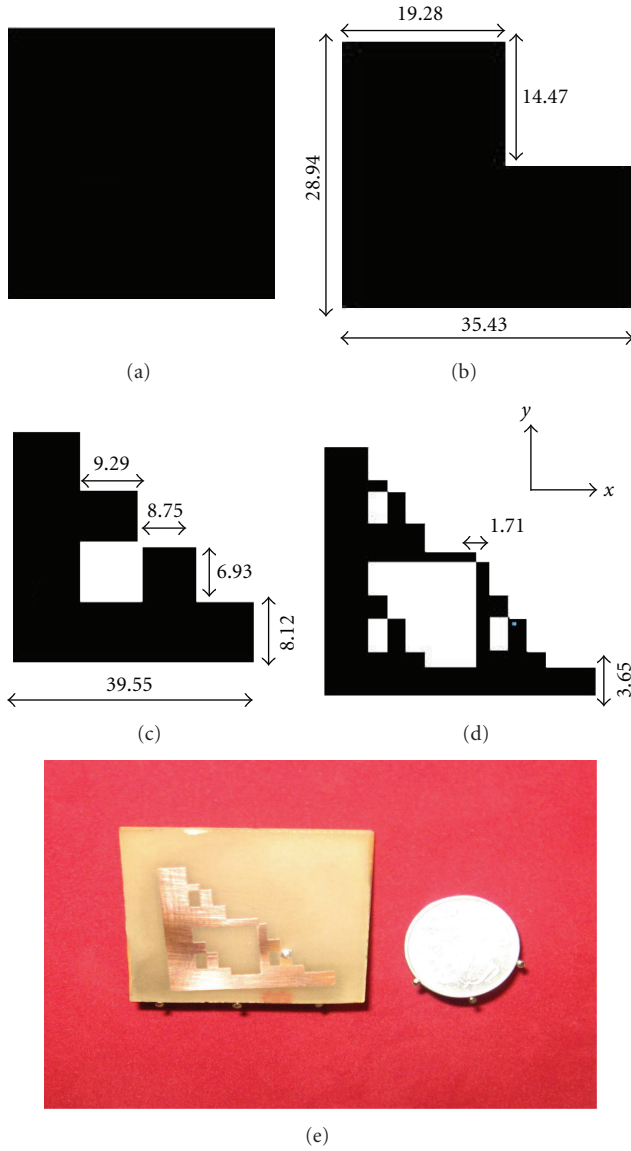


FIGURE 2: (a) Initiator (S1), (b) first iteration (S2), (c) second iteration (S3), (d) third iteration (S4), (e) prototype of the planar antenna (all dimensions are in mm).

The performance of self-affine cantor which is obtained at -10 dB references covers the nearby frequency bands. The antenna covers the neighboring frequency bands thereby providing a S_{11} greater than -20 dB for a feed position and multiband characteristics for all the other positions. As iteration (n) increases, the slots grow at the centre and the staircase projections increase diagonally from to right revealing the affinity concept. Simulated S_{11} covers and fulfills the GSM band, WLAN, IEEE 802.11, Bluetooth, WiMAX, PCS, DCS, and UMTS requirements.

2.3. Antenna Fabrication and Testing. The proposed cantor is etched on FR4 substrate whose specifications have been discussed in Section 2.2, with 8 : 1 ratio of ferric chloride and dilutes hydrochloric acid. The optimized antenna measures

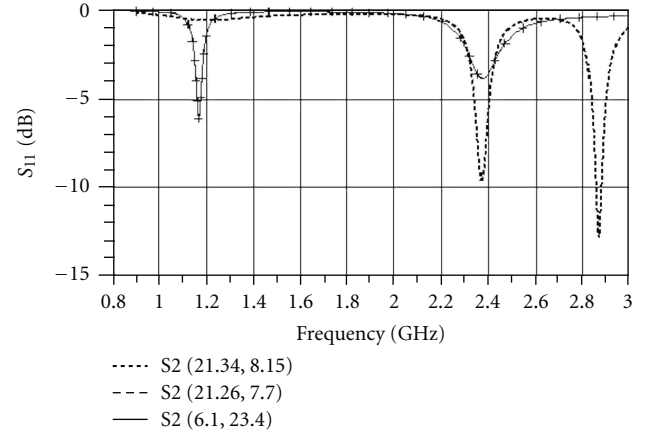


FIGURE 3: Comparison between different feed positions for second iteration (S3).

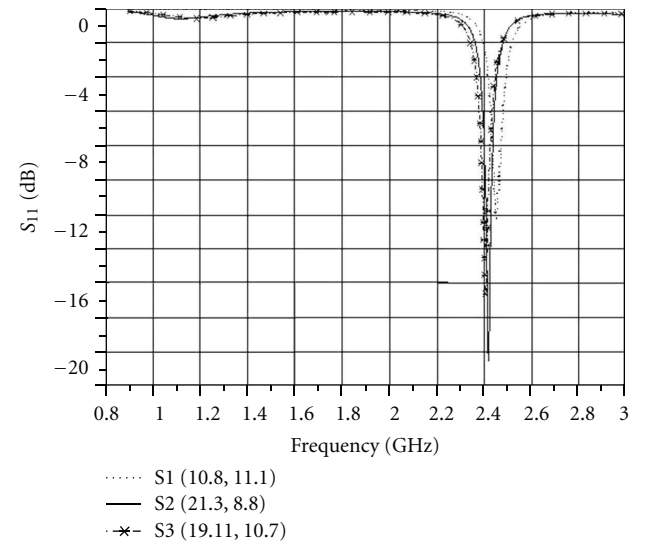


FIGURE 4: Performance comparison between initiator (S1), first iteration (S2), and second iteration (S3).

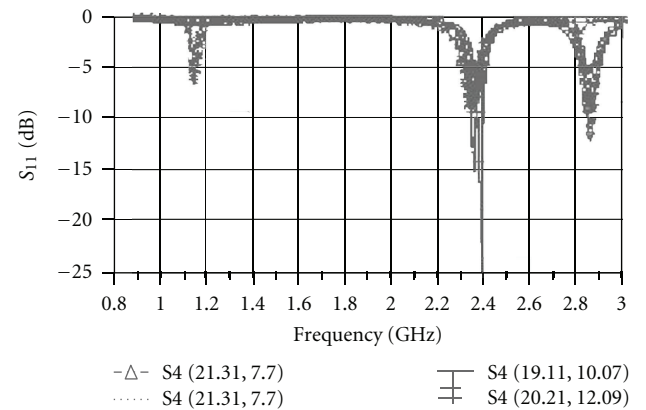
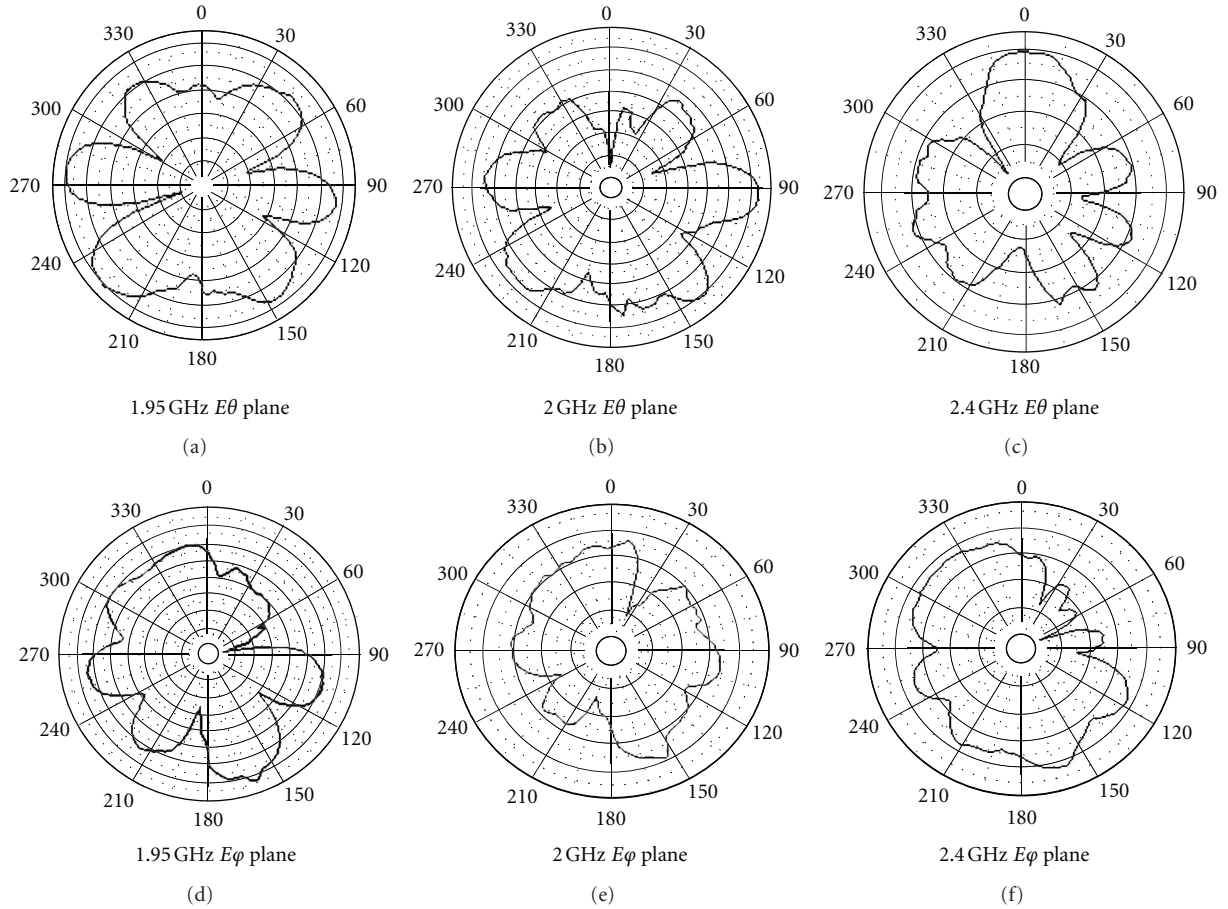


FIGURE 5: Comparison between different feed positions for third iteration (S4).

TABLE 1: Simulated returnloss at various iterations for an self-affine antenna.

S. no	S1			S2			S3			S4*		
	Freq (GHz)	S_{11} (dB)	BW (MHz)	Freq (GHz)	S_{11} (dB)	BW (MHz)	Freq (GHz)	S_{11} (dB)	BW (MHz)	Freq (GHz)	S_{11} (dB)	BW (MHz)
1	2.425	-12.29	19	2.419	-17	26	1.167	-6	—	2.369 (1)	-9.575	—
2							2.369	-9.58	—	2.865 (2)	-12.77	13
3										2.366 (3)	-9.687	—
4										2.863 (4)	-9.985	—
5							Feed position with respect to*			2.357 (5)	-16.03	25
6							21.3113, 7.7082 (1) and (2)			2.841 (5)	-6.198	—
7							21.4774, 6.5875 (2) and (3)			2.389 (6)	-23.55	—
8							21.5604, 1.8969 (5)			2.378 (7)	-24.55	26.1
9							19.113, 10.0742 (6) and (7)			1.15 (8)	-7.094	—
10							6.1000, 23.4 (8) and (9)			2.34 (9)	-9.375	—

* S4 feed position.

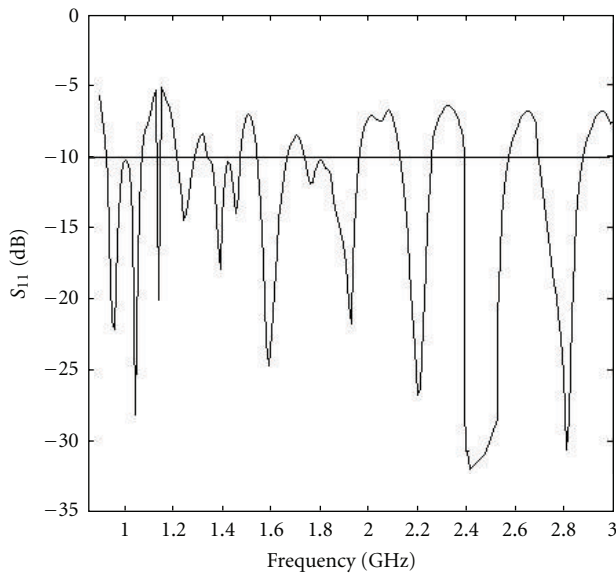
FIGURE 6: Measured radiation pattern for $E\theta$ and $E\phi$ planes for 1.95 GHz, 2 GHz, and 2.4 GHz.

38.734 mm \times 28.757 mm as shown in Figure 2(e). Here, coaxial feed is considered at 21.56 mm \times 1.89 mm. The radiation pattern is obtained in a anechoic chamber of 8 m \times 4 m \times 4 m ($L \times W \times H$) dimensions at 1.95 GHz, 2 GHz and 2.45 GHz, for $E\theta$ and $E\phi$ planes against, standard gain of

the pyramidal horn antenna (450 MHz–6 GHz) and Agilent PNA 5230A vector network analyzer (10 MHz–6 GHz) is shown in Figure 6. The antenna pattern is omnidirectional with slight variations; this may be because of the surrounding reflections caused during measurements. The resonant

TABLE 2: Measured S_{11} for an self-affine fractal antenna.

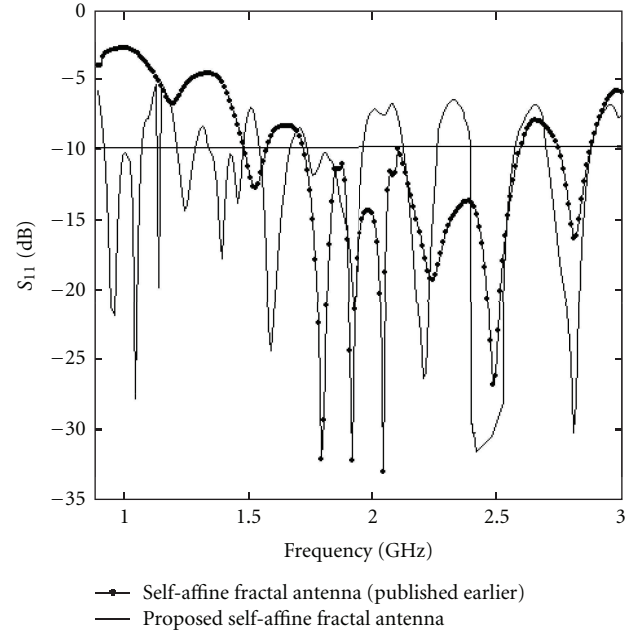
S. no	Centre freq in GHz	S_{11} (dB)	BW in MHz	Combined BW in MHz
1	0.963	-22.15	105	147
2	1.047	-28.2	147	
3	1.247	-14.46	74	
4	1.394	-17.92	116	
5	1.593	-24.76	116	
6	1.928	-21.75	221	
7	2.213	-26.26	76	
8	2.40	-30.69	186	
9	2.811	-30.63	189	

FIGURE 7: Measured S_{11} of self-affine fractal antenna structure.

behavior of the proposed antenna is measured using Agilent network analyzer with -10 dB as references is obtained and the corresponding values are tabulated in Table 2. The simulated and measured S_{11} gives a good agreement as shown in Figure 7. The performance of the antenna is compared against earlier published self-affine fractal antenna as depicted in Figure 8. The antenna designed for 2.4 GHz resonates for 0.9 GHz, 1.075 GHz, 1.25 GHz, and 1.95 GHz with 11.5931 dBi, 9.43717 dBi, 8.25 dBi, and 3.69 dBi gain in that order. The self-affine fractal cantor provides multi-band characteristics at 2.402 GHz with a S_{11} parameter -30.69 dB.

3. Conclusion

A compact multiband low profile planar antenna designed at 2.4 GHz exhibiting multiband characteristics which covers WLAN IEEE 802.11b and IEEE802.15, PCS, GSM lower-band, GSM higher band, DCS, IMT, UMTS, Wi-Fi, and WLAN wireless applications. The compact multiband self-affine antenna maintains a S_{11} of -30.69 at design frequency. The gain of the antenna is simulated at 0.9 GHz, 1.075 GHz,

FIGURE 8: Performance comparisons of measured S_{11} parameter between self-affine fractal antennas.

and 1.25 GHz with a gain of 11.5931 dBi, -9.43717 dBi, and 8.25 dBi, respectively. At design frequency the $E\theta$ and $E\phi$ planes have gain 4.46 dBi and 7.17 dBi, respectively. The authors have chosen a FR4 substrate which is low in cost and lossy in nature, approximately 30% of the wave form is above the reference level and this might be due to the imperfect finishing caused by fabrication.

Acknowledgment

This work was supported by Agilent-Multipurpose Lab Station, PSG College of Technology, Coimbatore India.

References

- [1] Y.-B. Kwon, J.-I. Moon, and S.-O. Park, "An internal triple-band planar inverted-F antenna," *IEEE Antennas and Wireless Propagation Letters*, vol. 2, pp. 341–344, 2003.
- [2] M.-C. Huynh and W. L. Stutzman, "A low-profile compact multi-resonant antenna for wideband and multi-band personal wireless applications," in *Proceedings of the IEEE Antennas and Propagation Society Symposium Digest Held in Conjunction with: USNC/URSI National Radio Science Meeting*, vol. 2, pp. 1879–1882, June 2004.
- [3] D. U. Sim, J.-I. Moon, and S.-O. Park, "An internal triple-band antenna for PCS/IMT-2000/bluetooth applications," *IEEE Antennas and Wireless Propagation Letters*, vol. 3, no. 1, pp. 23–25, 2004.
- [4] D. U. Sim, J.-I. Moon, and S.-O. Park, "A wideband monopole antenna for PCS/IMT-2000/Bluetooth applications," *IEEE Antennas and Wireless Propagation Letters*, vol. 3, no. 1, pp. 45–47, 2004.
- [5] Y. S. Shin, S.-O. Park, and M. Lee, "A broadband interior antenna of planar monopole type in handsets," *IEEE Antennas and Wireless Propagation Letters*, vol. 4, no. 1, pp. 9–12, 2005.

- [6] Y. S. Cao, C. L. Lu, and Y. L. Zhang, "A compact dual band miniaturized antenna for WLAN operation," in *Proceedings of the International Conference on Microwave and Millimeter Wave Technology (ICMMT '08)*, pp. 416–419, April 2008.
- [7] Q. Q. He, B. Z. Wang, and J. He, "Wideband and dual-band design of a printed dipole antenna," *IEEE Antennas and Wireless Propagation Letters*, vol. 7, pp. 1–4, 2008.
- [8] R. L. Li, B. Pan, J. Laskar, and M. M. Tentzeris, "A novel low-profile broadband dual-frequency planar antenna for wireless handsets," *IEEE Transactions on Antennas and Propagation*, vol. 56, no. 4, pp. 1155–1162, 2008.
- [9] M. N. Suma, R. K. Raj, M. Joseph, P. C. Bybi, and P. Mohanan, "A compact dual band planar branched monopole antenna for DCS/2.4-GHz WLAN applications," *IEEE Microwave and Wireless Components Letters*, vol. 16, no. 5, pp. 275–277, 2006.
- [10] M. J. Kim, C. S. Cho, and J. Kim, "A dual band printed dipole antenna with spiral structure for WLAN application," *IEEE Microwave and Wireless Components Letters*, vol. 15, no. 12, pp. 910–912, 2005.
- [11] M. F. Barnsley, *Fractals Everywhere*, Academic Press, San Diego, Calif, USA, 2nd edition, 1993.
- [12] H. O. Peitgen, H. Jurgens, and D. Saupe, *Chaos and Fractals*, NewFrontiers in Science, Springer, NewYork, NY, USA, 1992.
- [13] C. Puente, J. Romeu, R. Pous, X. Garcia, and F. Benitez, "Fractal multiband antenna based on the Sierpinski gasket," *Electronics Letters*, vol. 32, no. 1, pp. 1–2, 1996.
- [14] J. P. Gianvittorio and Y. Rahmat-Samii, "Fractal antennas: a novel antenna miniaturization technique, and applications," *IEEE Antennas and Propagation Magazine*, vol. 44, no. 1, pp. 20–36, 2002.
- [15] D. H. Werner and S. Ganguly, "An overview of fractal antenna engineering research," *IEEE Antennas and Propagation Magazine*, vol. 45, no. 1, pp. 38–57, 2003.
- [16] K. J. Vinoy, *Fractals shaped antenna elements for wide band multiband wireless applications [Ph.D. thesis]*, Department of Electrical Engineering, Pennslvania State University, University Park, Pa, USA, 2002.
- [17] J. C. Liu, C. Y. Wu, D. C. Chang, and C. Y. Liu, "Relationship between sierpenski and appolian packing monopole antennas," *Electronics Letters*, vol. 42, no. 15, 2006.
- [18] T. K. C. Lo and Y. Hwang, "Microstrip antennas of very high permittivity for personal communications," in *Proceedings of the Asia-Pacific Microwave Conference (APMC '97)*, pp. 253–256, December 1997.
- [19] R. A. Sainati, *CAD of Microstrip Antennas For Wireless Applications*, Artech House, Norwood, NJ, USA, 1996.
- [20] H. Y. Wang and M. J. Lancaster, "Aperture-coupled thin-film superconducting meander antennas," *IEEE Transactions on Antennas and Propagation*, vol. 47, no. 5, pp. 829–836, 1999.
- [21] P. E. Mayes, "Frequency-independent antennas and broadband derivatives thereof," *Proceedings of the IEEE*, vol. 80, no. 1, pp. 103–112, 1992.
- [22] C. Puente-Baliarda, J. Romeu, R. Pous, and A. Cardama, "On the behavior of the sierpinski multiband fractal antenna," *IEEE Transactions on Antennas and Propagation*, vol. 46, no. 4, pp. 517–524, 1998.
- [23] I. K. Kim, J. G. Yook, and H. K. Park, "Fractal-shape small size microstrip patch antenna," *Microwave and Optical Technology Letters*, vol. 34, no. 1, pp. 15–17, 2002.
- [24] S. N. Sinha and M. Jain, "A self-affine fractal multiband antenna," *IEEE Antennas and Wireless Propagation Letters*, vol. 6, pp. 110–112, 2007.
- [25] X. He, S. Hong, H. Xiong, Q. Zhang, and E. M. M. Tentzeris, "Design of a novel high-gain dual-band antenna for WLAN applications," *IEEE Antennas and Wireless Propagation Letters*, vol. 8, pp. 798–801, 2009.
- [26] W.-C. Liu, M. Ghavami, and W.-C. Chung, "Triple-frequency meandered monopole antenna with shorted parasitic strips for wireless application," *IET Microwaves, Antennas and Propagation*, vol. 3, no. 7, pp. 1110–1117, 2009.
- [27] R. Li, B. Pan, J. Laskar, and M. M. Tentzeris, "A compact broadband planar antenna for GPS, DCS-1800, IMT-2000, and WLAN applications," *IEEE Antennas and Wireless Propagation Letters*, vol. 6, pp. 25–27, 2007.
- [28] R. Azaro, L. Debiase, E. Zeni, M. Benedetti, P. Rocca, and A. Massa, "A hybrid prefractal three-band antenna for multistandard mobile wireless applications," *IEEE Antennas and Wireless Propagation Letters*, 2009.
- [29] M. N. Suma, R. K. Raj, M. Joseph, P. C. Bybi, and P. Mohanan, "A compact dual band planar branched monopole antenna for DCS/2.4-GHz WLAN applications," *IEEE Microwave and Wireless Components Letters*, vol. 16, no. 5, pp. 275–277, 2006.

Research Article

Design of Two Novel Dual Band-Notched UWB Antennas

Bing Li and Jing-song Hong

Institute of Applied Physics, University of Electronic Science and Technology of China, Chengdu 610054, China

Correspondence should be addressed to Bing Li, orangeirl-2008@163.com

Received 15 January 2012; Revised 20 May 2012; Accepted 20 May 2012

Academic Editor: Dalia N. Elshiekh

Copyright © 2012 B. Li and J.-s. Hong. This is an open access article distributed under the Creative Commons Attribution License, which permits unrestricted use, distribution, and reproduction in any medium, provided the original work is properly cited.

Two novel dual band-notched ultra-wideband (UWB) printed monopole antennas with simple structure and small size are presented. The size of both antennas is $25 \times 25 \times 0.8 \text{ mm}^3$. The bandwidth of one of the proposed antenna can be from 2.7 GHz to 36.8 GHz, except the bandwidth of 3.2–3.9 GHz for WiMAX applications and 5.14–5.94 GHz for WLAN applications. The bandwidth of the other is ranging for 2.7 to 41.1 GHz, except the bandwidth of 3.2–3.9 GHz for WiMAX applications and 4.8–5.9 GHz for WLAN applications. Bandwidths of the antennas are about 512% and 455% wider than those of conventional band-notched UWB antennas, respectively. In addition, the time-domain characteristics of the two antennas are investigated to show the difference between both antennas.

1. Introduction

There has been more and more attention in ultrawideband (UWB) antennas ever since the Federal Communications Commission (FCC)'s allocation of the frequency band 3.1–10.6 GHz for commercial use [1]. Over the designated bandwidth of UWB system, there are some other existing narrowband services that already occupy frequencies in the UWB band, such as wireless local-area network (WLAN) operating in the 5.15–5.875 GHz band and world interoperability for microwave access (WiMAX) service from 3.3 to 3.6 GHz. However, the uses of filters increase the complexity and cost. It is desirable to design the UWB antenna with dual band notches. The printed planar monopole antenna is a good candidate for the band-notched UWB system because of its low cost, low profile, light weight, omnidirectional radiation patterns, easy realization, and convenience for integrating with microwave monolithic integrated circuit (MMIC) technologies. Various kinds of printed monopole antennas with notched band have been reported in the literature. The band-notched UWB antennas in [2–5] are not able to satisfy the compact property, the antennas reported in [5–7] have high profile, the antennas mentioned in [4–8] have only single band-notches. Challenges of the feasible dual-notched UWB antenna design contain proper notched bandwidths and the above advantages which belong to printed planar monopole antennas.

Based on the background of the researches above, two novel, simple and compact ultra-wideband printed monopole antennas with dual band-notched characteristics are proposed in this paper. By cutting a wide slot on the patch and a narrow slot on the ground plane, dual frequency band notches can be obtained. The desired notched band frequencies can be easily achieved by adjusting the total lengths of the slots. By changing the widths and locations of the slots, the notched bandwidths can be efficiently controlled. The bandwidth of one antenna is from 2.7 GHz to 41.1 GHz, except the bandwidth of 3.2–3.9 GHz for WiMAX applications and 4.8–5.9 GHz for WLAN applications. The other has an impedance bandwidth ranging from 2.7 GHz to 36.8 GHz, eliminating the bandwidth of 3.2–3.9 GHz for WiMAX applications and 5.14–5.94 GHz for WLAN applications. The size of both the novel antennas is just $25 \times 25 \times 0.8 \text{ mm}^3$.

2. The Proposed Antenna Structure and Design

2.1. UWB Antenna Design. In this section, we will develop a novel UWB antenna which can be used to design the dual band-notched antennas. Figure 1(a) shows the geometry and configuration of the proposed antenna without slots that is UWB antenna fed by a 50Ω microstrip feed line. L ($L = 25 \text{ mm}$) and W ($W = 25 \text{ mm}$) denote the length

and width of the dielectric substrate, respectively. L_1 is the length of the patch which is equal to 10.4 mm. The most important parameter effect on the performance of the proposed antenna is the apex angle α which is given by [9]

$$\alpha = \frac{3}{4}\pi - \arctan\left(\frac{L - 2L_1}{W}\right). \quad (1)$$

The tapered microstrip line at the connection between the feeding line and the patch is employed for broadband matching of the antenna to the $50\ \Omega$ microstrip line. The width and length of the $50\ \Omega$ microstrip line are 1.5 mm and 10.9 mm, respectively. The arcs at edges of the patch and the ground plane are employed for reducing the radiation loss and the difficulties of fabricating. The proposed antenna is printed on the FR4 substrate with the thickness of 0.8 mm, relative permittivity 4.4 and loss tangent $\tan \delta = 0.02$. Shown in Figure 1(b) is the simulated VSWR result of the proposed UWB antenna; it can be seen that the impedance bandwidth (VSWR < 2) is from 2.9 GHz to 41 GHz.

2.2. Single Band-Notched UWB Antenna Design. Before developing the dual band-notched UWB antennas, we need to investigate the method generating the single notched band. Several novel antennas with filtering property operating in the 3.2–3.9 GHz band, 5.2–5.9 GHz and 5.14–5.94 GHz are designed to reduce the interference from the WiMAX or WLAN applications. Those band-notched functions are desirable in the UWB system. Figure 2 shows the geometry and configuration of those novel antennas. By etching a straight slot in the patch or the ground plane of UWB antenna, a frequency band notch is created. Note that when the band-notched design applied to UWB antenna, there is no retuning work required for the previously determined dimensions, since the filtering ability is generated by integrating filtering structures in the antenna. In addition, the design concept of the notch function is to adjust the total length of the straight slots to accord with Formula (2).

In single band-notched antenna 1, the wide slot etched in the patch shown in Figure 2(a) whose length and width are 13.8 mm and 0.8 mm, respectively, is employed to obtain the desired notched band which is from 3.2 GHz to 3.9 GHz and which is shown in Figure 3 so that the proposed antenna cannot interfere with WiMAX applications.

In single band-notched antenna 2, a narrow slot etched in the ground plane shown in Figure 2(b) whose length and width are 8.4 mm and 0.2 mm, respectively, is employed to obtain the desired notched band which is from 5.2–5.9 GHz (as shown in Figure 3). In addition, the narrow slot etched in the patch shown in Figure 2(c) whose length and width are 9.6 mm and 0.25 mm, respectively, is employed to obtain the desired notched band which is from 5.14–5.94 GHz (as shown in Figure 3) so that the proposed antenna cannot interfere with WLAN applications. Note that the bandwidth is shorted by adding a narrow slot on the patch; the reason is the narrow slot and the wide slot is so near that they interfere with each other. The notched frequency, given the

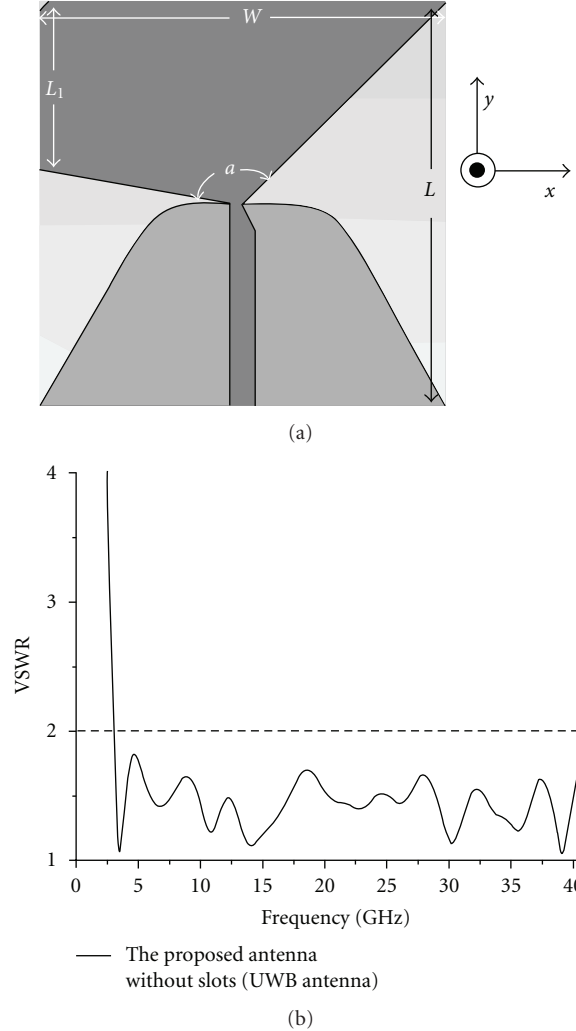


FIGURE 1: The geometry and the simulated VSWR result of the proposed antenna without slots (UWB antenna): (a) the geometry, (b) the simulated VSWR result.

dimensions of the band-notched feature, can be postulated as [10]

$$f_{\text{notch}} = \frac{c}{4L\sqrt{(\epsilon_r + 1)/2}}. \quad (2)$$

2.3. Dual Band-Notched Antenna Design. Based on single band-notched antennas aforementioned, the dual band-notched antennas will be investigated to reduce the interferences from the existing bands.

Figure 4 shows the geometries of two dual band-notched antennas. Their VSWR results are shown in Figure 5, respectively; it can be seen that the bandwidth of the UWB system is hardly affected by the slots, and the bandwidth of the low frequency band-notched antenna formed by only a wide slot and the bandwidth of the high frequency band-notched antenna formed by only a narrow slot do not interfere with each other.

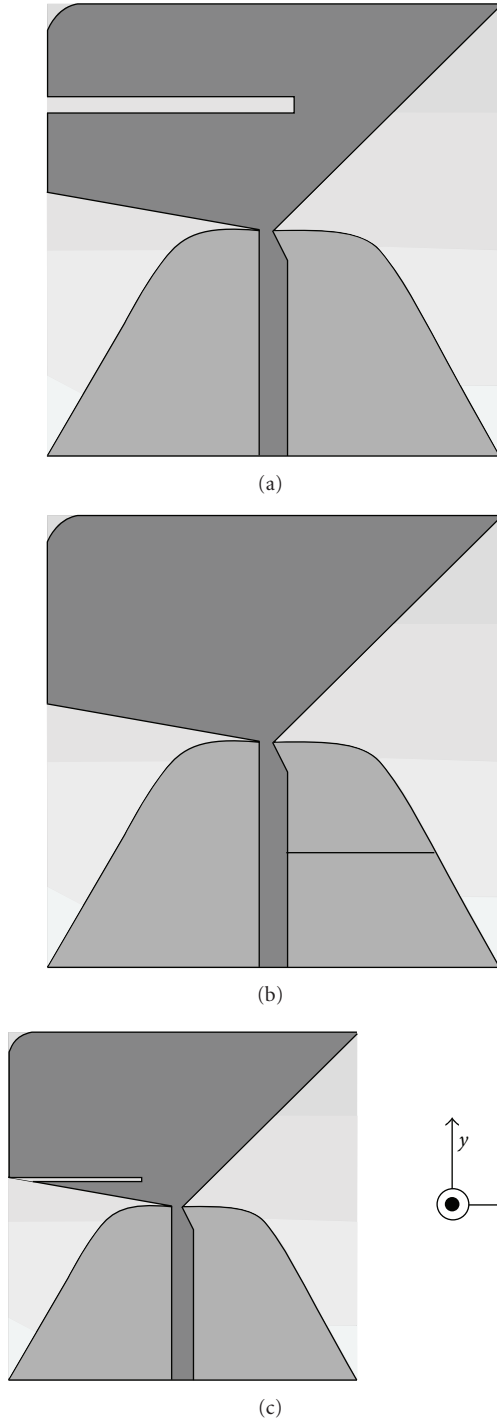


FIGURE 2: The geometry of the single band-notched antennas: (a) single band-notched antenna 1, (b) single band-notched antenna 2, (c) single band-notched antenna 3.

3. Results and Discussions

3.1. Frequency-Domain Performances. The dual band-notched UWB antennas were simulated and optimised using the business software CST. Shown in Figure 6 are prototypes of the antennas.

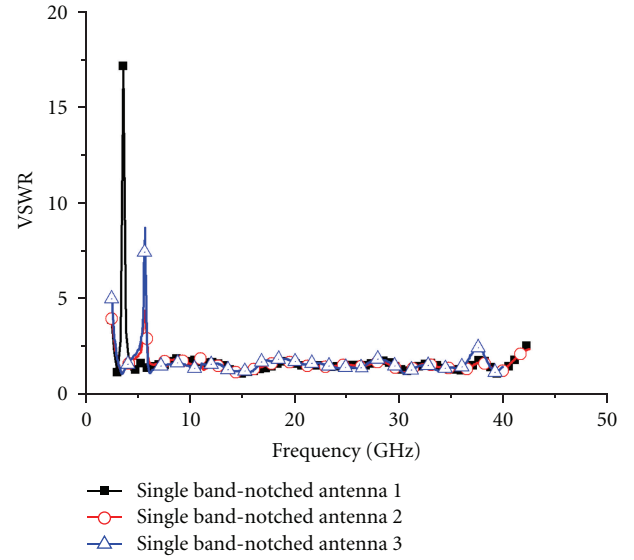


FIGURE 3: The simulated VSWR results of the single band-notched antennas.

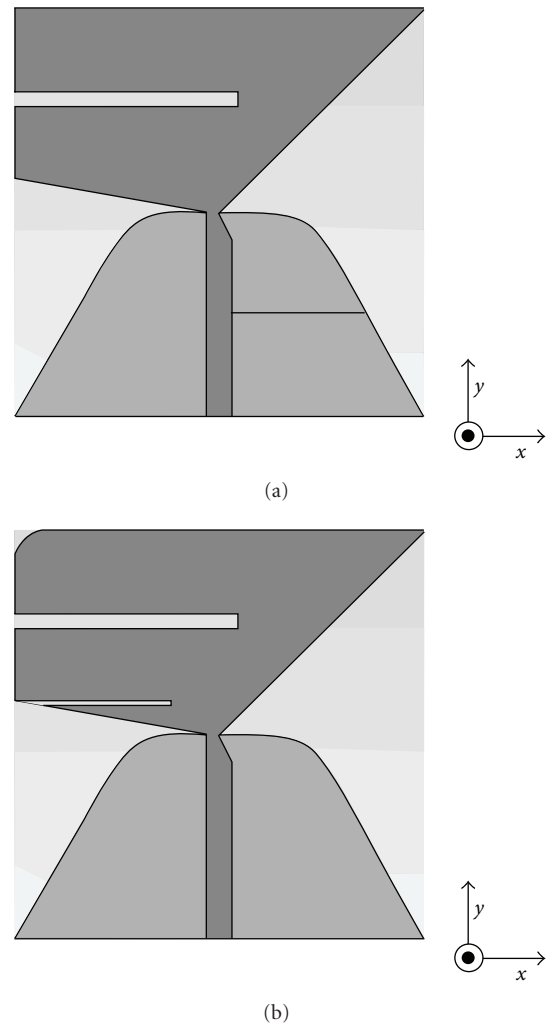


FIGURE 4: The geometries of the proposed antennas: (a) dual band-notched antenna 1, (b) dual band-notched antenna 2.

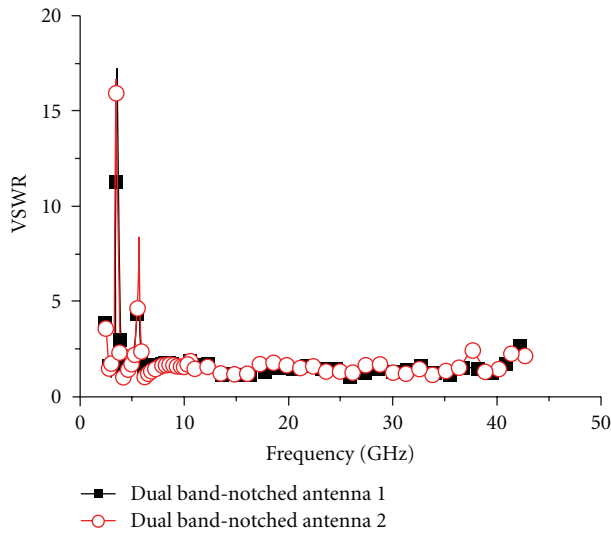
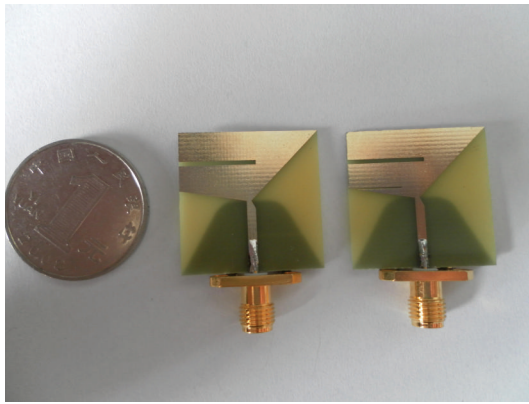
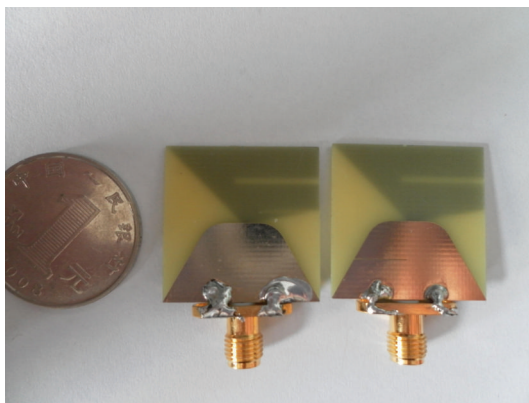


FIGURE 5: The simulated VSWR results of the dual band-notched antennas.

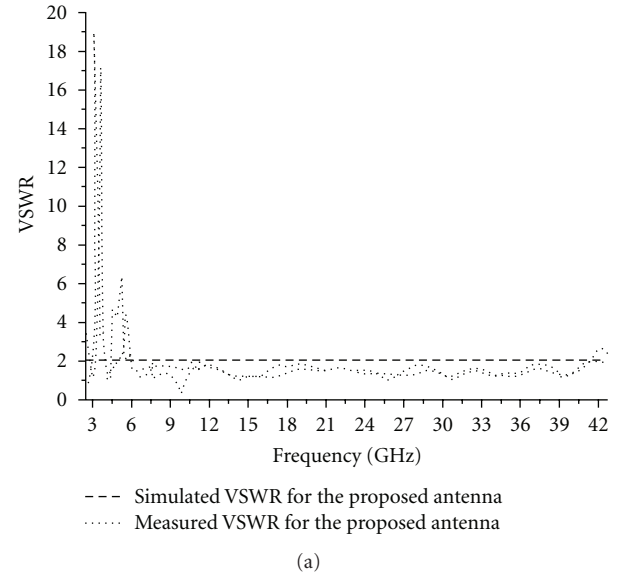


(a)

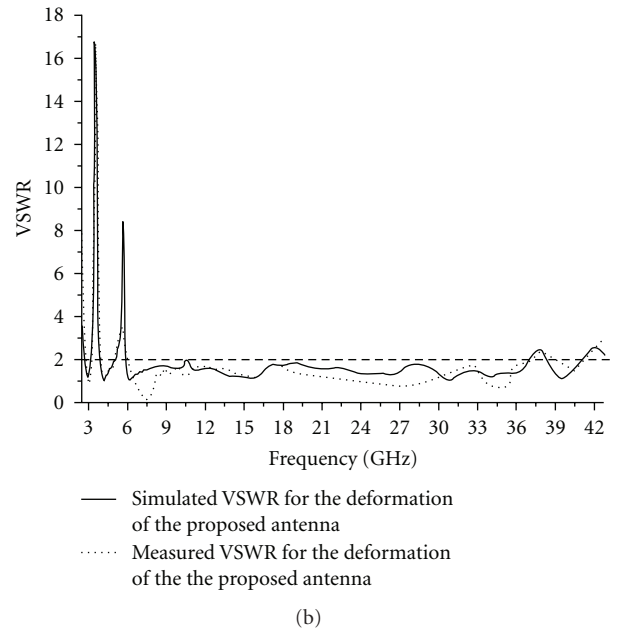


(b)

FIGURE 6: The photos of the proposed antenna: (a) the front of dual band-notched antennas, (b) the back of dual band-notched antennas.



(a)

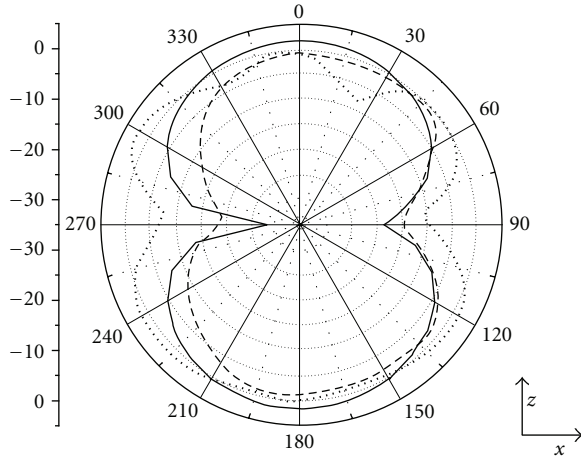


(b)

FIGURE 7: Simulated and measured VSWR results of the proposed antennas: (a) dual band-notched antenna 1, (b) dual band-notched antenna 2.

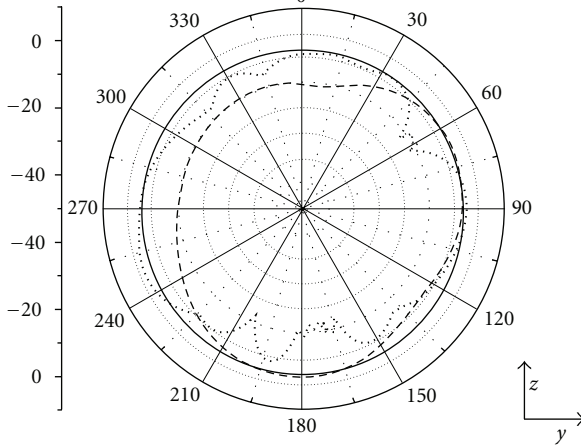
Shown in Figure 7, it can be seen that the simulated and measured results show relatively good agreement. As shown in Figure 7(a), the dual band-notched antenna 1 has two notched bands which can cover the WiMAX band (3.2–3.9 GHz) and the 4.8–5.9 GHz band. In addition, the dual band-notched antenna 2 can eliminate the 3.2–3.9 GHz band and the 5.14–5.94 GHz band, as Figure 7(b) shows.

The radiation patterns of the proposed antennas at 3.1 GHz, 10.6 GHz and 36 GHz are shown in Figures 8 and 9, respectively. The antennas give a nearly omnidirectional radiation patterns in the H -plane. The antennas gain in the entire operating band is presented in Figure 10. As desired,



— 3.1 GHz
 --- 10.6 GHz
 36 GHz

(a)



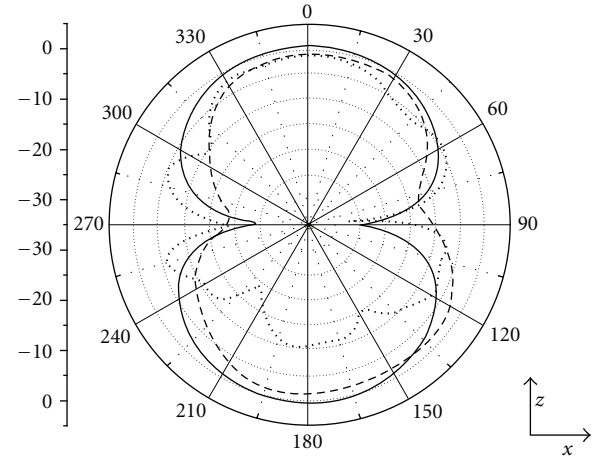
— 3.1 GHz
 --- 10.6 GHz
 36 GHz

(b)

FIGURE 8: Radiation patterns on E -plane (x - z plane) and H -plane (y - z plane) for the dual band-notched antenna 1 at 3.1 GHz, 10.6 GHz, and 36 GHz: (a) E -plane (b) H -plane.

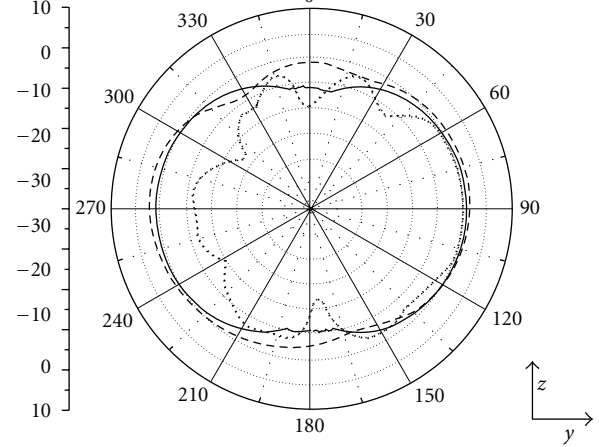
two sharp gains decrease in the vicinity of 3.55 GHz and 5.6 GHz, and the gains are stable in the entire operating band.

3.2. Time-Domain Behaviors. As shown in the previous section, the proposed antennas present the very wide band. However, as far as an UWB antenna is concerned, the good frequency-domain performances cannot necessarily ensure that the antenna also behaves well in time domain. Some multiresonant antennas, such as the Yagi-Uda and the log-periodic antennas [11], due to its multiple reflections in their structures, seriously widen the narrow pulse in time domain. Therefore, in order to ensure the usefulness of the



— 3.1 GHz
 --- 10.6 GHz
 36 GHz

(a)



— 3.1 GHz
 --- 10.6 GHz
 36 GHz

(b)

FIGURE 9: Radiation patterns on E -plane (x - z plane) and H -plane (y - z plane) for the dual band-notched antenna 2 at 3.1 GHz, 10.6 GHz, and 36 GHz: (a) E -plane (b) H -plane.

proposed antenna for time-domain applications, its time-domain responses must be investigated.

The transmit characteristic in time domain is measured in a manner shown in the inserted figure in Figure 11. The two identical proposed antennas are put face to face in a distance of 20 cm. The measured group delay of S_{21} , given in Figure 11, indicates far-field phase linearity and a quality of a pulse distortion and is derived from the first differential coefficient of the phase.

Group delays of the proposed antennas are shown in Figure 12. The variation of the group delay of the dual band-notched antenna 1 is about 1 ns across the whole UWB except the notched bands, in which the maximum group delay is

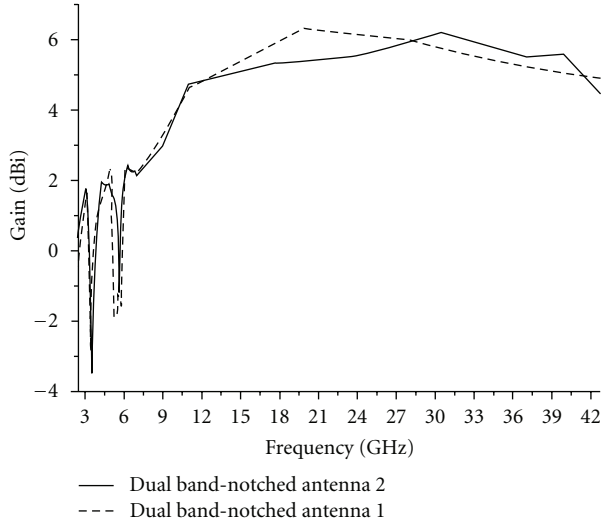


FIGURE 10: Gains of the proposed antennas.

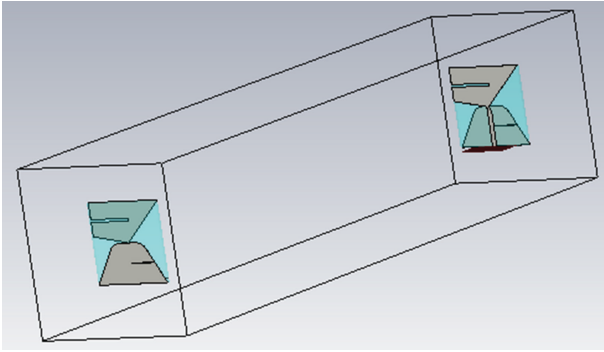


FIGURE 11: The setup of the group delay experiment.

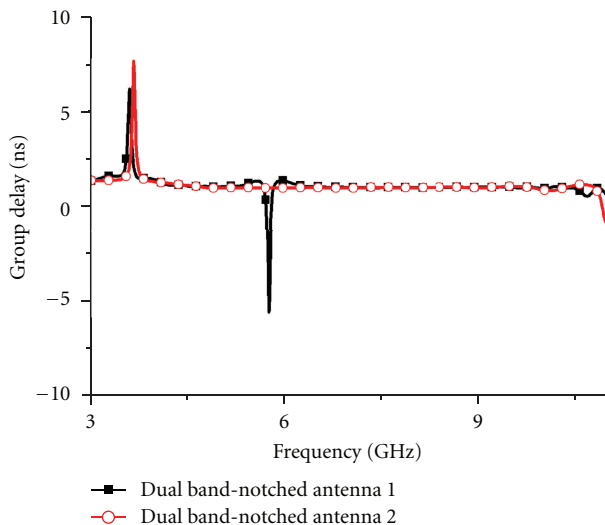


FIGURE 12: Group delays of the proposed antennas.

6 ns. On the other hand, the variation of the group delay of dual band-notched antenna 2 is about 1 ns across the whole UWB except the notched band, in which the maximum group delay is 7 ns. It is worthwhile to mention that the maximum group delay of dual band-notched antenna 2 only appears in the first notched band, but those of dual band-notched antenna 1 exist in the two notched bands. The monopole patch is the main element which transmits the pulse; when the slots etched outside the monopole patch, like dual band-notched antenna 2, the slots cannot effectively suppress the signals of the notched bands. As a result, there is a huge difference between the group delays of the two antennas.

In general, dual band-notched antenna 1 has a good time-domain characteristic and a small pulse distortion as well.

4. Conclusion

Two simple and compact ultra-wideband printed monopole antennas with dual band-notches are proposed in this paper. Using a monopole configuration, the antenna dimensions were optimised to gain the best VSWR response throughout the UWB frequency band. By embedding two slots in the antennas, dual band-notches will be created, which exempts from interference with existing WiMAX and WLAN operating bands, and measurement results show that the designed antennas satisfy the UWB design goals very well.

Acknowledgments

This work was supported by the National Natural Science Foundation of China (no. 61172115 and no. 60872029), the High-Tech Research and Development Program of China (no. 2008AA01Z206), the Aeronautics Foundation of China (no. 20100180003), and the Fundamental Research Funds for the Central Universities (no. ZYGX 2009J037).

References

- [1] First Report and Order in the matter of Revision of Part 15 of the Commission's Rules Regarding Ultra-Wideband Transmission Systems, Released by Federal Communications Commission, ET-Docket 98-153, 2002.
- [2] Q. X. Chu and Y. Y. Yang, "3.5/5.5 GHz dual band-notch ultra-wideband antenna," *Electronics Letters*, vol. 44, no. 3, pp. 172-174, 2008.
- [3] X. J. Liao, H. C. Yang, N. Han, and Y. Li, "Aperture UWB antenna with triple band-notched characteristics," *Electronics Letters*, vol. 47, no. 2, pp. 77-79, 2011.
- [4] C. Y. Huang, S. A. Huang, and C. F. Yang, "Band-notched ultra-wideband circular slot antenna with inverted C-shaped parasitic strip," *Electronics Letters*, vol. 44, no. 15, pp. 891-892, 2008.
- [5] H. H. Xie, Y. C. Jiao, Z. Zhang, and Y. Song, "Band-notched ultra-wideband monopole antenna using coupled resonator," *Electronics Letters*, vol. 46, no. 16, pp. 1099-1100, 2010.
- [6] R. Gayathri, T. U. Jisney, D. D. Krishna, M. Gopikrishna, and C. K. Aanandan, "Band-notched inverted-cone monopole

- antenna for compact UWB systems,” *Electronics Letters*, vol. 44, no. 20, pp. 1170–1171, 2008.
- [7] M. Ojaroudi, S. Yazdanifard, N. Ojaroudi, and R. A. Sadeghzadeh, “Band-notched small square-ring antenna with a pair of T-shaped strips protruded inside the square ring for UWB applications,” *IEEE Antennas and Wireless Propagation Letters*, vol. 10, pp. 227–230, 2011.
- [8] J. Kim, C. S. Cho, and J. W. Lee, “5.2 GHz notched ultra-wide-band antenna using slot-type SRR,” *Electronics Letters*, vol. 42, no. 6, pp. 315–316, 2006.
- [9] B. Ahmadi and R. Faraji-Dana, “A miniaturised monopole antenna for ultra-wide band applications with band-notch filter,” *IET Microwaves, Antennas and Propagation*, vol. 3, no. 8, pp. 1224–1231, 2009.
- [10] L. H. Ye and Q. X. Chu, “3.5/5.5 GHz dual band-notch ultra-wideband slot antenna with compact size,” *Electronics Letters*, vol. 46, no. 5, pp. 325–327, 2010.
- [11] J. D. Taylor, *Introduction to Ultra-Wideband Radar System*, CRC Press, London, UK, 1995.

Research Article

A Reconfigurable Coplanar Waveguide Bowtie Antenna Using an Integrated Ferroelectric Thin-Film Varactor

K. C. Pan,¹ D. Brown,¹ G. Subramanyam,¹ R. Penno,¹ H. Jiang,¹ C. H. Zhang,¹
M. Patterson,¹ D. Kuhl,² K. Leedy,² and C. Cerny²

¹Department of Electrical and Computer Engineering, University of Dayton, 300 College Park, Dayton, OH 45469, USA

²Air Force Research Lab, Sensors Directorate, WPAFB, Dayton, OH 45432, USA

Correspondence should be addressed to D. Brown, brownd7@udayton.edu

Received 10 March 2012; Revised 11 June 2012; Accepted 17 June 2012

Academic Editor: Hala A. Elsadek

Copyright © 2012 K. C. Pan et al. This is an open access article distributed under the Creative Commons Attribution License, which permits unrestricted use, distribution, and reproduction in any medium, provided the original work is properly cited.

A novel printed antenna with a frequency reconfigurable feed network is presented. The antenna consists of a bowtie structure patch radiating element in the inner space of an annulus that is on a nongrounded substrate with a ferroelectric (FE) Barium Strontium Titanate (BST) thin film. The bowtie patch is fed by a coplanar waveguide (CPW) transmission line that also includes a CPW-based BST shunt varactor. Reconfiguration of the compact 8 mm × 8 mm system has been demonstrated by shifting the antenna system's operating frequency 500 MHz in the 7–9 GHz band by applying a DC voltage bias.

1. Introduction

Because many antennas are narrowband in frequency, more than one antenna is usually needed in systems that operate over multiple frequency bands. Mobile phones and other portable communication devices, for example, are beginning to require broader bandwidths to support their numerous applications and communication protocols. Due to this growing spectrum usage in single devices, more versatile or reconfigurable antennas are desirable to reduce the total required parts as well as overall cost.

The purpose of this paper is to discuss the design of a reconfigurable CPW feed network for a single-layer-patch antenna. Previously presented microstrip patch antenna designs [1] utilized a thin-film ferroelectric (FE) barium strontium titanate (BST) layer and varactor [2] to the feed line. The system presented here improves upon this design by integrating the above varactor with a CPW-based antenna. By using the same transmission line architecture, the fabrication process is simplified and impedance matching between the two devices is much more straightforward.

An added benefit to using BST is that the film has a high dielectric constant, ϵ_r . This material attribute reduces the physical wavelength, thus allowing the antenna to be

more compact compared to an antenna on more traditional dielectric substrates.

The paper discusses the design of the antenna, electromagnetic simulation of the antenna. Experimental results of the antenna's impedance matching bandwidth and radiation performance are also be presented.

2. Antenna Design

As the overall purpose of this paper is to have an antenna system capable of reconfigurability, the design process was first approached by addressing a novel means of reconfiguration. As antennas and the rest of the RF chain typically require matching networks to allow for maximum power transfer, it was proposed that having a flexible, lumped element device close to the feed of an antenna would allow for a more versatile system.

By the addition of a shunt varactor to the feed network, the combination of which can be depicted by Figure 1, the antenna system's impedance can be adjusted. This reconfigurable matching network can be tuned based on the frequency band of interest. Looking at the admittance of the

antenna, transmission feed, and varactor, the input admittance of the system can be expressed by

$$Y_{11} = Y_{in} = Y_{in1} + j\omega C, \quad (1)$$

$$Y_{in1} = \frac{1}{Z_{in1}} = \frac{1}{Z_o} \left[\frac{Z_o + jZ_A \tan \beta L_6}{Z_A + jZ_o \tan \beta L_6} \right],$$

where Z_A is the antenna impedance and the C term is the capacitance of the shunt varactor. As this capacitance is adjustable, the system can thus be reconfigured to provide an ideal match across a wider range of frequencies.

The shunt thin-film device described in [2] provides a unique, thin-film varactor that can be used in the impedance matching network of the antenna system. With this particular device, the capacitance in the admittance equation above is a function of the applied bias voltage. The varactor is implemented using the four-layer structure shown in Figure 2.

As the thin-film varactor described in [2] was decided upon as the method of reconfiguration, requirements of the antenna's design and shape were defined in order to properly integrate with the varactor. First, the varactor is designed to work with a transmission line characteristic impedance of 50 ohms, so this was also the desired characteristic impedance of the designed antenna feed line. Next, to avoid losses from changing transmission line types, the antenna was designed to also have the same transmission line architecture as the varactor. As the varactor utilizes a CPW transmission line, this meant the antenna would involve surrounding the radiating element by a ground plane. This requirement was also selected as CPW-based antennas have been demonstrated as having low radiation loss [3]. Finally, the varactor utilizes both the bulk substrate and the thin-film BST dielectric. As the antenna will be a patch using one metal layer, the antenna will be designed to operate above both dielectrics with the radiator residing above the BST thin film.

It is desirable to have a large tuning range for the varactor to have the largest degree of reconfiguration in the resulting system. The dielectric constant, ϵ_r , of the BST is demonstrated having tunability of 4 : 1 max-to-min ratio for a thickness of $0.25 \mu\text{m}$ [4–6] on sapphire substrates. To leverage this versatility, the intended wafer for this design was decided to be a $600 \mu\text{m}$ thick sapphire substrate, with a $0.25 \mu\text{m}$ BST layer deposition.

Traditional bowtie antennas are known for large bandwidths while utilizing a single metallization layer, providing distinct advantages during fabrication [7]. This bandwidth was a desirable trait when designing the reconfigurable system as the goal was to achieve a wide operating range. For this reason a bowtie was selected as the basis of the radiating element for the reconfigurable system.

Starting from a CPW bowtie shape, antenna models were designed and simulated in the commercial microwave frequency simulation tool AWR. As the varactor used in the feed line loading was previously created in this software environment, creation of the resulting system involved only the design of the antenna. In an effort to constrain the resulting size of the system on the sapphire wafer, the target frequency range was selected to be C-Band. Antenna shape

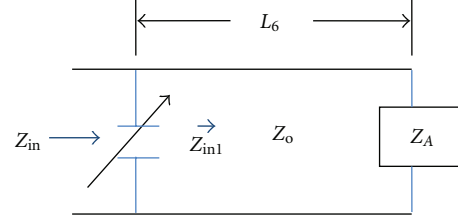


FIGURE 1: Model of the antenna system including CPW feed line and shunt varactor.

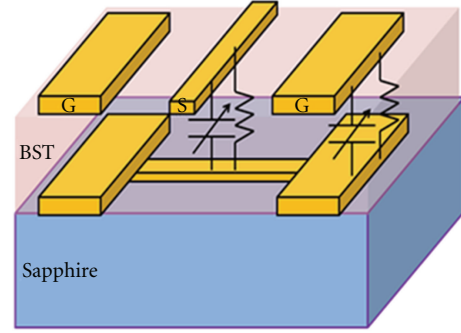


FIGURE 2: BST thin-film varactor structure.

and dimensions were revised incrementally until simulated performance met the desirable frequency bandwidth performance.

The resulting antenna system is shown in Figure 3. The varactor is integrated in front of the transmission line that feeds the CPW bowtie patch antenna. As can be seen, the actual radiating elements are $4.8 \text{ mm} \times 5.1 \text{ mm}$, or $0.12 \lambda_o \times 0.1275 \lambda_o$, where λ_o is the free space wavelength. The overall size of the antenna system is $8 \text{ mm} \times 8 \text{ mm}$ which is approximately $0.2 \lambda_o \times 0.2 \lambda_o$ which also shows the entire system works at dimensions that are fractions of the free space wavelength.

3. Testing Methodology

To analyze the performance of the antenna system, the frequency swept scattering parameters (S Parameters) were simulated using the AWR electromagnetic model and also measured on the fabricated device. The fabricated device also underwent testing in an anechoic chamber to analyze radiated fields produced by the antenna.

The S parameters of the fabricated antenna system were measured using an HP8720B vector network analyzer. An on-wafer probe station was fitted with a CASCADE SP-ACP40-GSG-150-C CPW probe for measurements. To test the tuning performance of the system, a Keithly 2400 source meter was used to provide the DC biasing voltage. The system was tested with biasing voltages ranging from 0 to 10 volts.

The far-field radiation patterns of the reconfigurable antenna under 0 volt bias voltage conditions were measured in the Radiation and Scattering Compact Antenna Laboratory (RASCAL) at the Air Force Research Laboratory.

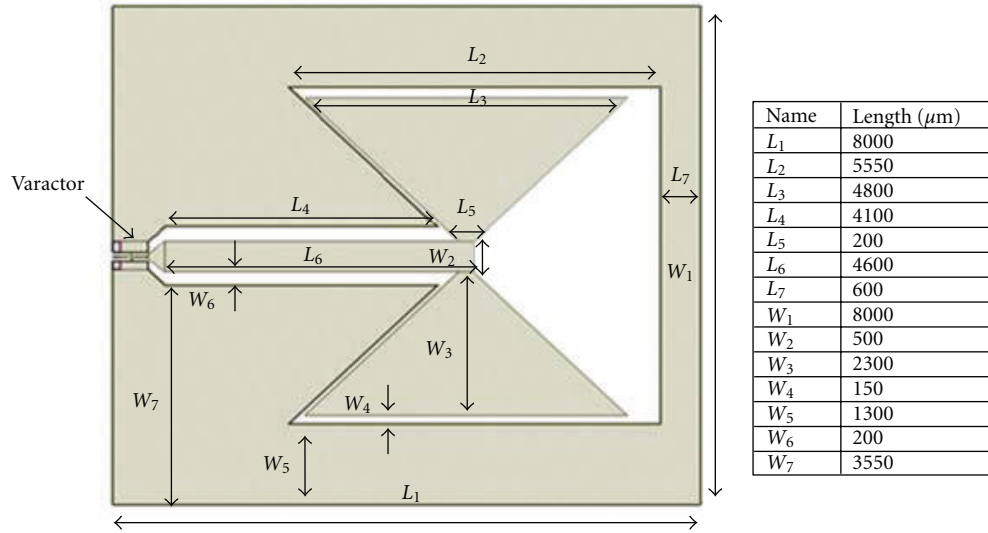


FIGURE 3: A CPW-Fed bowtie slot antenna connected with a BST thin-film varactor.

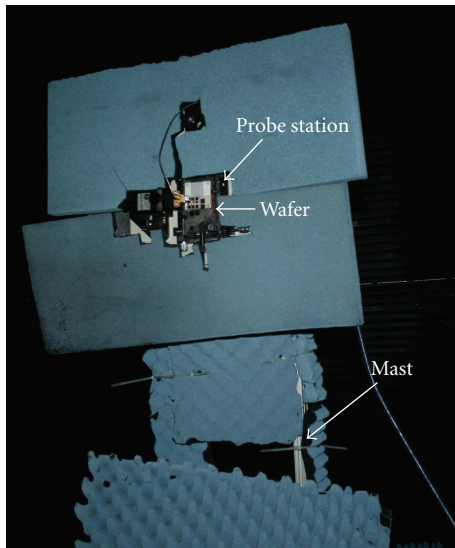


FIGURE 4: Radiation measurement setup in the RASCAL anechoic chamber.

To measure the far-field radiation patterns, the reconfigurable antenna was turned mechanically in an anechoic chamber. A rotating mast was in the center of the chamber, with a portable probe station connected to it. The probe station was used to hold the antenna as shown in Figure 4. The magnitude and phase data was collected and measured for the various angles in the mechanical sweep.

4. Results and Discussions

Plots of the simulated and measured system performance can be seen in Figures 5–9. Electromagnetic simulations of the antenna with the CPW feed line were run both with and

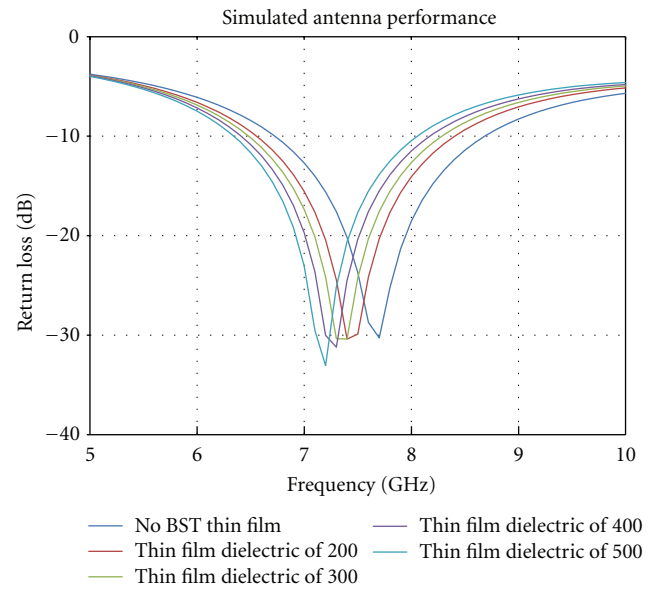


FIGURE 5: Bowtie antenna on different BST permittivities.

without a varactor connected in the AWR environment to show how the system changes with a varactor present.

Figure 5 shows the simulated results of the CPW patch antenna atop BST thin films of varying permittivity values as well as a reference design of the antenna above only the bulk sapphire. From the figure it is seen that the antenna undergoes a miniaturization, as shown by the notch point moving to lower frequency when above BST. The permittivity numbers simulated in this comparison also agree with those permittivity numbers from the tuning of previously published research [2].

Figures 6 and 8 show the electromagnetic simulation results of the antenna system under tuning of the varactor. The resulting S parameter of Figure 6 show the antenna

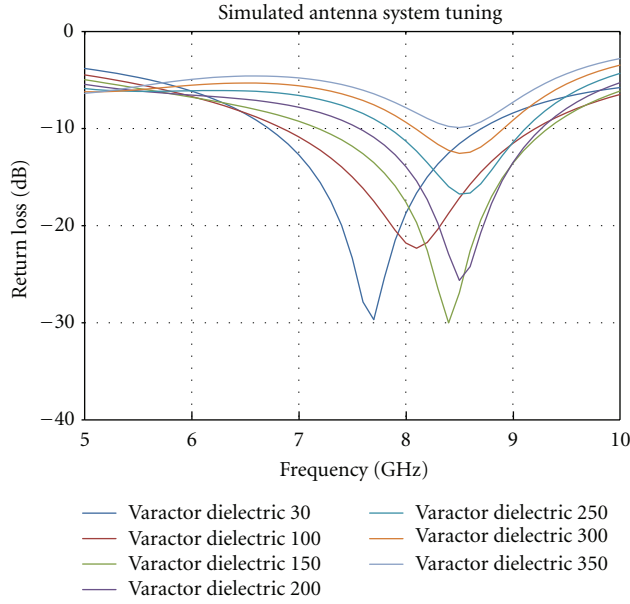
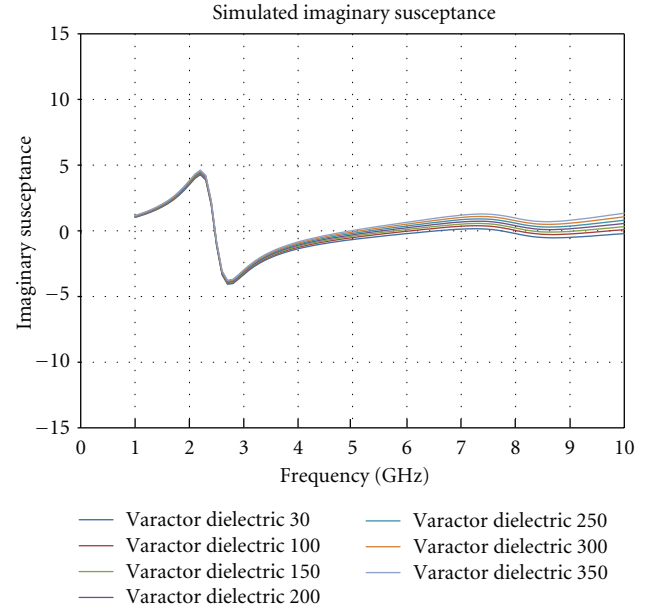
FIGURE 6: Simulated swept frequency S_{11} of the antenna system.

FIGURE 8: Simulated susceptance versus frequency for the antenna system.

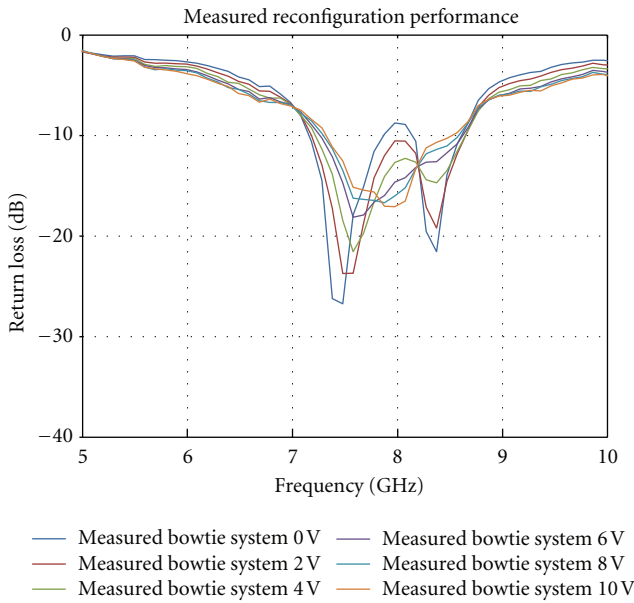
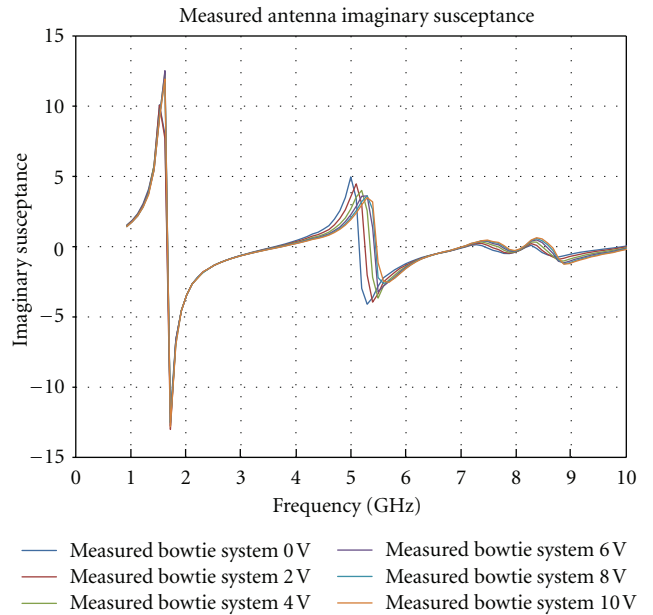
FIGURE 7: Measured swept frequency S_{11} of the antenna system under 0–10 V DC bias.

FIGURE 9: Measured susceptance versus frequency for the antenna system under 0–10 V DC bias.

system tuning from 7.7 to 8.4 GHz with altering the varactor's capacitance. As the capacitance is adjusted, both the notch points as well as the resulting S parameter curves are altered. This means some bias conditions may have narrower bandwidth than others, but the overall system is now capable of operating at multiple frequencies.

The measured varactor-loaded results are shown in Figures 7 and 9. In Figure 7 we again see that the notch points and S parameter curves are adjusted under differing biasing conditions. At a DC bias of 0 V, the antenna is best matched at 7.42 GHz. This point shifts to higher frequencies as bias

voltage increases beginning to level off at bias voltages above 6 V. The notch point shifts to 7.9 GHz under 10 V bias leading to a 500 MHz tuning of the system.

Comparing these results to the simulation plots, both the notch frequency and the overall reflection curves are different. The most noticeable difference is the appearance of the second notch at 8.36 GHz. The reasons for differing performance are under further analysis, but two conditions are

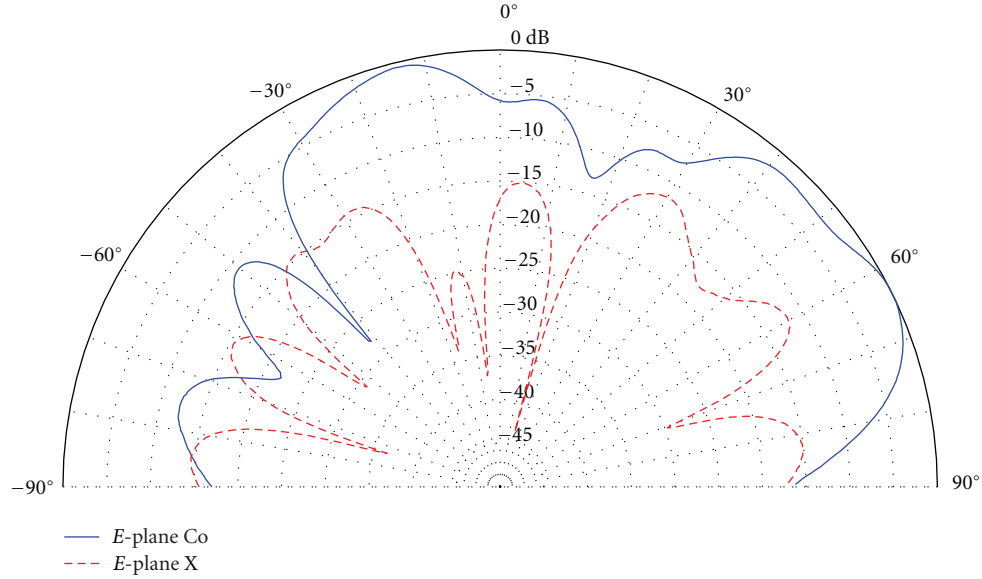


FIGURE 10: E-plane copolarization and crosspolarization measured at 7.4 GHz.

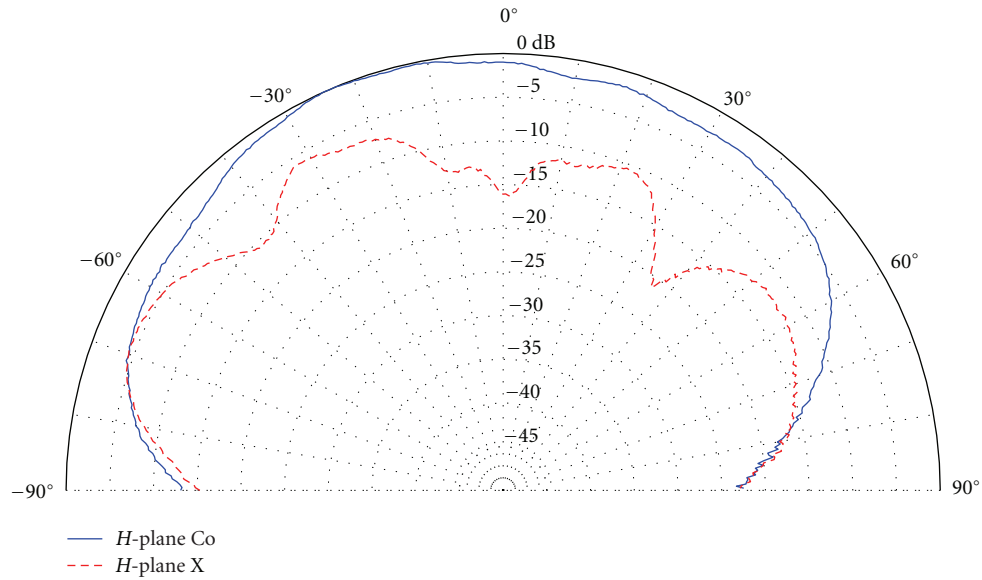


FIGURE 11: H-plane copolarization and crosspolarization measured at 7.4 GHz.

possible factors, varactor performance and BST modeling characteristics.

First the varactor performance in the system and simulation were compared by analyzing the susceptances. As can be seen in Figure 8, the addition of the shunt varactor in the simulated electromagnetic model increases the susceptance of the system across the frequency spectrum. The simulated system thus models the varactor as having very low inductance. For the measured system susceptance in Figure 9, the differences between the different bias voltages follow the same general variation up to approximately 7 GHz, at which point the curves appear to be tightly grouped. This may indicate inductive effects from the combination of the varactor and antenna that were not appropriately accounted

for. This more complex susceptance near the band of interest can greatly impact the resulting system's S parameter performance.

Second, the material characterization for BST in the electromagnetic AWR model was based on the performance of previous varactor devices. The model assumes a uniform ϵ_r permittivity across the BST film. If either the dielectric permittivity numbers differ under the larger area of the antenna or if the permittivity is not constant over the entire film, the simulation of the antenna will be inaccurate. These possible variations in material properties in a given wafer are a definite possibility for the cause of disagreement between simulation and measurement results.

Both copolarized and cross-polarized fields were collected for the E plane and H plane sweeps of the antenna system. Figures 10 and 11 show the resulting measurements at the 0 volt bias notch frequency of 7.4 GHz. From the radiation plots it is seen that the antenna does have a relatively wide beamwidth. Also, the large differences between the co-polarized and cross-polarized curves in Figures 10 and 11 indicate that the antenna operates under a highly linear polarization.

5. Conclusions

Improvements are needed in the correlation of electromagnetic modeling and physical performance. The combination of material and antenna characterization research will be a primary focus of future work. Investigations of additional varactor loading of antennas for improved tuning will also be of interest as well as variations to the size and type of shunt varactor used, improvements to the modeling of BST for antenna applications. As the bowtie antenna used herein is modified from the traditional structure, a more thorough analysis of the antennas mode of operation is also a point of interest.

In the end, a novel compact printed antenna for reconfigurable applications was demonstrated by employing the BST varactor in the feed network of an antenna system. This bowtie patch antenna has a compact structure with the total size of $8\text{ mm} \times 8\text{ mm}$ operating between 7 and 9 GHz. By tuning the bias voltage between 0 and 10 V DC, the notch frequency of the system is reconfigured up to 500 MHz.

References

- [1] H. Jiang, M. Patterson, C. Zhang, and G. Subramanyam, "Frequency agile microstrip patch antenna using ferroelectric thin film varactor technology," in *Proceedings of IEEE International Symposium on Antennas and Propagation and USNC/URSI National Radio Science Meeting (APSURSI '09)*, pp. 1–4, Charleston, SC, USA, June 2009.
- [2] G. Subramanyam, F. Ahamed, and R. Biggers, "A Si MMIC compatible ferroelectric varactor shunt switch for microwave applications," *IEEE Microwave and Wireless Components Letters*, vol. 15, no. 11, pp. 739–741, 2005.
- [3] E. A. Soliman, S. Brebels, G. Vandenbosch, and E. Beyne, "X-band brick wall antenna fed by CPW," *Electronics Letters*, vol. 34, no. 9, pp. 836–838, 1998.
- [4] B. Riehl, G. Subramanyam, R. Biggers et al., "Synthesis and characterization of nanostructured BSTO thin-films for microwave applications," *Integrated Ferroelectrics*, vol. 55, pp. 825–8379, 2003.
- [5] A. L. Campbell, R. R. Biggers, G. Subramanyam et al., "Microwave characterization of nanostructured ferroelectric $\text{Ba}_{0.6}\text{Sr}_{0.4}\text{TiO}_3$ thin films fabricated by pulsed laser deposition," *Nanotechnology*, vol. 19, no. 48, Article ID 485704, 2008.
- [6] H. Jiang, M. Patterson, D. Brown et al., "Miniaturized and reconfigurable CPW square-ring slot antenna using thin film varactor technology," in *Proceedings of IEEE MTT-S International Microwave Symposium Digest (MTT '11)*, pp. 1–4, June 2011.
- [7] Y. D. Lin and S. N. Tsai, "Coplanar waveguide-fed uniplanar bow-tie antenna," *IEEE Transactions on Antennas and Propagation*, vol. 45, no. 2, pp. 305–306, 1997.

Research Article

Flexible Microstrip Antenna for Skin Contact Application

Sudhir Shrestha, Mangilal Agarwal, Parvin Ghane, and Kody Varahramyan

*Integrated Nanosystems Development Institute (INDI), Indiana University-Purdue University Indianapolis (IUPUI),
723 West Michigan Street, Indianapolis, IN 46202, USA*

Correspondence should be addressed to Mangilal Agarwal, agarwal@iupui.edu

Received 10 March 2012; Revised 4 June 2012; Accepted 4 June 2012

Academic Editor: Dalia N. Elshiekh

Copyright © 2012 Sudhir Shrestha et al. This is an open access article distributed under the Creative Commons Attribution License, which permits unrestricted use, distribution, and reproduction in any medium, provided the original work is properly cited.

Microstrip antennas are finding a growing medical application in imaging, diagnosis, and treatment. This paper presents a flexible microstrip antenna that can be placed in contact with the human skin. The developed antenna is only 0.25 mm thick, has 32 mm × 31 mm dimensions, and −19 dB measured $|S_{11}|$ parameter at 2.45 GHz. A specific application of the antenna in microwave breast imaging is considered. Analytical results using simulation models and experimental results using skin phantoms are presented and discussed.

1. Introduction

Antennas have long been used in many medical applications including, microwave imaging, medical implants, hyperthermia treatments, and wireless wellness monitoring [1–9]. Reducing the size and complexity of the antennas used in these applications has been the primary objective of recent antenna research. Many of the above-mentioned medical applications still use bulky antenna systems which impede their efficiency and applicability despite high application potential. Microwave breast imaging can be taken as a very example [10]. The promises of microwave imaging in detecting early breast tumors without using any harmful radiation have drawn considerable attraction in the last decade [4]. However, antennas used in microwave breast imaging devices require to be immersed in intermediate matching liquid medium [11]. The use of such antennas makes the systems bulky, complicated, impractical, and expensive.

The planar and small form factor design of microstrip antennas has attracted growing medical applications [12–15]. Microstrip antenna design reported for medical applications thus far use nonflexible substrates. This paper presents a microstrip antenna designed on a non conventional flexible substrate that can be placed on the skin. The flexibility and the ability to operate in contact with the skin improve

the efficiency and practicality while reducing the form factor and cost. For example, the presented antenna in a microwave breast imaging device can remove the need for coupling liquid medium and thus enables the development of wearable breast imaging devices. The design methodology of the antenna, analytical results using simulation models in Ansoft high frequency simulation software (HFSS) [16], and experimental results using an in-house breast phantom are presented.

2. Design Methodology

The schematic of the proposed antenna is shown in Figure 1. A 0.25 mm thick flexible copper clad substrate was selected for the antenna design. With the substrate parameters given (shown in Figure 1(a)), a rectangular inset fed antenna at 2.45 GHz with 50 Ω input impedance was designed and optimized in Ansoft HFSS. A 1.5 mm skin layer (dielectric coefficient: $\epsilon_s = 39$ and conductivity: $\delta_s = 1.1$ S/m [17]) was added on the top of the antenna model (Figure 1(a), not drawn in scale). Considering the skin as a layer of the substrate, the antenna was optimized to achieve lower return loss, higher gain, and better radiation pattern by varying the antenna sizes, adding a matching stub at the input port, and moving the feed port towards the edge to increase the impedance of the antenna.

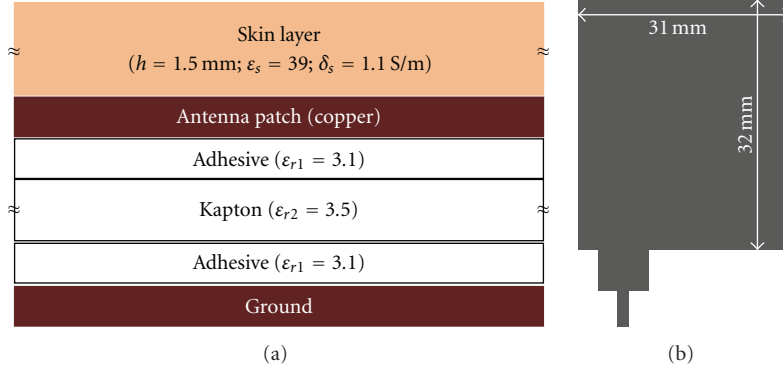


FIGURE 1: Schematics of (a) antenna-skin stack and (b) optimized antenna showing the matching stub at the input port (antenna dimensions: patch length: 32 mm; patch width: 31 mm).

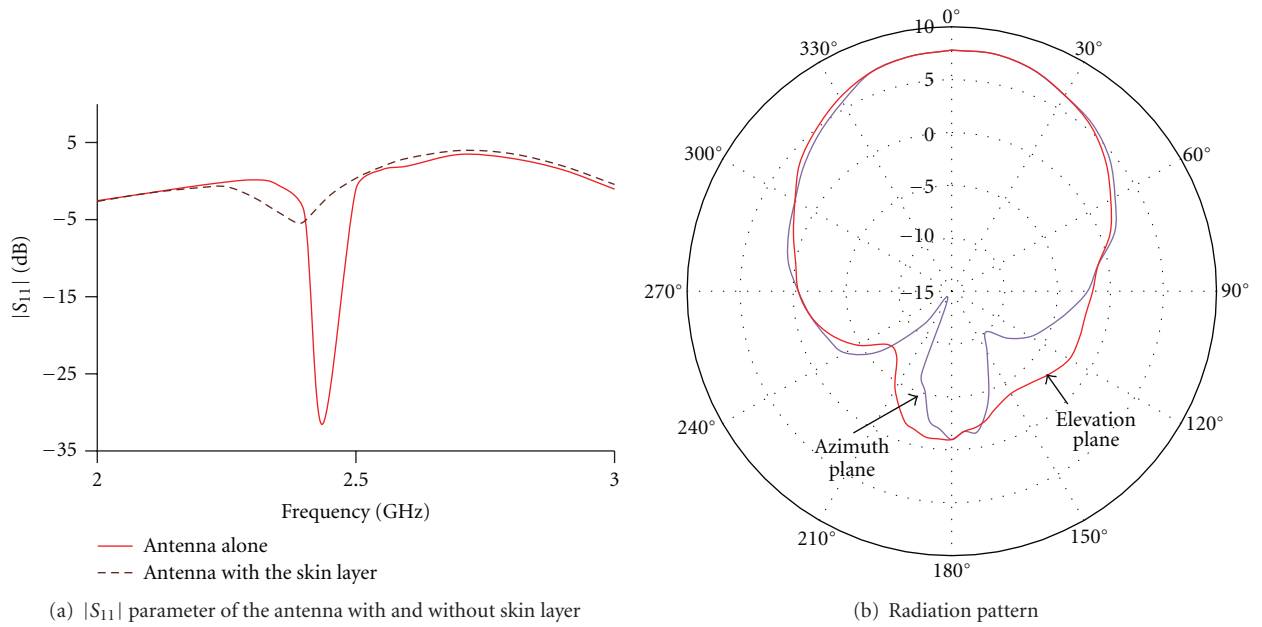


FIGURE 2: Simulation results of the initial flexible microstrip antenna design before modifying for optimized skin contact operation.

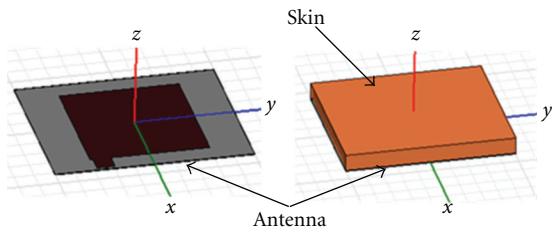


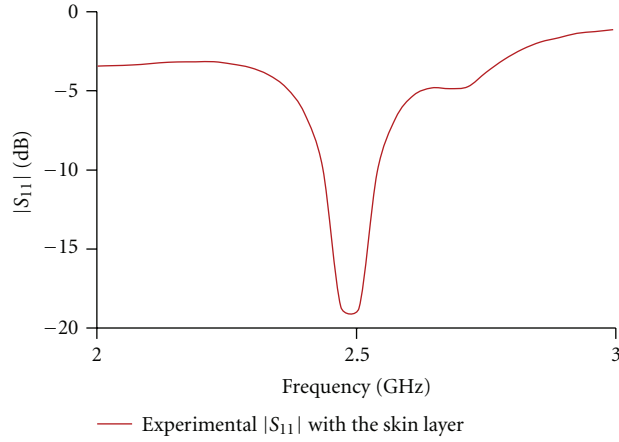
FIGURE 3: Images of antenna and antenna-skin simulation models.

3. Results and Discussion

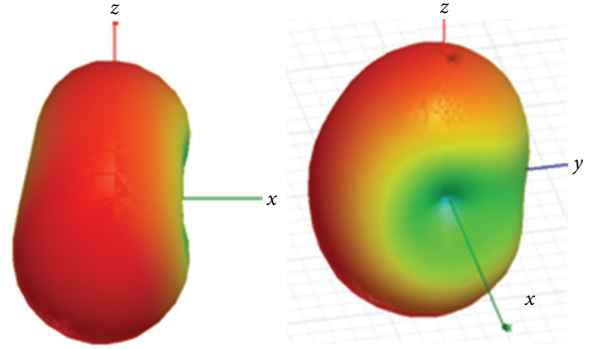
Using the substrate parameters, an initial rectangular patch antenna was designed and simulated without any skin layer. The simulated $|S_{11}|$ parameter in dB ($20 \log_{10}|S_{11}|$, will be called as $|S_{11}|$ hereafter) and the radiation pattern of

a flexible microstrip antenna are shown in Figure 2(a) (indicated as “antenna alone”) and Figure 2(b), respectively. It is seen that the antenna has -30 dB $|S_{11}|$ at 2.42 GHz with a good radiation pattern. A 1.5 mm thick skin model was then added on the top of the antenna model. As shown in Figure 1(a) (indicated as “antenna with the skin layer”), the $|S_{11}|$ of the antenna increased to -5 dB. It is observed that the ordinary antennas do not operate well when contacted with the skin. This requires the use of matching mediums between antenna and skin in many applications. For example, microwave breast imaging utilizes technique of immersing the antennas and the breast in liquid matching mediums [4].

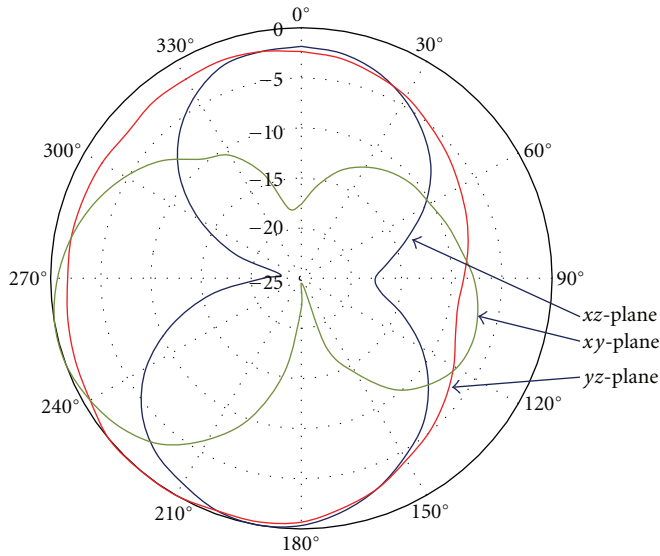
In the next step, the microstrip antenna design was modified for an optimized operation with the skin layer on the top. The optimized antenna design is shown in Figure 1(b). The simulation models of the antenna with and without skin layer are shown in Figure 3.



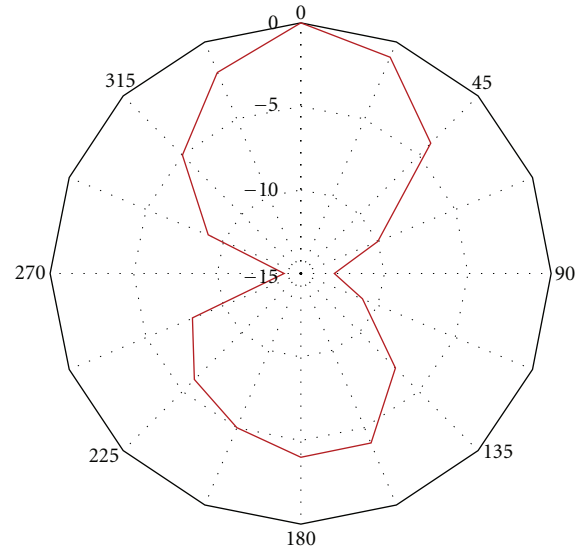
(a) Experimental $|S_{11}|$ of the antenna placed in contact with the skin phantom



(b) Simulated 3D radiation patterns



(c) Simulated 2D radiation patterns



(d) Experimental radiation pattern of the antenna placed in contact with the skin phantom

FIGURE 4: Experimental and simulation results of the antenna placed in contact with the skin.

The designed antenna was fabricated on a flexible copper clad substrate using standard photolithography technique. First, the design was transferred onto a transparent mask. The copper substrate was cleaned, dried, and a $50\text{ }\mu\text{m}$ positive photoresist (PR1813) was applied using a spinner. The substrate was heated for 2 min at 90°C and exposed to ultraviolet light through the mask. The substrate was subsequently developed in a developer solution, baked at 100°C for 15 min, and etched. The antenna was cleaned, and a reverse polarity female SMA connector was added. A 1.5 mm skin phantom was made using 1:1 corn and water mixture cooked until it became jelly (adopted from [18]) and was placed on the top of the fabricated antenna. The experimental $|S_{11}|$ (measured using Rohde and Schwarz ZVL-13 vector network analyzer) is shown in Figure 4(a). The simulated 3D and 2D radiation patterns (in xz , xy , and

yz -planes as indicated in Figure 3) are shown in Figure 4(b) and Figure 4(c), respectively. The experimental radiation pattern (on xz -plane) is shown in Figure 4(d).

To improve the radiation pattern of the antenna, a reflector configuration placed below the ground and separated by a 0.1 mm dielectric material, as shown in Figure 5(a), was considered. The design was simulated in Ansoft HFSS, and the improved radiation pattern is shown in Figure 5(b).

The simulation result shows a significant improvement (compared to Figure 4(b)) when a reflector configuration is added below the ground layer. A double-sided polyimide tape was used as the dielectric separator between ground and the reflector (indicated as “separator” in Figure 5(a)), and a copper tape was used as the reflector. The simulation result shows the possibilities of further improvement of the antenna for medical applications.

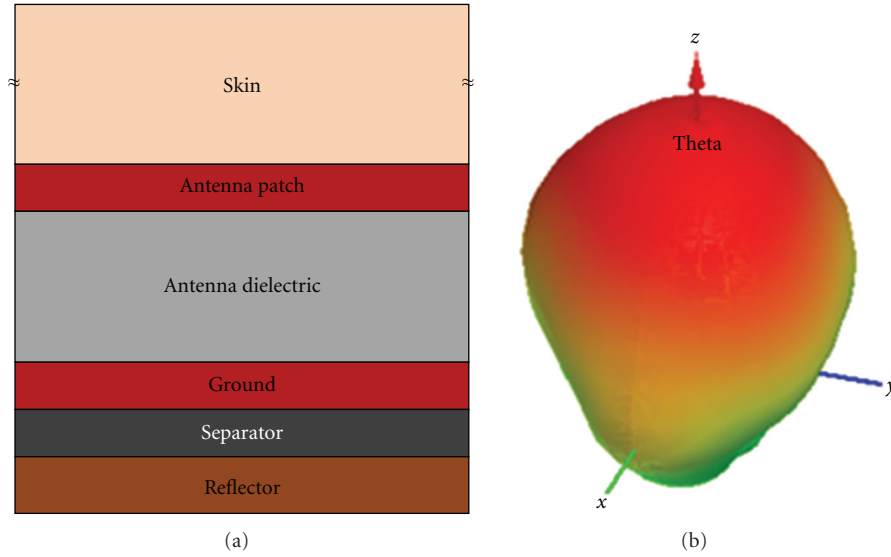


FIGURE 5: (a) Schematic showing the added reflector layer at the back of the ground and (b) 3D radiation pattern of the antenna with the reflector configuration.

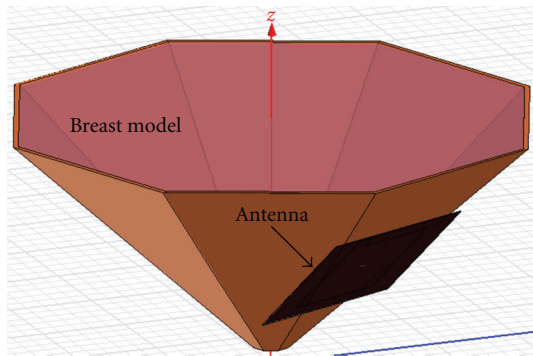


FIGURE 6: Simulation model in HFSS showing the breast and the antenna.

An application example of the antenna was considered in microwave breast imaging. Simulation model of the breast was developed in Ansoft HFSS with the antenna placed in contact with the skin model (Figure 6). The breast model was designed as a 10 cm wide and 5 cm high cone with eight facets. The breast skin was considered 1.5 mm thick layer with dielectric coefficient, $\epsilon_s = 39$, and conductivity, $\delta_s = 1.1 \text{ S/m}$ [17].

Many medical applications including microwave breast imaging require bending of the antenna. Experimentally, it was observed that the $|S_{11}|$ of the antenna was stable for bending up to 60 degrees. For a systematic study, an antenna simulation model was designed in Ansoft HFSS as shown in the inset of Figure 7. The model consisted of an antenna on a 10 cm wide and 5 cm high cone with multiple facets. The model was analysed for varying numbers of facets from 128 to 8 (representing increasing bending angles). As seen

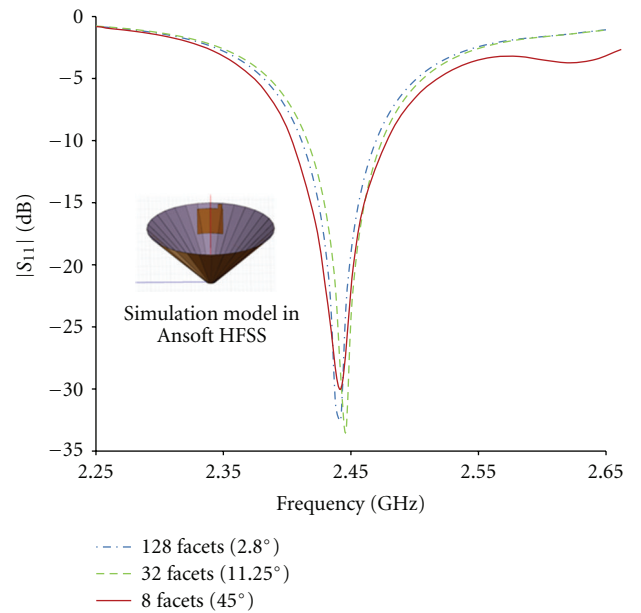


FIGURE 7: Simulation results showing $|S_{11}|$ of the antenna for 128, 32, and 8 facets of the cone representing 2.8°, 11.25°, and 45° bending.

in Figure 7, the results for 128, 32, and 8 facets show no significant change in $|S_{11}|$ with the bending. The effect of placing multiple antennas was studied experimentally. An in-house breast skin phantom was developed consisting of a 1.5 mm thick corn jelly placed on a cone mimicking breast skin. The antenna was fabricated through photolithography process and was placed on the phantom. The $|S_{11}|$ when one and four antennas were placed on the phantom were

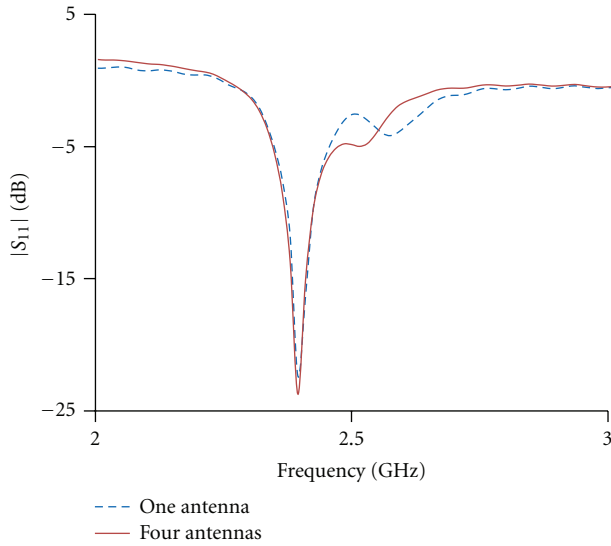


FIGURE 8: Experimental $|S_{11}|$ of the antenna when placed on breast phantom, when there was one antenna and four antennas.

measured. As shown in the Figure 8, no significant change was observed for one and four antennas.

4. Conclusion

A flexible microstrip antenna developed for skin contact application has been presented. Analytical results from simulation models and experimental results using in-house skin phantom have been presented and discussed. A specific application in microwave breast imaging has been presented with the help of simulation model and experimental testing. The presented planer flexible antenna can be used in wide varieties of medical applications, including, in developing wearable medical devices.

Acknowledgment

Acknowledgements are due to the Integrated Nanosystems Development Institute (INDI) for providing the laboratory facilities.

References

- [1] J. C. Bolomey, "Recent European developments in active microwave imaging for industrial, scientific, and medical applications," *IEEE Transactions on Microwave Theory and Techniques*, vol. 37, no. 12, pp. 2109–2117, 1989.
- [2] P. M. Meaney, K. D. Paulsen, A. Hartov, and R. K. Crane, "Microwave imaging for tissue assessment: initial evaluation in multitarget tissue-equivalent phantoms," *IEEE Transactions on Biomedical Engineering*, vol. 43, no. 9, pp. 878–890, 1996.
- [3] L. Garnerio, A. Franchois, J. P. Hugonin, C. Pichot, and N. Joachimowicz, "Microwave imaging—complex permittivity reconstruction by simulated annealing," *IEEE Transactions on Microwave Theory and Techniques*, vol. 39, no. 11, pp. 1801–1807, 1991.
- [4] K. Planche and S. Vinnicombe, "Breast imaging in the new era," *Cancer Imaging*, vol. 4, pp. 39–50, 2004.
- [5] M. Mark, T. Bjorninen, Y. D. Chen et al., "Wireless channel characterization for mm-size neural implants," in *Proceedings of the 32nd Annual International Conference of the IEEE Engineering in Medicine and Biology Society (IEEE-EMBS 10)*, pp. 1565–1568, September 2010.
- [6] M. Converse, E. J. Bond, S. C. Hagness, and B. D. Van Veen, "Ultrawide-band microwave space-time beamforming for hyperthermia treatment of breast cancer: a computational feasibility study," *IEEE Transactions on Microwave Theory and Techniques*, vol. 52, no. 8, pp. 1876–1889, 2004.
- [7] J. J. Lagendijk, "A microwave heating technique for the hyperthermic treatment of tumours in the eye, especially retinoblastoma," *Physics in Medicine and Biology*, vol. 27, no. 11, pp. 1313–1324, 1982.
- [8] G. B. Gentili, V. Tesi, M. Linari, and M. Marsili, "A versatile microwave plethysmograph for the monitoring of physiological parameters," *IEEE Transactions on Biomedical Engineering*, vol. 49, no. 10, pp. 1204–1210, 2002.
- [9] J. Montreuil and M. Nachman, "Multiangle method for temperature measurement of biological tissues by microwave radiometry," *IEEE Transactions on Microwave Theory and Techniques*, vol. 39, no. 7, pp. 1235–1239, 1991.
- [10] R. K. Amineh, A. Trehan, and N. K. Nikolova, "TEM horn antenna for ultra-wide band microwave breast imaging," *Progress In Electromagnetics Research B*, no. 13, pp. 59–74, 2009.
- [11] E. Alanen and I. V. Lindell, "Effect of skin in microwave detection of breast cancer," *IEEE Transactions on Microwave Theory and Techniques*, vol. 34, no. 5, pp. 584–588, 1986.
- [12] P. Soontornpipit, C. M. Furse, and Y. C. Chung, "Design of implantable microstrip antenna for communication with medical implants," *IEEE Transactions on Microwave Theory and Techniques*, vol. 52, no. 8, pp. 1944–1951, 2004.
- [13] S. Jacobsen, P. R. Stauffer, and D. G. Neuman, "Dual-mode antenna design for microwave heating and noninvasive thermometry of superficial tissue disease," *IEEE Transactions on Biomedical Engineering*, vol. 47, no. 11, pp. 1500–1509, 2000.
- [14] T. Karacolak, A. Z. Hood, and E. Topsakal, "Design of a dual-band implantable antenna and development of skin mimicking gels for continuous glucose monitoring," *IEEE Transactions on Microwave Theory and Techniques*, vol. 56, no. 4, pp. 1001–1008, 2008.
- [15] R. Nilavalan, I. J. Craddock, A. Preece, J. Leendertz, and R. Benjamin, "Wideband microstrip patch antenna design for breast cancer tumour detection," *IET Microwaves, Antennas and Propagation*, vol. 1, no. 2, pp. 277–281, 2007.
- [16] Ansoft HFSS, Ver. 12, Ansys Inc, <http://www.ansys.com/>.
- [17] S. Padhi, F. Liu, B. K. Li, N. Shuley, and S. Crozier, "On the accurate modeling of a complex antenna for breast tumor detection using a hybrid MOM/FDTD approach," in *Proceedings of the 29th Annual International Conference of IEEE-EMBS, Engineering in Medicine and Biology Society (EMBC '07)*, pp. 6636–6639, August 2007.
- [18] G. N. Bindu, A. Lonappan, V. Thomas, C. K. Aanandan, and K. T. Mathew, "Dielectric studies of corn syrup for applications in microwave breast imaging," *Progress In Electromagnetics Research*, vol. 59, pp. 175–186, 2006.

Research Article

High Gain and High Directive of Antenna Arrays Utilizing Dielectric Layer on Bismuth Titanate Ceramics

F. H. Wee,¹ F. Malek,² Farid Ghani,¹ S. Sreekantan,³ and A. U. Al-Amani³

¹ School of Computer and Communication Engineering, Universiti Malaysia Perlis (UniMAP), 02600 Arau, Malaysia

² School of Electrical Systems Engineering, Universiti Malaysia Perlis (UniMAP), 02600 Arau, Malaysia

³ School of Material and Mineral Resources, Universiti Sains Malaysia (USM), 11800 Gelugor, Malaysia

Correspondence should be addressed to F. H. Wee, weefwenhoon@gmail.com

Received 11 February 2012; Accepted 28 April 2012

Academic Editor: Hala A. Elsadek

Copyright © 2012 F. H. Wee et al. This is an open access article distributed under the Creative Commons Attribution License, which permits unrestricted use, distribution, and reproduction in any medium, provided the original work is properly cited.

A high gain and high directive microstrip patch array antenna formed from dielectric layer stacked on bismuth titanate (BiT) ceramics have been investigated, fabricated, and measured. The antennas are designed and constructed with a combination of two-, four-, and six-BiT elements in an array form application on microwave substrate. For gain and directivity enhancement, a layer of dielectric was stacked on the BiT antenna array. We measured the gain and directivity of BiT array antennas with and without the dielectric layer and found that the gain of BiT array antenna with the dielectric layer was enhanced by about 1.4 dBi of directivity and 1.3 dB of gain over the one without the dielectric layer at 2.3 GHz. The impedance bandwidth of the BiT array antenna both with and without the dielectric layer is about 500 MHz and 350 MHz, respectively, which is suitable for the application of the WiMAX 2.3 GHz system. The utilization of BiT ceramics that covers about 90% of antenna led to high radiation efficiency, and small-size antennas were produced. In order to validate the proposed design, theoretical and measured results are provided and discussed.

1. Introduction

Currently, microstrip antennas with attractive features, such as low profile, light weight, and easy fabrication, are being widely used. Microstrip antennas also possess major shortcomings, such as narrow impedance bandwidth and low efficiency and gain, which seriously limit their application [1–3].

A recent pull for microwave components made of ceramic has drawn attention, especially antennas, due to their particular advantages for some applications, including zero conductor loss and low profile [4–9]. It has been shown experimentally that this kind of element can be an efficient radiator [1]. Experimental and theoretical evaluations of the ceramic antenna (CA) have been reported by many investigators [1–9].

In the search for new types of ceramic materials that achieve high permittivity and low loss, bismuth titanate (BiT), a new type of ceramic material, has been constantly developed, characterized, and implemented into the working electrical microwave model with the help of microwave

simulator software and measurement hardware. In this study, we propose a novel CA with a new branching structure that uses ceramic material. This CA was designed with a rectangular cross-sectional area, referred to as “rectangular CA,” and was executed with ceramic material that exhibits a permittivity value of 21. The study of the BiT array antenna was designed for a target resonant frequency at 2.3 GHz. The design goal is to achieve an antenna reflectivity of less than –10 dB to accommodate an efficient antenna feed with high radiation efficiency as well as a miniaturized antenna.

Increasing the gain of an antenna can be done in different ways. For example, one could use two or more evenly distributed antenna elements to put together an antenna array. Arrays have been successfully used for many years, but they still suffer from some fundamental drawbacks; the attached 100% copper plate is inevitably lossy and large in size [7, 8]. On the other hand, arrays can provide useful features such as beam-steering capability, introduction of nulls in specific directions, and secondary lobe suppression by adjusting the phase and/or amplitude of signals feeding the individual

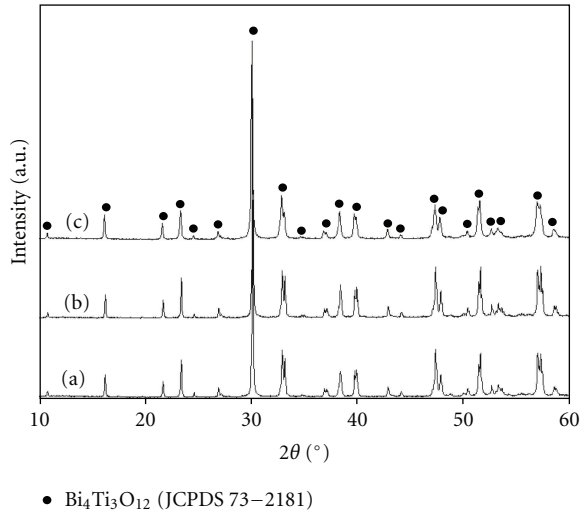


FIGURE 1: The XRD pattern of BiT powders at different calcination temperatures for 3 hours: (a) 900°C, (b) 1000°C, and (c) 1100°C.

elements. Thus, the antenna presented in this paper is based on the increasing number of patch elements that utilize BiT ceramic materials instead of copper plate as the conventional antenna uses. The analysis of BiT fabrication and outcome are thus addressed.

2. Bulk Bismuth Titanate (BiT) Analysis

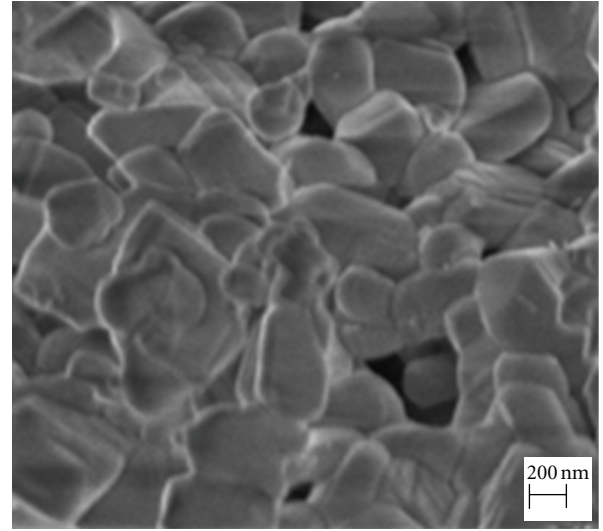
2.1. Sample Preparation. In the present study, the raw materials used consist of bismuth pentahydrate and titanium (IV) isopropoxide. Both raw materials were dissolved separately into a mixture of 2-methoxyethanol and acetylacetone. Ti solution and Bi solution were then formed from the raw material of bismuth pentahydrate and titanium (IV) isopropoxide, respectively. Both solutions were mixed and heated at 80°C to form a sticky gel and combusted to produce combusted powder. The calcination process was performed with high temperature and pressure of 750°C and 100 MPa, respectively to form a green body. Sintering was carried out at 1100°C for densification purposes.

2.2. Characterization. The X-ray diffraction (XRD) pattern in Figure 1 shows that crystallization of BiT was present as the temperature increased from 900°C to 1100°C.

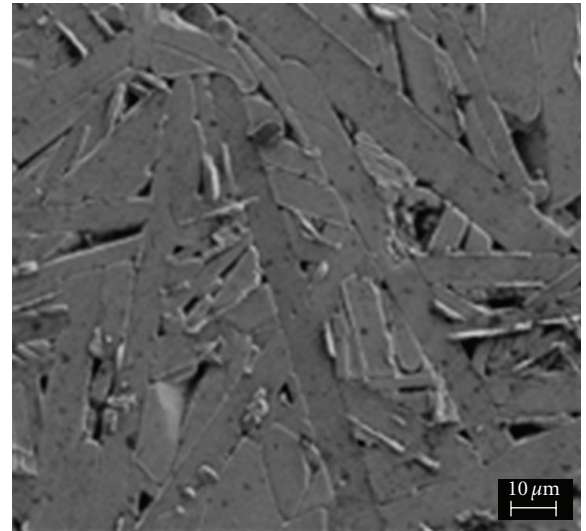
The peak in Figure 1 is centered at 2θ of 30°, which is the stable phase of pure BiT at high sintering temperature. This peak shows that the precursor had completely converted into the desired BiT compound.

The field emission scanning electron micrograph (FESEM) of BiT powder and the sintered pellet are shown in Figure 2, which shows that extensive grain growth has occurred, leading to platelet formation of the order of 200 nm to 10 μ m. The platelets of BiT form a brick-wall-like structure by aligning on top of each other, as expected with less platelets damaged during sample preparation.

In our research, we also investigated the new aspect of the development and utilization of the Agilent 85070B



(a)



(b)

FIGURE 2: FESEM image of BiT: (a) calcined powder at 750°C for 3 hours and (b) sintered bulk ceramic at 1100°C for 3 hours.

high-temperature dielectric probe kit in measuring the permittivity of the BiT ceramic material. The frequency dependence of permittivity for BiT ceramic, ϵ' , is shown in Figure 3. As can be seen, the parameter has a strong dependence on frequency, with the permittivity decreasing as frequency increases; however, for the frequency range of 2 to 3 GHz, the permittivity of BiT was on average 21, as shown in Table 1.

3. BiT Array Antenna Design and Structures

The proposed BiT array antennas have two layers, which are shown in Figure 4. The first layer is a transmission line, seen in Figure 4(a). Its optimal dimension is also presented in Figure 5. The transmission line uses copper, which is

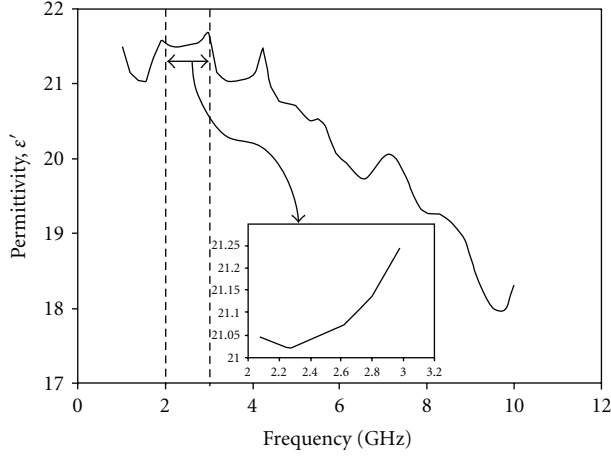
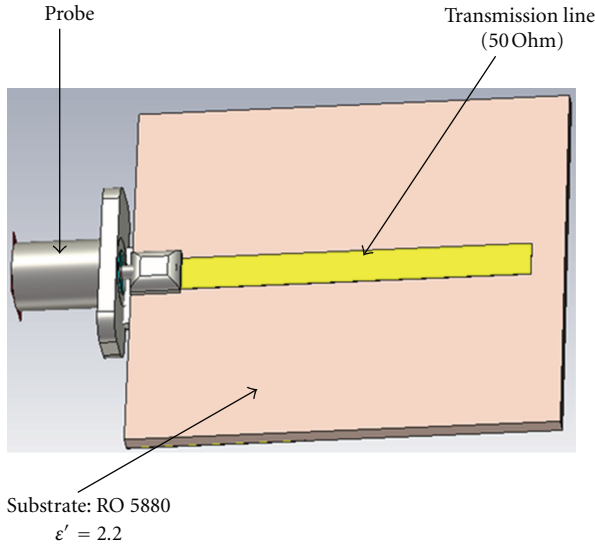
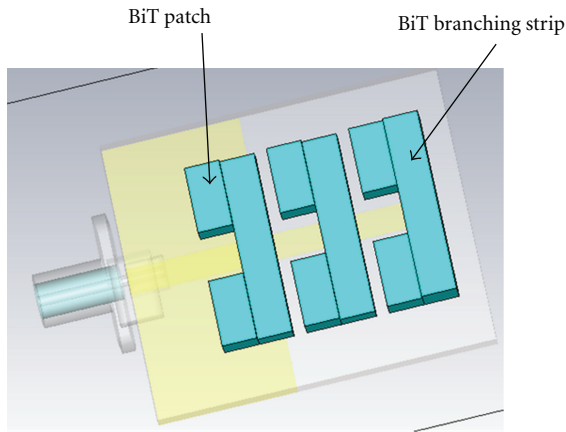


FIGURE 3: Permittivity of BiT ceramic at 1 to 10 GHz.



(a)



(b)

FIGURE 4: Configuration of the multilayers and its optimized dimensions, (a) first layer, (b) second layer.

TABLE 1: Permittivity of BiT at frequency 2 to 3 GHz.

Frequency, GHz	Permittivity, ϵ'
2.0800	21.0469
2.2600	21.0233
2.4400	21.0447
2.6200	21.0761
2.8000	21.1385
2.9800	21.2498

a conducting material, in order to function as a feeding channel.

For the second layer of this investigation, the effectiveness of BiT was determined as a radiating element itself. The novelty of this design is the BiT ceramics with high permittivity and low loss. The attenuation due to the conductor can be simplified as:

$$\alpha_c = \frac{8.68 R_s}{WZ} \text{ (dB/cm)}, \quad (1)$$

where R_s is the surface resistivity and is given by:

$$R_s = \sqrt{\frac{\omega \mu_0}{2\sigma_c}}, \quad (2)$$

$$\alpha_c = \frac{8.68}{WZ} \sqrt{\frac{\omega \mu_0}{2\sigma_c}} \text{ (dB/cm)}.$$

The attenuation due to dielectric material can be given by the following formula [2]:

$$\alpha_d = \frac{\omega}{2} \sqrt{(\mu_0 \epsilon_0 \epsilon_r) \tan \delta}, \quad (3)$$

where

$$\omega = 2\pi f_r,$$

$$\tan \delta = \frac{\epsilon_r''}{\epsilon_r'}, \quad (4)$$

$$\epsilon_r = \epsilon_r' - i\epsilon_r''.$$

The reflection loss of BiT is much smaller compared to that of conventional copper, which is often used in antenna application. At 2.30 GHz, reflection loss for BiT is 0.060 dB/cm, while for copper, the reflection loss achieves up to 1.028 dB/cm. The proper sizes, positions, and shapes were added to the second layer of antenna as shown in Figure 4(b).

Three types of BiT array antenna designs had been carried out in this study. There are two, four, and six elements of BiT ceramic in array antenna that had different respective dimensions. The geometry of the proposed BiT array antennas is shown in Figure 5, which presents both the front and side views. The antenna is realized on a low-loss RT/Duroid 5880 commercial microwave substrate from Roger Corporation (<http://www.rogerscorp.com/>), with a permittivity of 2.20, where the BiT branching strips and patches are of 21 in permittivity value. The transmission line width is

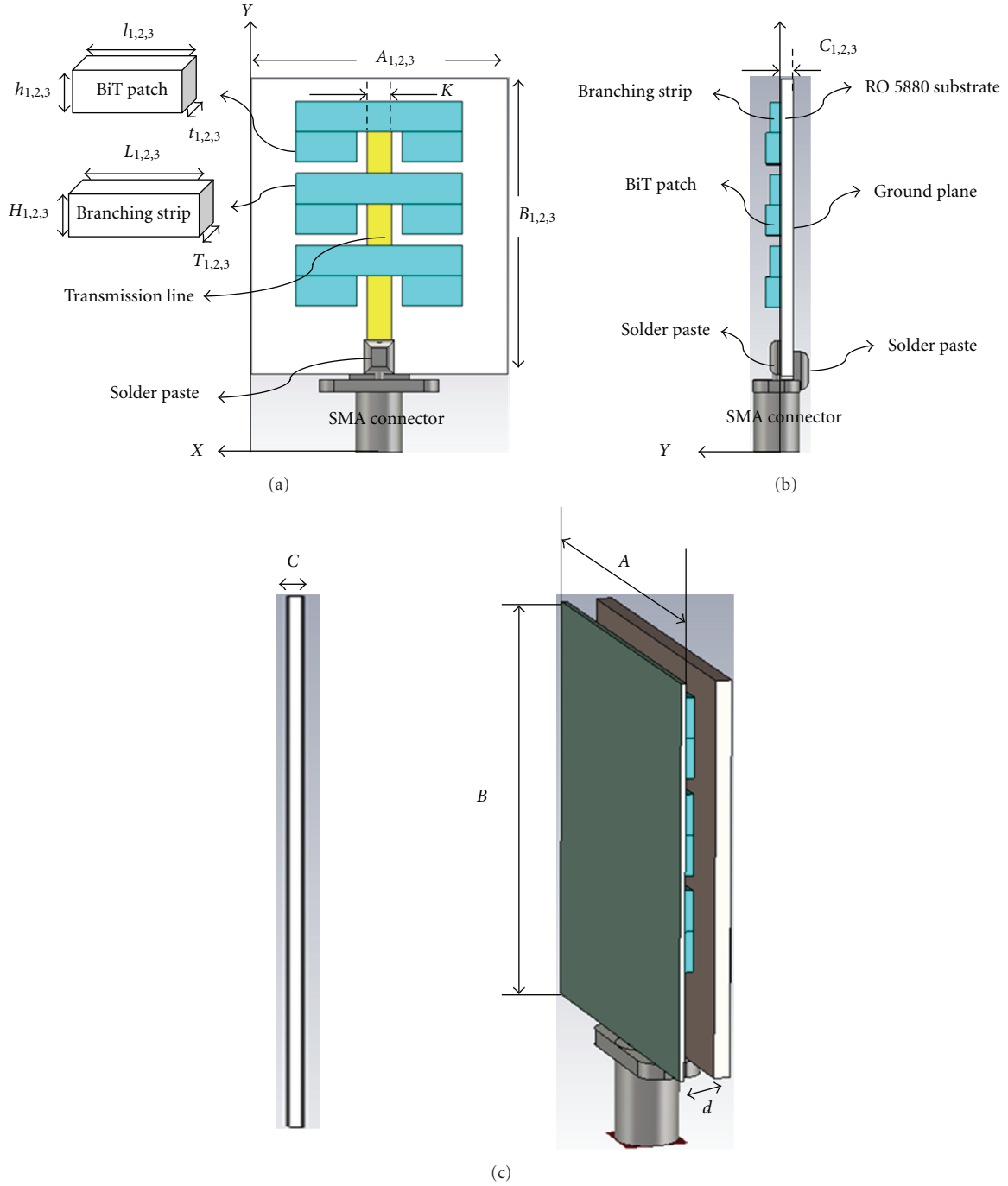


FIGURE 5: Geometry layout of proposed BiT array antenna (a) front (b) side views (c) stacked dielectric layer.

optimized to $K = 4.6$ mm in order to achieve the best 50Ω input impedance matching.

The number of elements and the wavelength of the ceramic array antenna, λ_g were approximated using:

$$\lambda_g = \frac{\lambda_0}{\sqrt{n\epsilon'}}, \quad (5)$$

where λ_g is the guided wavelength in CA, λ_0 is the freespace wavelength, ϵ' is the dielectric constant of the ceramic, and n denotes the number of ceramic elements. Hence, (5) shows

that the higher the number of ceramic elements, the smaller the size of the array antenna obtained. In addition, optimization was also carried out for the BiT ceramic dimensions in order to gain the best antenna performance.

The optimal antenna size for the quantity of two elements BiT is $A_1 = 30$ mm, $B_1 = 33$ mm, and $C_1 = 1.6$ mm. The parameter of BiT branching strip and patches are $H_1 = 2.5$ mm, $L_1 = 27$ mm, $T_1 = 1$ mm and $h_1 = 2.5$ mm, $l_1 = 4.5$ mm, and $t_1 = 0.8$ mm, respectively. Next, four elements of BiT were attached on the RT/Duroid 5880 substrate board with each



FIGURE 6: Photograph of fabricated BiT array antennas (a) two BiT ceramic elements (b) four BiT ceramic elements (c) six BiT ceramic elements (d) dielectric layer (i) front view (ii) perspective view.

edge of the BiT patch size being $h_2 = 2.5$ mm, $l_2 = 3.5$ mm, and $t_2 = 0.8$ mm; the length, l_2 , had been reduced 33% from the two elements of BiT antenna, while the BiT array antenna sizes for the four elements are $A_2 = 27$ mm, $B_2 = 29$ mm, and $C_2 = 1.6$ mm, which are on average 3 mm smaller than the two elements of BiT antenna. Branching strip dimensions were optimized to $H_2 = 2.5$ mm, $L_2 = 25$ mm, and $T_2 = 1$ mm to obtain good radiation properties. Lastly, the size of the six-element BiT antenna can be observed as the smallest compared to both the two- and four-BiT elements of the BiT array antenna, which are $A_3 = 22$ mm, $B_3 = 25$ mm, and $C_3 = 1.6$ mm, and each of the BiT patch element sizes is $h_3 = 2.5$ mm, $l_3 = 3$ mm, $t_3 = 0.8$ mm, while the BiT branching strip is $H_3 = 2.5$ mm, $L_3 = 20$ mm, and $T_3 = 1$ mm. Besides the modeling design, the prototype of the BiT array antennas were fabricated and measured, as can be seen in Figure 6.

This aimed to ensure a good agreement in performance between them.

In designing the BiT array antenna and the dielectric layer stacked as well, one must consider the possibility of high loss performed by the antenna. Numerical simulation shows high levels of the conduction loss and power loss with the utilization of the metallic structure on the antenna. Therefore, BiT array antennas were designed with low-loss BiT elements present with negligible metallic loss in antenna structure to reduce the loss factor that will lead to low antenna performance.

4. Dielectric Layer Design

To overcome the disadvantages of low gain and directivity, some papers have proposed gain enhancement methods

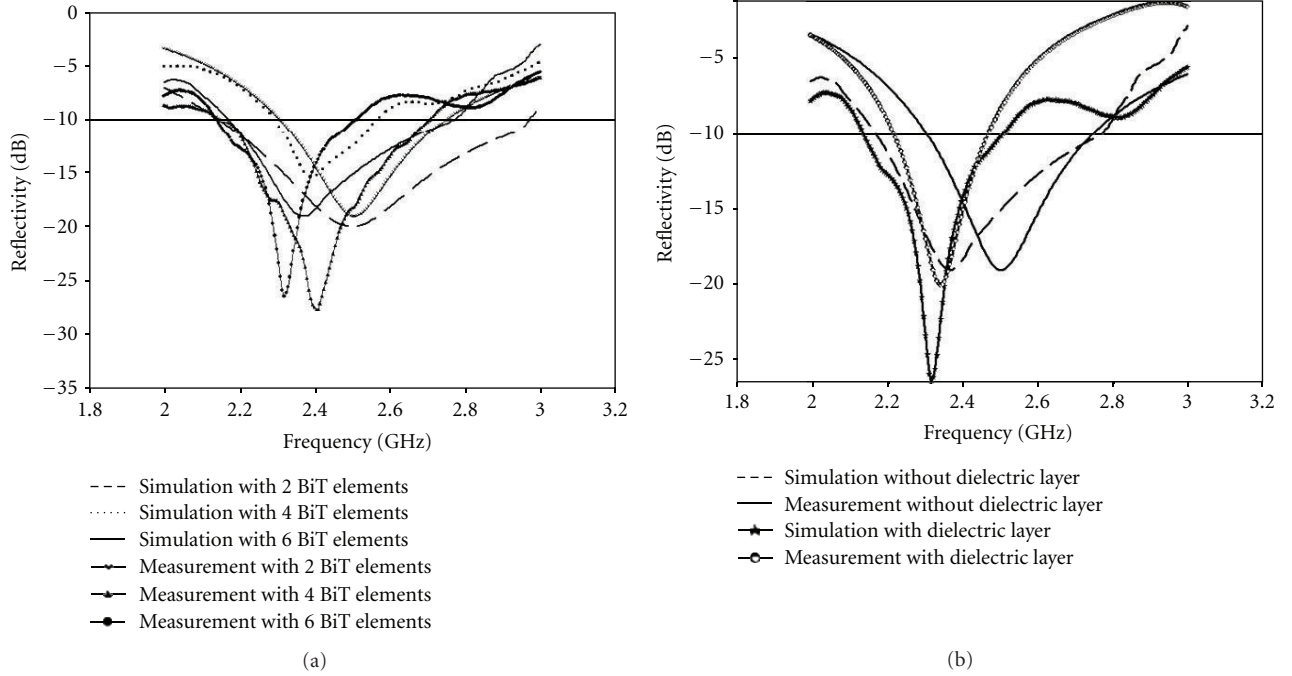


FIGURE 7: Simulated and measured reflectivity of the proposed BiT array antennas (a) two-, four-, and six-BiT element array antenna (b) with and without the dielectric layer.

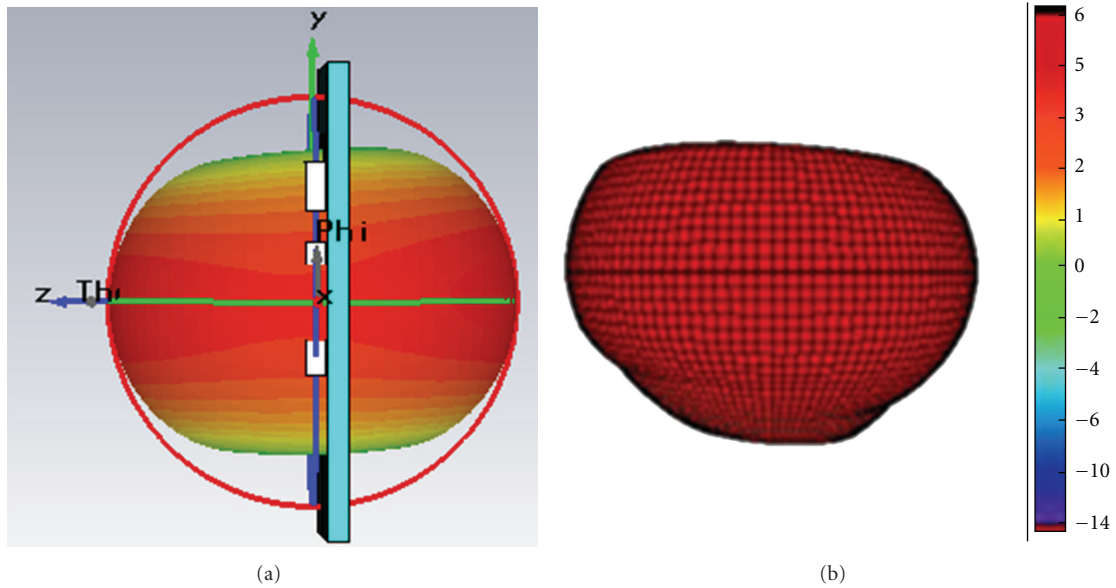


FIGURE 8: Radiation pattern of BiT in 3D view (a) simulated (b) measured.

using multiple dielectrics [7–9]. It has been reported that high gain and high directivity can be achieved if the substrate and dielectric layer are used appropriately [9].

In order to obtain high gain and directivity of this antenna, a suitable dielectric layer of appropriate thickness and loss tangent is chosen. Thinner dielectrics which help to reduce weight also able to reduce the surface wave losses. The dielectric's dielectric constant, ϵ' , plays an important role similar to that of the dielectric's thickness. A low value of ϵ'

for the dielectric will increase the fringing field of the patch and thus the radiated power. A low-loss tangent reduces the dielectric loss and therefore increases the antenna efficiency. Thus, the dielectric parameters so chosen are Tarconic CER-10, with a thickness of 0.5 mm, permittivity of $\epsilon' = 10$, and a loss tangent $\tan \delta = 0.0004$.

The dielectric with dimensions of $R = 25$ mm, $A = 20$ mm, and $C = 0.5$ mm as in Figure 5(c) is placed above the radiating patch BiT elements at a distance of $d = 5$ mm,

TABLE 2: Gain, directivity, and radiation efficiency of BiT Array Antennas.

Parameters (2.3 GHz)	Number of BiT element			BiT array antenna with dielectric layer
	2 elements	4 elements	6 elements	
Gain (dB)	6.559	7.188	7.514	8.920
Directivity (dBi)	7.174	7.697	7.913	9.230
Radiation Efficiency (%)	91.4	93.4	95.0	96.6

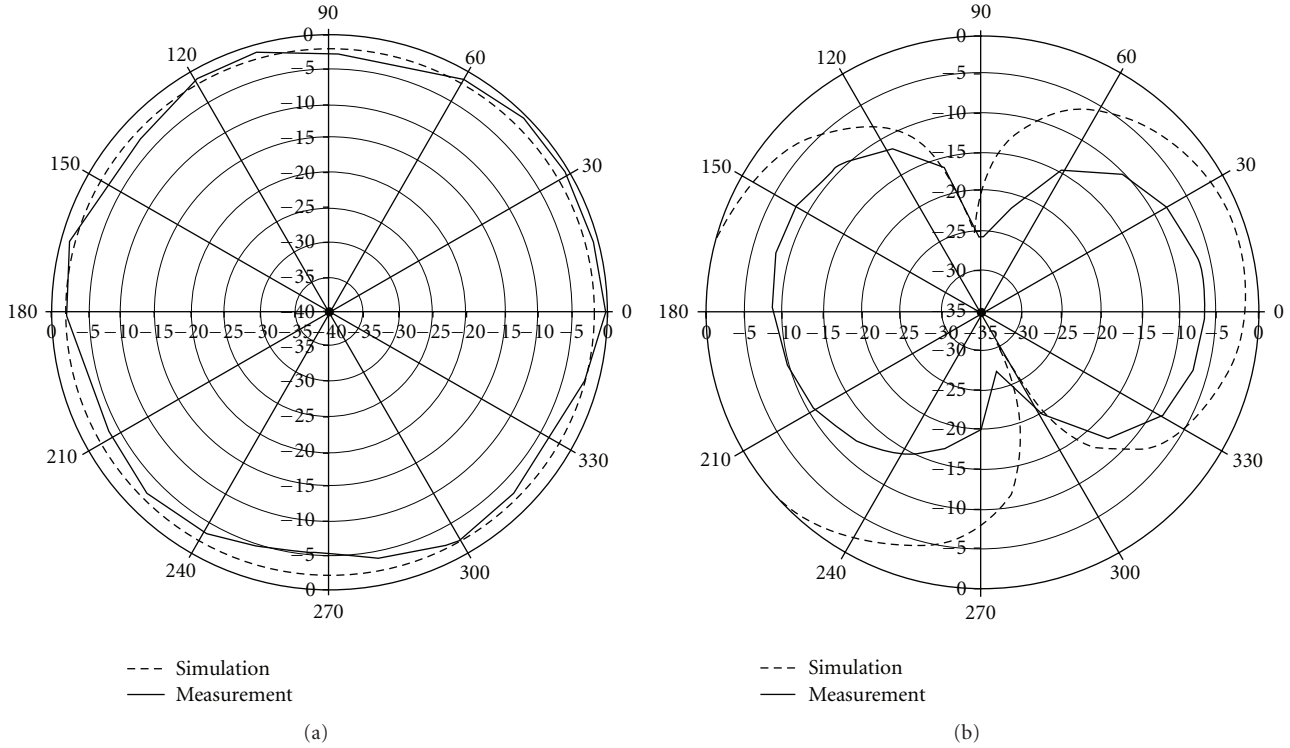


FIGURE 9: Simulated and measured 2D radiation plot for a six-BiT element array antenna at 2.30 GHz (a) horizontal plane (b) vertical plane.

which is the optimum distance at which to obtain high gain and high directivity. This paper experimentally investigates the effect of a dielectric layer as the superstrate layer for high gain and high directivity on the six elements of BiT array antenna and the comparison between BiT array antenna with and without the dielectric layer.

5. Results and Discussion

The performance of the simulated BiT array antennas with and without the dielectric layer is analysed using Computer Simulation Technology (CST) Microwave Studio, while the fabricated BiT array antennas with and without the dielectric layer were tested using a network analyser and a near-field test facility. Figure 7(a) shows a graph of reflectivity of two-, four-, and six-element BiT array antenna, which had been converted into log magnitude in dB.

The simulation and measurement results show that the reflectivity is the lowest at -27 dB at the centre frequency of 2.40 GHz for BiT array antenna without the dielectric layer. However, with the stackedness of the dielectric layer on BiT

array antennas, the frequency had been shifted to a lower frequency of 2.30 GHz. The frequency shift is also occurring when the number of BiT elements increases from a two-element to a six-element array antenna, as can be seen in Figure 7(b). This condition occurs due to the capacitive effects of placing the dielectric over the antenna.

The operating bandwidth of the proposed BiT array antennas for both with and without the dielectric layer was found to be about 350 MHz and 500 MHz, respectively, which is compatible with the specification of the WiMAX system. Overall, good agreements were found between the simulation and measurement results, although there was slight discrepancy between them, believed to be due to the environmental effect and mechanical tolerance, which were neglected in our simulations.

The simulated and measured radiation patterns in 3D view are observed in Figure 8. There were no top and bottom lobes at the rear end of the radiation pattern whilst the main directivity was directed at the vertical plane, which formed an omnidirectional signal level in the H-plane. The H-plane plays an important role as this parameter determines

the point of strongest signal, thus avoiding signal redundancy and interference with other antennae radiating at the same plane.

Figure 9 shows the radiation pattern of a six-element BiT array antenna in 2D view, which was analyzed in vertical plane (XZ, YZ) and in horizontal plane (XY) at 2.30 GHz. This antenna provides a 360-degree coverage signal, which is in all directions (horizontally) for two-way communication.

From Table 2, the gain of the six-element BiT array antenna, in radiation patterns, with dielectric layer does exhibit 8.920 dB and 9.230 dBi of gain and directivity, respectively. The simulation results show that the gain of the 4-element BiT array antenna has improved greatly compared to the common antenna.

6. Conclusions

In this paper, the application of rectangular bismuth titanate (BiT) material as a ceramic antenna (CA) in array form, which composed of two-, four-, and six-element BiT as well as a stacked dielectric layer, were investigated and successfully carried out. The antenna exhibited acceptable bandwidths, reflectivity, and radiation characteristics for WiMAX application. As a result, we find that BiT array antennas are attractive and can be practical for various systems. By taking into account all of the details of each component, including the dimensions and permittivity value, the antennas did perform up to expectation when the number of BiT element increased at the WiMAX band. In future work, bismuth titanate (BiT) can be investigated for other types of antenna in order to determine the level of performance improvement in term of bandwidth particularly in an optimized radiation pattern. In addition, antenna enhancement can be done by adjusting the distance d , and the resonance condition for high gain as well as high directivity can be obtained.

References

- [1] M. F. Ain, S. I. S. Hassan, J. S. Mandeep et al., "2.5 GHz batio₃ dielectric resonator antenna," *Progress in Electromagnetics Research*, vol. 76, pp. 201–210, 2007.
- [2] C. A. Balanis, *Antenna Theory: Analysis and Design*, Wiley Interscience, Hoboken, NJ, USA, 3rd edition, 2005.
- [3] S. Prabhu, J. S. Mandeep, and S. Jovanovic, "Microstrip band-pass filter at S band using capacitive coupled resonator," *Progress in Electromagnetics Research*, vol. 76, pp. 223–228, 2007.
- [4] R. K. Mongia, A. Ittipiboon, and M. Cuhaci, "Measurement of radiation efficiency of dielectric resonator antennas," *IEEE Microwave and Guided Wave Letters*, vol. 4, no. 3, pp. 80–82, 1994.
- [5] A. A. Kishk, X. Zhang, A. W. Glisson, and D. Kajfez, "Numerical analysis of stacked dielectric resonator antennas excited by a coaxial probe for wideband applications," *IEEE Transactions on Antennas and Propagation*, vol. 51, no. 8, pp. 1996–2006, 2003.
- [6] A. A. Kishk, "Wide-band truncated tetrahedron dielectric resonator antenna excited by a coaxial probe," *IEEE Transactions on Antennas and Propagation*, vol. 51, no. 10, pp. 2913–2917, 2003.
- [7] M. T. Lee, K. M. Luk, K. W. Leung, and M. K. Leung, "Small dielectric resonator antenna," *IEEE Transactions on Antennas and Propagation*, vol. 50, pp. 1485–1487, 2002.
- [8] J. Clerk Maxwell, *A Treatise on Electricity and Magnetism*, vol. 2, Clarendon, Oxford, UK, 3rd edition, 1892.
- [9] S. Sreekantan, A. F. M. Noor, Z. A. Ahmad, R. Othman, and A. West, "Structural and electrical characteristic of crystalline barium titanate synthesized by low temperature aqueous method," *Journal of Materials Processing Technology*, vol. 195, no. 1–3, pp. 171–177, 2008.